COLLECTIVE DYNAMICS IN DISPERSIONS OF ANISOTROPIC AND DEFORMABLE PARTICLES

A DISSERTATION

SUBMITTED TO THE DEPARTMENT OF MECHANICAL ENGINEERING

AND THE COMMITTEE ON GRADUATE STUDIES

OF STANFORD UNIVERSITY

IN PARTIAL FULFILLMENT OF THE REQUIREMENTS

FOR THE DEGREE OF

DOCTOR OF PHILOSOPHY

David Saintillan

August 2006

I certify that I have read this dissertation and that, in my opinion, it is fully adequate in scope and quality as a dissertation for the degree of Doctor of Philosophy.

_____

Eric S. G. Shaqfeh   Principal Co-Advisor

I certify that I have read this dissertation and that, in my opinion, it is fully adequate in scope and quality as a dissertation for the degree of Doctor of Philosophy.

_____

Eric Darve   Principal Co-Advisor

I certify that I have read this dissertation and that, in my opinion, it is fully adequate in scope and quality as a dissertation for the degree of Doctor of Philosophy.

_____

Juan G. Santiago

I certify that I have read this dissertation and that, in my opinion, it is fully adequate in scope and quality as a dissertation for the degree of Doctor of Philosophy.

_____

Sanjiva K. Lele

Approved for the University Committee on Graduate Studies.

Abstract

The modeling of complex fluids, such as particulate suspensions, emulsions and polymer solutions, remains a great challenge in spite of their omnipresence in many natural processes and industrial applications. A major difficulty in the understanding of these systems arises from the slow decay of hydrodynamic disturbances in low-Reynolds-number flows, which leads to long-ranged interactions between suspended particles and often results in strong velocity fluctuations and large-scale correlated motions. In this work, we use theory and numerical simulations to address a few problems in which hydrodynamic interactions result in collective dynamics, with emphasis on the effects of particle shape and deformability.

We first address the behavior of suspensions of anisotropic particles such as rigid fibers or spheroids under sedimentation. Hydrodynamic interactions in these systems are known to result in a concentration instability by which the particles aggregate into dense clusters surrounded by clarified fluid. Using newly developed efficient algorithms, we perform large-scale simulations of such suspensions with the aim of understanding the mechanism of the instability and of elucidating the wavenumber selection process reported in experiments. The salient features of the instability are adequately captured, and the formation of inhomogeneities is shown to be closely linked to the velocity fluctuations in the suspending fluid. In particular, simulations in finite containers exhibit a wavenumber selection, and we use a linear stability analysis to show that the size of the concentration fluctuations is controlled by vertical density gradients that are observed to form during the sedimentation process. The case of deformable particles, such as viscous droplets,

elastic microcapsules or flexible polymers, is also discussed, and a linear stability analysis and numerical simulations both demonstrate that a similar instability also exists in these systems.

We then investigate the dynamics in suspensions of uncharged polarizable rigid rods placed in an electric field. The polarization of a rod results in the formation of a dipolar charge cloud around its surface, leading to a non-linear fluid slip: this phenomenon, termed induced-charge electrophoresis, causes particle alignment with the applied field and creates a disturbance flow in the surrounding fluid. Under the thin double layer approximation, we derive a simple slender-body formulation for this effect valid for high-aspect-ratio particles, and use it to study hydrodynamic interactions between a pair of aligned rods. In particular, the pair probability density function in a dilute dispersion is calculated, and indicates that particle pairing can be expected. We also present results from large-scale numerical simulations that include both far-field and near-field hydrodynamic interactions as well as Brownian motion. Particle pairing is indeed observed to occur at high values of the Péclet number (weak Brownian motion), and results are reported for pair probabilities, orientation distributions and hydrodynamic diffusivities.

Finally, we apply Brownian dynamics to investigate the cross-streamline migration of short-chain polymers in a pressure-driven flow between two infinite flat plates, with emphasis on the effects of chain flexibility. We implement a simulation method that models a polymer molecule at the Kuhn step level as a chain of freely jointed Brownian rods, and includes multibody hydrodynamic interactions between the chain segments and channel walls. The results demonstrate the existence of shear-induced migration away from the solid boundaries toward the channel centerline as a result of wall hydrodynamic interactions. At a fixed ratio of the channel width to the bulk radius of gyration, and at a fixed value of the Weissenberg number or dimensionless flow strength, we find that migration is not significantly influenced by flexibility for chains longer than two Kuhn steps. Much weaker migration is observed for fully rigid chains, and a mechanism is proposed to explain migration in that case.

Acknowledgements

The research presented in this thesis would not have been possible without the support and guidance of my two research advisors, Eric Shaqfeh and Eric Darve. I am very lucky to have had the opportunity to work with both of them, and I have learnt tremendous amounts from them. Eric Shaqfeh is a dedicated researcher, who taught me much of what I know in fluid mechanics, and showed me the importance of tackling difficult problems. Eric Darve is a very sharp individual, to whom I owe much of my current knowledge in numerical methods and computation. I am grateful to both of them for their help and encouragements, and for giving me their curiosity and passion for scientific research.

On some of the problems described in this thesis, I benefited from advice, comments or suggestions from a number of people. On sedimentation, I worked closely in collaboration with Elisabeth "Babette" Guazzelli and her graduate student Bloen Metzger at Institut Universitaire des Systèmes Thermiques Industriels in Marseille, France, where experiments were being conducted. I thank them for their warm hospitality when I visited them in Marseille, and for the many discussions I had with them, some of which led to significant advances in my work. I am also grateful to Jason E. Butler for providing me with his codes, which helped me get started early on during my Ph.D., and to Michael P. Brenner for suggesting during a fruitful discussion that I consider the effects of stratification on the instability of sedimenting fibers. On electrokinetics, I enjoyed collaborating with Juan G. Santiago and his student Klint A. Rose, whose insight on electrokinetic phenomena was of tremendous use for some of the work described here. I also thank Fabio Baldessari for a number of insightful discussions on electro-osmosis and electrophoresis.

Hast Thou shaped the marvel of the whirling spheres,
A scientist passing Nature though his tubes
And played with numbers, measures, theorems, cubes,
O mathematician Mind that never errs...

Sri Aurobindo, *Creation.*

Contents

List of Tables

List of Figures

Chapter 1

Introduction

1.1   Transport phenomena in complex fluids

Dispersions of particles or macromolecules in viscous liquids, otherwise known as complex fluids, are ubiquitous in both natural phenomena and industrial applications. Suspensions of rigid particles, which are the main focus of the present work, are very common in environmental fluid mechanics, where sediments in rivers and estuaries or pollution particles in the atmosphere are but a few examples. In biological systems, blood plays a central role and can be viewed as a suspension of flexible particles (red blood cells) in a viscous liquid (plasma). Finally, particulate suspensions and macromolecular solutions are of paramount importance in industrial products and applications, including foodstuffs and cosmetics, inks and paints, waste matter treatment, the processing of fiber composites etc.

The macroscopic modeling of these materials often requires a precise understanding of their microscopic behavior, which is dictated by the interactions between the particles, the suspending fluid or solvent, solid boundaries, and various external fields (e.g. gravity, electric or magnetic fields). In such systems, a central role is played by hydrodynamic forces, which are mediated by the fluid and result from the disturbance of the fluid motion by the suspended particles. More precisely, a particle in a fluid modifies the velocity field around

it by creating a disturbance, which in turn influences the motion of the surrounding particles. When fluid and particle inertia can be neglected with respect to the viscous forces in the fluid (formally, when the Reynolds and Stokes numbers are vanishing, see Section 2.1), these hydrodynamic interactions decay very slowly with the separation distance between the particles (typically like the first or second power of the inverse separation, depending on the flow type). The interactions between widely separated particles therefore cannot be neglected, and in large suspensions this can result in significant effects, such as strong velocity fluctuations, large-scale correlated motions and other collective dynamics.

A central problem in the modeling of hydrodynamic interactions in particulate suspensions is the determination of the suspension microstructure, or configuration of the particles with respect to one another and to external flows or boundaries. The configuration of the particles is indeed determined by the fluid flow, which can convect, orient or deform the particles. In turn, the fluid flow is itself a function of the configuration of the particles, since these also induce significant disturbance flows. This two-way coupling between suspension microstructure and fluid flow renders the modeling and the understanding of these systems quite complex. Numerous theoretical investigations have therefore typically been limited to infinitely dilute suspensions, where interactions are altogether neglected, or very dilute suspensions, where interactions between pairs of particles are assumed to dominate: these models, which provide reasonable results in a few situations such as simple linear flows [14], are however unable to capture the dynamics in situations where long-ranged interactions play a stronger role as in sedimentation for instance [34, 103]. In these more complex situations computer simulations offer a valuable tool as demonstrated below.

The vast majority of investigations on particulate flows have focused on monodisperse suspensions of rigid spheres in a variety of situations. The sedimentation [46, 87, 150] and the rheology [15, 181] of such suspensions have been extensively studied, and even though questions remain a fair understanding is now available. Less can be said however of anisotropic or deformable particles, which occur quite commonly in natural and industrial processes, as is quite clear from the aforementioned examples. In this case, the particle configuration itself (orientation or shape) is determined by the local flow field and the

history of the particle motion, and must be solved for as part of the problem: anisotropic particles may orient preferentially in certain directions depending on the local fluid flow, while deformable particles may stretch or compress. In turn, this configuration has an influence on the particle dynamics as well as on the surrounding fluid flow: for instance, the sedimentation speed of an anisotropic particle depends strongly on its orientation, while the stress exerted by a polymer molecule or viscous drop on the surrounding fluid depends on its degree of stretching along the axes of flow extension.

In the present work we use theory and numerical simulations to investigate the effects of particle shape and particle deformability or flexibility in a variety of flow situations, including sedimentation, induced-charge electrophoresis and pressure-driven flows. First, a general introduction to these various flows is in order. More detailed reviews will be given in Chapters 4 through 7.

1.1.1   Sedimentation

Sedimentation occurs whenever a density mismatch exists between a suspended particle and the surrounding fluid. As a result of this mismatch, the particle is subject to a constant applied force $\boldsymbol{F}$ which causes the motion of the particle and drives a disturbance flow in the surrounding fluid. To leading order, this disturbance flow is the flow induced by a point force, also known as Stokeslet:

$$\boldsymbol{u}(\boldsymbol{r}) = \frac{1}{8\pi\mu}\left(\frac{\mathsf{I}}{r} + \frac{\boldsymbol{r}\boldsymbol{r}}{r^3}\right)\cdot\boldsymbol{F} + ..., \tag{1.1}$$

where μ is the viscosity of the fluid, and $\boldsymbol{r}$ is a position vector emanating from the center of mass of the particle. Because of the slow decay of this disturbance flow as $1/r$, the calculation of statistical quantities such as the mean velocity or the velocity variance typically results in diverging integrals [13, 86, 150].

Batchelor [13], working on the premise of homogeneity and diluteness, was the first to calculate the concentration correction of the mean sedimentation speed of non-Brownian spheres in an infinite fluid. His result was confirmed by others [86, 71, 64], although it

appears that the functional dependence of the hindered settling function depends on the statistical structure of the suspension [156]. As reviewed in more detail in Chapter 4, the problem of predicting the velocity variance in such a system remains however unresolved, with theories for random suspensions predicting a divergence of the velocity variance with the system size [34, 87] in contrast with experiments, which suggest that neither velocity fluctuations nor hydrodynamic diffusivities depend on the container dimensions [137]. This discrepancy suggests that other effects such as a non-random microstructure or interactions with container boundaries may play a role in determining the size of the fluctuations, and a variety of theories have been proposed to include these effects (e.g. [103, 28, 132]). As we discuss in Chapters 4, 5 and 6, sedimentation is yet more complex when the particles are non-spherical or are allowed to deform under flow: in that case we will show that an instability takes place that causes the particles to cluster [102], thereby reinforcing the velocity fluctuations.

1.1.2   Electrokinetic flows

When a charged surface is in contact with an electrolyte, counterions in solution migrate and accumulate near the surface, forming an electrical double layer (EDL) [153]. When an external field $\boldsymbol{E}_\infty$ is applied, the action of the field on the excess counterions causes them to migrate along the electric field lines, dragging the fluid with them. Near a fixed surface such as a channel wall, this effective body force exerted by the moving ions on the fluid inside the EDL drives an electro-osmotic flow in the fluid bulk. In the case of a freely suspended particle such as a colloid or macromolecule, electrophoretic migration occurs.

Electrophoresis of particles with a fixed and uniform surface charge has received considerable attention in the past (see Chapter 5 for a more thorough review), and is well understood. In particular, in the case of a thin EDL and weak external field, the particle migrates in the direction of the external field at the velocity:

$$\boldsymbol{U} = \frac{\varepsilon\zeta}{\mu}\boldsymbol{E}_\infty, \tag{1.2}$$

where ε and μ are the permittivity and viscosity of the electrolyte, and ζ is the zeta-potential of the surface, or potential drop across the EDL. In addition, the motion of the particle drives the following disturbance flow in the fluid [5]:

$$\boldsymbol{u}(\boldsymbol{r}) = \frac{\varepsilon\zeta}{2\mu}\left(\frac{a}{r}\right)^3\left(3\frac{\boldsymbol{rr}}{r^2} - \mathsf{I}\right)\cdot\boldsymbol{E}_\infty, \tag{1.3}$$

which is a potential dipole flow. In particular, the particle motion, which is interfacially driven, is force-free as the electric force on the particle is entirely screened by the opposing force on the counterions inside the EDL. Interactions between particles are therefore relatively weak (they decay as $1/r^3$). Furthermore, it can be shown that in a dispersion of identical spheres with same zeta-potential, the velocity of each sphere is equal to the velocity of an isolated particle, unchanged by hydrodynamic interactions [1].

As discussed in Chapter 5, many situations depart from the ideal case described above: non-uniform zeta-potential, polarizable surfaces, thick double layers, strong applied fields, surface conduction are all examples that commonly occur in applications and greatly enhance the richness and complexity of electrokinetic phenomena. In Chapter 5, we will discuss the case of polarizable particles, which can acquire a non-uniform surface charge in an applied field. In that particular case, we shall see that hydrodynamic interactions become significant, as they now decay more slowly as $1/r^2$ and result in relative motions.

1.1.3 Pressure-driven flows

Pressure-driven channel flows play a central role in industrial applications involving the processing of suspensions or polymers solutions, and have recently regained attention with the advent of micro- and nanofluidic devices. The main characteristics of these flows is that they involve non-uniform shear and rigid boundaries, both of which may have an effect on particle dynamics.

Numerous investigations have considered shear flows of sphere suspensions in both confined and infinite geometries. The reversibility of Stokes flow predicts that a single sphere in Poiseuille flow has zero cross-streamline velocity. As demonstrated experimentally [115, 67], such is no longer the case in more concentrated suspensions, where particles

are observed to migrate from regions of strong shear (near the walls) toward regions of low shear (channel centerline). This effect is also observed in simulations [140] and can be explained on the basis of hydrodynamic diffusion [172], which occurs as a result of particle/particle interactions and is dependent on flow strength: the gradient in shear rate results in a gradient in hydrodynamic diffusivity which leads to an effective drift toward the regions of low diffusivity or low shear.

More subtle effects come into play when the particles are non-spherical or deformable, and can result in an effective migration even in the limit of infinite dilution. A single Brownian anisotropic particle such as a rigid rod in shear flow aligns preferentially in the direction of the flow, with a degree of alignment that depends on the local flow strength. Because of the anisotropic mobility of the particle, this alignment results in a decrease of the effective diffusivity in the cross-streamline direction, which is stronger in regions of strong shear. The resulting gradient in cross-streamline diffusivity therefore causes an effective drift toward the regions of strong shear, i.e. an accumulation of particles near the walls in pressure-driven channel flows [139, 164]. In addition to this effect, hydrodynamic interactions with the walls also take place, and have been shown in the case of deformable viscous droplets [173] and long-chain flexible polymers [95, 97, 37, 189, 190] to result in a migration away from the walls toward the channel centerline. In Chapter 7, we will address the case of dilute solutions of rigid and short-chain flexible polymers, which are subject to both types of migration, and we will characterize the effect of chain flexibility.

1.2   Simulation techniques for complex fluids

Numerous simulation techniques have been proposed in the past to simulate the dynamics of complex fluids in various situations. While continuum models that represent a suspension as an effective fluid are sometimes convenient, more detailed models also enable the precise determination of the particle dynamics. In Sections 1.2.1 through 1.2.4 we review a few of the more common approaches.

1.2.1 Continuum descriptions and constitutive modeling

In situations where the length scales of interest are much larger than the size of the suspended particles, or when the overall effect of the particles on the flow is of interest rather than their precise dynamics, representing the suspension or polymer solution as an effective continuum medium can be a convenient approach. The effects of the particles on the fluid are then captured through a constitutive model for the effective stress tensor, which differs from the Newtonian stress for the suspending fluid. In the simplest cases, such as for dilute suspensions of neutrally buoyant spheres, the only modification to the stress arises through an effective scalar viscosity [11], in which case the effective medium is still Newtonian. More generally, the effective stress tensor is more complex and depends on a few variables describing the microscopic configuration of the particles at a given position in the fluid (e.g. moments of the particle orientation or polymer end-to-end vector). These microscopic variables are themselves unknown and depend on the local flow field: new equations must therefore be obtained for these variables, typically based on microscopic models [18, 113]. Often the derivation of closed equations for these variables from basic principles is not possible, and closure approximations are invoked, akin to those used in turbulence modeling for Reynolds-averaged stresses [54]. The full solution of the flow problem then consists of simultaneously integrating the Stokes or Navier-Stokes equations for the flow variables, coupled to the moment equations for the microscopic variables.

While this approach is by far the most efficient for large-scale complex flows, it also suffers from a few limitations. First, the closure approximations used for the moment equations are typically derived phenomenologically and tested on simple flows: their validity in more complex flows or geometries is questionable, and may lead to inaccuracies. Second, they are often based on local approximations, which are valid when the length scales of interest are much larger than the microscopic length scales (particle size): the models therefore break down at very short length scales, and for instance cannot be applied to strongly confined flows as occur in micro- and nanofluidic devices. Finally, detailed information about the particle dynamics and configuration is lost: such information can

become important when non-uniform particle distributions occur as a result of the flow (for instance in shear-induced migration [115]), or when several distinct micro-configurations can coexist in a given flow field (for example as a result of conformation hysteresis in solutions of long-chain polymers [47, 166]).

1.2.2 Navier-Stokes solvers for the fluid phase

If a precise description of the particle motions is required, a solution can be obtained by numerically integrating the flow equations (Stokes or Navier-Stokes) in the fluid domain, with appropriate boundary conditions at the particle surfaces. The wealth of solution techniques developed previously for the numerical calculation of various flow problems can then be applied (finite differences, finite volumes or finite elements), resulting in a very detailed description of the fluid flow. These numerical techniques require a discretization of the fluid domain (meshing), which fits the particle surfaces.

Several methods of this type have been implemented in the case of suspensions (e.g. [89, 108]). The clear limitation of this approach is the need for a fine enough mesh to resolve the geometry of the particles: when the particles are very numerous and much smaller than the macroscopic dimensions, the cost of remeshing the fluid domain at each time step renders these methods impractical. This is certainly true for very anisotropic particles such as the rods or fibers that we will consider in this work: in that case the thinnest dimension, which may be orders of magnitude smaller than the characteristic particle size, would have to be resolved.

A few remedies exist to resolve this issue. The immersed boundary method, pioneered by Peskin [145, 128], no longer requires the mesh to perfectly fit the geometry of the particles: grid cells are allowed to overlap with solid boundaries, in which case the effects of boundaries on the fluid flow are captured through an effective force density inside the boundary cells, determined to enforce the no-slip boundary condition at the interface. This method, which has been widely used in a variety of situations and is very powerful in particular when deformable or compliant boundaries are present, still remains quite expensive in the case of suspension flows, as the size of the grid cells is still required to

be smaller than the particle dimension. Another approach, termed force-coupling method and developed by Maxey and coworkers [125, 119], consists of solving for the fluid velocity throughout the suspension (including inside the solid particles), and by representing the effect of the particles on the flow through distributed force moments in the momentum equation. In this case the fluid flow is no longer accurately resolved on the length scale of the particles; yet the global effect of the particles on the fluid is correctly captured, and the cost of the simulation is greatly reduced as a fixed mesh can be used throughout the simulation. Similar methods have been implemented by other authors [22, 23, 31], and we will use an analogous approach in Chapters 4 and 5.

1.2.3 Lattice-Boltzmann and dissipative particle dynamics

The very high cost of the methods described in Section 1.2.2 results mainly from the direct solution of the incompressible Navier-Stokes or Stokes equations, in which the determination of the fluid velocity at a given point is non-local, in the sense that it is coupled to the rest of the flow field through the continuity equation. This difficulty can be circumvented using the Lattice-Bolztmann method, which is based on a statistical description of the fluid flow and only involves locally determined variables. The method was pioneered by Ladd [110] who applied it mostly to sedimentation [112, 134, 135] and channel flows [38] of suspensions, and is quite efficient as its cost scales linearly with the number of lattice points in the fluid, and as its computer implementation is easily parallelized. Other advantages include an easy treatment of complex geometries and boundary conditions. Yet the method is strictly applicable to positive Reynolds numbers (it becomes very stiff as $Re \rightarrow 0$), and necessitates a lattice which is finer than the smallest particle dimension: its use for the simulation of very anisotropic particles such as slender rods is again impractical.

A somewhat similar method is called dissipative particle dynamics, and relies on a discrete description of the fluid phase using mesoscopic particles, the motion of which is described based on statistical mechanics. These particles exchange momentum between themselves and with the boundaries of the fluid domain (walls or suspended particles), and the rules for this momentum exchange ensure that the laws for the fluid motion are

correctly reproduced. Once again, this method is attractive owing to its relatively low cost and ease of parallelization, and was applied successfully to the simulation of particle suspensions [90, 21] and polymer solutions [61, 62]. Similar limitations as for the Lattice-Boltzmann method apply: in particular, a large number of mesoscopic particles must be used on the scale of the solid particles in a suspension.

1.2.4   Boundary integral methods and Stokesian dynamics

In the Stokes flow regime ($Re = 0$), a wide range of additional methods have been devised that make use of the linearity of the Stokes equations. Most of these methods are based on or can be justified from the boundary integral equation for Stokes flow (or representation theorem), which is briefly presented in Section 2.2 and describes the velocity field at any point inside the fluid in terms of convolution integrals on the domain boundaries involving an unknown surface traction field. The great advantage of this approach is that it fully describes a three-dimensional field (the fluid velocity) in terms of a two-dimensional variable (the surface tractions). A direct solution of the surface tractions can be achieved using the boundary integral and boundary element methods [198, 147], which provide a very accurate description of the particle motions. The method can also be modified to include fast algorithms [199] and to simulate flows in bounded geometries [43, 180]. It remains however typically limited to relatively small assemblies of particles, as a fair amount of quadrature points are required on each particle surface for an accurate evaluation of the convolution integrals.

When larger suspensions are to be simulated, efficient methods based on multipole expansions of the boundary integral equation can be used. The multipole expansion, presented in Section 2.3, describes the velocity field in terms of basic singular flows induced by the moments of the traction field on the particle surfaces (total force, force dipole, force quadrupole etc.) and is valid far away from any given particle. The most notable simulation method based on this expansion, called Stokesian dynamics, is due to Brady and coworkers [25, 26, 55], and consists of truncating and summing the multipole flows induced by the suspended particles and supplementing them by near-field corrections based

on lubrication theory [41]. The method was applied very successfully to shear flows [172] and pressure driven flows [140] of sphere suspensions, and can also be used to simulate colloidal systems [146, 8]. Stokesian dynamics simulations, which have an unfavorable cost of $O(N^3)$ or $O(N^2)$ where N is the number of particles (depending on the level of truncation in the multipole expansion), can also be accelerated using various algorithms, resulting in a cost of $O(N \log N)$ [170] or $O(N)$ [162, 92].

1.3 Overview of the present work

A brief overview of fundamentals of microhydrodynamics is provided in Chapter 2. General properties of particulate flows are discussed in the case where particle and fluid inertia can be neglected with respect to viscous forces. The representation theorem and the multipole expansion for Stokes flow, which are the basis of a wide range of numerical methods for suspension flows as explained previously, are briefly discussed. Finally, a discussion of slender-body theory is provided with emphasis on the description of the dynamics of rod-like particles.

In Chapter 3 a fast simulation method, called Smooth Particle-Mesh Ewald (SPME) algorithm, is developed and implemented. The method, which allows the simulation of particulate flows with an $O(N \log N)$ cost with respect to the number of particles, is applied to simulate the sedimentation of a suspension of rod-like particles with periodic boundary conditions. The sedimentation of orientable particles such as fibers or disks, and deformable particles such as viscous droplets, is further investigated in Chapters 4 and 5, with the aim of understanding the concentration instability in these systems. A very efficient method based on a point-particle approximation is developed and applied to simulate suspensions of realistic sizes with both periodic and no penetration boundary conditions. In the case of deformable particles a linear stability analysis is also proposed to confirm the existence of an instability. For both types of systems, it is argued that the size of the concentration fluctuations resulting from the instability is to a large extent governed by the vertical density gradients (stratification) that appear inside the suspensions.

Chapter 6 then discusses the collective dynamics that occur in suspensions of rod-like colloidal particles under induced-charge electrophoresis, the non-linear electrokinetic phenomenon that arises whenever a polarizable particle is placed in an electric field. The basic theory for this phenomenon is derived in the case of rod-like particles, and is applied to study the interactions of a pair of particles, where pairing is shown to occur. This is then confirmed using large-scale simulations of both non-Brownian and Brownian suspensions, and results for pair distributions, hydrodynamic diffusivities and orientation distributions are presented.

In Chapter 7, the pressure-driven flow of a dilute polymer solution between two infinite flat plates is analyzed in the case where the polymer chain is short and where the channel width is comparable to the chain contour length. A Brownian dynamics algorithm is described that accounts for both chain/chain and chain/wall hydrodynamic interactions, and is applied to characterize the effect of chain flexibility on the shear-induced migration that occurs as a result of hydrodynamic interaction of the polymer with the surrounding walls.

Finally, a conclusion and directions for future work are given in Chapter 8.

Chapter 2

Elements of microhydrodynamics

2.1   Generalities

As described in Chapter 1, this work is concerned with the description of the dynamics of suspended particles in a viscous fluid, where the particles may be solid, flexible (as in the case of polymers or elastic particles), or fluid (as in the case of suspended droplets of an immiscible fluid). In the most general case, the motion of a given particle is governed by Newton's equations of motion, which relate the external forces (including hydrodynamic forces exerted by the fluid) to the acceleration of the particle, while the motion of the suspending fluid is governed by the Navier-Stokes equations (in the case of a Newtonian fluid), which is a continuum version of Newton's second law applied to the material particles inside the fluid. In the present work, we only consider situations in which both particle and fluid inertia can be neglected with respect to the effects of viscous forces. Formally, this can be expressed in terms of the particle Reynolds and Stokes numbers as:

$$Re = \frac{\rho U a}{\mu} \to 0, \quad St = \frac{mU}{6\pi\mu a^2} \to 0, \tag{2.1}$$

where ρ and μ are the density and viscosity of the suspending fluid, a and m are the particle size and mass respectively, and U is a characteristic scale for the velocity of the particle with respect to the fluid.

When the Reynolds number is small ($Re \to 0$), the inertial terms in the Navier-Stokes equations can be neglected and the fluid motion is well described by the following Stokes equations:

$$-\mu \nabla^2 \boldsymbol{u} + \boldsymbol{\nabla} p = \boldsymbol{0}, \quad \boldsymbol{\nabla} \cdot \boldsymbol{u} = 0, \tag{2.2}$$

which describe the conservation of momentum and of mass in the fluid. These equations are subject to boundary conditions on the surfaces of the fluid domain. On the surface ∂S_α of a given solid particle α, the no-slip boundary condition applies, stating that the relative velocity between the solid and fluid phases is zero:

$$\boldsymbol{u}(\boldsymbol{x}) = \boldsymbol{U}_\alpha + \boldsymbol{\Omega}_\alpha \times \boldsymbol{x} \quad \text{as } \boldsymbol{x} \in \partial S_\alpha, \tag{2.3}$$

where $\boldsymbol{U}_\alpha$ and $\boldsymbol{\Omega}_\alpha$ are the rigid-body linear and angular velocities of the particle of interest, and $\boldsymbol{x}$ is a position vector. In the case of a fluid particle such as a droplet of an immiscible fluid, more complex boundary conditions relating hydrodynamic stresses on both sides of the interface must be enforced [11]. Far away from particle surfaces or solid boundaries, the fluid velocity must decay to the externally applied fluid velocity $\boldsymbol{u}^\infty$, which is assumed to be known:

$$\boldsymbol{u}(\boldsymbol{x}) \to \boldsymbol{u}^\infty(\boldsymbol{x}) \quad \text{as } |\boldsymbol{x}| \to \infty. \tag{2.4}$$

If the particle motions are prescribed (i.e. if $\boldsymbol{U}_\alpha$ and $\boldsymbol{\Omega}_\alpha$ are known for all particles α), Equations (2.2)–(2.4) can be solved for the velocity $\boldsymbol{u}$ and pressure p at every point in the fluid. In most cases of interest the particle motions are unknown and must be determined as part of the problem. In that case, equations of motion for the particles must also be used. In the limit of zero Stokes number ($St \to 0$), particle inertia can be neglected and Newton's equations for particle α read as follows:

$$\boldsymbol{F}_\alpha^h + \boldsymbol{F}_\alpha^e = \boldsymbol{0}, \quad \boldsymbol{T}_\alpha^h + \boldsymbol{T}_\alpha^e = \boldsymbol{0}, \tag{2.5}$$

where $\boldsymbol{F}_\alpha^{h,e}$ and $\boldsymbol{T}_\alpha^{h,e}$ denote the hydrodynamic and externally imposed forces and torques on the particle. In particular, the hydrodynamic forces and torques are related to the
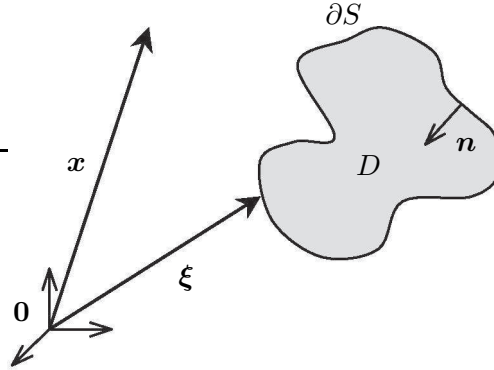
Figure 2.1: Geometry considered in the representation theorem of Section 2.2.

traction distribution on the particle surface as

$$\boldsymbol{F}_\alpha^h = \int_{\partial S_\alpha} \boldsymbol{\sigma}(\boldsymbol{x}_\alpha) \cdot \boldsymbol{n}_\alpha \mathrm{d}S_\alpha, \quad \boldsymbol{T}_\alpha^h = \int_{\partial S_\alpha} \boldsymbol{x}_\alpha \times [\boldsymbol{\sigma}(\boldsymbol{x}_\alpha) \cdot \boldsymbol{n}_\alpha] \, \mathrm{d}S_\alpha, \tag{2.6}$$

where $\boldsymbol{\sigma}(\boldsymbol{x}) = -p\mathsf{I} + \mu \left[\boldsymbol{\nabla}\boldsymbol{u}(\boldsymbol{x}) + \boldsymbol{\nabla}\boldsymbol{u}(\boldsymbol{x})^T \right]$ is the hydrodynamic stress tensor in the fluid. If the external forces and torques and the external fluid velocity are known, Equations (2.2)–(2.6) can now be solved for the fluid velocity and pressure fields along with the particle linear and angular velocities. As discussed in Section 1.2, numerous solution techniques have been developed for this problem. Next, we review the integral equation or representation theorem for Stokes flow, which is the basis of a large class of solution methods.

2.2 The representation theorem

The integral equation for Stokes flow, also known as representation theorem or Green's third identity, represents the velocity field at any point inside a fluid domain in terms of the traction fields on the boundaries of the domain. The theorem is a classic result of Stokes flow and is a consequence of the linearity of the Stokes equations. Its derivation is typically based on a generalized version of the Lorentz reciprocal theorem [101]. Here we only state the theorem and discuss its implications; the reader is referred to References [101, 147] for detailed derivations.

Consider the configuration of Figure 2.1, in which a surface ∂S separates a finite domain D from the rest of space, and let $\boldsymbol{n}$ denote the inward unit normal on ∂S. The boundary ∂S may correspond to the surface of a particle, and may be either fluid or solid or both. The representation theorem expresses the fluid velocity at a point $\boldsymbol{x}$ in the fluid as a sum of two convolution integrals on the surface ∂S. In index notation:

$$u_i(\boldsymbol{x}) = u_i^\infty(\boldsymbol{x}) - \frac{1}{8\pi\mu} \int_{\partial S} K_{ij}(\boldsymbol{x} - \boldsymbol{\xi}) f_j(\boldsymbol{\xi}) \mathrm{d}S - \frac{1}{4\pi} \int_{\partial S} T_{ijk}(\boldsymbol{x} - \boldsymbol{\xi}) u_j(\boldsymbol{\xi}) n_k(\boldsymbol{\xi}) \mathrm{d}S, \quad (2.7)$$

where $\boldsymbol{f}(\boldsymbol{\xi}) = \boldsymbol{\sigma}(\boldsymbol{\xi}) \cdot \boldsymbol{n}$ is the traction on ∂S, K is the Green's function for a point force or Oseen-Burgers tensor, and T is its associated stress tensor:

$$K_{ij}(\boldsymbol{x}) = \frac{\delta_{ij}}{x} + \frac{x_i x_j}{x^3}, \quad T_{ijk}(\boldsymbol{x}) = \frac{1}{2}\left[K_{ij,k}(\boldsymbol{x}) + K_{ik,j}(\boldsymbol{x})\right] = -3\frac{x_i x_j x_k}{x^5}. \quad (2.8)$$

In particular, Equation (2.7) shows that the knowledge of the traction field $\boldsymbol{f}(\boldsymbol{\xi})$ and of the velocity $\boldsymbol{u}(\boldsymbol{\xi})$ on the surface ∂S entirely determines the entire velocity field outside the surface. This result is quite powerful as it replaces the determination of a three-dimensional variable by that of two two-dimensional variables on the boundaries of the domain. The first integral in Equation (2.7) is called *single-layer potential*, while the second is called *double-layer potential*, by analogy with the expressions for the electric field induced by surface distributions of charges and dipoles in electrostatics. The boundary integral and boundary element methods discussed in Section 1.2.4 are based on Equation (2.7) and consist of discretizing the surface ∂S and solving for the tractions and velocities on the boundaries.

In the case where ∂S is the surface of a solid particle, Equation (2.7) simplifies further as the double-layer potential can be shown to vanish. In that case, the no-slip boundary condition states that the fluid velocity on the particle surface must be equal to the rigid body motion of the particle: $\boldsymbol{u}(\boldsymbol{\xi}) = \boldsymbol{U} + \boldsymbol{\Omega} \times \boldsymbol{\xi}$. Substituting this into Equation (2.7), and noting that [147]

$$\int_{\partial S} T_{ijk}(\boldsymbol{x} - \boldsymbol{\xi}) n_j(\boldsymbol{\xi}) \mathrm{d}S = 0 \quad \text{and} \quad \varepsilon_{ilm} \int_{\partial S} x_m T_{ijk}(\boldsymbol{x} - \boldsymbol{\xi}) n_k(\boldsymbol{\xi}) \mathrm{d}S = 0 \quad (2.9)$$

for a point $\boldsymbol{x}$ outside of ∂S, we find that the representation theorem reduces to

$$u_i(\boldsymbol{x}) = u_i^\infty(\boldsymbol{x}) - \frac{1}{8\pi\mu} \int_{\partial S} K_{ij}(\boldsymbol{x} - \boldsymbol{\xi}) f_j(\boldsymbol{\xi}) \mathrm{d}S_{\boldsymbol{\xi}}. \tag{2.10}$$

Equation (2.10) would still hold for a collection of particles by taking the union of the surfaces for the domain of integration, provided that all the particles are located inside a bounded region (i.e. that a surface ∂S_∞ can be found that encloses all the particles).

2.3   The multipole expansion

The previous boundary representation, which is exact but requires the knowledge of the tractions everywhere on the surface of a solid particle, is the starting point for a simpler but approximate evaluation method for the disturbance velocity far away from the particle, in terms of moments of the surface tractions [55, 101].

Consider again a single rigid particle in an unbounded fluid, and assume for convenience that the origin $\mathbf{0}$ is located inside the particle. Far away from the particle surface (i.e. when $|\boldsymbol{x}| \gg |\boldsymbol{\xi}|$), the Oseen-Burgers tensor in Equation (2.10) can be expanded in a Taylor series about $\boldsymbol{\xi} = \mathbf{0}$ as follows:

$$K_{ij}(\boldsymbol{x} - \boldsymbol{\xi}) = \sum_{n=0}^{\infty} \frac{1}{n!} (\boldsymbol{\xi} \cdot \boldsymbol{\nabla}_{\boldsymbol{\xi}})^n K_{ij}(\boldsymbol{x} - \boldsymbol{\xi})|_{\boldsymbol{\xi}=0} = \sum_{n=0}^{\infty} \frac{(-1)^n}{n!} \xi_{k_1}...\xi_{k_n} K_{ij,k_1...k_n}(\boldsymbol{x}). \tag{2.11}$$

Inserting this expansion into the boundary integral equation for a rigid particle gives:

$$\begin{aligned}
u_i(\boldsymbol{x}) &= u_i^\infty(\boldsymbol{x}) - \frac{1}{8\pi\mu} \sum_{n=0}^{\infty} \frac{(-1)^n}{n!} \int_{\partial S} \xi_{k_1}...\xi_{k_n} K_{ij,k_1...k_n}(\boldsymbol{x}) f_j(\boldsymbol{\xi}) \mathrm{d}S_{\boldsymbol{\xi}} \\
&= u_i^\infty(\boldsymbol{x}) + \frac{1}{8\pi\mu} \sum_{n=0}^{\infty} \frac{(-1)^n}{n!} K_{ij,k_1...k_n}(\boldsymbol{x}) Q_{jk_1...k_n},
\end{aligned} \tag{2.12}$$

where we have defined the n-th multipole moment of the particle by:

$$Q_{jk_1...k_n} = - \int_{\partial S} \xi_{k_1}...\xi_{k_n} f_j(\boldsymbol{\xi}) \mathrm{d}S_{\boldsymbol{\xi}}. \tag{2.13}$$

Equation (2.12) is exact if the infinite sum is actually performed. In practical calculations and simulations, only the first few terms in the expansion are retained when the evaluation point $\boldsymbol{x}$ is sufficiently far away from the particles. Hence the first few moments play a very important role and deserve some attention. The monopole, or zeroth moment of the force density, is the total force exerted by the particle on the fluid (compare to Equation (2.6)):

$$F_j = - \int_{\partial S} f_j(\boldsymbol{\xi})\mathrm{d}S_{\boldsymbol{\xi}}. \tag{2.14}$$

The first moment, usually called *force dipole*, is:

$$D_{jk} = - \int_{\partial S} f_j(\boldsymbol{\xi})\xi_k \mathrm{d}S_{\boldsymbol{\xi}}. \tag{2.15}$$

The dipole is a second-order tensor and can be decomposed into symmetric and antisymmetric parts. After removing the isotropic portion:

$$D_{jk} - \frac{1}{3}D_{ii}\delta_{jk} = S_{jk} + R_{jk}. \tag{2.16}$$

The symmetric part is known as the *stresslet* S_{jk}:

$$S_{jk} = -\frac{1}{2} \int_{\partial S} \left[f_j(\boldsymbol{\xi})\xi_k + f_k(\boldsymbol{\xi})\xi_j - \frac{2}{3}f_i(\boldsymbol{\xi})\xi_i\delta_{jk} \right] \mathrm{d}S_{\boldsymbol{\xi}}. \tag{2.17}$$

The antisymmetric part R_{jk} is sometimes called the *rotlet*:

$$R_{jk} = -\frac{1}{2} \int_{\partial S} [f_j(\boldsymbol{\xi})\xi_k - f_k(\boldsymbol{\xi})\xi_j] \, \mathrm{d}S_{\boldsymbol{\xi}}, \tag{2.18}$$

and can be interpreted as the total torque exerted by the particle on the fluid and measured relative to the origin $\boldsymbol{0}$ (compare to Equation (2.6)):

$$R_{jk} = \frac{1}{2}\epsilon_{jkl}T_l = \frac{1}{2}\epsilon_{jkl} \underbrace{\left[- \int_{\partial S} \epsilon_{lpq}f_p(\boldsymbol{\xi})\xi_q \mathrm{d}S_{\boldsymbol{\xi}} \right]}_{\text{total torque } T_l}. \tag{2.19}$$

We see that if the multipole expansion Equation (2.12) is truncated after the first two terms (as is customary for instance in Stokesian dynamics simulations, cf. Section 1.2.4), the knowledge of the total force $\boldsymbol{F}$, total torque $\boldsymbol{T}$, and stresslet S, completely determines the far-field velocity disturbance $\boldsymbol{u}(\boldsymbol{x}) - \boldsymbol{u}^\infty(\boldsymbol{x})$. There are certain situations, for simple geometries and simple flows (e.g. translating and rotating sphere in quiescent fluid), where the multipole expansion only contains a finite number of terms. In these cases, the obtained velocity disturbance is exact over the entire domain (not only in the far-field). Certain methods of solution for Stokes flow around solid bodies, called singularity methods (e.g. [147]), consist of looking for an exact solution written as a finite multipole expansion which satisfies the no-slip boundary condition on the surface of the body (any such solution verifying the boundary conditions is guaranteed to be the unique solution to the problem). This type of method may be compared with the method used in two-dimensional potential flow where simple flow fields (uniform flow, sources and sinks, doublets etc.) are added to satisfy the tangential flow condition on the solid boundaries.

2.4 Slender-body theory and fiber dynamics

2.4.1 The slender-body equation

When the particle of interest is very elongated such as a slender fiber or filament, the effects of the strong shape anisotropy on the flow are not adequately captured by a truncated multipole expansion, which is based on force moments about the center of the particle. Such an expansion will indeed fail to capture the local variations of the flow, and another approach may be desirable. In that case the representation theorem can be greatly simplified by replacing the traction field on the particle surface by an effective linear force density along the particle axis. This slender-body theory dates back to Batchelor [12] and Cox [45], and was later refined by Keller & Rubinow [105] and Johnson [100]. The theory can be justified based on matched asymptotic expansions, where the flow field near the surface of the particle, which locally is similar to the flow near an infinite cylinder and
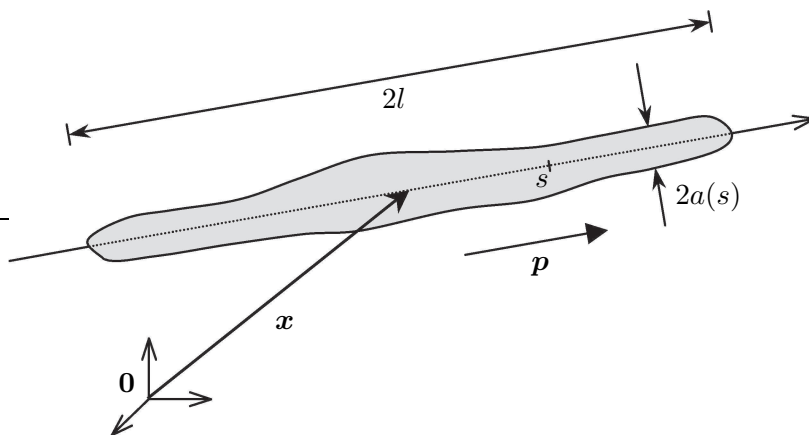
Figure 2.2: Geometry considered in the slender-body theory of Section 2.4.

grows logarithmically with the distance from the axis, is matched with the flow field far away from the cylinder surface, which decays algebraically.

Consider a slender axisymmetric particle of length $2l$ and thickness $2a$, where a may vary along the length of the particle, and denote by $A = l/a_0$ its aspect ratio (Figure 2.2). Denote by $\boldsymbol{x}$ the position of its center of mass and by $\boldsymbol{p}$ a unit vector aligned with its major axis, and let $s \in [-l,\, l]$ denote a linear coordinate along the axis with origin the center of the particle. The result of Batchelor [12] relates the linear and angular velocities of the rod to the external fluid velocity $\boldsymbol{u}^\infty$ and to the force density $\boldsymbol{f}(s)$ along the axis:

$$
\begin{aligned}
8\pi\mu\left[\dot{\boldsymbol{x}} + s\dot{\boldsymbol{p}} - \boldsymbol{u}^\infty(\boldsymbol{x} + s\boldsymbol{p})\right] = {} & 2\left[\log 2A + \log\frac{(l^2 - s^2)^{1/2}}{a(s)}\right](\mathsf{I} + \boldsymbol{pp})\cdot\boldsymbol{f}(s) \\
& + (\mathsf{I} - 3\boldsymbol{pp})\cdot\boldsymbol{f}(s) + (\mathsf{I} + \boldsymbol{pp})\cdot\int_{-l}^{l}\frac{\boldsymbol{f}(s') - \boldsymbol{f}(s)}{|s' - s|}\mathrm{d}s'.
\end{aligned}
\tag{2.20}
$$

Note that in Equation (2.20), $\boldsymbol{f}(s)$ represents the tractions exerted by the particle on the fluid, unlike in Section 2.2 where the opposite convention was used. Equation (2.20) is an integral equation for the force distribution $\boldsymbol{f}(s)$ along the axis of the particle. Unless the motion of the particle is prescribed (i.e. unless $\dot{\boldsymbol{x}}$ and $\dot{\boldsymbol{p}}$ are known), it must be supplemented by a force balance such as that of Equation (2.5), where the hydrodynamic forces

and torques are now given by the simpler expression:

$$\boldsymbol{F}^h = -\int_{-l}^{l} \boldsymbol{f}(s)\mathrm{d}s \quad \text{and} \quad \boldsymbol{T}^h = -\boldsymbol{p} \times \int_{-l}^{l} s\boldsymbol{f}(s)\mathrm{d}s. \tag{2.21}$$

Equation (2.20), together with Equation (2.5), can be solved for the force distribution $\boldsymbol{f}(s)$ and particle velocities $\dot{\boldsymbol{x}}$ and $\dot{\boldsymbol{p}}$: a solution may for instance be obtained by discretizing the rod axis and using a quadrature to evaluate the integral in Equation (2.20) (note however that the integrand is singular, so that special care must be taken). Once the force distribution has been determined, the disturbance velocity induced by the slender-body at a given position $\boldsymbol{y}$ in the surrounding fluid is obtained as a convolution:

$$\boldsymbol{u}'(\boldsymbol{y}) = \frac{1}{8\pi\mu} \int_{-l}^{l} \mathsf{K}(\boldsymbol{y} - \boldsymbol{x} - s\boldsymbol{p}) \cdot \boldsymbol{f}(s)\mathrm{d}s. \tag{2.22}$$

If more than one slender-body is present in solution, the disturbance velocities induced by the particles other than that of interest should be added to the imposed velocity in Equation (2.20): this effectively couples the force distributions on all the rods, which must then be determined simultaneously. This situation where multiple slender bodies are interacting hydrodynamically will be described in more detail in Chapter 3.

In the limit of very high aspect ratio ($A \gg 1$), Equation (2.20) can be simplified as follows by only retaining the $O(\log 2A)$ term on the right-hand side:

$$\dot{\boldsymbol{x}} + s\dot{\boldsymbol{p}} - \boldsymbol{u}^\infty(\boldsymbol{x} + s\boldsymbol{p}) = \frac{\log 2A}{4\pi\mu} (\mathsf{I} + \boldsymbol{p}\boldsymbol{p}) \cdot \boldsymbol{f}(s). \tag{2.23}$$

This approximation, sometimes called local slender-body theory, essentially neglects hydrodynamic interactions between different sections of the slender body, but preserves its drag anisotropy. It also greatly simplifies the problem in the case of a single rod, as Equation (2.23) can be inverted analytically for $\boldsymbol{f}(s)$; however, when multiple rods are interacting, the force densities become coupled again through the disturbance velocities, and numerical solutions are again required. In the following discussion we focus on Equation (2.23), as it will be used extensively in Chapters 3, 6 and 7.

2.4.2   Particle dynamics

Simple expressions for the linear and angular velocities $\dot{\boldsymbol{x}}$ and $\dot{\boldsymbol{p}}$ of the particle can be obtained from Equation (2.23). Indeed, taking the average of Equation (2.23) easily yields:

$$\dot{\boldsymbol{x}} = \frac{1}{2l} \int_{-l}^{l} \boldsymbol{u}^{\infty}(\boldsymbol{x} + s\boldsymbol{p})\mathrm{d}s + \frac{\log 2A}{8\pi\mu l} \left(\boldsymbol{\mathsf{I}} + \boldsymbol{pp}\right) \cdot \boldsymbol{F}^{(0)}, \tag{2.24}$$

where $\boldsymbol{F}^{(0)}$ is the zeroth-order moment of the force distribution, and is equal to the total force exerted by the particle on the fluid: $\boldsymbol{F}^{(0)} = -\boldsymbol{F}^{h} = \boldsymbol{F}^{e}$. In addition, calculating the first moment of Equation (2.23) and projecting in the plane perpendicular to $\boldsymbol{p}$ gives:

$$\dot{\boldsymbol{p}} = \frac{3}{2l^3} \left(\boldsymbol{\mathsf{I}} - \boldsymbol{pp}\right) \cdot \int_{-l}^{l} s\boldsymbol{u}^{\infty}(\boldsymbol{x} + s\boldsymbol{p})\mathrm{d}s + \frac{3\log 2A}{8\pi\mu l^3} \left(\boldsymbol{\mathsf{I}} - \boldsymbol{pp}\right) \cdot \boldsymbol{F}^{(1)}. \tag{2.25}$$

Here $\boldsymbol{F}^{(1)}$ denotes the first moment of the force distribution:

$$\boldsymbol{F}^{(1)} = \int_{-l}^{l} s\boldsymbol{f}(s)\mathrm{d}s, \tag{2.26}$$

and is related to the total torque $\boldsymbol{T} = -\boldsymbol{T}^{h}$ exerted by the particle on the fluid by $\boldsymbol{T} = \boldsymbol{p} \times \boldsymbol{F}^{(1)}$ and $(\boldsymbol{\mathsf{I}} - \boldsymbol{pp}) \cdot \boldsymbol{F}^{(1)} = \boldsymbol{T} \times \boldsymbol{p}$.

Equations (2.24)–(2.25) allow the simple calculation of $\dot{\boldsymbol{x}}$ and $\dot{\boldsymbol{p}}$ if the imposed flow field and applied force and torque on the particle are known. In particular, if these quantities are known, the full determination of the force distribution along the rod axis is not required for the sole purpose of determining the particle motion. If several slender-bodies are interacting, however, the force distributions will appear in Equations (2.24)–(2.25) through the disturbance velocities that must be added to the imposed flow field, and will need to be solved for.

2.4.3   Spectral expansion of the force distribution

When several slender bodies are interacting, the full solution of the coupled integral equations for the force distributions and particle velocities can be quite costly: typically it

requires the inversion of a linear system of $(3M + 5) \times N$ unknowns, where N is the number of particles and M is the number of discretization points along each particle. The inversion of such a system can be prohibitive in large collections of particles, and more efficient alternate methods become desirable. As mentioned earlier, the multipole expansion of Section 2.3 is not adequate in the case of slender particles, as it does not capture the local geometric anisotropy. However, other types of expansions for the force distribution $\boldsymbol{f}(s)$ along the rod axis can prove useful.

Here, we present a spectral approximation of $\boldsymbol{f}(s)$ based on Legendre polynomials, which also represents the force distribution in terms of moments. This approximation was first proposed by Harlen, Sundararajakumar & Koch [80] and later used by Butler & Shaqfeh [32, 33]. It consists of decomposing the function $\boldsymbol{f}(s)$ over the interval $[-l, l]$ on the basis of Legendre polynomials P_n:

$$\boldsymbol{f}(s) = \sum_{n=0}^{\infty} \boldsymbol{g}_n P_n(\hat{s}), \tag{2.27}$$

where $\hat{s} = s/l \in [-1, 1]$. The vectors $\boldsymbol{g}_n$ are coefficients to be determined. Using the orthogonality property of Legendre polynomials, these coefficients can be expressed as:

$$\boldsymbol{g}_n = \frac{2n + 1}{2l} \int_{-l}^{l} \boldsymbol{f}(s) P_n(\hat{s}) \mathrm{d}s. \tag{2.28}$$

Truncating the expansion Equation (2.27) therefore reduces the calculation of the force distribution $\boldsymbol{f}(s)$ to the determination of the first few vector coefficients in the expansion, in much the same way that truncating the multipole expansion of Equation (2.12) reduced the calculation of the surface tractions on a particle surface to the determination of its first few moments about the center of the particle. Yet Equation (2.27) still contains information about the spatial distribution of the forces through the basis polynomials which vary with s along the rod axis.

In the practical simulations of Chapters 3, 6 and 7, we will only retain the first two terms ($n = 0$ and 1) in Equation (2.27), which is similar to the truncation of the multipole expansion after the dipole term in Stokesian dynamics simulations. Recalling that $P_0(\hat{s}) =$

1 and $P_1(\hat{s}) = \hat{s}$, the expansion becomes: $\boldsymbol{f}(s) \approx \boldsymbol{g}_0 + \boldsymbol{g}_1 s/l$, where the coefficients are expressed in terms of the zeroth and first force moments as

$$\boldsymbol{g}_0 = \frac{1}{2l} \int_{-l}^{l} \boldsymbol{f}(s)\mathrm{d}s \quad \text{and} \quad \boldsymbol{g}_1 = \frac{3}{2l^2} \int_{-l}^{l} s\boldsymbol{f}(s)\mathrm{d}s. \tag{2.29}$$

In particular, the zeroth moment is related to the total force as $\boldsymbol{g}_0 = \boldsymbol{F}^{(0)}/2l$. By analogy with the force dipole of Equation (2.15), we decompose the first force moment in symmetric part (along $\boldsymbol{p}$) and antisymmetric part (perpendicular to $\boldsymbol{p}$):

$$\boldsymbol{g}_1 = \frac{3}{2l^2} \left[\boldsymbol{pp} \cdot \int_{-l}^{l} s\boldsymbol{f}(s)\mathrm{d}s + (\mathsf{I} - \boldsymbol{pp}) \cdot \int_{-l}^{l} s\boldsymbol{f}(s)\mathrm{d}s \right] = \frac{3}{2l^2} \left[\mathscr{S}\boldsymbol{p} + (\mathsf{I} - \boldsymbol{pp}) \cdot \boldsymbol{F}^{(1)} \right]. \tag{2.30}$$

As in the case of the force dipole in the multipole expansion, the antisymmetric part is related to the first force moment $\boldsymbol{F}^{(1)}$ on the particle (or equivalently to the total torque $\boldsymbol{T}$), while the symmetric part involves a scalar stresslet $\mathscr{S}$:

$$\mathscr{S} = \int_{-l}^{l} s\boldsymbol{p} \cdot \boldsymbol{f}(s)\mathrm{d}s. \tag{2.31}$$

To summarize, the spectral expansion of the force distribution becomes:

$$\boldsymbol{f}(s) \approx \frac{1}{2l}\boldsymbol{F}^{(0)} + \frac{3s}{2l^3} \left[\mathscr{S}\boldsymbol{p} + (\mathsf{I} - \boldsymbol{pp}) \cdot \boldsymbol{F}^{(1)} \right]. \tag{2.32}$$

If the zeroth and first force moments $\boldsymbol{F}^{(0)}$ and $\boldsymbol{F}^{(1)}$ are known, the calculation of the force distribution is therefore reduced to the determination of a single scalar $\mathscr{S}$. Inverting the slender-body equation (2.23) for $\boldsymbol{f}(s)$, and substituting the result into the definition of $\mathscr{S}$ (Equation (2.31)) allows the stresslet to be expressed in terms of the imposed fluid velocity:

$$\mathscr{S} = -\frac{2\pi\mu}{\log 2A} \int_{-l}^{l} s\boldsymbol{p} \cdot \boldsymbol{u}^{\infty}(\boldsymbol{x} + s\boldsymbol{p})\mathrm{d}s. \tag{2.33}$$

If the external fluid velocity $\boldsymbol{u}^{\infty}$ is known *a priori*, as in the case of a single rod in a prescribed flow field, the stresslet can be calculated using Equation (2.33), from which the linearized force distribution Equation (2.32) is inferred. However, if several rods are interacting, $\boldsymbol{u}^{\infty}$ contains a contribution from the disturbance velocity induced by the other

rods, and Equation (2.33) can be used together with Equations (2.22) and (2.32) to write a linear systems for the stresslets on all the rods. This procedure will be described in more detail in Chapter 3.

2.5 Complex geometries

The discussion of this Chapter has focused on particles suspended in an unbounded fluid. In many situations of interest, as described for example in Chapters 4 and 7, container boundaries play a significant role on the particle dynamics and must be included. Here we briefly review two major approaches to account for solid boundaries.

- **Boundary integral equation**: A natural approach consists of treating the container boundaries as part of the bounding surface ∂D in the representation theorem of Section 2.2: the boundaries can then be discretized and the surface tractions solved for in a similar fashion as on the particle surfaces. The advantage of this approach is that complex surfaces (such as curved walls, corners etc.) are easily handled. Yet the method is in most cases impractical as it creates a very large number of additional variables (tractions at all the discretization points on the surfaces), and is not easily applied when the bounding surfaces are infinite (as in channel flows for instance).

- **Green's functions methods**: An alternate approach consists of using the Green's function for the geometry of interest in place of the Oseen-Burgers tensor **K** in the representation theorem, multipole expansion or slender-body equation. In that case, the no-slip boundary condition is automatically enforced on the boundaries, with no additional work. The limitation of this approach is that analytical Green's functions only exist in simple geometries, such as for the flow over an infinite plane [19], flow between two infinite flat plates [117, 17, 99], or flow in a cylindrical tube [118]. In more complex geometries, the Green's function has sometimes been obtained numerically [97]. A method of this type will be applied in Chapter 7.

Chapter 3

A smooth particle-mesh Ewald algorithm for Stokes suspensions

3.1   Introduction

In the Stokes flow regime, the disturbance of a point force or Stokeslet on the flow decays as the inverse of the distance from the force location, so that even distant particle pairs can have significant interactions. Evaluating the disturbance velocity at each particle location due to the presence and motion of the other particles is typically an $O(N^2)$ operation, where N is the number of particles, and can become very prohibitive when the size of the system increases. Several alternate methods for the summation of these interactions have been suggested in the last few years, most of which were inspired by existing algorithms used in molecular dynamics simulations, where the electrostatic potentials have the same slow decay as the disturbance velocity in creeping flow. Sangani & Mo [162] developed an $O(N)$ fast-multipole method for hydrodynamic interactions, based on the famous algorithm by Greengard & Rokhlin [73]. In the fast-multipole method the simulation domain is decomposed into a tree of cells, and in each cell a compressed representation of the flow disturbances is constructed using a truncated multipole expansion. Far-field interactions with the particles located in distant cells are then calculated by means of this compressed

representation. The fast-multipole method was also applied more recently to suspensions of many deformable drops [199], and to Stokesian dynamics simulations with finite numbers of particles [92]. As discussed in Section 1.2.3, other efficient methods include the Lattice-Boltzmann method developed by Ladd [110]; this technique however only applies to finite Reynolds numbers.

The most notable method for both electrostatic and hydrodynamic interactions is the Particle-Particle Particle-Mesh (PPPM) algorithm [88]. This algorithm and its many variants have been used for over a decade in plasma simulations, astrophysics and molecular dynamics, and are based on a decomposition of the interactions into two fast-converging contributions, one of which is efficiently evaluated using an underlying grid and the fast Fourier transform algorithm. A good choice of parameters allows one to reduce the cost of evaluating the interactions to $O(N \log N)$, which is a significant improvement for large systems. A thorough review of different variants of the method for electrostatic interactions can be found in Deserno & Holm [49].

A version of the PPPM algorithm, called Particle-Mesh Ewald (PME), was first applied to hydrodynamic interactions between suspended spheres by Guckel [75], and was subsequently made systematic by Sierou & Brady [170] in their Accelerated Stokesian Dynamics (ASD). ASD is a new version of the Stokesian dynamics method [25], in which the direct calculation of the far-field grand mobility matrices is replaced by the use of the PME algorithm along with an iterative solver for the matrix inversion. ASD was proven to be very efficient in evaluating the rheological properties of suspensions of spheres [171], allowing the simulation of systems of up to 1,000 spheres.

In this Chapter, we develop and implement a variant of the PME algorithm, called Smooth Particle-Mesh Ewald (SPME), and based on the work by Essman *et al.* [57] for electrostatic interactions. The main advantage of SPME over the original PME method is the improved accuracy resulting from the new force assignment and interpolation schemes used for the Fourier sum, which are based on an approximation of structure factors using high-order B-splines. The common points and differences with accelerated Stokesian dynamics will become apparent in the subsequent discussion.

As a way of illustration, we apply the method to the simulation of the periodic sedimentation of suspensions of fibers, a phenomenon further investigated in Chapter 4. The sedimentation of non-spherical particles such as rigid fibers is known to be quite complex, as both experiments [83, 84, 126] and theoretical arguments [102] show that it is characterized by a concentration instability: an initially well-mixed homogeneous suspension is observed to become highly inhomogeneous, with the formation of high-concentration streamers surrounded by clarified regions.

Several attempts have been made to numerically simulate this instability. First, Mackaplow & Shaqfeh [122] performed both Monte-Carlo simulations and point-particle dynamic simulations, and managed to capture most of the qualitative features of the instability in the dilute regime. More recently, Butler & Shaqfeh [32] performed simulations in which they accounted for both far-field hydrodynamic interactions and short-range lubrication forces. The fibers were no longer approximated as point particles, but modeled using slender-body theory as line distributions of point forces (cf. Section 2.4). A spectral approximation of the line distributions was used, in which they retained the first two moments, namely the total force and dipole term, whose anti-symmetric and symmetric parts are the total torque and particle stresslet. Short-range pairwise interactions were also included using the lubrication approximation. The results they obtained were dependent on the aspect ratio of their periodic simulation box, but good orientation and velocity statistics were obtained using boxes that were highly elongated in the direction of gravity. The size of the systems they were able to simulate was however greatly limited by the cost of evaluating the inter-particle long-range hydrodynamic interactions, so that only very few clusters were typically observed in their simulations. Moreover the size of the clusters was influenced by the boundary conditions. In particular, the limitations on the box aspect ratio and number of fibers did not allow them to observe more than one vertical streamer. To reduce the influence of the boundary conditions, and study in more details the structure of the suspension (e.g. wavenumber selection, cluster size and dynamics), larger systems need to be simulated: this strongly motivates the use of efficient algorithms such as the SPME method developed here for the calculation of the long-ranged

hydrodynamic interactions.

In Section 3.2, we give an overview of the mathematical formulation of the sedimentation problem, which follows closely the simulation method of Butler & Shaqfeh [32] and is analogous to the discussion of Section 2.4: the equations for the motion of the fibers, lubrication forces and hydrodynamic interactions are all presented in detail. We then proceed to explain the smooth particle-mesh Ewald algorithm in Section 3.3, and assess its performance by comparing it to the standard Ewald summation technique. In Section 3.4 we discuss the iterative method and preconditioning techniques used to solve for the stresslets and lubrication forces. Finally the results of the simulations are given in Section 3.5, where the structure of the suspension, orientation and velocity statistics are discussed.

3.2 Mathematical formulation

The simulation method follows the previous work by Butler and Shaqfeh [32]. Slender-body theory is used to model the motion of the fibers, along with a spectral approximation of the force distribution in which the total force, torque and particle stresslet are retained. The fundamental periodic solution of the Stokes equation is used for hydrodynamic interactions, and short-range interactions are calculated using the lubrication approximation.

3.2.1 Motion of the fibers: slender-body theory

The position and orientation of each fiber α is determined by the location $\boldsymbol{x}_\alpha$ of its center of mass and by a unit vector $\boldsymbol{p}_\alpha$ parallel to its major axis (cf. Figure 2.2). The time evolution of $\boldsymbol{x}_\alpha$ and $\boldsymbol{p}_\alpha$ can be tracked using Batchelor's slender-body theory [12] introduced in Section 2.4, which represents the disturbance due to the presence and motion of the fiber in the fluid by a line distribution of point forces. To a leading order approximation in $\log 2A$, where A is the fiber aspect ratio, the translational and rotational velocities $\dot{\boldsymbol{x}}_\alpha$ and $\dot{\boldsymbol{p}}_\alpha$ are related to the fluid disturbance velocity and force distribution along the fiber by the slender-body equation (cf. Section 2.4):

$$\dot{\boldsymbol{x}}_\alpha + s\dot{\boldsymbol{p}}_\alpha - \boldsymbol{u}'_\alpha(\boldsymbol{x}_\alpha + s_\alpha \boldsymbol{p}_\alpha) = \frac{\log 2A}{4\pi}(\boldsymbol{\mathsf{I}} + \boldsymbol{p}_\alpha \boldsymbol{p}_\alpha) \cdot \boldsymbol{f}_\alpha(s_\alpha) \quad \alpha = 1, ..., N. \qquad (3.1)$$

Here $\boldsymbol{u}'_\alpha$ is the disturbance velocity of the fluid surrounding fiber α due to the motion of the other fibers, s_α is an abscissa along the fiber length, and $\boldsymbol{f}_\alpha$ is the line distribution of point forces. Equation (3.1) has been non-dimensionalized using the following characteristic velocity, length and time scales:

$$u_c = \frac{gV\Delta\rho}{4\pi\mu l}\log(2A), \qquad l_c = l, \qquad t_c = l_c/u_c = \frac{4\pi\mu l^2}{gV\Delta\rho\log(2A)}. \qquad (3.2)$$

V and $\Delta\rho$ are the volume and relative density of a fiber, μ is the viscosity of the solvent and g the acceleration of gravity. The characteristic length scale l is the fiber half-length, so that positions s along the fibers range from -1 to $+1$. The characteristic time scale, or Stokes time, is the time required for an isolated vertical fiber to sediment over its half-length.

As we saw in Section 2.4.2, Equation (3.1) can be used to determine the linear and angular velocity of the fiber as:

$$\dot{\boldsymbol{x}}_\alpha = \frac{1}{2}\int_{-1}^{1}\boldsymbol{u}'_\alpha(\boldsymbol{x}_\alpha + s_\alpha \boldsymbol{p}_\alpha)\mathrm{d}s_\alpha + \frac{\log(2A)}{8\pi}(\boldsymbol{\mathsf{I}} + \boldsymbol{p}_\alpha \boldsymbol{p}_\alpha)\cdot\boldsymbol{F}^{(0)}_\alpha, \qquad (3.3)$$

$$\dot{\boldsymbol{p}}_\alpha = \frac{3}{2}(\boldsymbol{\mathsf{I}} - \boldsymbol{p}_\alpha \boldsymbol{p}_\alpha)\cdot\int_{-1}^{1}s_\alpha\boldsymbol{u}'_\alpha(\boldsymbol{x}_\alpha + s_\alpha \boldsymbol{p}_\alpha)\mathrm{d}s_\alpha + \frac{3\log(2A)}{8\pi}(\boldsymbol{\mathsf{I}} - \boldsymbol{p}_\alpha \boldsymbol{p}_\alpha)\cdot\boldsymbol{F}^{(1)}_\alpha, \quad (3.4)$$

where $\boldsymbol{F}^{(0)}_\alpha$ and $\boldsymbol{F}^{(1)}_\alpha$ denote the zeroth and first force moments on fiber α:

$$\boldsymbol{F}^{(0)}_\alpha = \int_{-1}^{1}\boldsymbol{f}_\alpha(s_\alpha)\mathrm{d}s_\alpha, \qquad \boldsymbol{F}^{(1)}_\alpha = \int_{-1}^{1}s_\alpha\boldsymbol{f}_\alpha(s_\alpha)\mathrm{d}s_\alpha. \qquad (3.5)$$

Given $\boldsymbol{F}^{(0)}_\alpha$, $\boldsymbol{F}^{(1)}_\alpha$ and the fluid velocity $\boldsymbol{u}'_\alpha$ along the axis due to the motion of the other fibers, Equations (3.3)–(3.4) can be used to integrate the motion of the fiber in time.

3.2.2   Forces and torques on the fibers

In addition to the long-range hydrodynamic interactions which will be discussed in Section 3.2.3, the forces and torques on the fibers can come from three contributions: gravity

which causes sedimentation, lubrication forces when two fibers get close to each other (typically when the distance between their surfaces falls below one fiber diameter), and strong repulsive contact forces when this distance becomes of the order of the roughness length scale of the fiber surfaces. Gravity poses no special difficulty, and only creates a force at the center of the particle. In dimensionless form: $\boldsymbol{F}^{(0),g} = -\hat{\boldsymbol{z}}$ and $\boldsymbol{F}^{(1),g} = \boldsymbol{0}$.

The slender-body formulation of Section 3.2.1, which represents the fibers as line distributions of point forces, is a far-field approximation and therefore does not capture the near-field effects which are dependent on the exact geometry of the fiber surfaces. These effects can be accounted for through additional lubrication forces, as is commonly done in Stokesian dynamics simulations [25]. As sedimenting fiber suspensions are known to form inhomogeneities, correctly capturing these short-range interactions can be critical, and Butler & Shaqfeh [32] indeed observed that including lubrication forces in their simulations modified the sedimentation rates and pair probabilities. The modeling is quite straightforward and is derived from the formulae of Claeys & Brady [41]. Four types of lubrication interactions can occur: body-body interactions (parallel and non-parallel cases), end-body interactions and end-end interactions. In each case the explicit form of the lubrication force will differ, and the various formulae can be found in Butler & Shaqfeh [32]. For the most general case where the fibers interact along their lengths and are non-parallel, the force between two fibers α and β is given by:

$$\boldsymbol{F}_{\alpha\beta}^{(0),l} = \pm \frac{6\pi\dot{h}}{A^2|\boldsymbol{p}_\alpha \times \boldsymbol{p}_\beta|h}\boldsymbol{n}, \tag{3.6}$$

where $\boldsymbol{n}$ is a unit vector normal to both fiber surfaces, h is the minimum separation distance between the two surfaces and $\dot{h}$ is the relative velocity projected along $\boldsymbol{n}$. The appropriate sign is chosen such that the force is repulsive for approaching fibers ($\dot{h} > 0$) and attractive for separating fibers ($\dot{h} < 0$). In all cases these forces also create torques.

As argued by Harlen, Sundararajakumar & Koch [80] in their similar simulations of neutrally buoyant fibers, lubrication interactions between high-aspect ratio particles are quite weak and will usually not be sufficient to prevent mechanical contact. Harlen *et al.* treated these contacts by solving a constraint problem and determining exactly the

normal reaction forces that prevent fiber crossing. An alternate approach consists of adding strong and short-range repulsive forces that act at the same points and in the same directions as the lubrication forces [55]:

$$\boldsymbol{F}_{\alpha\beta}^{(0),c} = \pm a_0 \frac{\tau \mathrm{e}^{-\tau h}}{1 - \mathrm{e}^{-\tau h}} \boldsymbol{n}. \tag{3.7}$$

The values of the parameters a_0 and τ used in the simulations are 1×10^{-4} and 1×10^3 respectively, and are chosen such that the repulsive force remains small over most of the range of the lubrication force; the actual values are typically shown to have little impact on the simulation results [140, 32].

3.2.3 Hydrodynamic interactions

Hydrodynamic interactions are accounted for through the disturbance velocity $\boldsymbol{u}'_\alpha$ in Equations (3.3)–(3.4). As explained in Section 2.4, the disturbance velocity is obtained as a convolution as:

$$\boldsymbol{u}'(\boldsymbol{x}_\alpha + s_\alpha \boldsymbol{p}_\alpha) = \frac{1}{8\pi} \sum_{\beta=1}^{N} \int_{-1}^{1} \mathsf{J}(\boldsymbol{x}_\alpha + s_\alpha \boldsymbol{p}_\alpha - \boldsymbol{x}_\beta - s_\beta \boldsymbol{p}_\beta) \cdot \boldsymbol{f}_\beta(s_\beta) \mathrm{d}s_\beta, \tag{3.8}$$

where J is the Green's function for the geometry of interest. For a finite number of point forces, J is given by the Oseen-Burgers tensor K (Equation (2.8)). However when the suspension is infinite, summing an infinite number of Stokeslets becomes intractable and convergence is not guaranteed [26]. This issue can be circumvented by using a periodic suspension obtained by replicating a unit cell in all three space dimensions. In the case of a periodic distribution of point forces an exact solution K_p was derived by Hasimoto [81]. The details of the Hasimoto solution are given in Appendix A and Section 3.3 along with a discussion on the method used to calculate it. Hence for a periodic suspension:

$$\mathsf{J}(\boldsymbol{x}_\alpha + s_\alpha \boldsymbol{p}_\alpha - \boldsymbol{x}_\beta - s_\beta \boldsymbol{p}_\beta) = \begin{cases} \mathsf{K}_p(\boldsymbol{x}_\alpha + s_\alpha \boldsymbol{p}_\alpha - \boldsymbol{x}_\beta - s_\beta \boldsymbol{p}_\beta) & \text{if } \alpha \neq \beta, \\ \mathsf{K}_p(s_\alpha - s_\beta) - \mathsf{K}(s_\alpha - s_\beta) & \text{if } \alpha = \beta. \end{cases} \tag{3.9}$$

When $\alpha = \beta$, the Oseen-Burgers tensor must be subtracted from the periodic solution so that the disturbance velocity due to fiber α is not included. When $\alpha = \beta$ and $s_\alpha = s_\beta$ the

limit of $\mathbf{K}_p(s_\alpha - s_\beta) - \mathbf{K}(s_\alpha - s_\beta)$ is used.

3.2.4 Linearization of the force distribution

The system of equations, as presented in the previous sections, is a coupled integral system for the force distribution $\boldsymbol{f}_\alpha(s_\alpha)$ along each fiber α. As previously suggested by Harlen *et al.* [80] and Butler & Shaqfeh [32], we make use of the spectral expansion described in Section 2.4.3 and expand the force distribution along the rods using Legendre polynomials:

$$
\begin{aligned}
\boldsymbol{f}_\alpha(s_\alpha) &\approx \frac{1}{2} \int_{-1}^{1} \boldsymbol{f}_\alpha(s_\alpha) \mathrm{d}s_\alpha + \frac{3s_\alpha}{2} \int_{-1}^{1} s_\alpha \boldsymbol{f}_\alpha(s_\alpha) \mathrm{d}s_\alpha \\
&\approx \frac{1}{2} \boldsymbol{F}_\alpha^{(0)} + \frac{3s_\alpha}{2} \left[\mathscr{S}_\alpha \boldsymbol{p}_\alpha + (\mathbf{I} - \boldsymbol{p}_\alpha \boldsymbol{p}_\alpha) \cdot \boldsymbol{F}^{(1)} \right],
\end{aligned}
\tag{3.10}
$$

where the dimensionless stresslet $\mathscr{S}_\alpha$ is now given by (cf. Equation (2.33)):

$$
\mathscr{S}_\alpha = -\frac{2\pi}{\log 2A} \int_{-1}^{1} s \boldsymbol{p}_\alpha \cdot \boldsymbol{u}'_\alpha(\boldsymbol{x}_\alpha + s_\alpha \boldsymbol{p}_\alpha) \mathrm{d}s.
\tag{3.11}
$$

This method is analogous in essence to that used by Claeys & Brady in their Stokesian dynamics simulations of prolate spheroids [42], although the path followed is different. Instead of using a spectral expansion of the force distribution as in our case, Stokesian dynamics is based on a multipole expansion of the Green's function into centered moments, which is typically truncated after the dipole term (Section 2.3). Claeys & Brady then argue that in the case of spheroids the multipole moments are equivalent to distributed singularities along the focal axis of the particles. The equations they obtain are slightly more general as they also involve distributions of potential dipoles and their derivatives, which arise from the finite thickness of the particles but become negligible for very high-aspect-ratio particles.

3.2.5 Method of solution

Substituting the linearized force Equation (3.10) into the expression for the disturbance velocity Equation (3.8), and then Equation (3.8) into the equations for the motion of the fibers Equations (3.3)–(3.4) yields a general expression for the translational and rotational

velocities as functions of the gravity force $\boldsymbol{F}^{(0),g}$ (which is the same for all fibers), the stresslets $\mathscr{S}_\beta$, and the lubrication forces $\boldsymbol{F}_m^{(0),l}$ where the index $m = 1, ..., M$ refers to a specific lubrication interaction between two fibers. It can be written in the general form:

$$\dot{\boldsymbol{x}}_\alpha = \sum_{\beta=1}^{N} \left[\mathsf{L}_{\alpha\beta} \cdot \boldsymbol{F}^{(0),g} + \boldsymbol{M}_{\alpha\beta} \mathscr{S}_\beta \right] + \sum_{m=1}^{M} \mathsf{N}_{\alpha m} \cdot \boldsymbol{F}_m^{(0),l}, \tag{3.12}$$

$$\dot{\boldsymbol{p}}_\alpha = \sum_{\beta=1}^{N} \left[\boldsymbol{\mathsf{P}}_{\alpha\beta} \cdot \boldsymbol{F}^{(0),g} + \boldsymbol{Q}_{\alpha\beta} \mathscr{S}_\beta \right] + \sum_{m=1}^{M} \mathsf{R}_{\alpha m} \cdot \boldsymbol{F}_m^{(0),l}. \tag{3.13}$$

For a given pair (α, β), $\mathsf{L}_{\alpha\beta}$, $\mathsf{N}_{\alpha m}$, $\boldsymbol{\mathsf{P}}_{\alpha\beta}$ and $\mathsf{R}_{\alpha m}$ are second-order tensors, and $\boldsymbol{M}_{\alpha\beta}$ and $\boldsymbol{Q}_{\alpha\beta}$ are vectors (since the stresslets are scalar quantities).

The tensors $\mathsf{L}_{\alpha\beta}$ and $\boldsymbol{\mathsf{P}}_{\alpha\beta}$ give contribution to the velocities due to gravity, and can be shown to be:

$$\mathsf{L}_{\alpha\beta} = \frac{1}{4} \iint_{-1}^{1} \mathsf{K}(s_\alpha, s_\beta) \mathrm{d}s_\alpha \mathrm{d}s_\beta + \delta_{\alpha\beta} \frac{\log(2A)}{8\pi} (\mathsf{I} + \boldsymbol{p}_\alpha \boldsymbol{p}_\alpha), \tag{3.14}$$

$$\boldsymbol{\mathsf{P}}_{\alpha\beta} = \frac{3}{4} (\mathsf{I} - \boldsymbol{p}_\alpha \boldsymbol{p}_\alpha) \cdot \iint_{-1}^{1} \mathsf{K}(s_\alpha, s_\beta) s_\alpha \mathrm{d}s_\alpha \mathrm{d}s_\beta, \tag{3.15}$$

where in each case $\mathsf{K}(s_\alpha, s_\beta)$ stands for $\mathsf{K}(\boldsymbol{x}_\alpha + s_\alpha \boldsymbol{p}_\alpha - \boldsymbol{x}_\beta - s_\beta \boldsymbol{p}_\beta)$ and takes the form given in Equation (3.9). The vectors $\boldsymbol{M}_{\alpha\beta}$ and $\boldsymbol{Q}_{\alpha\beta}$ used to relate the fiber stresslets $\mathscr{S}_\beta$ to the velocities are also easily obtained:

$$\boldsymbol{M}_{\alpha\beta} = \frac{3}{4} \iint_{-1}^{1} \mathsf{K}(s_\alpha, s_\beta) \boldsymbol{p}_\beta s_\beta \mathrm{d}s_\alpha \mathrm{d}s_\beta, \tag{3.16}$$

$$\boldsymbol{Q}_{\alpha\beta} = \frac{9}{4} (\mathsf{I} - \boldsymbol{p}_\alpha \boldsymbol{p}_\alpha) \cdot \iint_{-1}^{1} \mathsf{K}(s_\alpha, s_\beta) \boldsymbol{p}_\beta s_\alpha s_\beta \mathrm{d}s_\alpha \mathrm{d}s_\beta. \tag{3.17}$$

The two remaining tensors $\mathsf{N}_{\alpha m}$ and $\mathsf{R}_{\alpha m}$ give the contribution of lubrication forces to the velocity, which is of two types: a direct contribution, through the second term on the right-hand sides of Equations (3.3)–(3.4), and an indirect contribution through the disturbance velocity. This second contribution is a multibody interaction, in the sense that each lubrication force affects all the fibers. Given a lubrication interaction m $(1 \le m \le M)$, let a and b be the two fibers between which the interaction takes place,

and let λ_{ma} and λ_{mb} be the corresponding abscissae where the force is applied. If $\boldsymbol{F}_m^{(0),l}$ is the force on fiber a, the force on fiber b will be $-\boldsymbol{F}_m^{(0),l}$. Introduce the two matrices:

$$A_{\alpha m} = \delta_{\alpha a} - \delta_{\alpha b}, \quad B_{\alpha m} = \delta_{\alpha a}\lambda_{ma} - \delta_{\alpha b}\lambda_{mb}.$$

The two tensors $\mathbf{N}_{\alpha l}$ and $\mathbf{R}_{\alpha l}$ then take on the following form:

$$\mathbf{N}_{\alpha l} = \frac{1}{4} \iint_{-1}^{1} \mathbf{K}(s_\alpha, s_\beta) \cdot [\mathbf{I} + 3\lambda_{la}s_a(\mathbf{I} - \boldsymbol{p}_a\boldsymbol{p}_a)]\,\mathrm{d}s_a\mathrm{d}s_\alpha \tag{3.18}$$

$$-\frac{1}{4} \iint_{-1}^{1} \mathbf{K}(s_\alpha, s_\beta) \cdot [\mathbf{I} + 3\lambda_{lb}s_b(\mathbf{I} - \boldsymbol{p}_b\boldsymbol{p}_b)]\,\mathrm{d}s_b\mathrm{d}s_\alpha + \frac{\log(2A)}{8\pi}(\mathbf{I} + \boldsymbol{p}_\alpha\boldsymbol{p}_\alpha)A_{\alpha l},$$

$$\mathbf{R}_{\alpha l} = \frac{3}{4}(\mathbf{I} - \boldsymbol{p}_\alpha\boldsymbol{p}_\alpha) \cdot \left\{ \iint_{-1}^{1} \mathbf{K}(s_\alpha, s_\beta) \cdot [\mathbf{I} + 3\lambda_{la}s_a(\mathbf{I} - \boldsymbol{p}_a\boldsymbol{p}_a)]\,\mathrm{d}s_a s_\alpha \mathrm{d}s_\alpha \right. \tag{3.19}$$

$$\left. - \iint_{-1}^{1} \mathbf{K}(s_\alpha, s_\beta) \cdot [\mathbf{I} + 3\lambda_{lb}s_b(\mathbf{I} - \boldsymbol{p}_b\boldsymbol{p}_b)]\,\mathrm{d}s_b s_\alpha \mathrm{d}s_\alpha + \frac{\log(2A)}{2\pi}B_{\alpha l} \right\}.$$

The repulsive contact forces, which are not included in the above equations, are treated in exactly the same way as the lubrication forces.

The method of solution proceeds as follows. In Equations (3.12)–(3.13) the tensors $\mathbf{L}_{\alpha\beta}$, $\mathbf{N}_{\alpha l}$, $\mathbf{P}_{\alpha\beta}$ and $\mathbf{R}_{\alpha l}$ and vectors $\boldsymbol{M}_{\alpha\beta}$ and $\boldsymbol{Q}_{\alpha\beta}$ are only functions of the positions and orientations of the fibers and are hence known. The gravitational force $\boldsymbol{F}^{(0),g}$ and the repulsive forces $\boldsymbol{F}_m^{(0),c}$ are also known, so that the unknowns are: the translational and rotational velocities $\dot{\boldsymbol{x}}_\alpha$ and $\dot{\boldsymbol{p}}_\alpha$ of the fibers, as well as the stresslets $\mathscr{S}_\alpha$ and lubrication forces $\boldsymbol{F}_m^{(0),l}$. The first step consists of solving for the latter two in the following manner. Substituting the linearized force distribution Equation (3.10) (where the total force and torque are functions of the lubrication interactions and stresslets which are unknown) into the disturbance velocity Equation (3.8), and in turn substituting Equation (3.8) into the definition of the stresslets Equation (3.11) yields a linear system for the stresslets and magnitudes of the lubrication forces. Once this system is inverted, using an iterative solver discussed in Section 3.4, Equations (3.12)–(3.13) can be used to obtain the velocities of the fibers. The positions of the fibers can then be advanced using a fourth-order Runge-Kutta time-marching method. The time step is chosen so as to avoid collisions or overlap, and so that no fiber moves by more than half a fiber diameter at each step. For a more extensive

discussion on the time integration method, the reader is referred to Butler & Shaqfeh [32].

3.3   The smooth particle-mesh Ewald algorithm

3.3.1   Periodic fundamental solution and Ewald summation formula

The disturbance velocity Equation (3.8) must be evaluated along each fiber. In practical simulations the integrals over the lengths of the fibers are computed numerically using Gauss-Legendre quadrature, so that we are left with calculating the disturbance field created by a distribution of point forces at each point force location. Consider a distribution of N point forces $\boldsymbol{F}_1, \boldsymbol{F}_2, \ldots \boldsymbol{F}_N$ at positions $\boldsymbol{x}_1, \boldsymbol{x}_2, \ldots \boldsymbol{x}_N$ in a unit cell of volume τ_0; to alleviate the notations, assume that the quadrature weights resulting from the discretization of the integrals have been included in the force vectors $\boldsymbol{F}_n$. Denote by $\boldsymbol{a}_i$, $i = 1, 2, 3$, the lattice vectors forming the edges of the unit cell. To simulate an infinite suspension we use periodic boundary conditions, so that each point force $\boldsymbol{F}_n$ at position $\boldsymbol{x}_n$ has periodic images at all the locations $\boldsymbol{x}_n + p_1 \boldsymbol{a}_1 + p_2 \boldsymbol{a}_2 + p_3 \boldsymbol{a}_3$ for all integers p_1, p_2, p_3. With these notations, the disturbance velocity at location $\boldsymbol{x}_m$ created by the point forces other than $\boldsymbol{F}_m$ is written as:

$$\boldsymbol{u}(\boldsymbol{x}_m) = \sum_{\boldsymbol{p}} \sum_{n=1}^{N} \mathsf{K}(\boldsymbol{x}_n - \boldsymbol{x}_m + \boldsymbol{p}) \cdot \boldsymbol{F}_n, \quad m = 1, \ldots, N, \tag{3.20}$$

where K is the Oseen-Burgers tensor (Equation (2.8)). The term corresponding to $n = m$ and $\boldsymbol{p} = \boldsymbol{0}$ is omitted in the sum. Because of the decay of the Oseen-Burgers tensor as $1/r$, the infinite sum in Equation (3.20) is generally divergent. This is typically remedied by realizing that the average force $\langle \boldsymbol{F} \rangle \neq \boldsymbol{0}$ creates a backflow, and that only the velocity relative to this backflow has a physical significance [26, 25]. Hasimoto [81] took advantage of the spatial periodicity of the problem and used Fourier series to derive a convergent expression for Equation (3.20). His solution, which is rederived in Appendix A, can be written:

$$\boldsymbol{u}(\boldsymbol{x}_m) = \frac{1}{4\pi\mu} \left[\boldsymbol{S}^1 - \boldsymbol{\nabla}(\boldsymbol{\nabla} \cdot \boldsymbol{S}^2) \right], \tag{3.21}$$

where $\boldsymbol{S}^1$ and $\boldsymbol{S}^2$ are the following sums:

$$\boldsymbol{S}^2 = -\frac{1}{4\pi^3\tau_0} \sum_{\boldsymbol{k}\neq\boldsymbol{0}} \frac{\mathrm{e}^{2\pi\mathrm{i}\boldsymbol{k}\cdot\boldsymbol{x}_m}}{k^4} \hat{\boldsymbol{F}}(\boldsymbol{k}) \quad\text{and}\quad \boldsymbol{S}^1 = \boldsymbol{\nabla}^2 \boldsymbol{S}^2 = \frac{1}{\pi\tau_0} \sum_{\boldsymbol{k}\neq\boldsymbol{0}} \frac{\mathrm{e}^{2\pi\mathrm{i}\boldsymbol{k}\cdot\boldsymbol{x}_m}}{k^2} \hat{\boldsymbol{F}}(\boldsymbol{k}). \quad (3.22)$$

The vectors $\boldsymbol{k}$ are the reciprocal lattice unit vectors: $\boldsymbol{k} = k_1\boldsymbol{b}_1 + k_2\boldsymbol{b}_2 + k_3\boldsymbol{b}_3$, where the vectors $\boldsymbol{b}_i$, $i = 1, 2, 3$, define the unit cell in the reciprocal or Fourier space:

$$\boldsymbol{b}_1 = \frac{\boldsymbol{a}_2 \times \boldsymbol{a}_3}{\tau_0}, \quad \boldsymbol{b}_2 = \frac{\boldsymbol{a}_3 \times \boldsymbol{a}_1}{\tau_0}, \quad \boldsymbol{b}_3 = \frac{\boldsymbol{a}_1 \times \boldsymbol{a}_2}{\tau_0}. \quad (3.23)$$

$\hat{\boldsymbol{F}}(\boldsymbol{k})$ is the Fourier transform of the distribution of point forces, or structure factor:

$$\hat{\boldsymbol{F}}(\boldsymbol{k}) = \sum_{n=1}^{N} \boldsymbol{F}_n \mathrm{e}^{2\pi\mathrm{i}\boldsymbol{k}\cdot\boldsymbol{x}_n}. \quad (3.24)$$

The presence of this structure factor in the periodic fundamental solution suggests that the disturbance velocity could be evaluated using the fast Fourier transform algorithm; this observation will be exploited below. It is important to notice the absence of the term $\boldsymbol{k} = \boldsymbol{0}$ in the Fourier representation of the velocity: this term corresponds to the mean backflow alluded to above, and should be set to zero if the fluid is globally quiescent. The absence of this term arises naturally in the derivation of Equation (3.21), where it is shown that the mean pressure gradient cancels exactly the mean force term $\hat{\boldsymbol{F}}(\boldsymbol{0})$, so that the latter does not contribute to the disturbance velocity [81] (cf. Appendix A).

Equations (3.21)–(3.22) constitute an exact and absolutely convergent expression for the disturbance velocity, and can be used as such in computations. However the relatively slow decay in $1/k^2$ makes this direct method quite inefficient as many terms are needed to achieve a reasonable accuracy. The convergence can be accelerated by recasting Equations (3.21)–(3.22) into a slightly different form called Ewald summation formula. It was first used by Ewald for electrostatic interactions [58], and the present form for hydrodynamic interactions is due to Hasimoto [81]. The starting point is an integral representation for $1/k^{2m}$ for $m = 1, 2$, and the introduction in the integral of a cutoff parameter α, called

Ewald coefficient. The derivation is classic [58, 57, 81, 170] and is presented in Appendix A. The final result expresses the disturbance velocity as follows:

$$u(\boldsymbol{x}_m) = \sum_{\boldsymbol{p}} \sum_{n=1}^{N} \mathbf{A}(\alpha, \boldsymbol{x}_m - \boldsymbol{x}_n + \boldsymbol{p})\boldsymbol{F}_n + \sum_{\boldsymbol{k} \neq \boldsymbol{0}} e^{-2\pi i \boldsymbol{k} \cdot \boldsymbol{x}_m} \mathbf{B}(\alpha, \boldsymbol{k})\hat{\boldsymbol{F}}(\boldsymbol{k}) \qquad (3.25)$$

for $m = 1, \ldots, N$. The two tensors $\mathbf{A}$ and $\mathbf{B}$ are given by:

$$\mathbf{A}(\alpha, \boldsymbol{x}) = \pi\alpha^{-3/2}\phi_{1/2}(\pi\alpha^{-1}|\boldsymbol{x}|^2)\left(|\boldsymbol{x}|^2\mathbf{I} + \boldsymbol{x}\boldsymbol{x}\right) - 2\alpha^{-1/2}\exp(-\pi\alpha^{-1}|\boldsymbol{x}|^2)\mathbf{I}, \quad (3.26)$$

$$\mathbf{B}(\alpha, \boldsymbol{k}) = \pi\alpha^2\tau_0^{-1}\phi_1(\pi\alpha|\boldsymbol{k}|^2)(|\boldsymbol{k}|^2\mathbf{I} - \boldsymbol{k}\boldsymbol{k}), \qquad (3.27)$$

where the functions ϕ_ν are incomplete Γ-functions:

$$\phi_{1/2}(x) = \frac{\exp(-x)}{x} + \frac{1}{2}\frac{\mathrm{erfc}(\sqrt{x})}{2x} \quad \text{and} \quad \phi_1(x) = \frac{\exp(-x)}{x^2}(1+x). \qquad (3.28)$$

The Ewald coefficient α is a user-defined parameter that determines the relative importance of the two sums: its choice is typically dictated by cost considerations. The two tensors $\mathbf{A}$ and $\mathbf{B}$ decay exponentially in their second arguments, so that both sums in Equation (3.25) converge rapidly.

3.3.2   Description of the algorithm

The Ewald summation formula Equation (3.25) is the basis for most simulations with periodic boundary conditions. A standard and widely used method, sometimes called the Ewald summation technique, consists of truncating both sums after a few terms and choosing the coefficient α so as to minimize the overall cost [26, 122, 32]. In spite of the rapid convergence of the sums, this direct method can still be quite expensive for very large systems. Also, it does not typically exploit the presence of the Fourier transform in the second sum. The smooth particle-mesh Ewald method proceeds quite differently: the parameter α is chosen so as to reduce the cost of the first sum (or real sum), and a fast algorithm based on the fast Fourier transform on a Cartesian grid is used for the second sum (or Fourier sum). More details are provided below.

Real sum

The calculation of the real sum at all the point force locations $\boldsymbol{x}_m$ is *a priori* an $O(N^2)$ operation, as it involves summing over all the other point forces and their images. However the exponential decay of the tensor **A** can be exploited to restrict the evaluation of the sum to close particle pairs. Given a tolerance ϵ and a cutoff radius r_c, the Ewald coefficient α can be chosen to make all the coefficients of $\mathbf{A}(\alpha, \boldsymbol{x})$ less than ϵ whenever $|\boldsymbol{x}| \geq r_c$. Once α is obtained following this procedure, the real sum in Equation (3.25) only needs to be performed over the point forces located within a sphere of radius r_c, i.e. over a small number independent of the system size. The evaluation of the sum at all the point force locations $\boldsymbol{x}_m$ then has an $O(N)$ cost, with a constant of proportionality that can be adjusted through the cutoff radius.

Fourier sum

The real gain is achieved in the evaluation of the Fourier sum. As mentioned previously, the presence of the structure factors suggests use of the fast Fourier transform algorithm. As the point forces can be located anywhere inside the unit cell, prior interpolation to a Cartesian grid is necessary. This can be done formally using Cardinal B-splines, which are introduced briefly in Appendix B. A mesh is defined inside the reciprocal unit cell by choosing three integers K_1, K_2 and K_3 corresponding to the numbers of points along the reciprocal lattice vectors $\boldsymbol{b}_1$, $\boldsymbol{b}_2$ and $\boldsymbol{b}_3$. Given a point $\boldsymbol{x}$ in the unit cell, we define its scaled fractional coordinates by $\xi_i = K_i \boldsymbol{b}_i \cdot \boldsymbol{x}$ for $i = 1, 2, 3$.

We wish to approximate the structure factor $\hat{\boldsymbol{F}}(\boldsymbol{k})$ using a discrete Fourier transform on the grid defined above. This is achieved by interpolating the complex exponentials in the definition of $\hat{\boldsymbol{F}}(\boldsymbol{k})$ using Cardinal B-splines. Appendix B shows that in one dimension we can write:

$$\exp\left(2\pi\mathrm{i}\frac{k\xi}{K}\right) \approx b(k) \sum_{m=-\infty}^{+\infty} M_p(\xi - m) \exp\left(2\pi\mathrm{i}\frac{km}{K}\right), \qquad (3.29)$$

where the coefficients $b(k)$ and M_p are easily computed using a recursive definition. p is

the order of interpolation, and the sum over m is in fact limited to p terms as the functions M_p have compact support. Generalizing Equation (3.29) to three dimensions we obtain the following approximation for the structure factor:

$$\hat{\boldsymbol{F}}(\boldsymbol{k}) \approx b_1(k_1)b_2(k_2)b_3(k_3)\mathscr{F}(\boldsymbol{Q})(\boldsymbol{k}), \tag{3.30}$$

where $\mathscr{F}(\boldsymbol{Q})$ is the three-dimensional discrete Fourier transform of the following array:

$$\boldsymbol{Q}(\boldsymbol{m}) = \sum_{n=1}^{N} \sum_{p_1,p_2,p_3} \boldsymbol{F}_n M_p(\xi_1^n - m_1 + p_1 K_1) M_p(\xi_2^n - m_2 + p_2 K_2) M_p(\xi_3^n - m_3 + p_3 K_3). \tag{3.31}$$

The algorithm for the computation of the Fourier sum can now be summarized. The first step is the assignment of the point forces $\boldsymbol{F}_n$ to the Cartesian grid using Cardinal B-splines, i.e. the calculation of the array $\boldsymbol{Q}(\boldsymbol{m})$ using the interpolation formula Equation (3.31). The discrete Fourier transform $\mathscr{F}(\boldsymbol{Q})$ is then computed using the fast Fourier transform algorithm (FFT), and is multiplied in turn by $b_i(k_i)$ to yield the approximation to the structure factor Equation (3.30), and by the Fourier convolution kernel $\mathbf{B}(\alpha, \boldsymbol{k})$. The result is multiplied by $b_i^*(k_i)$ (where * denotes the complex conjugate) and the inverse FFT is applied, yielding the Fourier sum in Equation (3.25) but evaluated at the grid points. The sum can then be interpolated from the grid points to the particle locations, again using B-splines (transpose operation of the force assignment Equation (3.31)).

As we explained above, the real sum need only be performed on a small number of neighbors for each point force, resulting in an $O(N)$ cost for N point forces. The cost of computing the Fourier sum using the previous algorithm is limited by the two fast Fourier transforms, which have a cost of $O(K \log K)$ where K is the number of points in each direction on the Cartesian mesh, and is chosen proportional to the system size N. Therefore the total cost of the method scales as $N \log N$, which can be a significant improvement for large systems compared to the original cost of $O(N^2)$. Comparisons of the CPU times for the traditional Ewald summation technique and the smooth particle-mesh Ewald algorithm are presented in Section 3.3.4.

The use of the Cardinal B-splines for the force assignment and interpolation schemes is the major difference between SPME and the accelerated Stokesian dynamics method of Sierou & Brady [170]. Accelerated Stokesian dynamics uses a Taylor series expansion to assign the forces to the grid, after which it applies the fast Fourier transform algorithm; Lagrange interpolation is then used to go back from the grid to the particle locations. Exploiting instead the interpolation properties of Cardinal B-splines for complex exponentials gives directly a smooth approximation to the structure factors [57, 165], which are the relevant quantities appearing in the Fourier sum of the Ewald summation formula. The final interpolation is done again using B-splines and is completely analogous to the force assignment, as it should be considering the symmetric nature of the two operations. Another advantage of using B-splines is their smooth behavior at high interpolation order, while Lagrange interpolation is known to become unstable as the order increases. Essmann *et al.* [57] compared both methods for electrostatic interactions, and obtained better accuracies using B-splines for both the forces and interaction energies.

3.3.3 Accuracy

The accuracy and efficiency of the method depend on several parameters: the tolerance ϵ and cutoff radius r_c for the real sum (the two of which uniquely define the Ewald coefficient α, as explained in Section 3.3.2), and the number of grid points K and the order p of the B-spline interpolation for the evaluation of the Fourier sum. These parameters are typically adjusted to maximize the accuracy while minimizing the cost.

To investigate the accuracy of the method and the influence of the parameters in more detail, tests are performed in a square box with a distribution of 100 point forces at random locations, with random orientations and unit strengths. In all the tests, the value of the real-space tolerance is set to $\epsilon = 10^{-10}$. The disturbance velocity at the force locations is computed using the smooth particle-mesh Ewald method, and is compared to the solution obtained with converged Ewald sums. The measure of accuracy used here is the root-mean square (rms) error between the two solutions:
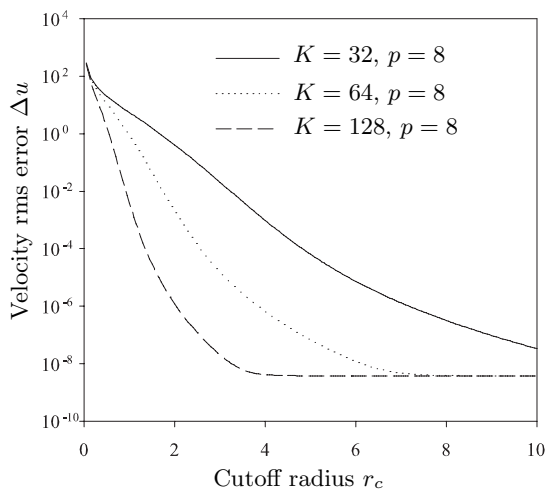
Figure 3.1: Velocity rms error as a function of the cutoff radius r_c. The three curves correspond to the three different grid sizes $K = 32$, 64 and 128 for the evaluation of the Fourier sum.

$$\Delta u = \left[\frac{1}{N}\sum_{n=1}^{N}(\boldsymbol{u}^{\mathrm{SPME}}(\boldsymbol{x}_n) - \boldsymbol{u}^{\mathrm{EWALD}}(\boldsymbol{x}_n))^2\right]^{1/2}. \tag{3.32}$$

Since our method is based on evaluation of sums such as Equation (3.8) which only involve point force distributions, we limit our attention to this measure of accuracy. It should be noted however that such a measure does not guarantee that other quantities such as higher force moments are as adequately captured.

The rms error as a function of the cutoff radius at constant values of K and p is plotted in Figure 3.1. The three curves correspond to the three grid sizes $K = 32$, 64 and 128. In all cases the rms error becomes large as $r_c \to 0$, but decays very rapidly when r_c increases; for large values of r_c, it reaches a plateau at around $\Delta u = 10^{-9}$. These curves are easily interpreted. Whatever the value of the cutoff radius, the error in the real sum is of order ϵ and accounts for the plateau at around 10^{-9}: indeed the Ewald coefficient is chosen precisely so as to make the real sum converge within ϵ. The remainder of the error (i.e. all the values above the plateau) stems from the evaluation of the structure factor using the discrete Fourier transform, and from the assignment of the point forces to the grid and back. The Fourier sum accounts for the smooth and long-range part of the solution, and
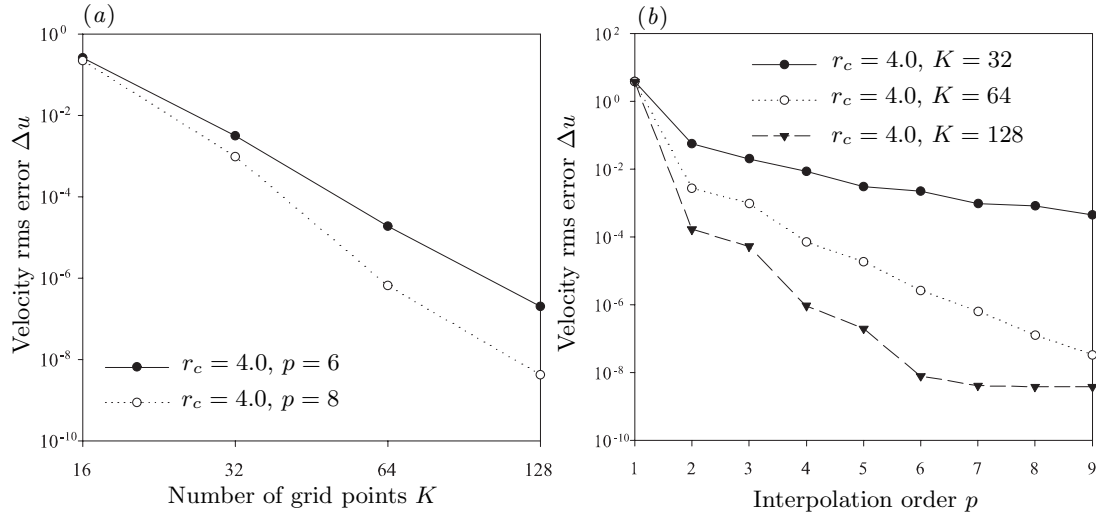
Figure 3.2: Velocity rms error as a function of (a) the number of grid points K used for the evaluation of the Fourier sum, and (b) the interpolation order p of the force assignment scheme.

cannot capture the short-range singular part; this explains why for a given number of grid points K the error increases rapidly when the cutoff and hence the Ewald coefficient become small.

The influence of K and p on the accuracy is shown in Figure 3.2. As already suggested in Figure 3.1, increasing the number of points for the fast Fourier transform improves the accuracy of the Fourier sum: Figure 3.1(a) shows the decay of the error with increasing K, at constant cutoff radius and interpolation order. On a log-log plot the curves are essentially straight, suggesting an algebraic decay; the exponents obtained from the curves in Figure 3.1(a) are respectively -6.7 and -8.5 and are close to the value of the interpolation order p, confirming the scaling of the error with K^{-p} for the B-spline interpolation [57, 165]. Another way of making the Fourier sum more accurate is to choose a higher order of interpolation for the force assignment scheme, and is illustrated in Figure 3.2(b). Increasing K or p has the same effect on the accuracy, so that either one or both can be done and the final choice of their values depends on the computational expense.
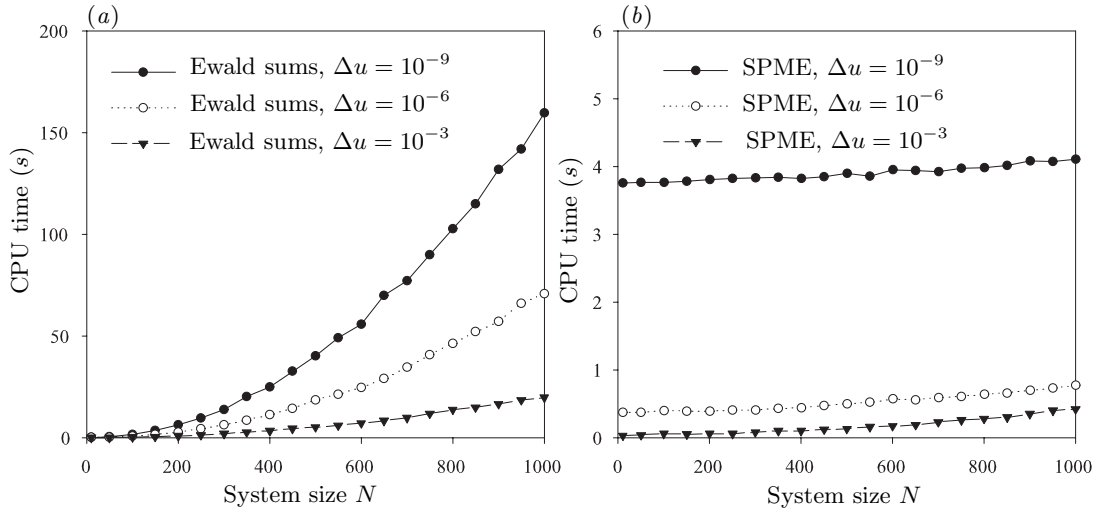
Figure 3.3: CPU times for the calculation of the Ewald sums using (a) the traditional Ewald summation technique, and (b) the SPME method, as a function of the system size.

3.3.4   Efficiency

The efficiency of the method is assessed by comparing the CPU times required by the traditional Ewald summation technique and our smooth particle-mesh Ewald algorithm. These are shown in Figure 3.3, where simulations were performed for the same systems as in the previous section (unit-strength forces with random locations and orientations), for different system sizes N and levels of accuracy. A quick observation of Figure 3.3 suffices to show the superiority of the SPME method in terms of efficiency. Except for very small systems, the CPU times are all smaller for SPME than for the Ewald sums at a given accuracy. In fact, even the high-accuracy SPME is more advantageous than the low-accuracy Ewald sums. It becomes even more so for large systems: at the same level of accuracy (root mean square error of the order of 10^{-9}), SPME is about 40 times faster than the Ewald sums for 1,000 point forces, and 300 times faster for 5,000 points forces. While the cost scales quadratically with size for the Ewald sums, it increases almost linearly with SPME when the grid size is fixed in Fourier space (the three curves for SPME correspond to three different grid resolutions in Fourier space).

It must still be noted that the CPU times of Figure 3.3 are for the calculation of the

disturbance velocity only. To assess the actual cost of our simulations, we should also take into account the inversion of the linear system for the stresslets and lubrication forces, which cannot be performed using standard elimination procedures when SPME is used. The additional cost of this system inversion does somewhat impede the performance of SPME, but for large systems it still remains far superior to the standard Ewald sums. A detailed discussion on the system inversion follows.

3.4 The iterative solver

3.4.1 Generalities

Solving for the particle stresslets and amplitudes of the lubrication forces involves inverting a linear system. This operation, which in general can be quite costly, becomes more complicated when the SPME method is used. Indeed in SPME the coefficients in the Ewald summation formula Equation (3.20) are not computed directly, and the reciprocal sum is instead calculated as a whole using the fast Fourier transform. In other words, the matrix that needs to be inverted is not explicitly accessible: the SPME algorithm provides us with a 'black box' that performs matrix-vector multiplications in an efficient manner. Classical methods for inverting linear systems such as the LU factorization used by Butler & Shaqfeh [32] are therefore not applicable, and we must resort to a different approach. An attractive method is the use of an iterative solver to compute an approximate solution, such as the Generalized Minimum Residual (GMRES) method of Saad & Schultz [154], which applies to large nonsymmetric linear systems. At each iteration of the solver, only one matrix-vector multiplication is needed, so that this type of method can be used in conjunction with SPME[1].

In SPME, the real sum in Equation (3.20) is still computed directly, and is written as the multiplication of a matrix **A** with a vector containing the point forces. The coefficients of the matrix depend on the spatial configuration of the suspension, and therefore

---

[1]The implementation that we used in this work was that by V. Frayssé, L. Giraud, S. Gratton and J. Langou (CERFACS Technical Report TR/PA/03/3 (2003)) available from http://www.cerfacs.fr/algor/Softs/GMRES.

Time, t	Number of lubrication interactions	Condition number
0	19	8
50	134	55
100	218	381
150	251	729

Table 3.1: Dependence of the condition number on the inhomogeneity of the suspension and on the presence of lubrication interactions. The results are for 200 fibers, $A = 11$, $nl^3 = 0.1$ and a box of aspect ratio L_x:L_y:L_z=1:1:2.

do not change from one solver iteration to the next within a given time step. This seemingly benign observation allows one to pre-compute the real-space matrix before applying GMRES, so that at each iteration of the solver the real sum is simply obtained by a matrix-vector multiplication of a stored matrix with the current iterate. This spares the expense of computing the real sum coefficients at each step and reduces the time of the algorithm by an order of magnitude, the only downside being the additional storage of the matrix.

3.4.2   Preconditioning

To benefit fully from the efficiency of the SPME method, the number of iterations required by the solver to achieve a reasonable convergence must be kept to a minimum. This number of iterations is a function of the condition number of the linear system, defined as the ratio of the largest to the smallest eigenvalue. For our problem, the condition number was shown not to increase significantly with the problem size at a given fiber concentration, but rather to depend on the spatial configuration of the fibers and on the presence of lubrication forces: for very dense or inhomogeneous suspensions with many lubrication interactions (such as the ones that occur when the sedimenting fibers form clusters), the linear system is typically quite stiff and a large number of iterations is required. This is illustrated in Table 3.1, which shows how the condition number increases over the course of a simulation as a result of the concentration instability. Sangani & Mo [162] already encountered this issue with their fast-multipole method, where they observed
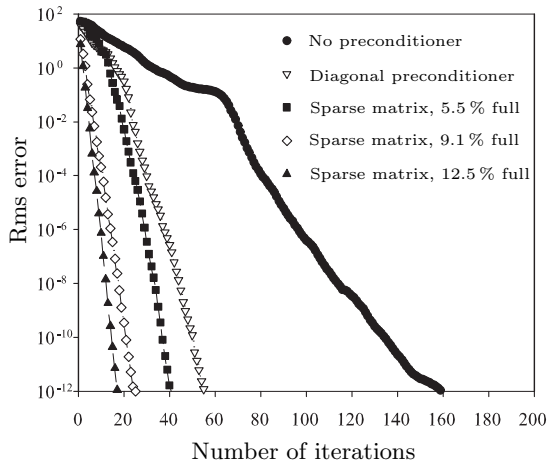
Figure 3.4: Convergence of the GMRES solver depending on the preconditioner, for an inhomogeneous system of 200 fibers, $A = 11$, $nl^3 = 0.1$ and a box aspect ratio of $L_x{:}L_y{:}L_z$=1:1:2.

that the inclusion of lubrication forces in their simulations of sedimenting spheres greatly decreased their convergence rates. A similar problem was reported in accelerated Stokesian dynamics simulations [170].

The classic approach to accelerate convergence is the preconditioning of the system, which consists of multiplying it by an approximate inverse of the original matrix. Numerous methods are available [155]: sparse approximate inverse, incomplete LU factorization etc., which are typically very efficient for large sparse matrices. Our problem however is quite atypical in a few ways. First the coefficients of the matrix are not known if SPME is used: applying any kind of preconditioner will require calculating some of these coefficients using direct summation of the Ewald sums, which is an expensive operation as was established earlier. Second, the matrix is full, whereas most preconditioners are designed for the sparse systems arising in finite difference and finite element codes. Finally the matrix is relatively small, from a few hundred to a few thousand rows and columns: unlike most situations where iterative solvers are used, the limiting factor is not the system size but the difficulty of constructing the matrix efficiently.

In accelerated Stokesian dynamics, Sierou & Brady [170] showed that using an incomplete Cholesky preconditioner greatly improved the efficiency of their solver. This method however is only valid for symmetric matrices, which is not the case of the system in our simulation method. Other preconditioning techniques were therefore investigated, and the convergence rates are compared in Figure 3.4. A first method consists of calculating the diagonal of the matrix, which is very dominant, and preconditioning the system by this diagonal. This alone reduces the number of iterations by a factor of two or three, but is not quite sufficient for very inhomogeneous systems. The next step consists of calculating a sparse approximation of the matrix, trying to compute the terms of large magnitude. The relative importance of the different terms in the matrix depends on the configuration of the suspension and cannot be known exactly *a priori*, but a good rule of thumb is to assume that the interactions between close particles dominate. A sparse approximate matrix is therefore obtained by only computing the interactions between particles within a cut-off distance d_c, which is chosen by trial and error to minimize the number of iterations while keeping the cost of computing the approximate matrix small. This sparse matrix is then inverted, either exactly using LU factorization or approximately using incomplete LU factorization, and the inverse is used to precondition GMRES. A good choice of d_c can reduce the number of iterations by an order of magnitude, and cut the total time for the system inversion by a factor of four for a system of 200 fibers. Table 3.2 gives more details on the efficiency of these preconditioners. In all cases the terms in the approximate matrix must be calculated directly using Ewald summation; however since the sparse matrix is only approximate the Ewald summation need not be fully converged and the first few terms in the sums are typically sufficient to improve convergence.

3.5   Simulation results and discussion

3.5.1   General remarks

This section presents some simulations results, all obtained on a single-processor workstation. We first show some comparisons with the Monte-Carlo simulations of Mackaplow

Type of preconditioner	Number of GMRES iterations	Number of terms in the sparse matrix	CPU time to compute the sparse matrix (s)	Total CPU time to solve the system (s)
No preconditioner	138	—	—	558
Diagonal preconditioner	56	451 (0.2 %)	12	242
Sparse matrix, $d_c = 0.4$	46	11237 (5.5 %)	12	232
Sparse matrix, $d_c = 0.8$	26	18432 (9.1 %)	27	154
Sparse matrix, $d_c = 1.2$	19	25260 (12.5 %)	48	144
Sparse matrix, $d_c = 1.6$	14	32047 (15.7 %)	75	148
Sparse matrix, $d_c = 2.0$	13	38580 (18.9 %)	101	171

Table 3.2: Efficiency of various preconditioning techniques for an inhomogeneous system of 200 fibers of aspect ratio $A = 11$ at $nl^3 = 0.1$ in a box of aspect ratio $L_x{:}L_y{:}L_z{=}1{:}1{:}2$. Using fuller and fuller matrix approximations decreases the number of GMRES iterations, but increases the overhead cost of computing the sparse matrix. For this example, the optimal value for the cutoff distance is around $d_c = 1.2$.

& Shaqfeh [122] for random dispersions. Mackaplow & Shaqfeh used slender-body theory combined with a boundary integral formulation to compute the sedimentation rate of fixed random arrays of fibers: comparing our results to theirs is therefore a good way of evaluating the consequences of the force linearization described in Section 3.2.4. Figure 3.5 shows sedimentation rates for random arrays of high-aspect-ratio particles ($A = 100$) as a function of the effective volume fraction nl^3 (where n is the particle number density and l is the fiber half-length); the velocities are normalized by the velocities at infinite dilution. Our method slightly overestimates the sedimentation rates, but the agreement is within error bars up to $nl^3 = 1$, which is quite remarkable as the force linearization cannot be expected to perform well at high concentrations. Other differences between the two methods may also contribute to the differences observed in the sedimentation rates: Mackaplow & Shaqfeh retained an additional term in the slender-body theory asymptotic expansion Equation (3.1), but did not include lubrication interactions which should become more and more important at high concentrations. Given these differences, the agreement with our data shown in Figure 3.5 is quite good, and we can expect our method to perform well in the dilute regime.

The code was also benchmarked by comparison with the previous work of Butler & Shaqfeh [32] for small systems of up to 128 fibers: the results obtained with our new implementation were in all respects similar, so that only larger simulations of 512 fibers are discussed below. For ease of comparison with the experimental results of Herzhaft & Guazzelli [84], all the simulations presented in the next subsections are for a fiber aspect ratio of $A = 11$ and an average effective volume fraction of $nl^3 = 0.05$. A systematic investigation of the effects of slenderness and volume fraction will be deferred to a subsequent study.

Unless otherwise mentioned, all the initial distributions were obtained by assigning the fibers to random positions and with random orientations. In the event of two fibers intersecting, one of them was repositioned at another random location in the box. This ensured that the initial suspensions were homogeneous, as would be the case with a well-mixed
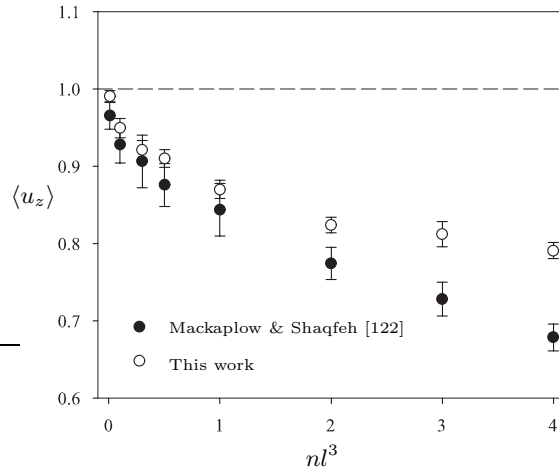
Figure 3.5: Sedimentation rates of fixed random arrays of fibers as a function of the effective volume fraction nl^3, obtained with our simulation method (open symbols) and by Mackaplow & Shaqfeh [122] (full symbols). The sedimentation rates are scaled by their value at infinite dilution. The results were obtained by averaging over 20 random configurations of approximately 300 fibers in a square unit cell. The error bars are 95% confidence intervals.

suspension in an experiment. As already observed on small systems, the local concentration fluctuations inherently present in such a random distribution cause the suspension to evolve towards very inhomogeneous states where the fibers form concentrated streamers surrounded by clarified fluid. By adjusting the dimensions of the periodic unit cell, we were able to observe the formation of one to two or three streamers for the system sizes considered here. We discuss in turn the structure of the suspension in the vertical direction (inside a given streamer) and in the horizontal direction (formation of distinct streamers).

3.5.2 Suspension microstructure and cluster formation

Vertical structure

Figure 3.6 shows the evolution of the suspension for a simulation box of high aspect ratio (L_x:L_y:L_z=1:1:8). Initially small clusters of only a few fibers form at random locations in the simulation box. These clusters have an increased sedimentation rate and entrain the fluid around them, creating a backflow in the other areas, and eventually converge to
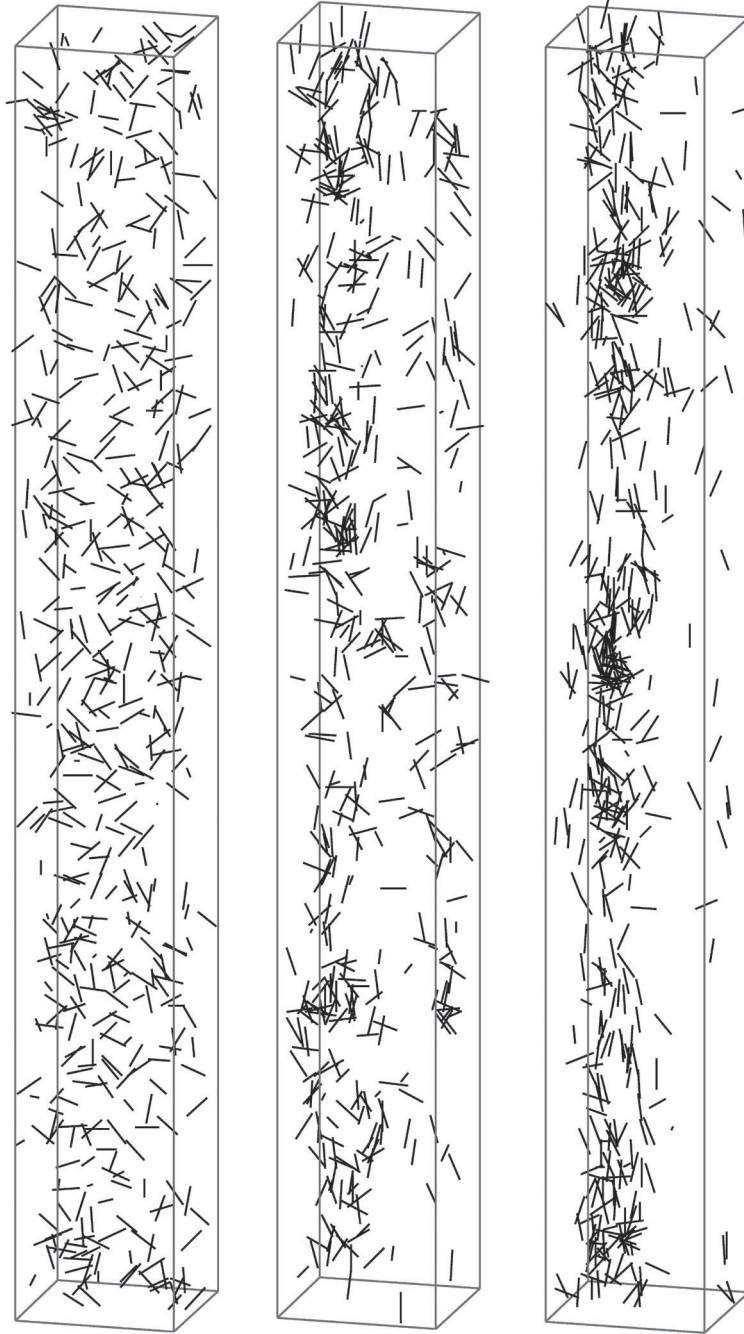
Figure 3.6: Fiber distribution in the simulation box at $t = 0.0$ (random homogeneous distribution), $t = 60.0$ and $t = 120.0$ (left to right). The simulation is for 512 fibers of aspect ratio $A = 11$ with an average concentration of $nl^3 = 0.05$. The box aspect ratio is L_x:L_y:L_z=1:1:8.
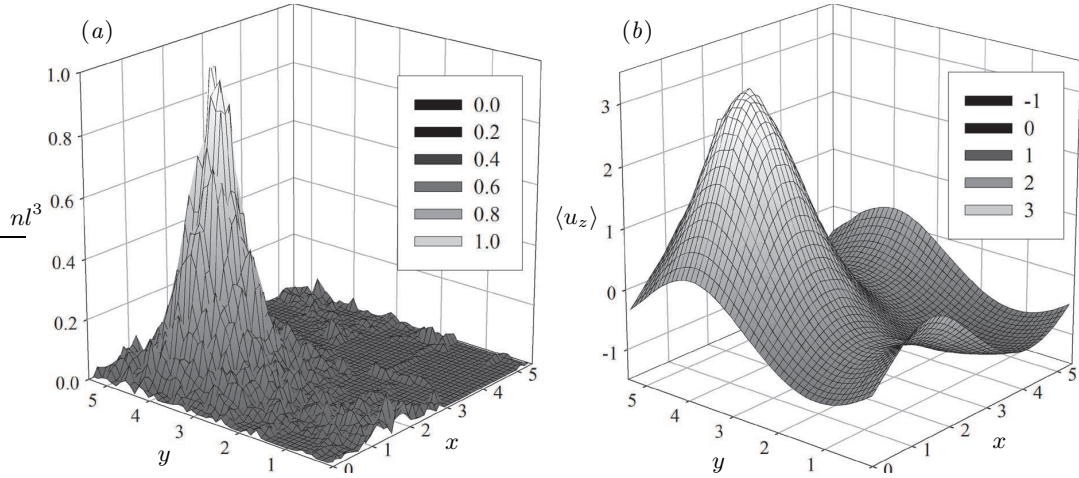
Figure 3.7: Vertically averaged local number density nl^3 (*a*) and fluid vertical velocity $\langle u_z \rangle$ (*b*) for the simulation of Figure 3.6. Positive values of $\langle u_z \rangle$ correspond to downwards velocities. The position of the streamer is where the two maxima occur. Note the negative velocities (backflow) outside the streamer.

form a streamer of high velocity. The correlation between the position of the streamers and the fluid velocity is very obvious, as shown in Figure 3.7. Because the fluid is globally quiescent, a relatively strong backflow exists outside the streamer, capable of carrying isolated fibers upwards.

As can be observed in Figure 3.6, the streamers are not uniform in the vertical direction, but composed of several distinct clusters of various sizes. Because they have different sizes, they also have different sedimentation velocities, so that their relative positions inside the streamers change: large clusters catch up with smaller ones, forming yet larger clusters and so on. The clusters do not always contain the same fibers, as fibers constantly enter and leave the clusters as they sediment. These interesting dynamics can be quantified using the following procedure, summarized in Figure 3.8. A density function of the vertical positions of the fibers at a given time can be computed by dividing the simulation box along the vertical axis into equally sized bins and counting the number of fibers in each bin: such a function presents peaks at the locations of the clusters and valleys between them, and the heights and breadths of the peaks are good indicators of the cluster sizes. More precisely we define a cluster as a region where the local particle volume fraction
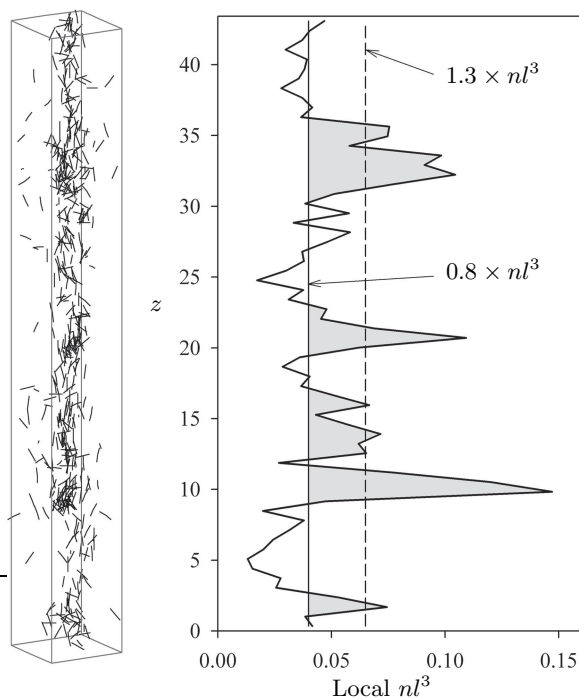
Figure 3.8: Procedure for the systematic determination of cluster positions and sizes. A density function of the vertical distribution of fibers is obtained by dividing the box into bins and counting the fibers in each bin. Clusters are defined as regions where the local particle volume fraction peaks above 1.3 times its average value nl^3 and always remains above 0.8 times the average nl^3. In the example shown, the procedure finds five clusters, of sizes 52, 47, 30, 17 and 12 fibers.

peaks above a threshold of 1.3 times its average value nl^3, and the limits of the cluster are taken to be the locations on each side where it decreases below 0.8 times the average nl^3. Integrating the particle density function over the extent of the cluster then provides an estimate of the number of fibers inside the cluster. Quite obviously the values of the two thresholds could be chosen differently: the values suggested here are such that the clusters defined by this procedure correspond to what one would define to be clusters by simply looking at the suspension.

The procedure is easily programmed on a computer and can be repeated at different times, allowing one to track the cluster positions and to perform statistics on their numbers and sizes. Figure 3.9 shows the evolution in time of the numbers of large (> 30 fibers) and

small (< 30 fibers) clusters in the simulation of Figure 3.6. To remove the high-frequency noise present in the original data, the curves have been smoothed by convolution with a top-hat function of width $\Delta t = 8$ and unit area, which explains the non-integer values for the numbers of clusters. The early values (up to $t = 15$ approximately) are not very significant as the streamer is not properly formed yet, and are therefore omitted on the graph. Both curves initially present slow oscillations at nearly the same frequency, where the peaks in the number of small clusters correlate with the valleys in the number of large clusters and vice-versa. This observation has an easy interpretation and confirms the dynamics alluded to above: up to approximately $t = 100$, there is a periodic build-up mechanism by which small clusters merge into larger clusters, which end-up breaking up into small clusters again and so forth. Progressively the number of small clusters decreases to the benefit of larger clusters, until a steady state is reached where a combination of clusters of different sizes cohabit (two small and two large clusters on average). Note that some oscillations can still be observed after the steady state is reached, but typically at a higher frequency and weaker amplitude.

The periodic boundary conditions in the vertical direction can be expected to have a significant influence on the observed oscillations. In fact it can be seen that the period of the oscillations is of the same order as the time that it takes for a fiber to sediment one box height at the mean sedimentation speed (cf. Section 3.5.4 for a discussion on the sedimentation rate). The decrease of the period that can observed in Figure 3.9 is therefore a direct consequence of the increase in the sedimentation velocity as a result of the streamer formation. This periodicity can be understood in the following way: big clusters attaining the bottom of the simulation box reappear at the top and therefore catch up with the smaller clusters that they left behind during the previous period of oscillation. It is unlikely that such oscillations would be observed in an experiment, where a segregation would occur between the different cluster sizes (with the large clusters reaching the bottom of the vessel first). However the fact that very big clusters break up and that the cluster size reaches a steady state in Figure 3.9 bears some significance: it suggests that there is a maximum size beyond which cluster growth becomes unfavorable and clusters either
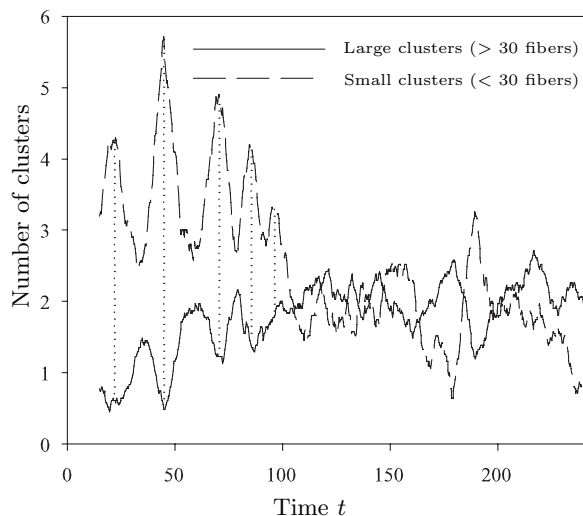
Figure 3.9: Time evolution of the numbers of clusters of a given size in a streamer. The results are for the same simulation as in Figure 3.6: 512 fibers, $A = 11$, $nl^3 = 0.05$ and $L_x:L_y:L_z$=1:1:8. The estimates of the numbers of clusters were obtained using the procedure described in Figure 3.8. To remove the high-frequency noise, the curves have been smoothed by convolution with a unit-area top-hat function of width $\Delta t = 8$.

break up or abandon fibers in their wakes.

Since the spatial wavelength in the vertical direction and the cluster size distribution (in terms of number of fibers) reach steady state values, it is interesting to investigate the densification of clusters through the pair distribution function, which specifies the fraction of pairs of fibers having a center-to-center separation at a given distance. The pair distribution function in the horizontal plane, which is the most interesting, is shown in Figure 3.10. Each curve corresponds to the time average of the function over a different time interval. Note that the functions are only plotted over half a box width $L_x/2$, whereas the maximum horizontal distance between two fibers is $\sqrt{2}L_x/2$ (owing to the periodicity in x and y). Starting from a linear profile, corresponding to a uniform distribution of fibers, the function evolves until a maximum appears at a finite distance, which represents the most probable separation between two fibers in the horizontal plane. This peak in the distribution function slowly increases and migrates towards lower values, while the amplitude of the tail decreases. The interpretation is rather simple: the streamer progressively
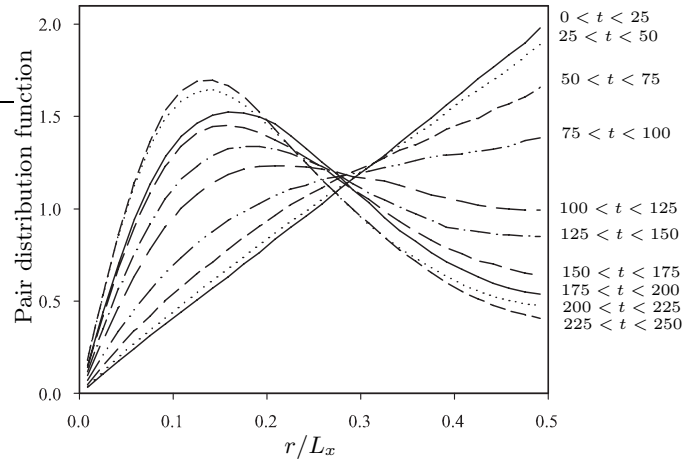
Figure 3.10: Pair distribution function in the (x, y)-plane for the simulation of Figure 3.6, averaged over various time intervals. The pair distribution function specifies the fraction of fibers with a center-to-center separation at a given distance.

becomes thinner and denser, capturing more and more fibers into its core. This process appears to be extremely slow, and continues even after the cluster distribution reaches its steady state in Figure 3.9. We can expect this densification to eventually slow down and stop, as excluded volume effects become more and more important as the fibers get more tightly packed. Limitations in computation time however did not allow us to run our simulations until a true steady state was observed.

Horizontal structure and wavenumber selection

Obtaining more than one concentrated streamer in the lateral direction is a challenging task, and to the knowledge of the authors no previous simulations have been successful at doing so. In all the previous computational studies only one streamer was obtained, and it was not clear whether this was an artifact of the periodic boundary conditions or a consequence of the limited size of the simulated systems. Only very recently have experiments systematically measured the evolution of the cluster size in suspensions of sedimenting fibers [126, 127], and they suggest that the streamers typically contain very large numbers of particles (of the order of thousands and higher). In this section we
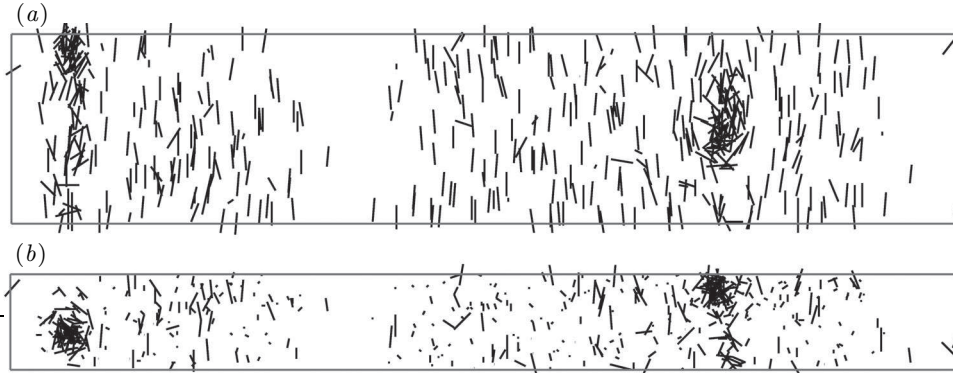
Figure 3.11: Distribution of fibers at $t = 140$ for a highly elongated box in the horizontal direction (box aspect ratio: L_x:L_y:L_z=10:1:2); the top plot (a) shows a side view of the suspension, while the bottom plot (b) provides a vertical view. The simulation is for 512 fibers of aspect ratio $A = 11$ with an average effective volume fraction of $nl^3 = 0.05$. Two distinct streamers separated by clarified regions can be observed.

investigate the horizontal structure and wavenumber selection in small periodic systems: a more thorough investigation of the wavenumber will be performed in more realistic systems in Chapter 4 using both numerical simulations and a stability analysis.

By increasing the horizontal dimensions of our simulation box we were able to obtain more than one streamer in the lateral direction, as shown in Figure 3.11 for instance. For the system sizes that we considered, the only way to achieve this was to drastically reduce the height of the box as well as its width in one horizontal direction: the aspect ratio of the box in Figure 3.11 is L_x:L_y:L_z=10:1:2. This choice of box dimensions is likely to have an influence on the structure of the suspension, first because choosing very different values of L_x and L_y introduces an artificial anisotropy in the horizontal plane, and second because the small values of L_y and L_z make the suspension essentially homogeneous in both the y- and z-directions. The precise consequences are difficult to assess until larger simulations are performed, so one should be cautious when trying to extrapolate the results presented here to full-scale suspensions.

The structure of the suspension in Figure 3.11 is quite interesting, as it exhibits a broad region between the core of the streamers and the clarified fluid where most of the
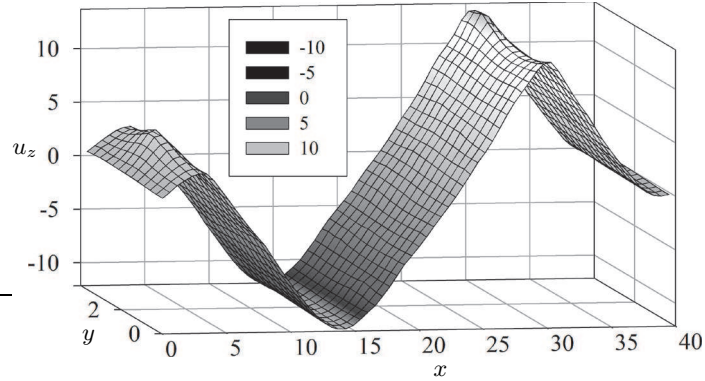
Figure 3.12: Vertically averaged vertical velocity field for the simulation of Figure 3.11. The positive values correspond to downwards velocities. The two peaks are located at the core of the concentrated streamers, and a backflow occurs in the clarified regions. Large regions of almost linear shear exist between streamers and clarified fluid.

fibers are very well oriented with gravity, and simply sediment vertically with little horizontal motion; a more detailed observation shows that fibers in this region slowly migrate towards the streamers. The vertically averaged fluid velocity field for the simulation of Figure 3.11 is shown in Figure 3.12 and provides an explanation. As expected the vertical fluid velocity peaks in the core of the streamers, and presents a backflow in the clarified regions; between those two, a large region of shear exists where the velocity varies almost linearly. The alignment of the fibers in the direction of the velocity is then a simple consequence of Equation (3.4) for the slender-body orientation dynamics, which predicts a stable equilibrium with no rotational velocity in linear shear when the fiber is aligned in the direction of shear. The reorientation of fiber suspensions in a simple shear flow is a well-known phenomenon [182, 149, 196, 60]. Unless subjected to lubrication or contact forces, the fibers located in this region can only undergo very weak horizontal motion as their horizontal mobility is close to zero. It is worthwhile here to consider the limitations of this simulation. First the orientation dynamics as described by slender-body theory are inexact as they cannot predict the tumbling motion of an isolated particle in shear flow: the consequences of this approximation are discussed in more detail in Section 3.5.5. Second and perhaps most importantly, the quasi homogeneity of the suspension in the

vertical direction as created by the small box dimension and periodic boundary condition helps make the configuration of Figure 3.11 stable: vertical inhomogeneities would be likely to perturb this configuration at least during the onset of the instability, and may disrupt these large regions of shear.

The simulation of Figure 3.11 was repeated for different random initial distributions: sometimes only one streamer formed, and in very rare cases three streamers were observed. This strong dependence of the structure formation on the initial distribution calls for a more systematic investigation. Simulations were run in which the initial distribution was perturbed artificially by a superposition of two planar waves in the x-direction of wavenumbers $k = 1$ and $k = 2$ (where k is non-dimensionalized by the box length L_x): $c(x, y, z) = \hat{c}_0 + \hat{c}_1 \exp(2\pi \mathrm{i} x / L_x) + \hat{c}_2 \exp(4\pi \mathrm{i} x / L_x)$; the ratio $\hat{c}_1 / \hat{c}_2$ of the amplitudes of the two waves was varied. The initial velocity fields were computed and compared to the final fiber distributions, and the results are summarized in Table III. Several observations can be made. Depending on the ratio of the two initial wave amplitudes, either one or two streamers form; only for very small values of $\hat{c}_1 / \hat{c}_2$ do two concentrated streamers develop, and in all other cases only one streamer is observed. It is enlightening to compare these observations to the initial velocity fields, and more precisely to the ratio $\hat{u}_1 / \hat{u}_2$ of the $k = 1$ and $k = 2$ coefficients of the Fourier transform in the x-direction of the vertical component of the velocity, and to the number of distinct backflow regions in the velocity field. The number of concentrated streamers in the final distribution seems to be correlated to the number of backflow regions, which itself is determined by the ratio $\hat{u}_1 / \hat{u}_2$. More precisely, backflow regions seem to act as barriers that cause the fibers to rotate and migrate towards the denser 'velocity wells'. Since, from the periodic fundamental solution Equation (3.21), the Fourier coefficients of the velocity scale as $\hat{u}_k \sim \hat{c}_k / k^2$, the flow is typically dominated by the $k = 1$ mode and only one streamer forms.

At the other end of the spectrum, it is observed that perturbations in concentration usually decay at high wavenumbers. Simulations were run in which a high-frequency perturbation ($k = 4$ to 7) was applied to the initial distribution; in most cases fewer streamers were obtained than initial waves. This phenomenon, that we term streamer

$\hat{c}_1/\hat{c}_2$	$\hat{u}_1/\hat{u}_2$	Backflow regions	Streamers
0.20	0.88	2	2
0.66	3.07	1	1
0.87	3.86	1	1
1.29	5.80	1	1
1.59	7.07	1	1

Table 3.3: Influence of the initial distribution on the streamer formation. Simulations were performed in boxes of aspect ratio L_x:L_y:L_z=10:1:2, in which the initial random distribution was perturbed by the superposition of two waves of wavenumbers $k = 1$ and $k = 2$: $c(x, y, z) = \hat{c}_0 + \hat{c}_1 \exp(2\pi i x/L_x) + \hat{c}_2 \exp(4\pi i x/L_x)$. The ratio $\hat{c}_1/\hat{c}_2$ of the amplitudes of the two waves was varied. The table reports: the ratio $\hat{u}_1/\hat{u}_2$ of the $k = 1$ and $k = 2$ coefficients of the Fourier transform in the x-direction of the vertical component of the initial disturbance velocity field; the number of distinct backflow regions in the initial velocity field; the number of concentrated streamers in the final distribution.

coalescence, is illustrated in Figure 3.13 for the case $k = 6$. Starting from six initial waves, only four concentrated streamers are observed in the final distribution (Figure 3.13(a)). The initial vertical velocity field (Figure 3.13(b)) somewhat modifies our previous criterion and shows that streamers form in the local minima or 'wells' of the velocity field, although they need not be surrounded by independent backflows. Figure 3.14 shows the discrete Fourier transforms in the x-direction of the initial concentration perturbation and of the initial velocity field. Although the $k = 6$ mode dominates the initial concentration, it only creates a very small disturbance in the velocity spectrum, which is swamped by the low wavenumber modes (mostly $k = 1$) arising from random concentration fluctuations. Therefore high-wavenumber perturbations cannot survive as even tiny low-wavenumber fluctuations will typically dominate the velocity field.

The presence in most simulations of this strong $k = 1$ mode in the velocity field is reminiscent of the large recirculation vortices observed in experiments on sphere suspensions. Guazzelli [74] studied the sedimentation of suspensions of spheres using particle image velocimetry, and observed that during the initial moments of her experiments the velocity field is dominated by large vortices of the size of the container; after a while these vortices decay and leave place to smaller vortices whose size is found to be independent
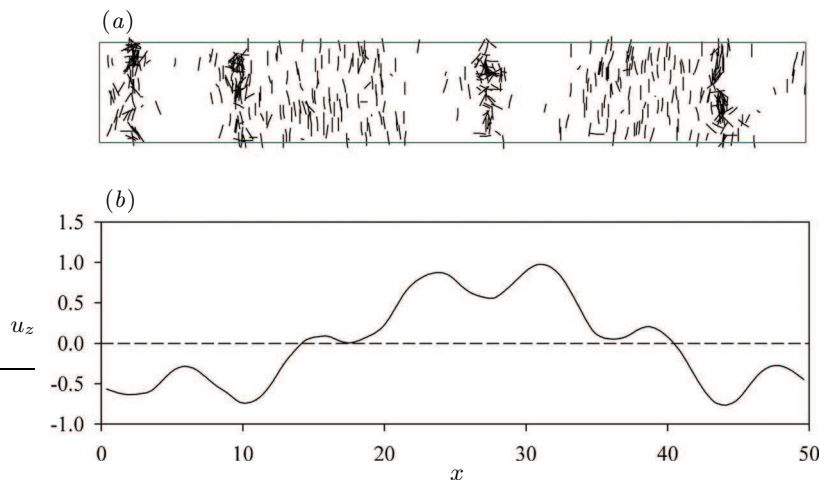
Figure 3.13: Final fiber distribution (a) and initial disturbance velocity field (b) for an initial plane wave perturbation at wavenumber $k = 6$: $c(x, y, z) = \hat{c}_0 + \hat{c}_6 \exp(12\pi i x / L_x)$. Only four concentrated streamers can be observed, which are located in the 'wells' of the initial velocity field.

of the container dimensions. As explained by Hinch [87], these large convection currents in the initial times are due to the difference in weight between the two sides of the suspension; these currents have the effect of homogenizing the two sides, after which they decay. The strong $k = 1$ mode observed in our simulations has the same origin, but is not allowed to decay because of the periodic boundary conditions in the vertical direction, which effectively prevent the horizontal convection currents that would otherwise occur in a bounded system. Fiber suspensions are more complex due to the strong coupling between the concentration and velocity fields, and even though a similar recirculation as in sphere suspensions may occur in a container with a bottom wall and may lead to some type of homogenization, the instability on the contrary acts against the homogenization of the suspension and tends to accentuate the fluctuations. The combination of these two effects may lead to a qualitatively different behavior than is observed in sphere suspensions, and deserves further attention: it will be described in more detail in Chapter 4, where we perform simulations of larger systems in non-periodic boundary conditions. In these systems, we will see that the presence of a bottom wall indeed causes a decay of
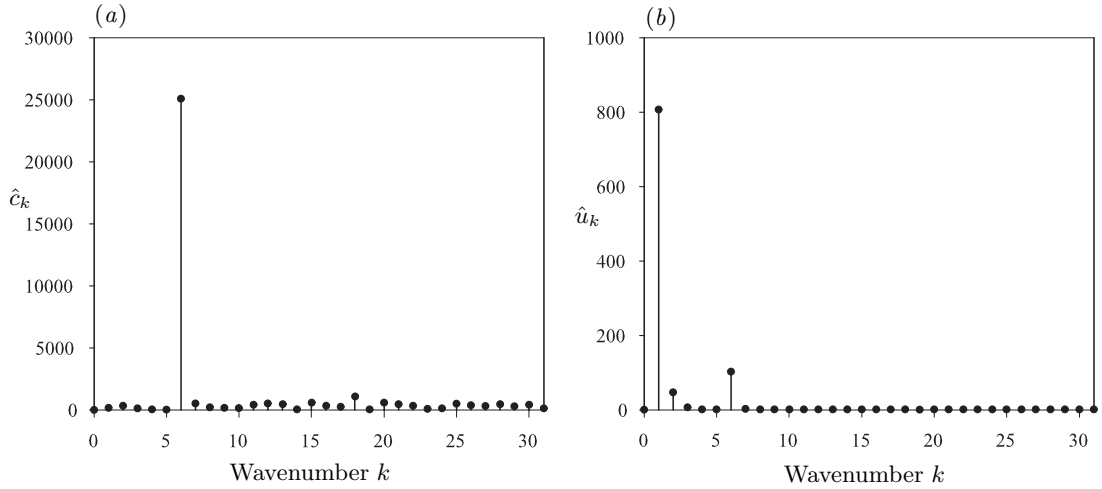
Figure 3.14: Magnitude of the coefficients of the Fourier transform in the x-direction of (a) the initial concentration field and (b) the vertical component of the initial disturbance field for the simulation of Figure 3.13. A strong peak at $k = 6$ can be observed in the initial concentration field; the velocity field however is dominated by the random low-wavenumber fluctuations ($k = 1$).

the size of the density fluctuations over time, which as we argue in Section 4.3.2 may be attributed to the stratification that appears in the suspension.

3.5.3 Orientation dynamics

Both experiments [84] and previous simulations [32] showed a reorientation of the fibers in the direction of gravity, with occasional flips. This is confirmed in our results and is illustrated in Figure 3.15, which shows the evolution of the projected angle of a typical sedimenting fiber (the projected angle being defined as the angle formed by the projection of p onto a vertical plane with respect to the horizontal). After a transient phase lasting until $t = 100$ approximately, the fiber ends up spending most of its time aligned in the vertical direction. The trajectory of Figure 3.15 is very similar to those observed in experiments [84].

The evolution of the orientation statistics can be studied by looking at the average square orientation of the fibers in the direction of gravity $\langle p_z p_z \rangle$. Its time evolution is presented in Figure 3.16 for three simulations with the same numbers of fibers, aspect
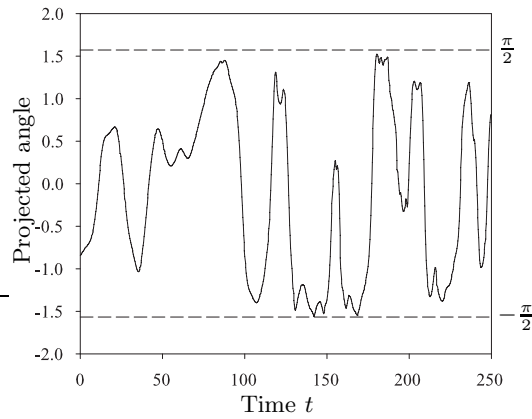
Figure 3.15: Time evolution of the projected angle for a typical fiber (angle of the projection of $\boldsymbol{p}$ onto a vertical plane with respect to the horizontal). After a transient phase, the fiber spends most of its time almost aligned with gravity (projected angle of $\pm\pi/2$), with occasional flippings.
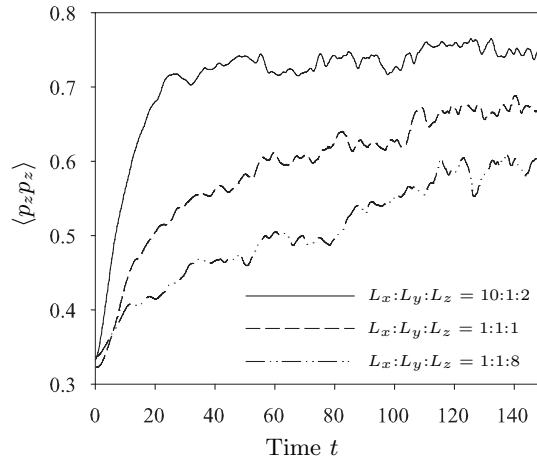
Figure 3.16: Time evolution of the average square orientation in the direction of gravity. All three curves are for 512 fibers, $A = 11$ and $nl^3 = 0.05$ and different box dimensions. Note how the time to steady state and the value of the steady state depend on the periodic cell aspect ratio.

ratios and volume fractions but different periodic cell dimensions. In all three simulations $\langle p_z p_z \rangle$ starts from a value close to 1/3 corresponding to an initial distribution with random orientations, and increases progressively as the fibers begin to align. The three curves eventually reach a steady state, the value of which differs in each case and gives an indication of the average orientation. A lower steady state value is obtained with high-aspect ratio boxes, corresponding to fewer fibers being aligned with gravity: this had already been observed in smaller simulations [32], and is corroborated by the orientation distributions presented below. The time to steady state also depends on the simulation box dimensions: it is much quicker in general for low aspect ratio boxes.

Figure 3.17 compares the orientation distributions of the two simulations of Figures 3.6 and 3.11 to the experimental results of Herzhaft & Guazzelli [84]. In all three cases the distribution presents a clear peak slightly below $\pi/2$, which was expected and indicates that a large number of fibers are almost aligned in the vertical direction. A second local maximum near zero can also be observed in the experimental data, showing that the horizontal direction is also a preferred fiber orientation, but this maximum is not reproduced by either of the two simulations.

The breadth and height of the main peak differs greatly between the two simulations. In the first case (high-aspect-ratio periodic cell), the peak is rather broad and weak, and the tail of the distribution is quite thick, indicating that quite a large number of fibers are not aligned; in the case of the second simulation (wide and thin periodic cell), the peak is quite higher and narrower and the tail is finer, and the overall profile of the distribution compares somewhat more favorably with the experimental data. This is consistent with the findings of Figure 3.16, where we observed two different values for the steady-state average square orientations. A simple inspection of the suspensions of Figure 3.6 and 3.11 provides an explanation. In the case of the high simulation box, only the core of the streamers is really captured, where most of the fibers are entangled inside clusters and are not free to align. Figure 3.11 however demonstrates that in a wider box the streamers are surrounded by large regions of shear where the fibers are isolated and can align freely with gravity. In Figure 3.17(b) the height of the peak is slightly overestimated: this
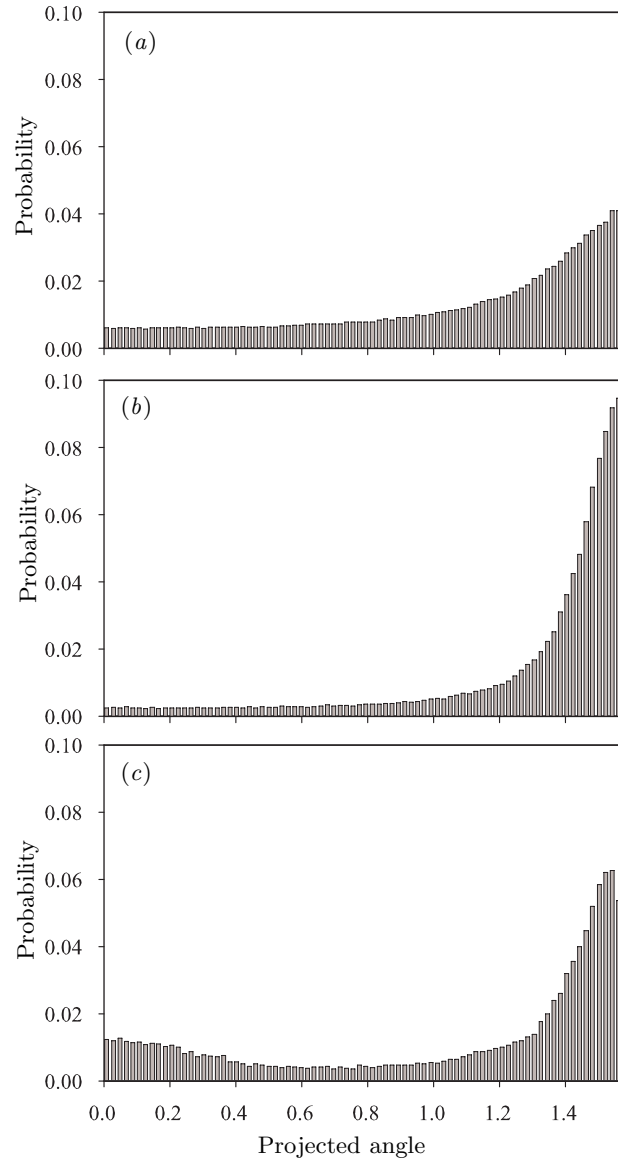
Figure 3.17: Comparison of the orientation distributions of two different simulations with the experiments of Herzhaft & Guazzelli [84]. The two upper plots are for simulations of 512 fibers of aspect ratio $A = 11$, with an average effective volume fraction of $nl^3 = 0.05$ and different simulation box aspect ratios: (a) L_x:L_y:L_z=1:1:8 (simulation of Figure 3.6), (b) L_x:L_y:L_z=10:1:2 (simulation of Figure 3.11). The bottom plot (c) shows the experimental distribution, obtained for the same particle volume fraction and fiber aspect ratio.
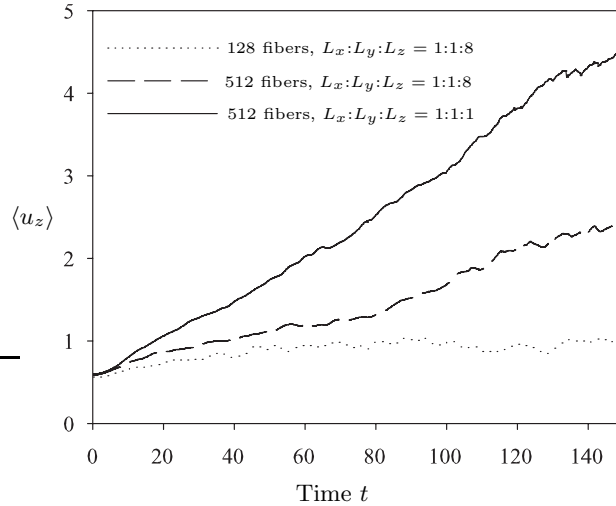
Figure 3.18: Time evolution of the average sedimentation rate for simulations of 128 and 512 fibers. In each case $A = 11$ and $nl^3 = 0.05$. While a steady state is reached rapidly with 128 fibers, the sedimentation rate keeps increasing with 512 fibers, and its value depends on the periodic cell aspect ratio.

may be a consequence of the very short height of the box and of the periodic boundary conditions, as in a real system inhomogeneities in the vertical direction would perturb to some extent the shear regions between the streamers. Still these results suggest that these large regions should not be ignored if we want to obtain accurate orientation statistics, hence the necessity to use wide enough boxes to capture the full extent of the horizontal structures.

3.5.4   Sedimentation rate and velocity statistics

The formation of dense clusters has a strong influence on the average sedimentation speed of the suspension, which is enhanced in the dilute and semi-dilute regimes. This phenomenon is really a consequence of the concentration instability, as the velocity is generally hindered in dilute suspensions such as homogeneous suspensions of spheres [13]. Note that in the concentrated regime suspensions of fibers also exhibit velocity hindrance [188], presumably because strong entanglements present in concentrated suspensions prevent the instability from developing.
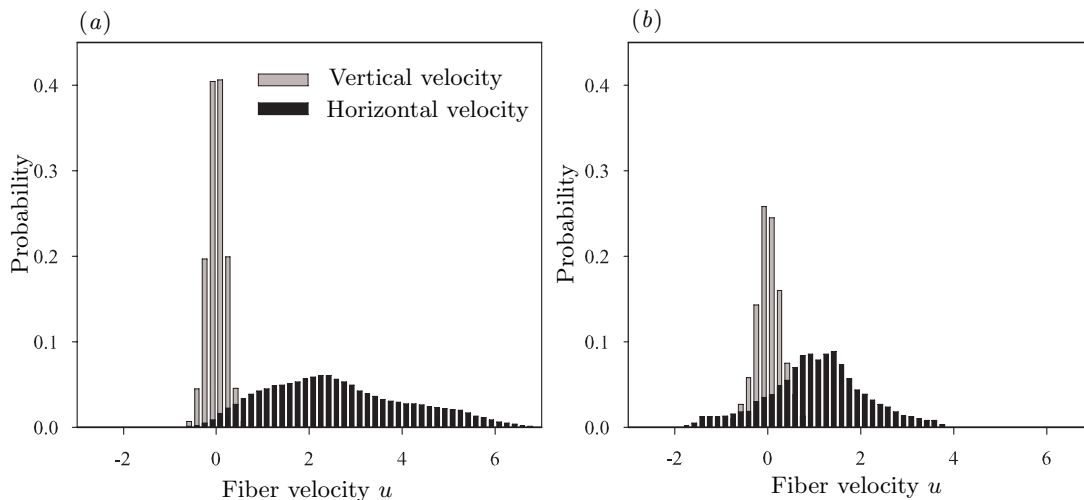
Figure 3.19: Comparison of the velocity distributions with the experimental data of Herzhaft & Guazzelli [84]. The upper plot (a) corresponds to the simulation of Figure 3.6 (512 fibers, $A = 11$, $nl^3 = 0.05$, $L_x:L_y:L_z$=1:1:8). The bottom plot (b) shows the experimental distribution, obtained for the same particle volume fraction and fiber aspect ratio.

In their small simulations, Butler & Shaqfeh [32] observed that the average sedimentation rate of the fibers slowly increases as the instability develops and eventually reaches a plateau, the value of which depends on the aspect ratio of the periodic cell. For the larger systems considered in this study, the time to steady state was generally very long (typically more than 200 time units), so that most of the simulations were stopped before reaching a steady state velocity (Figure 3.18). This is easily understood in the light of the earlier discussion on the pair probability functions: in the Stokes flow regime the sedimentation velocity is a function of the spatial configuration of the suspension only, and as was observed in Section 3.5.2 the clusters keep getting denser even after the cluster distribution and orientation statistics have reached their steady state. However, we also argued in Section 3.5.2 that the densification should eventually slow down due to excluded volume effects, and it is likely that a steady sedimentation rate would be reached if the simulations were run long enough.

Figure 3.18 also shows a strong dependence of the sedimentation rate on the dimensions

of the periodic cell: lower sedimentation rates are obtained in high aspect ratio boxes, in better agreement with the experimental values. Figure 3.19 compares the velocity distributions for such a simulation to the experimental results of Herzhaft & Guazzelli [84]: while the horizontal velocities are captured reasonably well, the vertical velocity distribution predicted by our simulation is slightly shifted to the right and somewhat broader than in the experiments; both the mean and the variance of the vertical velocity are overestimated, and this generally gets worse as the simulation box gets wider. Butler & Shaqfeh [32] encountered the same difficulty and came up with the following heuristic rule: for the system sizes they considered, they observed that setting the aspect ratio of the periodic cell to $L_z/L_x = N/16$, where N is the number of fibers, enabled them to obtain the right sedimentation rate and reasonable velocity distributions. Their rule however is not easily applied in the case of very large systems, as it would require extremely high and thin boxes, and preclude the capture of more that the core of a single streamer. If we want to resolve the large shear regions between the streamers, which as we established are important for obtaining correct orientation statistics, still larger systems may be needed, in which both the lateral and vertical box dimensions are large compared to the length of a fiber. As we shall see in Chapter 4, a bottom wall and non-periodic boundary conditions are in fact required.

3.5.5 Validation of the slender-body approximation

Earlier mention was made of the limitations of the slender-body approximation. The significant feature of the model is that slender-bodies in a linear shear flow simply align in the direction of the flow, while exact Stokes flow solutions suggest that an ellipsoid [93] and in fact any body of revolution [29] should undergo a periodic tumbling motion known as Jeffery's orbits. These poor orientation dynamics may influence our results in two ways: by modifying the dynamics inside the large shear regions observed around the streamers in Section 3.5.2, which in turn may have an impact on the orientation statistics presented in Section 3.5.3. In particular, we may expect the migration towards the streamers to be enhanced in the presence of tumbling.

To assess more precisely the consequences of the slender-body dynamics, we implemented a slightly different model in which Equation (3.4) for the orientation dynamics was replaced by the following:

$$\dot{\boldsymbol{p}}_\alpha = (\mathbf{I} - \boldsymbol{p}_\alpha \boldsymbol{p}_\alpha) \cdot \left[\frac{3}{4} \int_{-1}^{1} (1 - s_\alpha^2) \left[\frac{A^2 - 1}{A^2 + 1} \mathbf{E}(s_\alpha) + \boldsymbol{\Omega}(s_\alpha) \right] \cdot \boldsymbol{p}_\alpha \mathrm{d}s_\alpha + \frac{3 \log(2A)}{8\pi} \boldsymbol{F}_\alpha^{(1)} \right],$$
$$(3.33)$$

where $\mathbf{E} = \left[\nabla \boldsymbol{u}' + (\nabla \boldsymbol{u}')^T \right] / 2$ and $\boldsymbol{\Omega} = \left[\nabla \boldsymbol{u}' - (\nabla \boldsymbol{u}')^T \right] / 2$ are respectively the rate of strain and rate of rotation tensors of the disturbance velocity field, evaluated at position $\boldsymbol{x}_\alpha + s_\alpha \boldsymbol{p}_\alpha$ along the axis of the fiber. Equation (3.33) is a simplified version of the exact equation for the orientation dynamics of a single spheroid [101], in which we neglected an additional term involving the Laplacian of the rate of strain on the basis that its coefficient $1/8(A^2 - 1)$ is very small for high aspect ratio particles. Letting $A \to \infty$ in Equation (3.33) and performing an integration by parts allows one to recover Equation (3.4) for the slender-body dynamics. Equation (3.33) can still be implemented using SPME: indeed taking the gradient of the velocity in Equation (3.25) allows one to derive similar Ewald summation formulae for the components of the rate of strain and rate of rotation tensors, which are then computed following the same algorithm as for the disturbance velocity (Section 3.3.2). While analytical expressions were used for the real sums, the Fourier sum of the gradient was computed numerically on the Fourier space grid using a fourth-order central finite difference scheme.

For the aspect ratios considered in this study, the modifications entailed by the use of Equation (3.33) were minor in general. This is illustrated in Figure 3.20, which compares the final distributions obtained with the two different formulations. In particular, the streamer formation is not affected, and neither are the shear regions surrounding the streamers where the alignment of the fibers is sensibly the same. Figure 3.21 compares for both simulations the time evolution of the average square orientation in the direction of gravity, which quantifies the degree of alignment of the suspension: the differences observed are within the statistical fluctuations of the data. This can be interpreted as follows: even though slender-bodies in a simple shear flow align with the flow, the disturbance field

(*a*) Slender-body

(*b*) Finite aspect ratio, $A = 11$
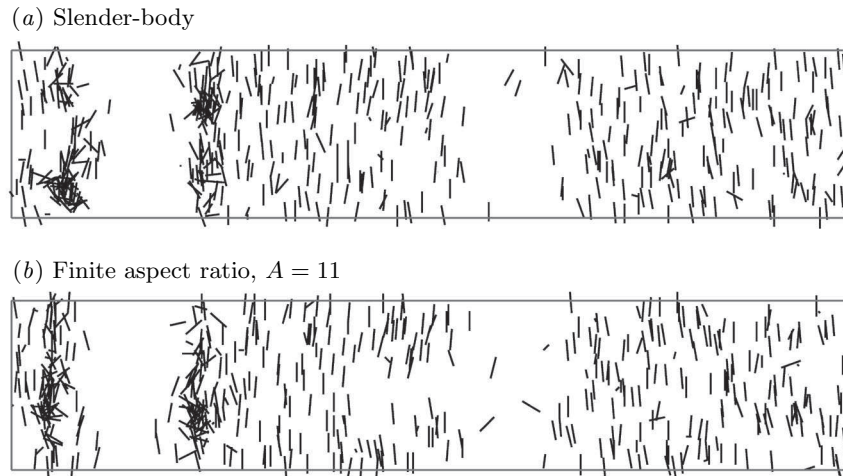
Figure 3.20: Comparison of the final fiber distributions obtained using the original slender-body formulation of Equation (3.4) (*a*), and the finite aspect ratio formulation of Equation (3.33) (*b*). The simulation is for 512 fibers, $A = 11$, $nl^3 = 0.05$ and L_x:L_y:L_z=10:1:2. The two simulations agree qualitatively, which justifies the use of the slender-body approximation.

between the streamers is not exactly linear and fluctuations in this disturbance field can still cause tumbling (and indeed such tumbling or 'flipping' events can be observed on Figure 3.15). Furthermore the correction entailed by Equation (3.33) is quite weak: the coefficient $(A^2 - 1)/(A^2 + 1)$ only changes from 1 to 0.98 when the aspect ratio is varied from infinity to 11. This suggests that the flipping induced by the velocity fluctuations dominates the tumbling due to the finite thickness of the particles, and under the assumption that the Laplacian term that we neglected to obtain Equation (3.33) is indeed small, these results confirm the validity of the slender-body approximation for simulations of high-aspect ratio particles.

3.6 Concluding remarks

We have implemented a fast algorithm, called smooth particle-mesh Ewald, that allows one to compute efficiently the hydrodynamic interactions between small particles suspended in a fluid. SPME is comparable to the accelerated Stokesian dynamics method of Sierou
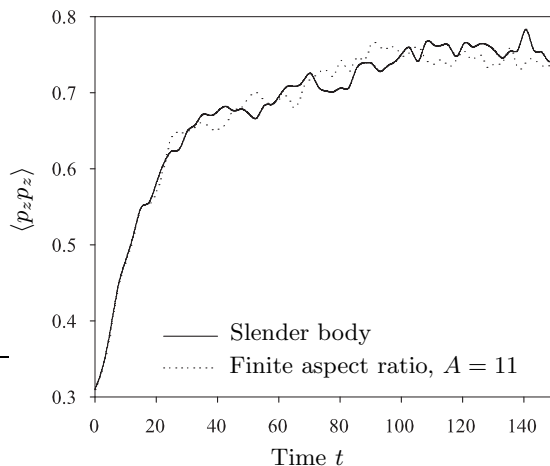
Figure 3.21: Time evolution of the average square orientation in the direction of gravity for the two simulations of Figure 3.20. Both models (slender-body formulation Equation (3.4), and finite aspect ratio formulation Equation (3.33)) give very similar results, confirming the validity of the slender-body approximation.

& Brady [170] for spherical particles, but is characterized by different force assignment and interpolation schemes using Cardinal B-splines, which are particularly well-suited for complex exponentials and provide stability at high orders of interpolation. The method, which allows one to efficiently compute the disturbance field induced by periodic distributions of point forces, has been applied to infinite suspensions of slender-bodies (line distributions of point forces) in a gravity field, but could easily be applied to different particle shapes (disks or platelike particles for instance, or arbitrary solid surfaces in a boundary element simulation), as well as different flow conditions (particulate flows in an imposed velocity field, pressure-driven flows, etc.). The algorithm can also be easily parallelized, as it is based on a summation of close particle pair interactions for which a domain decomposition is suitable, and on the fast Fourier transform algorithm for which parallel implementations are already available.

When applied to the sedimentation of rigid fibers at zero Reynolds number, our fast algorithm has allowed us to simulate large systems of up to 512 fibers on a single processor, while maintaining a good level of approximation in our simulation method where the force moments on each fiber are retained up to the stresslet term. In particular, the

concentration instability observed in sedimenting suspensions of non-spherical particles was captured very convincingly, and our simulations of larger systems have provided new valuable information on the microstructure of this type of suspension.

Using very elongated boxes in the direction of gravity, we were able to study the dynamics inside the core of the streamers that form as the fibers sediment. We observed that the streamers are in fact composed of distinct clusters of various sizes and velocities, which can either merge or break up. As the instability begins to develop, our simulations exhibited a mechanism by which small clusters aggregate into larger clusters, which can again break up. After a transient phase, a steady state is observed in which a combination of clusters of different sizes cohabit on average. The break-up phenomenon, along with the presence of a steady state, suggests that clusters beyond a certain size become unstable, and either break up or abandon fibers in their wakes.

More interestingly, our simulations managed to capture several concentrated streamers in the horizontal direction, which to our knowledge had never been achieved in previous studies. This was made possible by drastically increasing one of the horizontal dimensions of our simulation box. These simulations in wide boxes highlighted the presence of broad shear regions between the core of the streamers and the clarified fluid, where most of the fibers sediment almost vertically with little horizontal motion. These regions of shear had not been captured in previous simulations owing to the insufficient size of the periodic cells, and seem to account for some discrepancies that had been observed in the orientation distributions. While the exact process leading to the wavenumber selection is still poorly understood, our simulations provided partial answers: the formation of concentrated streamers seems to be linked to the presence of velocity wells in the initial disturbance field, created by concentration fluctuations in the distribution of fibers. A simple argument shows that for a random suspension the initial disturbance field is dominated by perturbations of long wavelengths ($k = 1$ mode). While experiments on the sedimentation of spheres suggest that this initial recirculation cell should decay, this is not observed in our simulations owing to the periodic boundary conditions in the vertical direction.

Obtaining accurate sedimentation rates and velocity distributions remains a very difficult task, as these two quantities depend strongly on the aspect ratio of the periodic cell. Using high aspect ratio boxes in general gives acceptable results, but the rule defined previously by Butler & Shaqfeh [32] on the box aspect ratio does not allow to capture more that the core of the streamers. In order to capture correct velocity statistics while resolving the structure of the suspension, larger systems or more realistic boundary conditions at the container walls may be needed: these two issues are addressed in Chapter 4.

Chapter 4

The dilute sedimentation of orientable particles

4.1 Introduction

Although conceptually quite simple, the steady sedimentation of a dilute dispersion of particles in a liquid at low Reynolds number remains an unresolved problem of non-equilibrium statistical mechanics [150]. Even in the simplest case of a random dilute dispersion of spheres, Caflisch & Luke used a simple physical argument to suggest that the velocity variance should diverge, growing unbounded with the linear dimension of the sedimenting system: $\langle \Delta v^2 \rangle \sim L$ [34, 87]. Since the work of Caflisch & Luke numerous experiments have tried to test this scaling, but typically manifest a saturation of the velocity fluctuations in stark contrast with the theoretical prediction [137, 167, 20]. Precise particle image velocimetry measurements by Guazzelli [74] in fact showed the following: during the early period after the cessation of mixing, large recirculation vortices of the size of the container are observed, confirming the Caflisch & Luke argument, but these quickly decay and give way to smaller less intense vortices and velocity fluctuations that are independent of the container dimensions.

Several theoretical explanations have been proposed to resolve this contradiction, most

of which relax one of the fundamental assumptions of the original argument, namely homogeneity. The close relationship between the microstructural arrangement of the particles in the suspension and the velocity fluctuations was first highlighted by Koch & Shaqfeh [103], who related the amplitude of the velocity fluctuations to the structure factor of the suspension, which is the Fourier transform of the pair probability function. Koch & Shaqfeh then argued that a specific form of the pair probability function, in which there is a net deficit of neighboring particles in the vicinity of each particle, would lead to a screening of the velocity disturbance as a result of three-particle hydrodynamic interactions, and is therefore a potential mechanism for the saturation of the velocity fluctuations. This mechanism however has not been verified, and is not consistent with more recent results from numerical simulations, which do show a decay of the velocity fluctuations (e.g. [112, 134, 135, 132]).

The key idea that microstructural changes occurring during sedimentation are responsible for the decay of the velocity fluctuations is supported by recent experiments by Lei, Ackerson & Tong [114], which showed the suppression of random number density fluctuations during sedimentation. Two mechanisms have been suggested for this suppression. Following an original idea by Luke [120], it has been argued that a small vertical stratification in the suspension may be responsible for the decay [131, 132]. More precisely, Mucha *et al.* [132] suggest that in thin cells in which stratification is weak the velocity fluctuations scale with the thickness of the container, while in larger cells stratification is more significant and causes the decay of the fluctuations. Experiments by the same authors seemed to confirm this mechanism [186, 132], although such a strong stratification was not observed in other studies [20], suggesting that polydispersity in the size of the particles may have been a factor. Recent lattice-Boltzmann simulations by Nguyen & Ladd [134, 135] also captured the suppression of the number density fluctuations but did not show any significant broadening of the front.

A second explanation was proposed by Hinch [87]: in a finite cell with a bottom wall, random density fluctuations create strong convection currents spanning the width of the cell, which should lead to a homogenization and may remove the horizontal fluctuations in the number density. If this process continues down to the interparticle separation

length scale, the final velocity fluctuations may no longer depend on the system dimensions. The mechanism speculated by Hinch is supported by the observations of Guazzelli [74] described previously, in which large recirculation cells in the initial instants of the experiments are observed to decay. The importance of the role of the bottom wall was also emphasized by Ladd using lattice-Boltzmann simulations: in periodic systems Ladd observes the divergence of the velocity fluctuations without any microstructural changes [111], whereas in systems bounded by horizontal walls the velocity variance is found to saturate and the horizontal density fluctuations are strongly suppressed [112, 134, 135].

The cases of non-spherical or non-rigid particles, which we address in this Chapter and the following one, have received much less attention in the past, in spite of their common occurrence in both natural phenomena and industrial applications. One illustrative example in which both anisotropy and deformability play a significant role is the sedimentation of red blood cells, which is a widely used tool for the screening of diseases [151]. Other examples are as diverse as the separation of biological macromolecules by centrifugation, the fabrication of fiber-reinforced materials, or the treatment of waste materials.

It is unclear *a priori* how anisotropy or deformability will influence the physical mechanism described above, by which the suppression of number density fluctuations leads to a decay of the velocity variance in suspensions of spheres. The fundamental difference between anisotropic and isotropic particles is that the former orient in flow, and depending on their orientation can migrate in the directions perpendicular to gravity. Koch & Shaqfeh [102] first studied this coupling between the velocity fluctuations and the anisotropic mobility of the particles for dispersions of spheroids. They modeled the suspension with continuum variables, and using a linear stability analysis they showed that small density fluctuations at low wavenumbers should amplify. They proposed a simple physical mechanism: the disturbance flow induced by the density fluctuations causes the particles to orient in such a way that they migrate towards the regions of higher particle density. Based on a linearized model for an unbounded fluid, the theory of Koch & Shaqfeh [102] predicted that the longest wavelengths should grow the fastest.

The sedimentation of fiber suspensions, which behave like high-aspect-ratio spheroids,

has been the subject of a few experimental studies, some of which confirmed the instability predicted by Koch & Shaqfeh [102]. In an early study, Kumar & Ramarao [106] reported the formation of large floc-like structures in dilute suspensions, settling at larger velocities; at higher concentrations interaction between the flocs was observed to cause velocity hindrance. Later, Turney *et al.* [188] used magnetic resonance imaging to determine the mean sedimentation velocity in concentrated suspensions of rodlike particles; they reported velocity hindrance but did not provide any information on the homogeneity of the bulk.

More recently, Herzhaft *et al.* [83] and Herzhaft & Guazzelli [84] studied the sedimentation of fibers in the dilute and semi-dilute regimes, in which the instability can be expected to be the strongest. They adapted a particle tracking technique previously used for sphere suspensions [77, 138], in which the position, orientation and velocity of a few silver-coated particles are measured, while the remainder of the particles are made invisible by matching their index of refraction with the index of the solvent. They observed that the particles strongly oriented in the direction of gravity, with occasional flipping between the two vertical orientations. They also reported an increase in the mean velocity in the dilute regime beyond the maximum velocity of an isolated vertical fiber, followed by velocity hindrance in the semi-dilute regime. The velocity fluctuations measured were typically very large, up to one order of magnitude larger than the mean velocity in the semi-dilute regime. While no systematic investigation of the microstructure was undertaken, snapshots of the suspension suggested that the particles gathered to form dense clusters or streamers slightly elongated in the direction of gravity and surrounded by clarified fluid; the size of the clusters, although not measured precisely, was estimated to be on the order of a few particle lengths.

The sedimentation of axisymmetric particles was also tackled in a few computational studies, with varying degrees of approximation. Mackaplow & Shaqfeh [122] performed dynamic simulations of fiber sedimentation at zero Reynolds number with periodic boundary conditions, in which they approximated the disturbance of a given particle on the fluid by a point force. Although very simple, their model captured all the salient features of the

instability: the fibers were observed to converge towards one dense streamer and to orient vertically. While the orientation distributions were found to reach a steady state, the mean velocity however kept increasing and did not show any signs of saturation. Butler & Shaqfeh [32] devised a more sophisticated method in which the fibers were represented by line distributions of point forces, which were linearized to correctly capture the total force, total torque and stresslet on each particle; they also included close particle hydrodynamic interactions through lubrication forces, and excluded volume interactions using short-range repulsive forces. Their simulations greatly improved on the results of Mackaplow & Shaqfeh [122], and reasonable agreement with the experimental data of Herzhaft & Guazzelli [84] was found using very elongated boxes in the direction of gravity. In particular, such boxes allowed the mean velocity to reach a steady state. The effects of inertia were also considered by Kuusela and coworkers, who performed simulations of the sedimentation of spheroids at small but finite Reynolds number [107, 108]. The principal effect of inertia was on the orientation distributions, which showed a preferential alignment in the horizontal direction in very dilute dispersions, followed by a transition towards a vertical alignment at higher concentrations. The mean velocities showed qualitative agreement with the inertialess experiments of Herzhaft & Guazzelli [84]; clustering was reported, although no further information was given on the structure of the suspension.

In an attempt to study more precisely the microstructure in suspensions of sedimenting fibers, we improved the simulation method of Butler & Shaqfeh [32] in Chapter 3 by implementing a smooth particle-mesh Ewald algorithm allowing the efficient computation of the far-field hydrodynamic interactions [157]. This fast algorithm allowed us to simulate up to 512 particles, providing new insight into the large-scale collective dynamics and their coupling to the disturbance flow. In particular, in our periodic systems we found that the formation of dense clusters was directly linked to the initial disturbance flow in the fluid, which is typically dominated by low-wavenumber fluctuations, therefore resulting in the formation of a unique streamer in most simulations. We speculated that the presence of a bottom wall may play a role in selecting a wavelength for the instability, by breaking the initial low-wavenumber fluctuations in the same way as is observed in sphere suspensions

[74, 112]. This mechanism remained however an open question: while the presence of a bottom wall may indeed lead to a homogenization and result in a decay of the large-scale fluctuations, the instability on the contrary feeds the inhomogeneities; the balance between these two effects is difficult to predict and is addressed in this Chapter. The results of Chapter 3 also showed the difficulty in reaching a steady state simulation in large periodic systems: even after the instability had picked a wavelength, streamers were observed to become denser and denser, resulting in the steady increase of the mean velocity. The assumption that a steady state indeed exists, which is the basis for simulations with periodic boundary conditions, therefore deserves closer attention.

In this Chapter we study the microstructure and concentration fluctuations in sedimenting suspensions of spheroids, focusing on the coupling between the large-scale fluctuations in the concentration and velocity fields and on the influence of solid boundaries. In particular we wish to determine whether a steady-state structure can be achieved in such suspensions and identify the mechanisms affecting this structure. We use rigid spheroids as prototypes of orientable particles; the case of deformable particles will also be examined in Chapter 5. In Section 4.2.1, we describe an efficient method for the simulation of realistic-size systems of rigid spheroids, both in periodic and non-periodic domains. Results are then discussed in Sections 4.2.2 to 4.2.6, where we show that in non-periodic systems a wavenumber selection occurs for the concentration fluctuations. In Section 4.3, we revisit the linear stability analysis of Koch & Shaqfeh [102] to demonstrate that the stratification that appears over the course of sedimentation may be responsible for this wavenumber selection.

4.2 Point-particle simulations

4.2.1 Method of simulation

Motivated by the conclusions of the simulations of Chapter 3 [157], we have developed an efficient method allowing the simulation of suspensions of realistic sizes in both periodic and bounded geometries. The method is based on a point-force approximation which is

analogous to the original model of Koch & Shaqfeh [102] and to the point-fiber simulations of Mackaplow & Shaqfeh [122]. However the disturbance velocity is calculated numerically from the Stokes equations using smooth localized force representations in a similar manner to the force-coupling method of Lomholt & Maxey [119]; this approximate method allows for a very efficient calculation of the velocities in flow cells with various boundary conditions while removing the singularities from the disturbance field.

Dynamic equations

We consider a system of N spheroids of aspect ratio A in a box of dimensions $L_x \times L_y \times L_z$, where gravity points in the vertical direction: $\boldsymbol{g} = -g\hat{\boldsymbol{z}}$. The configuration of a given particle $\alpha = 1, ..., N$ is entirely determined by the position $\boldsymbol{x}_\alpha$ of its center of mass and by a unit vector $\boldsymbol{p}_\alpha$ aligned with its major axis. In the dilute limit the disturbance velocity induced by the motion of the particles varies over length scales that are much larger than the size of a particle, so that locally the flow field experienced by a given spheroid can be approximated as:

$$\boldsymbol{u}(\boldsymbol{x}) \approx \boldsymbol{u}(\boldsymbol{x}_\alpha) + \boldsymbol{\nabla}\boldsymbol{u}(\boldsymbol{x}_\alpha) \cdot (\boldsymbol{x} - \boldsymbol{x}_\alpha) + ... \quad \text{for} \quad |\boldsymbol{x} - \boldsymbol{x}_\alpha| \ll L, \tag{4.1}$$

where L is the characteristic length for the variation of the velocity. Typically this characteristic length is the mean interparticle distance $L = n^{-1/3}$, where n is the number density in the suspension. Under this approximation the translational velocity of a particle is calculated as the sum of its settling velocity $\boldsymbol{U}_s$ in orientation $\boldsymbol{p}_\alpha$ and of the disturbance velocity $\boldsymbol{u}$ evaluated at its center of mass:

$$\dot{\boldsymbol{x}}_\alpha = \boldsymbol{U}_s(\boldsymbol{p}_\alpha) + \boldsymbol{u}(\boldsymbol{x}_\alpha). \tag{4.2}$$

The settling velocity in a pure fluid is the product of the particle mobility by the gravity force acting upon the particle, and for a spheroid is written as

$$\boldsymbol{U}_s(\boldsymbol{p}_\alpha) = (\lambda_0 \boldsymbol{\mathsf{I}} + \lambda_1 \boldsymbol{p}_\alpha \boldsymbol{p}_\alpha) \cdot \boldsymbol{F}. \tag{4.3}$$

The gravity force is $\boldsymbol{F} = \Delta\rho V_p \boldsymbol{g}$ where $\Delta\rho$ is the relative density and V_p is the volume of a particle. The two constants λ_0 and λ_1 are mobility coefficients, and are functions of the aspect ratio defined for arbitrary A; their expressions for spheroidal particles can be found elsewhere (cf. References [79, 102]). The rotational motion of the particle is described using Jeffery's equation [93]:

$$\dot{\boldsymbol{p}}_\alpha = (\mathsf{I} - \boldsymbol{p}_\alpha \boldsymbol{p}_\alpha) \cdot \left(\frac{A^2 - 1}{A^2 + 1} \mathsf{E}(\boldsymbol{x}_\alpha) + \boldsymbol{\Omega}(\boldsymbol{x}_\alpha) \right) \cdot \boldsymbol{p}_\alpha, \tag{4.4}$$

in which $\mathsf{E}(\boldsymbol{x}) = \left[\boldsymbol{\nabla}\boldsymbol{u}(\boldsymbol{x}) + (\boldsymbol{\nabla}\boldsymbol{u}(\boldsymbol{x}))^T \right]/2$ and $\boldsymbol{\Omega}(\boldsymbol{x}) = \left[\boldsymbol{\nabla}\boldsymbol{u}(\boldsymbol{x}) - (\boldsymbol{\nabla}\boldsymbol{u}(\boldsymbol{x}))^T \right]/2$ denote the disturbance rate of strain and rate of rotation tensors, respectively. Provided that the disturbance velocity $\boldsymbol{u}(\boldsymbol{x})$ and its gradient $\boldsymbol{\nabla}\boldsymbol{u}(\boldsymbol{x})$ can be calculated at the center of mass of each particle, we can determine the motion of the particles by time integration of the dynamic equations (4.2) and (4.4).

Hydrodynamic interactions

Far-field hydrodynamic interactions between the suspended particles are captured through the disturbance velocity field. If the suspension is dilute, the effect of a particle on the fluid is to first order a point force equal to the gravitational force $\boldsymbol{F}$ and applied at its center of mass (cf. Section 2.3). The disturbance velocity can therefore be calculated as a solution of the Stokes equations:

$$-\mu\nabla^2\boldsymbol{u} + \boldsymbol{\nabla}p = \boldsymbol{f}, \quad \boldsymbol{\nabla} \cdot \boldsymbol{u} = 0, \tag{4.5}$$

with a body force equal to:

$$\boldsymbol{f}(\boldsymbol{x}) = \sum_{\alpha=1}^{N} \boldsymbol{F}\delta(\boldsymbol{x} - \boldsymbol{x}_\alpha), \tag{4.6}$$

where $\delta(\boldsymbol{x})$ is the three-dimensional Dirac delta function.

The solution of Equation (4.5) in an infinite fluid is a sum of point-force singularities or Stokeslets:

$$\boldsymbol{u}(\boldsymbol{x}) = \frac{1}{8\pi\mu} \sum_{\alpha=1}^{N} \left(\frac{\mathsf{I}}{|\boldsymbol{x} - \boldsymbol{x}_\alpha|} + \frac{(\boldsymbol{x} - \boldsymbol{x}_\alpha)(\boldsymbol{x} - \boldsymbol{x}_\alpha)}{|\boldsymbol{x} - \boldsymbol{x}_\alpha|^3} \right) \cdot \boldsymbol{F}, \tag{4.7}$$

and the solution in a periodic domain is also known (cf. Appendix A). Equation (4.7) and its periodic counterpart suffer from some limitations: the solution indeed grows unbounded near the center of mass of the particles as a consequence of the point-force approximation which is an asymptotic result valid far from the particle surface. Furthermore, the calculation of this disturbance velocity at each particle location is an expensive operation, scaling with the square of the number of particles. Fast algorithms have been devised in the past to reduce the cost of this calculation [170, 157], but were based on periodic boundary conditions and typically only allowed the simulation of a few hundred to a few thousand particles.

Here we present a method for the evaluation of the disturbance velocity which completely neglects close particle interactions by smoothing the disturbance field at short distances. The singularity in the point-force solution arises from the Dirac delta functions in the forcing term Equation (4.6). Instead of calculating the exact flow field induced by these point singularities, we use a Cartesian grid and assign the point forces exerted by the particles on the fluid to the neighboring mesh points $\boldsymbol{x}_i$:

$$\boldsymbol{f}(\boldsymbol{x}_i) = \sum_{\alpha=1}^{N} \boldsymbol{F} M(\boldsymbol{x}_i - \boldsymbol{x}_\alpha). \tag{4.8}$$

$M(\boldsymbol{x})$ is the assignment function and depends on the nature and the order of the interpolation method used. The choice of $M(\boldsymbol{x})$ is somewhat arbitrary, provided that it satisfies a few basic conditions. We require that the sum of $M(\boldsymbol{x}_i)$ over all the grid points be one for the total force to be conserved, and that M have spherical symmetry. M should also be small beyond a certain cutoff radius for the force to remain local; ideally (although not necessarily) M should have a compact support. A good class of functions satisfying these properties are Cardinal B-splines (cf. Appendix B and References [165, 88, 49]). Other choices are possible: Maxey and coworkers for instance in their similar force-coupling method use Gaussian interpolants, which do not have a compact support [125, 119].

The level of approximation of the simulation method described here, in which each particle only exerts a point force on the fluid at its center (Equations (4.5) and (4.8))

and feels the linearized disturbance flow induced by the other particles (Equations (4.2) and (4.4)) can be discussed in the light of the considerations of Chapter 2: it corresponds indeed to the leading-order term in the multipole expansion of Section 2.3. This level of approximation is not capable of capturing velocity variation on length scales of the order of the particle size, and is strictly valid for widely separated particles (dilute suspensions).

Solution of the Stokes equations

Equation (4.8) defines a body force field on the Cartesian grid and can be substituted into the Stokes equations, which are then solved numerically with appropriate boundary conditions. In this work two types of boundary conditions are considered. One of our objectives is to investigate the effects of solid boundaries, and to this end we follow the approach of Bergougnoux *et al.* [20] and seek a solution of the Stokes equations satisfying a tangential flow boundary condition (i.e. 'slip', but no penetration) on the walls of the container. While this differs from the exact no-slip boundary condition for viscous flow, it allows for a very efficient solution while capturing some effects of the walls: in particular the no-flux boundary condition at the bottom wall will lead to large-scale recirculation in the lateral direction and homogenization, both of which have been suggested as potential mechanisms for the decay of the fluctuations in sphere suspensions [112, 20]. The effects of the tangential flow along the walls are investigated more precisely in Appendix C, where the present solution is compared to a more accurate solution satisfying the no-slip boundary condition on two of the side walls [132]; in particular, tangential flow along the walls is shown to result in slightly overestimated velocity fluctuations.

We first observe that $\boldsymbol{f}(\boldsymbol{x}) = f(\boldsymbol{x})\hat{\boldsymbol{z}}$, and transform the scalar-valued function $f(\boldsymbol{x})$ as follows using sine and cosine series:

$$f(\boldsymbol{x}) = \sum_{\boldsymbol{k}} \hat{f}(\boldsymbol{k}) \cos\left(\frac{\pi k_x x}{L_x}\right) \cos\left(\frac{\pi k_y y}{L_y}\right) \sin\left(\frac{\pi k_z z}{L_z}\right), \qquad (4.9)$$

in which the wavevector $\boldsymbol{k}$ in an orthogonal lattice is defined as

$$\boldsymbol{k} = \frac{k_x}{L_x}\hat{\boldsymbol{x}} + \frac{k_y}{L_y}\hat{\boldsymbol{y}} + \frac{k_z}{L_z}\hat{\boldsymbol{z}} \qquad (4.10)$$

with k_x, k_y and k_z integers. We then seek a solution for the velocity written as:

$$\boldsymbol{u}(\boldsymbol{x}) = \sum_{\boldsymbol{k}} \hat{u}(\boldsymbol{k}) \times \begin{cases} \dfrac{k_x k_z}{L_x L_z} \sin\left(\dfrac{\pi k_x x}{L_x}\right) \cos\left(\dfrac{\pi k_y y}{L_y}\right) \cos\left(\dfrac{\pi k_z z}{L_z}\right), \\[2mm] \dfrac{k_y k_z}{L_y L_z} \cos\left(\dfrac{\pi k_x x}{L_x}\right) \sin\left(\dfrac{\pi k_y y}{L_y}\right) \cos\left(\dfrac{\pi k_z z}{L_z}\right), \\[2mm] -\left(\dfrac{k_x^2}{L_x^2} + \dfrac{k_y^2}{L_y^2}\right) \cos\left(\dfrac{\pi k_x x}{L_x}\right) \cos\left(\dfrac{\pi k_y y}{L_y}\right) \sin\left(\dfrac{\pi k_z z}{L_z}\right). \end{cases} \tag{4.11}$$

Equation (4.11) automatically satisfies continuity and the tangential flow boundary condition. Substituting Equations (4.9) and (4.11) into the Stokes equations (4.5) allows one to solve for the Fourier coefficients of the velocity:

$$\hat{u}(\boldsymbol{k}) = \frac{\hat{f}(\boldsymbol{k})}{\pi^2 \left[\left(\dfrac{k_x}{L_x}\right)^2 + \left(\dfrac{k_y}{L_y}\right)^2 + \left(\dfrac{k_z}{L_z}\right)^2\right]^2}. \tag{4.12}$$

The Fourier series expansions (4.9) and (4.11) can be truncated in each space dimension beyond a maximum wavenumber K_x, K_y, K_z, which should be chosen to as to make the shortest resolved wavelength shorter than the mean interparticle distance; the precise effects of the level of truncation are discussed in Appendix C. The velocity field and its gradient are then easily solved for using fast sine and cosine series algorithms.

For the sake of comparison we also consider periodic systems, and solve the Stokes equations spectrally. The velocity field is expanded as a Fourier series

$$\boldsymbol{u}(\boldsymbol{x}) = \sum_{\boldsymbol{k}} \hat{\boldsymbol{u}}(\boldsymbol{k}) \exp(-2\pi \mathrm{i} \boldsymbol{k} \cdot \boldsymbol{x}). \tag{4.13}$$

As described in Appendix A, Hasimoto [81] solved for the Fourier coefficients of the velocity:

$$\hat{\boldsymbol{u}}(\boldsymbol{k}) = -\frac{1}{4\pi^2 \mu \tau_0 k^2} \left(\mathbf{I} - \frac{\boldsymbol{k}\boldsymbol{k}}{k^2}\right) \cdot \hat{\boldsymbol{f}}(\boldsymbol{k}), \tag{4.14}$$

where τ_0 is the volume of the periodic cell and $\hat{\boldsymbol{f}}(\boldsymbol{k})$ are the Fourier coefficients of the force distribution. As in the periodic case, the series are truncated at a finite number of terms, and the fast Fourier transform algorithm is used for good efficiency.

It should be noted that in the method described above each particle feels its own disturbance, since the force field (Equation (4.8)) used in the Stokes equations includes a

contribution from the particle itself. Further adding this self-disturbance to the free-space sedimentation velocity $\boldsymbol{U}_s(\boldsymbol{p}_\alpha)$ in Equation (4.2) would lead to a systematic overestimation of the sedimentation rates. In the simulations the disturbance velocity $\boldsymbol{u}(\boldsymbol{x})$ felt by each particle was therefore corrected by subtracting this self-contribution, which can be calculated independently on the grid using a similar method.

In all of the following distances are made dimensionless with the length $l_c = 2l$ of the major axis of a particle, velocities with the sedimentation speed $u_c = (\lambda_0 + \lambda_1)\Delta\rho V_p g$ of an isolated vertical spheroid in an infinite fluid, and times with the time $t_c = l_c/u_c$ for an isolated vertical spheroid to sediment over the length of its major axis. In all simulations third-order B-spline interpolation was used for the calculation of the body force field, and the number of Fourier modes was chosen so as to resolve the velocity field over distances on the order of half a particle length. The time integration was performed using a fourth-order Runge-Kutta scheme. For the most part we treat the case of prolate spheroids ('fibers'), for which comparison with experimental data is presently possible; the case of oblate particles ('disks') is briefly addressed in Section 4.2.7. Unless otherwise stated the results shown are for non-periodic systems with slip boundary conditions.

4.2.2   Particle distribution and concentration fluctuations

Figure 4.1(a) shows a typical particle distribution, obtained for a simulation of 29,702 spheroids of aspect ratio $A = 15$ in a box of dimensions $L_x = 32$, $L_y = 12$, $L_z = 180$ (particle volume fraction $\phi = 0.1$ %). The initial condition is a homogeneous dispersion with random positions and orientations. As the sedimentation proceeds, a broad suspension front forms at the interface with the clear fluid and keeps growing in time. Careful observation of the bulk shows that the suspension does not remain homogeneous: particles instead tend to aggregate into clusters as predicted by Koch & Shaqfeh [102]. Particles are also observed to rotate and to orient preferentially in the vertical direction, with a strong correlation between center-of-mass position and orientation: while the orientation remains random inside the dense clusters, the alignment in the vertical direction is much clearer in their periphery, where we will see that a strong vertical shear exists (e.g. Section 4.2.4).
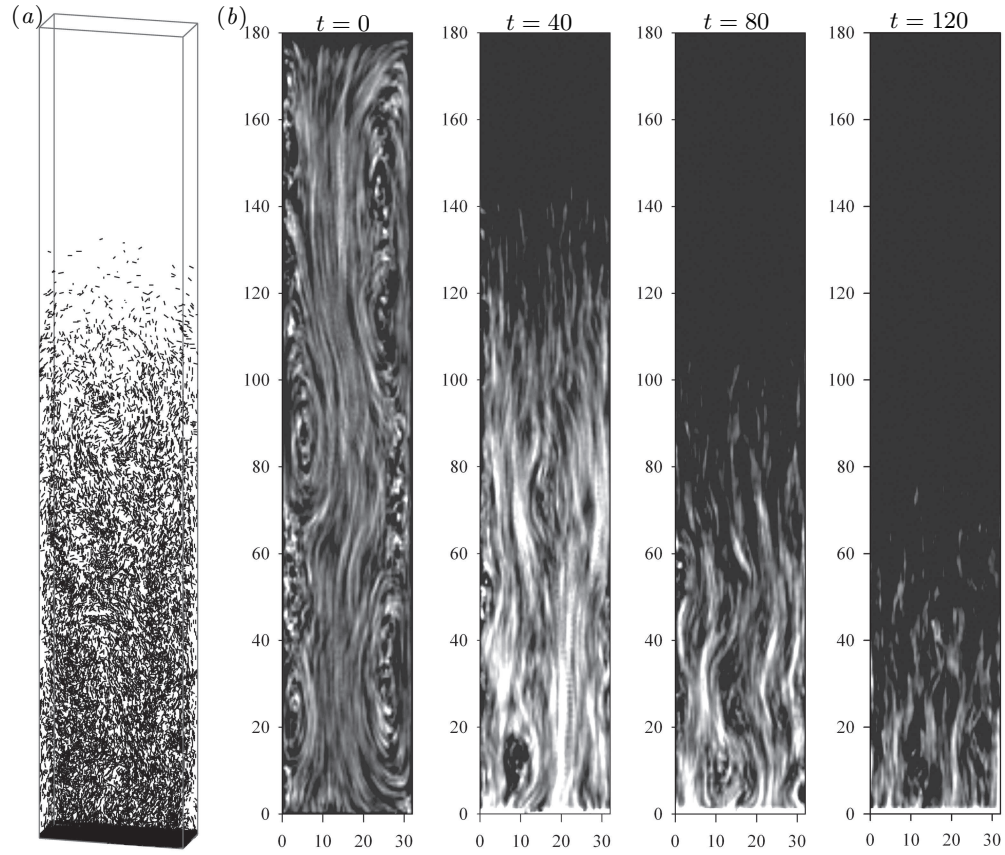
Figure 4.1: (a) Particle distribution at $t = 80$ for a simulation of 29,702 spheroids of aspect ratio $A = 15$ in a box of dimensions $L_x = 32$, $L_y = 12$, $L_z = 180$ (volume fraction $\phi = 0.1$ %). (b) Time trace of the concentration field over a short interval $\Delta t = 4$ in the mid-plane $y = L_y/2$, at various stages of the sedimentation (cf. Equation 4.15)

We focus our analysis on the clustering phenomenon, and try to define measures for the concentration fluctuations in the bulk.

A good way of visualizing the inhomogeneities consists of considering the time trace over a short time interval of the smooth concentration field obtained by B-spline interpolation as explained in Section 4.2.1:

$$\bar{c}(\boldsymbol{x}, t) = \frac{1}{\Delta t} \int_t^{t+\Delta t} \sum_{\alpha=1}^N M(\boldsymbol{x} - \boldsymbol{x}_\alpha(t')) \mathrm{d}t', \tag{4.15}$$

where a small value on the order of a few Stokes units is chosen for Δt ($\Delta t = 4$ in the results

presented here). The advantage of this measure is that it allows one to visualize both the concentration fluctuations and the correlation in the motion of the particles. Figure 4.1(b) shows $\bar{c}(\boldsymbol{x}, t)$ in the vertical mid-plane $y = L_y/2$ at different times t over the course of the simulation of Figure 4.1(a). In the initial instants weak density fluctuations are present due to the random nature of the initial distribution. A relatively strong flow is observed away from the walls at the center of the cell, with recirculation vortices on the sides. This strong initial streamer spans the entire box width, in agreement with the scaling of Hinch [87], according to which velocity fluctuations in a random sedimenting suspension occur over length scales comparable to the width of the container. Interestingly the streamer also spans the entire height of the box, in contrast to the circular vortical structures that are typically observed in sphere sedimentation [74]; this very long autocorrelation in the vertical direction will be further explored in Section 4.2.4. At later times ($t = 40$ to 80), this initial streamer is observed to break up into smaller structures; yet the concentration fluctuations intensify as a result of the Koch & Shaqfeh instability, leading to the formation of dense vertical streaks. Several streaks can be observed in the lateral direction (up to three or four at $t = 40$), suggesting that a wavenumber selection may be occurring. The inhomogeneities are found to persist up until the arrival of the sedimentation front, in spite of the decay of the velocity fluctuations in the fluid (cf. Section 4.2.5). As the concentration in the suspension finally decreases owing to stratification (Figure 4.3), the concentration fluctuations gradually become less intense ($t = 120$).

The fluctuations in the bulk can be measured more quantitatively by calculating the instantaneous Fourier transform of the concentration field over a section of the box:

$$\hat{c}(\boldsymbol{k}, t) = \int_{V'} c(\boldsymbol{x}, t) \exp(2\pi i \boldsymbol{k} \cdot \boldsymbol{x}) d\boldsymbol{x}. \tag{4.16}$$

Practically $c(\boldsymbol{x}, t)$ is obtained by binning the particle positions, and $\hat{c}(\boldsymbol{k}, t)$ is calculated as a discrete Fourier transform. Figure 4.2 shows the time evolution of the magnitude of a few Fourier coefficients, obtained for a simulation in a box of dimensions $L_x = 32$, $L_y = 32$, $L_z = 180$ at a volume fraction of $\phi = 0.2$ %, in both non-periodic and periodic
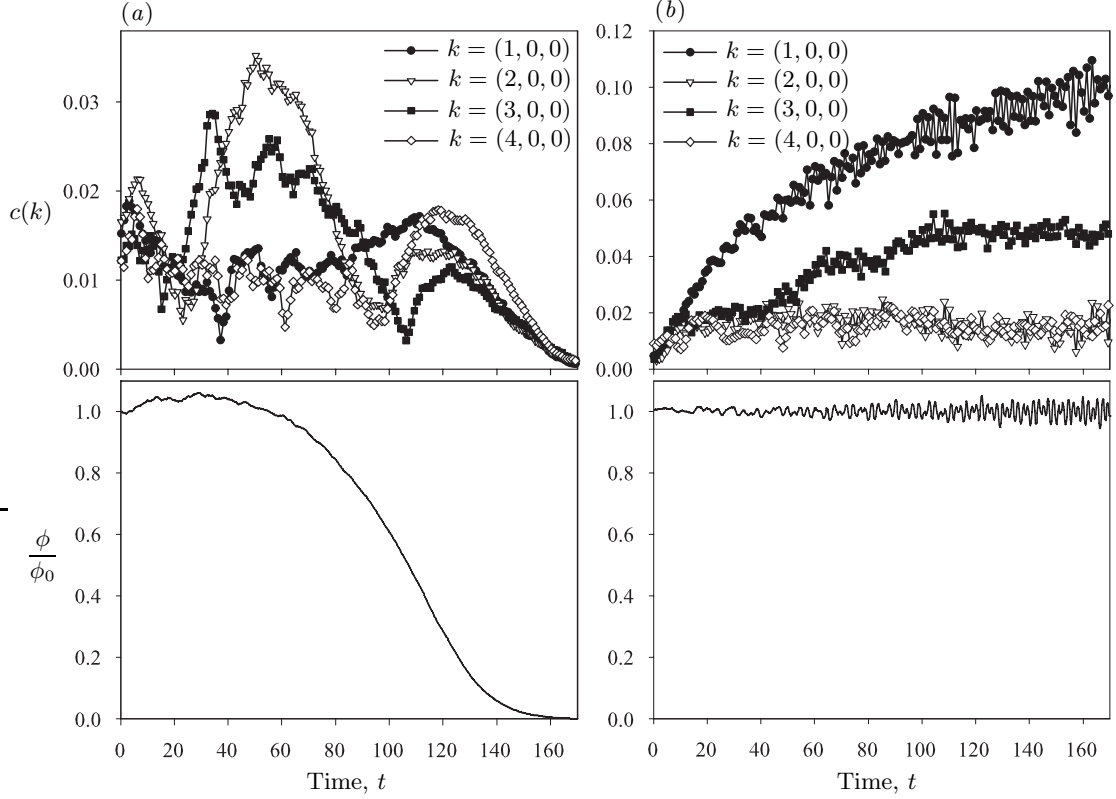
Figure 4.2: Time evolution of the Fourier coefficients of the concentration field for a simulation of 158,411 spheroids of aspect ratio $A = 15$ in a box of dimensions $L_x = 32$, $L_y = 32$, $L_z = 180$ (volume fraction $\phi = 0.2$ %), in both (a) non-periodic and (b) periodic boundary conditions. The spectra were calculated over a subsection of the container: $20 < z < 52$, and were averaged over four simulations. The bottom plots show the evolution of the mean volume fraction in the section in which the spectra were obtained.

boundary conditions. In the periodic case (Figure 4.2(b)), the longest wavelength in the horizontal direction $\boldsymbol{k} = (1, 0, 0)$ clearly dominates the spectrum, which corresponds to the formation of one main streamer (here each component of $\boldsymbol{k}$ is made dimensionless with the inverse size of the box in the corresponding direction). This is in agreement with the linear stability analysis of Koch & Shaqfeh [102] which predicts that the shortest wavenumber (longest wave) should grow the fastest, and was also reported in previous simulations of periodic systems [122, 32, 157]. The behavior is quite different in the non-periodic case (Figure 4.2(a)), where the two wavevectors $\boldsymbol{k} = (2, 0, 0)$ and $\boldsymbol{k} = (3, 0, 0)$ are observed to
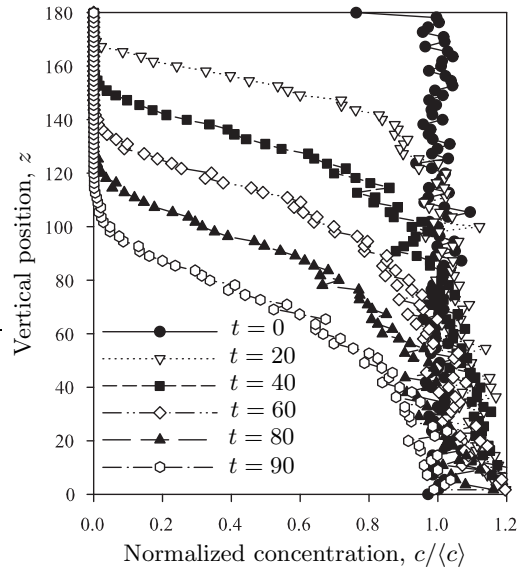
Figure 4.3: Cross-section averaged concentration profile in the vertical direction at various times during the sedimentation of a suspension of 148,510 spheroids of aspect ratio $A = 15$ in a box of dimensions $L_x = 32$, $L_y = 12$, $L_z = 180$ (volume fraction $\phi = 0.5$ %). The concentration profile is normalized by its average value $\langle c \rangle$.

grow and dominate the spectrum, corresponding to two or three dense streamers in the lateral direction. This is consistent with Figure 4.1(b) where in a finite box several vertical streaks were shown to appear in the concentration field. After about 100 time units the arrival of the front leads to a decay of the fluctuations at all wavenumbers, whereas in the periodic case the fluctuations keep growing and do not show any sign of saturation.

The stratification and fluctuations in the vertical direction are illustrated in Figure 4.3, showing the time evolution of the concentration profile in the z-direction (where concentration has been averaged in the horizontal plane). Initially the transition from the bulk concentration $c = \langle c \rangle$ to zero (clear fluid) is quite sharp. As time goes on the dispersion in orientation and anisotropic mobility of the particles result in the broadening of the interface: this is demonstrated by the change in the slope of the profile inside the front, which indicates a much smoother transition. Such a smooth transition is not typically observed in suspensions of spherical particles where the interface remains quite sharp throughout
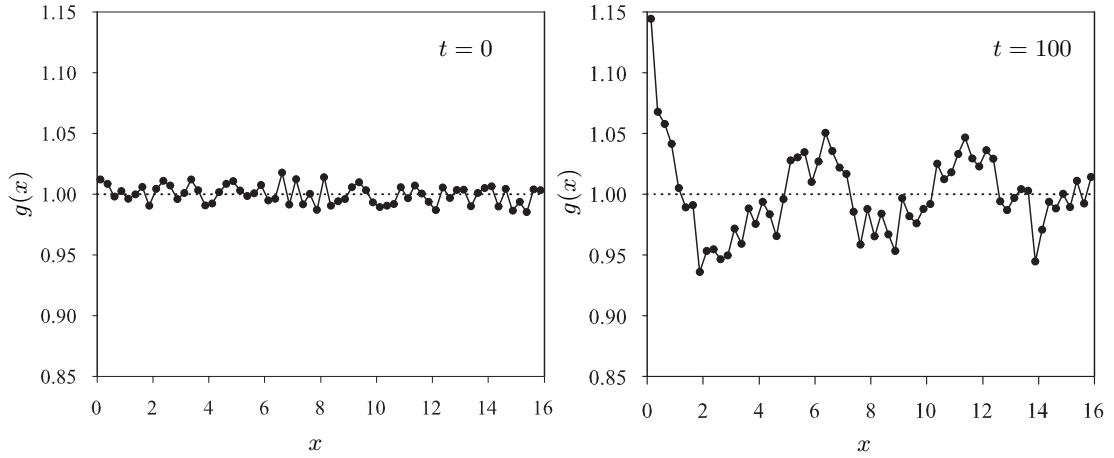
Figure 4.4: Pair distribution function in the lateral direction at $t = 0$ and $t = 100$ for a simulation of 29,952 spheroids of aspect ratio $A = 15$ in a box of dimensions $L_x = 32$, $L_y = 12$, $L_z = 180$ (volume fraction $\phi = 0.1$ %). $g(x)$ was calculated over the subdomain $20 < z < 30$.

the sedimentation process (cf. Reference [20] for instance, as well as Figure 5.4(b)). Figure 4.3 also presents another interesting feature, as the concentration in the suspension and in particular near the bottom of the container is observed to exceed the mean bulk value $\langle c \rangle$. This constitutes another proof of clustering, and also suggests an additional mechanism for the broadening of the front, which may not only be due to the dispersion in orientation but also to the segregation of the clusters near the bottom of the box, as particle aggregates have enhanced sedimentation speeds. The effects of stratification on the instability, and more specifically on the wavenumber selection, will be discussed in more detail in Section 4.3.

4.2.3 Pair distribution function and structure factor

The microstructural arrangement of the particles in the suspension is well captured by the pair distribution function, which is the distribution of pairs of particles at a given center-of-mass to center-of-mass distance [109]. As observed in the previous Section the microstructure in the suspension is highly anisotropic; to confirm the arrangement of the spheroids into several vertical streamers in the horizontal direction we define a pair

distribution function in the lateral direction:

$$g(x) = \frac{V}{N^2} \langle \sum_i \sum_{j \neq i} \delta(x - x_{ij}) \rangle, \tag{4.17}$$

where $x_{ij} = |x_i - x_j|$ is the separation distance along the x–axis between particles i and j, and $\langle \cdot \rangle$ denotes the ensemble average. To avoid artifacts due to the container side walls the suspension is replicated periodically in the x-direction and the closest separation distance is used when calculating $g(x)$. Figure 4.4 shows the pair distribution function at $t = 0$ and $t = 100$ for a typical simulation. At $t = 0$, $g(x)$ is essentially constant as the particle distribution is uniform; this is a consequence of our simulation model in which excluded volume interactions are completely neglected. $g(x)$ does not remain uniform however, as shown in the second plot in Figure 4.4. A peak near $x = 0$ is observed to form: this maximum, which had been reported in previous studies [32, 108], is a sign of clustering and means that there is an excess of particles in the vicinity of any given particle. Quite interestingly oscillations also appear away from $x = 0$, i.e. the arrangement of the particles does not remain uniform and random, but becomes structured at long wavelengths as a result of the formation of the streamers in the lateral direction.

The data from the pair distribution function are best analyzed by taking the Fourier transform of their fluctuating part, yielding the structure factor:

$$S(k) = \int \exp(-2\pi \mathrm{i} k x / L_x) \left(g(x) - 1 \right) \mathrm{d}x. \tag{4.18}$$

The evolution of the structure factor for the same simulation as in Figure 4.4 is shown in Figure 4.5. At $t = 0$ no particular frequency dominates the spectrum. Progressively a peak appears at $k = 1$ and $k = 2$ ($t \approx 40$), and slowly migrates towards $k = 3$ while becoming more intense. The data are very well reproducible from one simulation to another for a given set of parameters, and this suggests that a wavenumber selection is indeed taking place. As shown in Figure 4.5, the wavenumber selection is associated with the decay or break-up of the initial mode $k = 1$, and is linked to the presence of container walls as it is not observed in periodic boundary conditions where the longest mode dominates
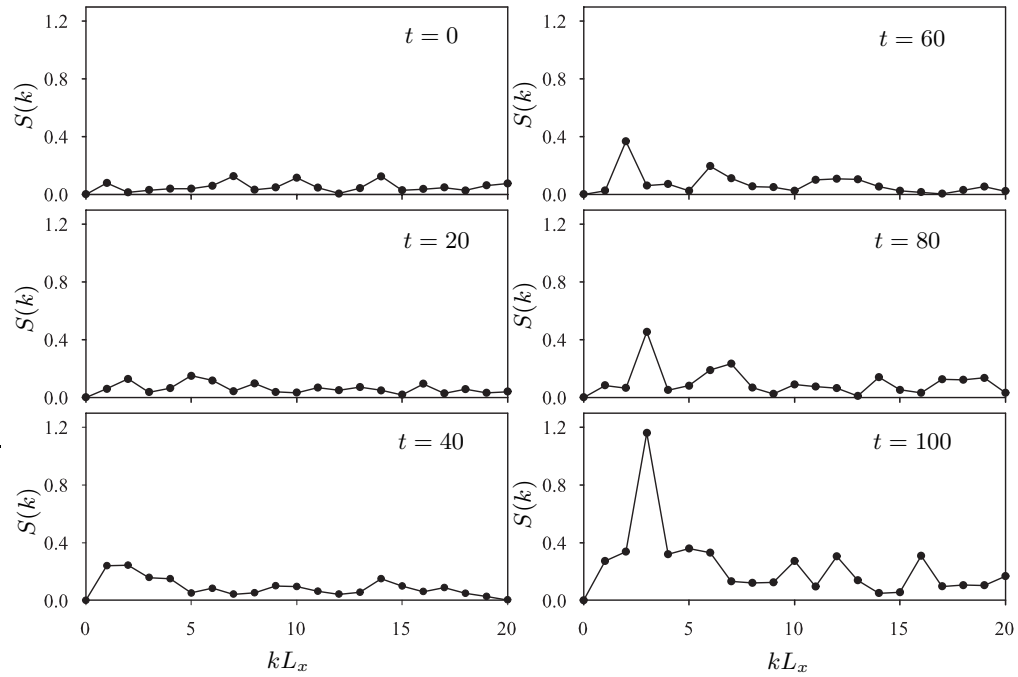
Figure 4.5: Time evolution of the structure factor for the simulation of Figure 4.4 (29,952 spheroids, $A = 15$, $L_x = 32$, $L_y = 12$, $L_z = 180$, $\phi = 0.1$ %). The structure factor was obtained by taking the Fourier transform of the fluctuating part of the pair distribution $g(x)$ shown in Figure 4.4 (Equation 4.18).

throughout the simulation.

The dependence of the final wavelength of the fluctuations on the dimensions of the container is investigated in Table 4.1, where the final position of the second peak in the pair distribution function $g(x)$, which gives an estimate of the spacing between streamers, is shown for various box dimensions. At given values of the volume fraction and of the particle aspect ratio, the position of the peak is fairly insensitive to the lateral dimensions L_x and L_y of the simulation box; at $\phi = 0.1$ % and $A = 15$ the data of Table 4.1 give a spacing of approximately 6 particle lengths in the lateral direction. This confirms that the initial fluctuations over the width of the box give way to fluctuations at a wavelength that does not depend on the container dimensions, and must therefore scale with the interparticle distance in the suspension. This transition from box-dependent to box-independent concentration fluctuations is analogous to what was previously reported for the velocity

Box dimensions (L_x, L_y, L_z)	Final spacing between streamers
(16, 12, 180)	6.61
(32, 12, 180)	5.83
(48, 12, 180)	6.80
(64, 12, 180)	6.56
(32, 32, 180)	5.94

Table 4.1: Influence of the container dimensions on the wavenumber selection in suspensions of spheroids of aspect ratio $A = 15$ at a volume fraction of $\phi = 0.1$ %. The spacing between streamers is estimated using the position of the second peak that appears in the pair distribution function $g(x)$ (cf. Figure 4.4). At given values of A and ϕ the final wavelength of the fluctuations is insensitive to the size of the container.

fluctuations in suspensions of rigid spheres [137, 74], suggesting that similar mechanisms may be at play. A potential mechanism for the transition will be described in Section 4.3, where we argue that the stratification that develops in the suspension may cause a decay of the size of the concentration fluctuations.

4.2.4   Velocity disturbance field

The inhomogeneous microstructure described above is also visible from the velocity disturbance field. Typical velocity fields are shown in Figure 4.6 at the beginning of the sedimentation and at a later time ($t = 60$). At $t = 0$ a strong flow is observed near the center of the box with recirculation near the walls, in agreement with the observations made previously on the time trace of the concentration field (Figure 4.1(b)). Note that the non-zero disturbance velocity at the walls is an artifact of the slip boundary condition used in the simulations, and would not be observed in an experiment. However backflow near the walls can still be expected even in no-slip boundary conditions because of the depletion layer existing near the walls due to excluded volume, which has a characteristic thickness of the order of half a particle length [129]. As already observed in Figure 4.1(b), this initial flow spans most of the box height, unlike the stacking of circular cells that has been reported for spheres [74]; this may be a consequence of the depletion layer, which is almost nonexistent in sphere suspensions at the volume fractions considered here. Over
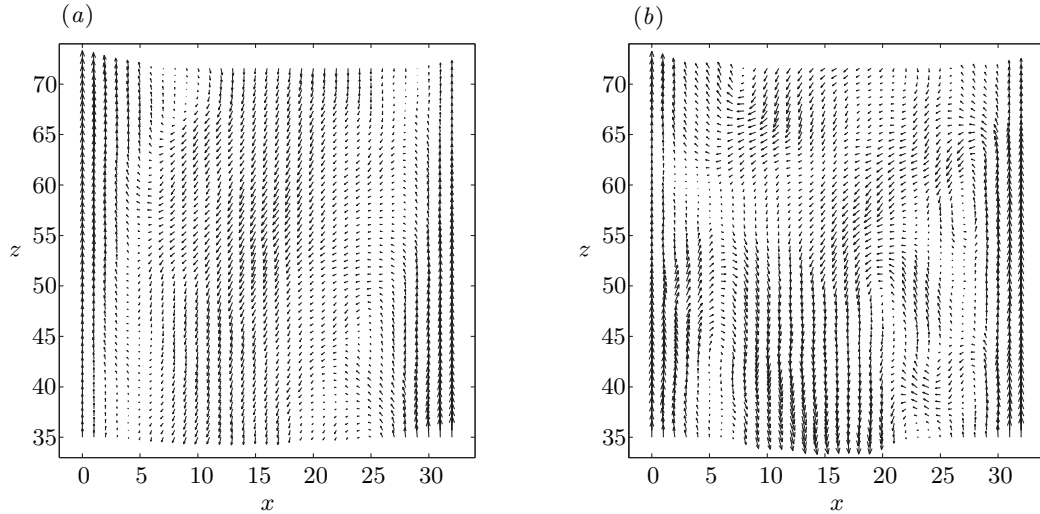
Figure 4.6: Velocity disturbance field at (a) $t = 0$ and (b) $t = 60$ in the midplane $y = L_y/2$, for a simulation of 59,904 spheroids of aspect ratio $A = 15$ in a box of dimensions $L_x = 32$, $L_y = 12$, $L_z = 180$ (volume fraction $\phi = 0.2$ %).

the course of the sedimentation smaller structures appear in the velocity field, as shown in Figure 4.6(b) at $t = 60$. The disturbance field now looks more chaotic, and presents distinct swirls over shorter lengths scales. The vortices are slightly stretched in the vertical direction, suggesting that the correlation is stronger in the direction of gravity.

These qualitative observations are confirmed in Figure 4.7, which shows the evolution of the autocorrelation functions of the velocity field. Figure 4.7(a) shows the autocorrelation $C_{zz}(x)$ in the lateral direction x of the vertical velocity component u_z. At $t = 0$ the function decorrelates very slowly and reaches a minimum beyond $x = 15$ which is approximately half a box width: this very slow decay in the lateral direction was expected as a result of the aforementioned streamer spanning the entire box width at the beginning of sedimentation. Progressively a clearer minimum appears and shifts towards lower values of x. At $t = 40$ the minimum near $x = 4$ corresponds to an anticorrelation in the vertical velocity field, i.e. to the presence of fluid streams flowing in opposite directions. A second peak is then observed again near $x = 7$. This negative correlation followed by an increase in the correlation is indicative of a succession of similar vortex structures in the lateral
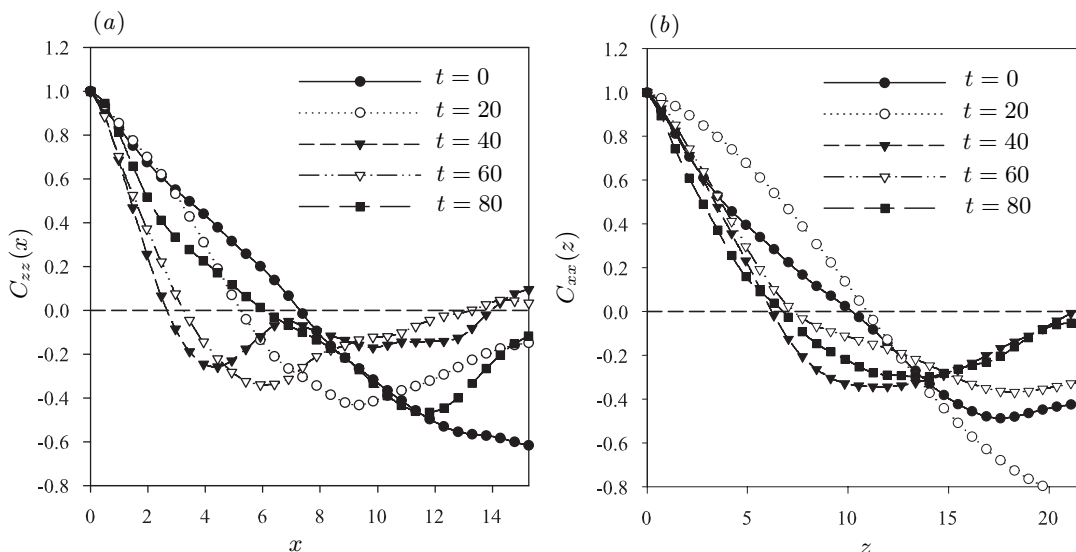
Figure 4.7: Time evolution of the autocorrelation function of: (*a*) the vertical velocity component in the lateral direction, and (*b*) the horizontal velocity component in the vertical direction. The results are for a simulation of 59,904 spheroids of aspect ratio $A = 15$ in a box of dimensions $L_x = 32$, $L_y = 12$, $L_z = 180$ (volume fraction $\phi = 0.2$ %).

direction, corresponding to the clusters or streamers observed in the particle distribution. In particular the position of the peak $x = 7$ can be used as a rough estimate of the spacing between the clusters; in a box of width $L_x = 32$ this corresponds to approximately four structures, which is in relatively good agreement with the wavenumber obtained from the structure factor. Note that after a while ($t = 80$ and beyond), the position of the minimum in the correlation function starts increasing again as a result of the arrival of the sedimentation front, and of the very strong damping of all the fluctuations in the fluid.

Figure 4.7(*b*) shows the autocorrelation $C_{xx}(z)$ in the vertical direction z of the horizontal velocity component u_x. The behavior is somewhat similar: starting from a very long correlation length (of the order of 15 to 20 particle lengths), the position of the minimum shifts to a lower value $z \approx 10$. This value however remains substantially greater than the shortest length of 4 observed in the lateral direction. This confirms that the structures in the velocity field and the particle distribution are stretched in the vertical direction, typically by a factor greater than two.

The evolution of the disturbance field is reminiscent of observations made previously on sphere suspensions (e.g. [167, 74, 186]). In the case of spheres the initial disturbance field is characterized by large recirculation cells induced by the random Poisson statistics due to the initial mixing; these cells are then observed to break up into smaller swirls, whose characteristic size in most experiments is found to be of the order of 15 mean interparticle distances, and therefore does not depend on the container dimensions. Several mechanisms have been proposed for the decay of the correlation length and of the fluctuations as reviewed in Section 4.1. The clear analogy with the results reported here suggests that the same mechanisms leading to the decay of velocity fluctuations in sphere suspensions may play a role in the wavenumber selection process observed in our simulations. In particular, the initial strong convection current may be decaying as a result of homogenization at long wavelengths before the strongest mode ($k = 1$) of the instability has any time to grow significantly. As we discuss in Section 4.3, the strong stratification illustrated in Figure 4.3 also plays an important part (in fact much more important than for spheres because of the dispersion in orientation which acts like a polydispersity), and is in part responsible for the continuous decay of the velocity fluctuations with no steady state as discussed in Section 4.2.5, and for the evolution of the wavelength of the instability. Despite the qualitative similarities, the previous discussion also casts light on several important differences. While the decay of the velocity correlation length in sphere sedimentation is accompanied with and possibly a result of the homogenization of the particle distribution in the horizontal direction [114, 134, 135], homogenization only occurs down to the wavelength of the instability in the case of spheroids; quite strong density fluctuations persist between the core of the streamers and the clarified fluid, as discussed in Section 4.2.2. A detailed comparison of the length scales of the fluctuations in both situations would be worthwhile in order to fully appreciate the effects of the instability. As a result of the clustering, the velocity field in the case of spheroids also maintains a much stronger correlation in the vertical direction: long streamers of dense fluid alternate with clarified regions of backflow, unlike the circular swirls induced by the much weaker density fluctuations in sphere suspensions.
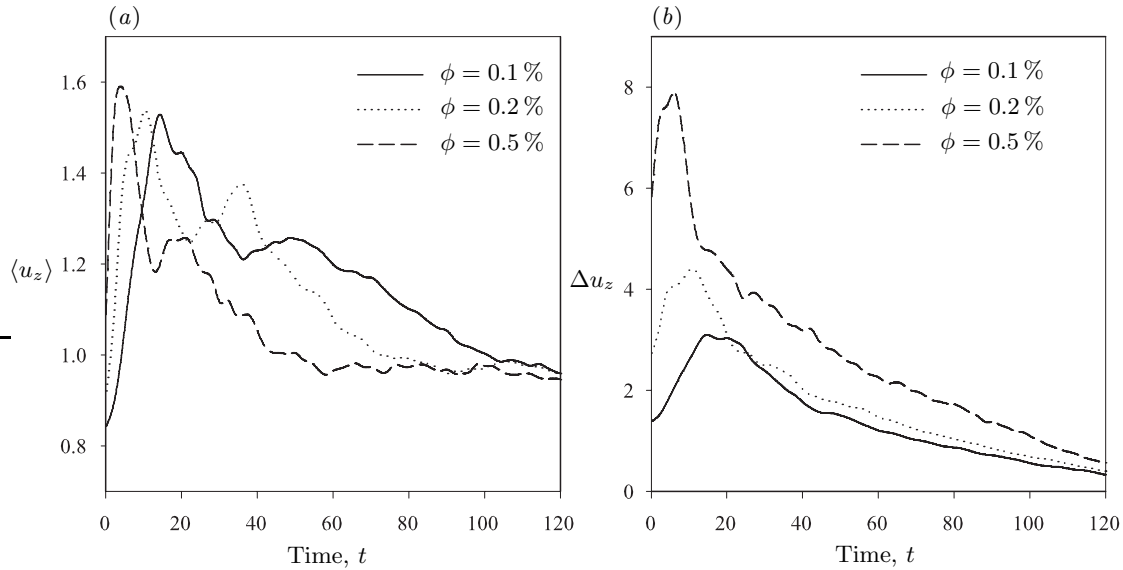
Figure 4.8: (*a*) Mean sedimentation velocity $\langle u_z \rangle$, and (*b*) velocity fluctuations Δu_z in the *z*-direction at various volume fractions. The results are for spheroids of aspect ratio $A = 15$ in a box of dimensions $L_x = 32$, $L_y = 12$, $L_z = 180$. The results were obtained in a subsection of the box: $45 < z < 67.5$, and are averaged over ten simulations to remove statistical fluctuations.

4.2.5   Velocity statistics

The effects of the instability on the sedimentation velocity are twofold. As will be discussed in Section 4.2.6 the strong vertical shear between the dense and clarified regions causes the spheroids to orient vertically, resulting in an increase of their individual sedimentation speed. More interestingly the arrangement of the particles into dense clusters allows for the clusters to sediment faster, which can be viewed as a shielding effect. The combination of these two effects can result in sedimentation velocities that exceed the maximum velocity for an isolated particle, as illustrated in Figure 4.8 where the velocities are made dimensionless by the velocity of a single vertically oriented spheroid. Figure 4.8(*a*) shows the evolution of the mean sedimentation velocity at various volume fractions. Starting from an initial value close to the sedimentation rate of 0.83 for spheroids of aspect ratio of $A = 15$ at infinite dilution, the mean sedimentation velocity rapidly increases to reach a maximum value ranging from 1.5 in the more dilute case ($\phi = 0.1$ %) to approximately 1.6

at $\phi = 0.5$ %. After this strong peak the mean velocity decays slowly back towards smaller values, until the arrival of the front in which the velocities are found to be much weaker. Quite interestingly the curves do not present any steady state, i.e. the particle velocity at a given vertical station varies continually; the mean velocity is also observed to depend slightly on the height at which it is measured. This differs from the experimental observations of Herzhaft & Guazzelli [84], who reported a mean velocity steady state; this may be a consequence of the limited height of the box in our simulations, or of the approximate boundary conditions on the side walls. Herzhaft & Guazzelli [84] observed an increase of the mean sedimentation speed with concentration in the dilute regime, in agreement with our results. The values they report for the mean velocity are (for cylindrical fibers of aspect ratio $A = 11 \pm 2$): 1.1 ± 0.2 at $\phi = 0.1$ % and 0.26 %, and 1.5 ± 0.3 at $\phi = 0.48$ %, which fall slightly below the peak values shown in Figure 4.8(a), but are of the same order as the simulated velocities after the initial peak.

A more precise comparison to the experiments of Herzhaft & Guazzelli [84] is shown in Figure 4.9, which compares the distributions of the vertical and horizontal velocity components from our simulations with the experimental measurements at $\phi \approx 0.26$ %. Because no steady state is observed as noted previously, the velocity distribution evolves with time. The choice of a specific time to calculate the distributions is therefore *ad hoc*; Figure 4.9(a) shows the distribution measured after the initial velocity peak, when the initial box-dependent streamer has started to decay and when the concentration fluctuations have had time to develop. The two distributions show very good qualitative and quantitative agreement. As already mentioned the mean sedimentation speed and variance are very slightly overestimated in the simulations. However it should be emphasized that the agreement with the experimental results is significantly better than that obtained in Chapter 3 using periodic boundary conditions [32, 157] (cf. Figure 3.19), where a strong dependence on the system size and box aspect ratio was found, and where both the mean and variance of the vertical velocity were strongly overpredicted.

Figure 4.8(b) shows the evolution of the velocity fluctuations in the suspension. The fluctuations are found to be very strong shortly after the start of sedimentation (sensibly at
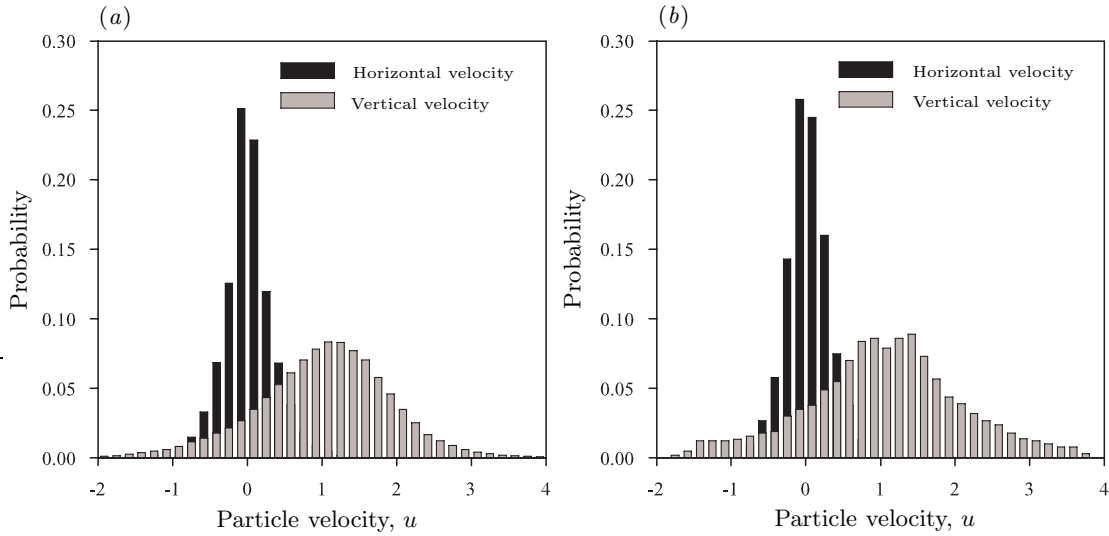
Figure 4.9: Velocity distributions obtained from: (a) simulations, and (b) the experiments of Herzhaft & Guazzelli [84]. The simulation results are for a suspension of 41,530 spheroids of aspect ratio $A = 11$ in a box of dimensions $L_x = 32$, $L_y = 12$, $L_z = 180$ (volume fraction $\phi = 0.26$ %); the distribution shown was obtained shortly after the peak of the mean velocity (cf. Figure 4.8). The experimental distribution of Herzhaft & Guazzelli was obtained in a suspension of cylindrical fibers of aspect ratio $A = 11 \pm 2$, at a volume fraction of $\phi = 0.26 \pm 0.01$ %.

the same time as the velocity peak), reaching values of up to four times the mean velocity for $\phi = 0.5$ %; very high values for the fluctuations had also been reported by Herzhaft & Guazzelli [84]. These fluctuations are partly caused by the strong initial flow at the center of the box, which is accompanied by an equally strong backflow near the walls. Shortly after reaching their maximum value the fluctuations are then observed to decay rapidly towards zero; again no steady state is observed. The steady decay of the fluctuations after the initial peak is similar to what is observed for spheres [138, 112, 186, 20, 132]. While in the case of spheres steady velocity fluctuations are reached in some cases, they have also been predicted to decay *ad infinitum* in suspensions in which stratification is significant [120, 131]. Stratification is very strong in anisotropic suspensions such as the ones of this study and therefore most likely plays a role in the damping of the velocity variance shown in Figure 4.8(b): this effect will studied further in Section 4.3.

Note that inaccuracies in the particle velocities and velocity fluctuations can be expected given our simulation method. Most importantly, the zero tangential stress boundary condition on the side walls differs significantly from the exact no-slip boundary condition for viscous flow, with possible consequences on the rate of decay of hydrodynamic interactions. This was pointed out by Brenner [28], who investigated the effects of side walls on fluctuations in sedimenting sphere suspensions and showed that the no-slip boundary condition results in a screening of interactions beyond a few wall separation distances. While enforcing the correct boundary condition on all container walls is difficult, we also implemented the Green's function of Mucha *et al.* [132] which satisfies no-slip on two of the side walls. The results, which are described in more detail in Appendix C, indeed show that tangential flow on the side walls leads to a systematic overestimation of the velocity fluctuations (as well as the mean velocity, albeit to a lesser extent). The velocity fluctuations in a real system are therefore likely to be quite weaker than those shown in Figure 4.8(b), which is indeed the case for the values reported by Herzhaft & Guazzelli [84]. Yet the qualitative behavior of the fluctuations (sharp increase followed by a steady decrease) is likely to be captured correctly. Other sources of inaccuracies may come from the substitution of a finite B-spline for the original point force at the center of the particles, which introduces an error by smoothing the velocity disturbance field at high wavenumbers, and from the point-force model that completely neglects higher force moments on the particles such as stresslets, which are responsible for the velocity hindrance observed in suspensions of spheres [13].

4.2.6 Orientation statistics

Figure 4.10(a) shows the time evolution of the mean-squared orientation $\langle p_z p_z \rangle$ in the direction of gravity, which is a measure of the degree of alignment of the suspension in the vertical direction. The initial value of 1/3 corresponds to the isotropic orientation distribution in the initial configuration. Immediately after the start of sedimentation $\langle p_z p_z \rangle$ sharply increases to reach a peak value of approximately 0.7, i.e. a very large number of spheroids quickly orient in the direction of gravity (Figure 4.10(b)). As already
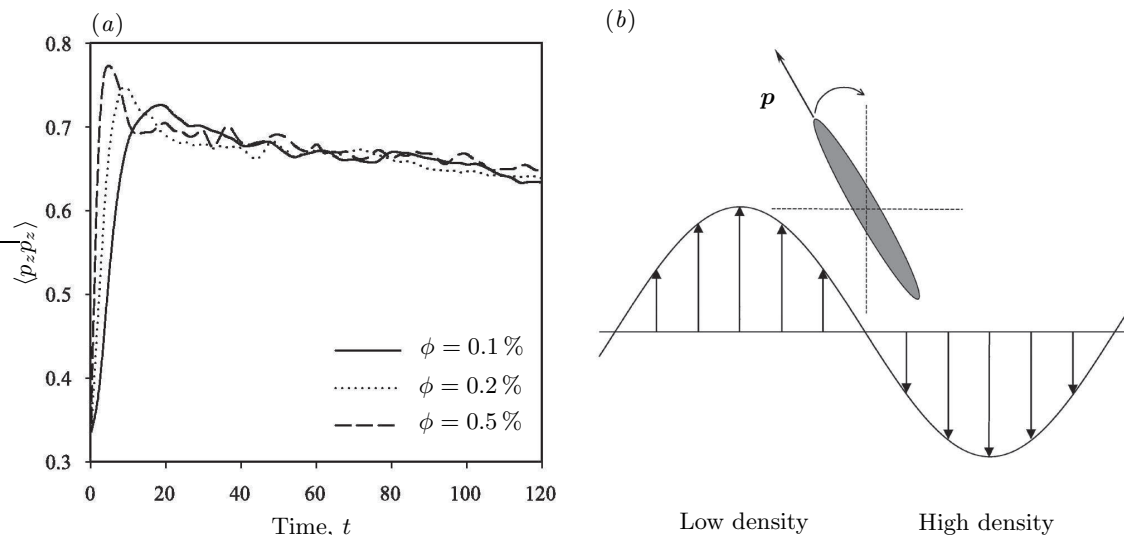
Figure 4.10: (a) Time evolution of the mean squared orientation in the direction of gravity $\langle p_z p_z \rangle$, at various volume fractions. The results are for spheroids of aspect ratio $A = 15$ in a box of dimensions $L_x = 32$, $L_y = 12$, $L_z = 180$. The results were obtained in a subsection of the box: $67.5 < z < 90$, and are averaged over ten simulations. (b) Diagram showing the mechanism for the orientation of a prolate spheroid along the vertical axis (after Koch & Shaqfeh [102]).

mentioned earlier, this is a consequence of the strong vertical shear between the streamer at the center of the box and the backflow near the walls. The fastest increase and the highest peak value are obtained in the more dense suspensions ($\phi = 0.5$ %), as a result of the stronger velocity fluctuations (Figure 4.8(b)). After the peak is reached, $\langle p_z p_z \rangle$ very slowly and steadily decreases as fluctuations decay; its value remains however above 0.6 for the remainder of the simulation, suggesting that the alignment remains strong. It is interesting to note that after the initial peak the value of $\langle p_z p_z \rangle$ is nearly the same for all volume fractions considered, even though the velocity fluctuations are typically stronger in more concentrated suspensions. This observation, however unexpected, was also made previously by Herzhaft & Guazzelli [84], who found that the orientation distributions from their experiments were nearly identical at all concentrations.

A typical distribution of the projected angle (i.e. the angle made by the projection of the orientation vector $\boldsymbol{p}$ onto the (x, z)-plane with respect to the x-direction) is shown in
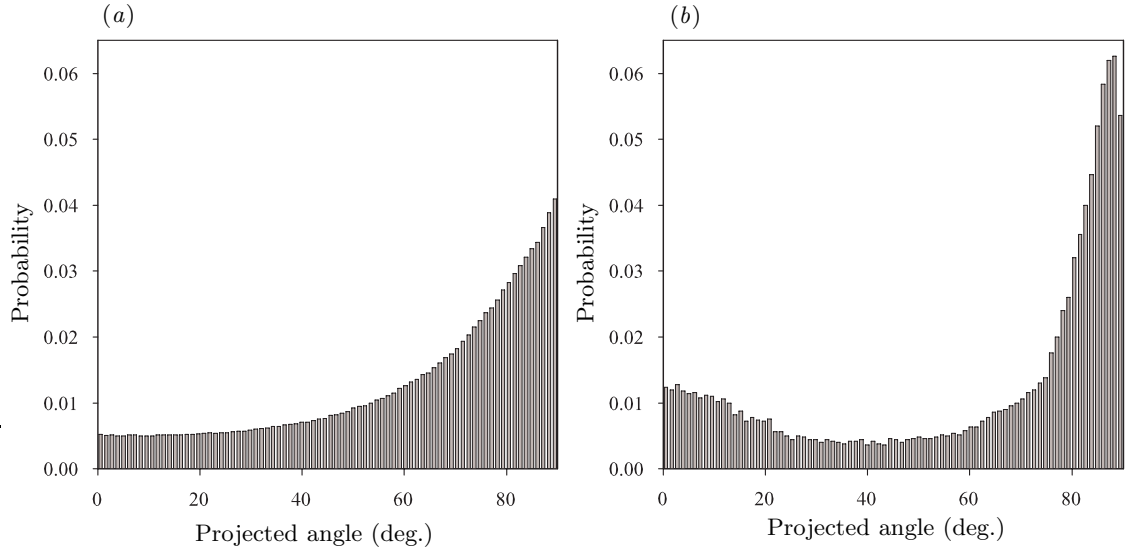
Figure 4.11: Distributions of the projected angle (angle of the projection of the orientation vector of the particles onto a vertical plane with respect to the horizontal) obtained from: (a) simulations, and (b) the experiments of Herzhaft & Guazzelli [84]. The simulation results are for a suspension of 41,530 spheroids of aspect ratio $A = 11$ in a box of dimensions $L_x = 32$, $L_y = 12$, $L_z = 180$ (volume fraction $\phi = 0.26$ %); the distribution shown was obtained shortly after the peak of the mean squared orientation $\langle p_z p_z \rangle$ (cf. Figure 4.10). The experimental distribution of Herzhaft & Guazzelli was obtained in a suspension of cylindrical fibers of aspect ratio $A = 11 \pm 2$, at a volume fraction of $\phi = 0.26 \pm 0.01$ %.

Figure 4.11 and compared to the experimental distribution of Herzhaft & Guazzelli [84]. The strong peak near 90° confirms the vertical alignment of many of the particles in the suspension. While the agreement between the two distributions is qualitatively fair, the peak is slightly underestimated in the simulations. Also the experimental distribution presents a second peak near zero (corresponding to a horizontal alignment), whose origin is not clear and which is not captured in the simulations. Close particle interactions, which are completely neglected in our simulations, may slightly influence the shape of the distribution: the strong entanglements inside the clusters due to excluded volume may indeed have an effect on the orientation of the particles. Yet the second minimum in the experimental distribution must have another origin, as it was not reproduced either in the previous simulations by Butler & Shaqfeh [32] and in the simulations of Chapter 3 (Figure 3.17 and Reference [157]). These also underpredicted the height of the main peak
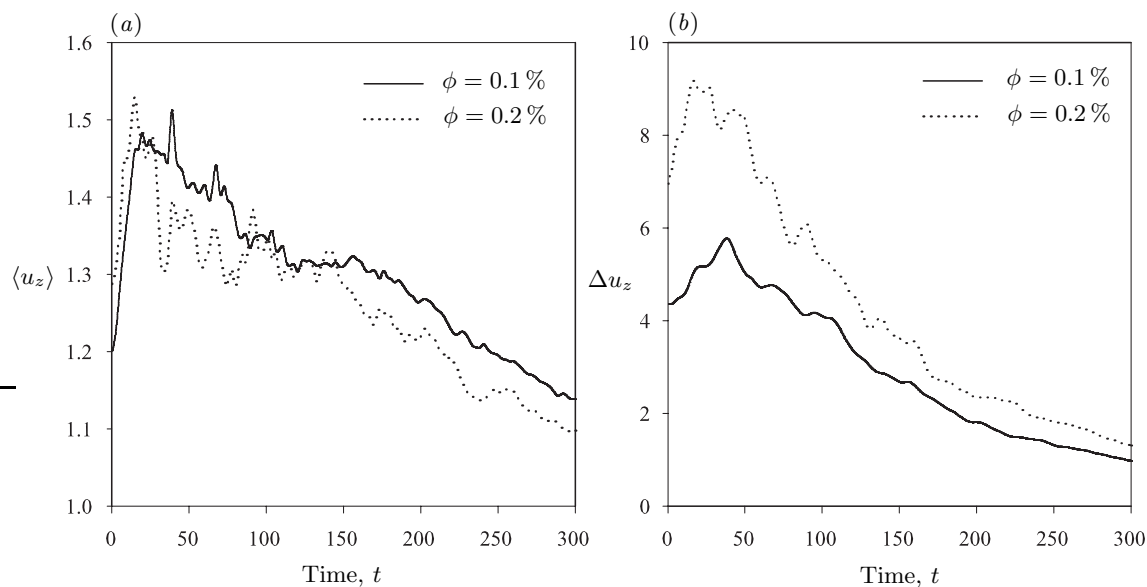
Figure 4.12: (*a*) Mean sedimentation velocity $\langle u_z \rangle$, and (*b*) velocity fluctuations Δu_z in the z-direction at various volume fractions. The results are for oblate spheroids of aspect ratio $A = 0.3$ in a box of dimensions $L_x = 130$, $L_y = 40$, $L_z = 750$. The results were obtained in a subsection of the box: $187 < z < 281$, and are averaged over ten runs.

in most cases. The present simulations offer the improvement that the distribution does not significantly depend on the size or the aspect ratio of the sedimenting system. Future work should focus on including close interactions such as excluded volume with the hope of obtaining a more quantitative agreement with the experimental orientation distributions.

4.2.7   Oblate particles

The previous discussion has focused entirely on prolate spheroids ($A > 1$), for which experimental data are available. The case of oblate spheroids ($A < 1$), or disk-shaped particles, has received less attention in the past in spite of its common occurrence in environmental fluid mechanics for instance, where the sedimentation of clay is a relevant example. To our knowledge, the concentration instability has never been studied either experimentally or numerically for oblate particles since its theoretical prediction by Koch & Shaqfeh [102].
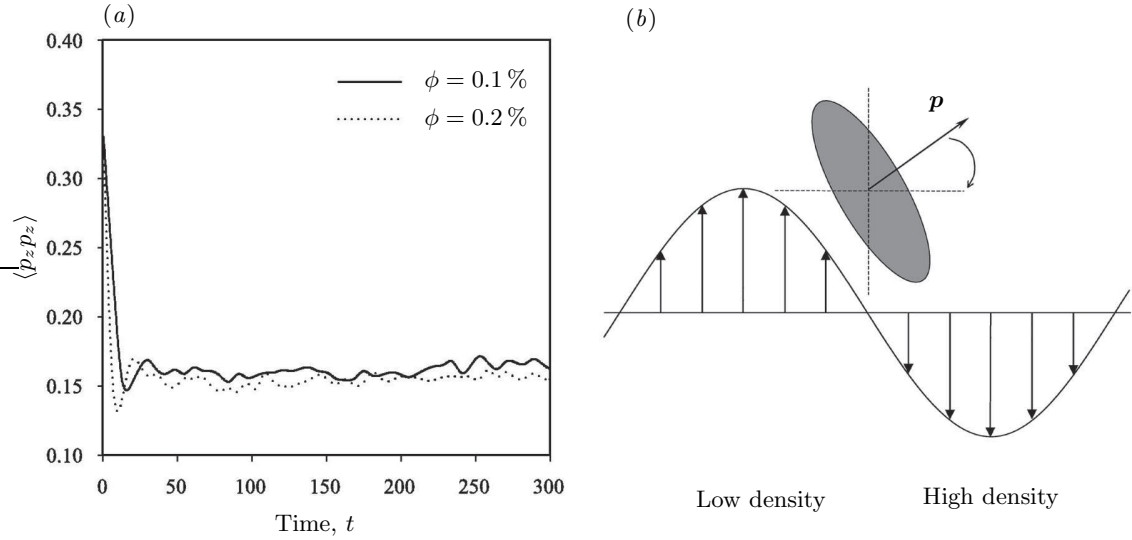
Figure 4.13: (a) Time evolution of the mean squared orientation in the direction of gravity $\langle p_z p_z \rangle$, at various volume fractions. The results are for oblate spheroids of aspect ratio $A = 0.3$ in a box of dimensions $L_x = 130$, $L_y = 40$, $L_z = 750$. The results were obtained in a subsection of the box: $94 < z < 187$, and are averaged over ten runs. (b) Diagram showing the mechanism for the orientation dynamics: in the case of oblate spheroids the orientation vector $\boldsymbol{p}$ aligns in a horizontal direction (after Koch & Shaqfeh [102]).

Simulations were run for oblate spheroids of aspect ratio $A = 0.3$ at various volume fractions. The results were found to be qualitatively similar to those discussed above for prolate particles, and only the main differences are summarized here. As in the case of prolate particles inhomogeneities are observed to develop in the suspension. This clustering is again accompanied by an enhancement of the mean sedimentation rate. Figure 4.12(a) shows the evolution of the mean velocity in the suspension at two different volume fractions. The velocities are scaled by the sedimentation velocity of a particle whose major axis points in the vertical direction (the slowest configuration for an oblate spheroid), hence a lower bound of 1 for the velocity. Starting from a value between 1.2 and 1.3 (compared to the expected value of 1.12 for spheroids of aspect ratio $A = 0.3$ at infinite dilution), the sedimentation velocity quickly increases and reaches a peak value around 1.6 at both $\phi = 0.1$ % and 0.2 %, which corresponds to an enhancement over the maximum

possible sedimentation velocity for an isolated spheroid, and is therefore mainly a consequence of clustering. Figure 4.12(b) shows the corresponding velocity fluctuations, which are found to be about twice as strong as in the prolate case at the same concentrations (Figure 4.8(b)). This can be explained as follows: oblate particles have a weaker mobility (because of their larger surface to volume ratio). At equivalent volume fraction they create the same fluctuations as prolate particles but sediment more slowly; when scaled by the mean sedimentation speed the fluctuations therefore appear much stronger. Note again that these fluctuations are also likely to be overestimated as a result of the zero tangential stress boundary condition at the side walls.

Interestingly the enhancement of the velocity (Figure 4.8(a)), as well as the concentration fluctuations (not shown), are found to be somewhat weaker than in the prolate case. A possible explanation is that the very strong velocity fluctuations observed above cause a more rapid alignment of the particles in the disturbance flow, which then hinders their lateral migration. Another likely reason is that the fluctuations result in more mixing, which limits the growth of the inhomogeneities. The strong alignment of the particles is illustrated in Figure 4.13(a), which shows the mean-squared orientation $\langle p_z p_z \rangle$ in the direction of gravity. Note that in the case of oblate particles the alignment occurs in such a way that the orientation vector $\boldsymbol{p}$ of the major axis points in a horizontal direction (Figure 4.13(b)). As shown in Figure 4.13(a) the mean orientation very quickly reaches a steady state, and remains constant until the arrival of the suspension front.

4.3   The effect of stratification on wavenumber selection

4.3.1   Introduction

The simulations described in Section 4.2 have demonstrated the existence of a wavenumber selection in finite containers for the concentration instability. More precisely, we found that unlike in periodic boundary conditions, simulations of bounded systems capture a transition from a single box-dependent streamer to multiple structures at shorter wavelengths

(Figures 4.1, 4.2 and 4.5). Such an evolution was also recently reported in experiments by Metzger, Guazzelli & Butler [126, 127], who observed that the sedimentation in suspensions of rigid fibers is initially characterized by the formation of one large-scale streamer spanning half of the container width, followed by a transition to multiple streamers and backflow regions alternating in the horizontal direction. The precise origin of such a transition, which is not predicted by the original stability analysis of Koch & Shaqfeh [102], however still remains unclear: while our simulations clearly showed that the transition only occurs in the presence of walls, the mechanism for the breakup of the initial large-scale streamer has not been elucidated. Based on the previous work on sphere suspensions reviewed in Section 4.1, several hypotheses can be formulated: the recirculation currents taking place as a result of the horizontal container boundaries may homogenize the suspension over large length scales, leading to the suppression of the fluctuations below a finite wavenumber; in addition, the strong stratification that is shown to develop in the suspensions (Figure 4.3) may have an effect on the instability by damping the velocity fluctuations.

The effects of stratification on the velocity fluctuations in suspensions of sedimenting spheres have been considered in a few studies [120, 186, 20, 132]. Luke [120] first suggested that a stable vertical density gradient should lead to a decay of the velocity fluctuations over time: the physical argument that he proposed is that density fluctuations settle rapidly toward their equilibrium position, after which they no longer contribute to the variance of the velocity. According to Luke [120], this mechanism should result in a decay of the velocity variance as $t^{-1/2}$, precluding the existence of a steady state. This original idea was then reexamined by Brenner and coworkers [186, 132], who argued that density fluctuations in a suspension are simultaneously damped by stratification and generated by random fluctuations in the particle motions; by balancing the effects of stratification and hydrodynamic dispersion, they were therefore able to derive a scaling for the velocity fluctuations, in good accord with results from their experiments and numerical simulations. Although there appears to be a consensus on the damping effect of a stable vertical density gradient on the fluctuations, the presence and the origin of stratification in sphere

suspensions are still debated [20, 135].

In the following sections, we examine the relationship between stratification and the concentration instability, with the aim of elucidating the wavenumber selection process observed experimentally [126, 127] and in the simulations of Section 4.2. First we revisit the linear stability analysis of Koch & Shaqfeh [102] in Section 4.3.2 in the case of a stably stratified suspension, where we also account for center-of-mass hydrodynamic dispersion. We show that stratification can provide a mechanism for wavenumber selection, and a scaling for the most unstable mode is derived in Section 4.3.3. This scaling is then tested in Section 4.3.4 against simulation results for both stratified and initially well-mixed suspensions.

4.3.2 Linear stability analysis

Governing equations

Following Koch & Shaqfeh [102], we describe a dilute suspension of spheroids using a continuous variable $c(\boldsymbol{x}, \boldsymbol{p})$ denoting the concentration of particles at location $\boldsymbol{x}$ with orientation $\boldsymbol{p}$. Particle conservation requires the following convective-diffusion equation to apply:

$$\frac{\partial c}{\partial t} + \boldsymbol{\nabla_p} \cdot (\dot{\boldsymbol{p}}c) + \boldsymbol{\nabla_x} \cdot (\dot{\boldsymbol{x}}c) - \boldsymbol{\nabla_x} \cdot (\mathbf{D} \cdot \boldsymbol{\nabla_x}c) = 0. \tag{4.19}$$

In addition to the convective terms previously considered by Koch & Shaqfeh, we also account for center-of-mass hydrodynamic dispersion through the diffusion tensor $\mathbf{D}$. We shall assume that the diffusion tensor does not depend on the particle orientations, but takes on the following anisotropic form: $\mathbf{D} = D_{\parallel}\hat{\boldsymbol{z}}\hat{\boldsymbol{z}} + D_{\perp}(\mathbf{I} - \hat{\boldsymbol{z}}\hat{\boldsymbol{z}})$, where $\hat{\boldsymbol{z}}$ is a unit vector in the vertical direction. Note that in a real system, rotational dispersion is also expected to occur: for simplicity this effect will be neglected here.

The convective fluxes in Equation (4.19) involve the linear and angular velocities of a particle. As in the simulations of Section 4.2, we make the dilute assumption and write the linear velocity $\dot{\boldsymbol{x}}$ as the sum of the sedimentation velocity for a given orientation $\boldsymbol{p}$ and of the bulk disturbance velocity at position $\boldsymbol{x}$:

$$\dot{\boldsymbol{x}} = \boldsymbol{U}_s(\boldsymbol{p}) + \boldsymbol{u}(\boldsymbol{x}). \tag{4.20}$$

For a spheroidal particle the sedimentation velocity is again obtained as:

$$\boldsymbol{U}_s(\boldsymbol{p}) = (\lambda_0 \mathsf{I} + \lambda_1 \boldsymbol{p}\boldsymbol{p}) \cdot \boldsymbol{F}. \tag{4.21}$$

where $\boldsymbol{F}$ is the net gravity force acting on a given particle $\boldsymbol{F} = -F\hat{\boldsymbol{z}} = -\Delta\rho V_p g\hat{\boldsymbol{z}}$. The disturbance fluid velocity $\boldsymbol{u}$ appearing in Equation (4.20) is driven by the density fluctuations in the suspension, and to leading order satisfies the Stokes equations including a body force proportional to the local concentration:

$$-\mu\nabla^2\boldsymbol{u} + \boldsymbol{\nabla}p = \boldsymbol{F}\int c(\boldsymbol{x},\boldsymbol{p})\mathrm{d}\boldsymbol{p}, \quad \boldsymbol{\nabla}\cdot\boldsymbol{u} = 0. \tag{4.22}$$

Finally, the angular velocity $\dot{\boldsymbol{p}}$ of a spheroid is induced by the local disturbance flow in the fluid, and in the dilute limit is captured using Jeffery's equation [93]:

$$\dot{\boldsymbol{p}} = (\mathsf{I} - \boldsymbol{p}\boldsymbol{p}) \cdot [\gamma\mathsf{E}(\boldsymbol{x}) + \boldsymbol{\Omega}(\boldsymbol{x})] \cdot \boldsymbol{p}, \tag{4.23}$$

where $\mathsf{E}(\boldsymbol{x}) = \left[\boldsymbol{\nabla}\boldsymbol{u}(\boldsymbol{x}) + \boldsymbol{\nabla}\boldsymbol{u}(\boldsymbol{x})^T\right]/2$ and $\boldsymbol{\Omega}(\boldsymbol{x}) = \left[\boldsymbol{\nabla}\boldsymbol{u}(\boldsymbol{x}) - \boldsymbol{\nabla}\boldsymbol{u}(\boldsymbol{x})^T\right]/2$ are the local disturbance rate of strain and rate of rotation tensors, respectively, and where we use the notation γ for Jeffery's parameter: $\gamma \equiv (A^2 - 1)/(A^2 + 1)$.

Base state and linearized equations

To extend the results of Koch & Shaqfeh [102], who only considered density fluctuations with respect to a uniform distribution of isotropically oriented particles, we now allow for a vertical density gradient in the background concentration. More precisely, we assume that the density field in the base state is linearly stratified. At $t = 0$:

$$c(\boldsymbol{x},\boldsymbol{p},0) = n\Psi(\boldsymbol{p})(1 - \beta z), \tag{4.24}$$

where n denotes the mean number density. In particular, we also allow for an anisotropic orientation distribution $\Psi(\boldsymbol{p})$ in the base state; the isotropic case is easily recovered by

setting $\Psi(\boldsymbol{p}) = (4\pi)^{-1}$. In the following discussion we shall only consider stably stratified suspensions, for which $\beta \geq 0$. Substitution of Equation (4.24) into the Stokes equations (4.22) shows that the density gradient is balanced by a pressure gradient $\boldsymbol{\nabla} p = -Fn(1 - \beta z)\hat{\boldsymbol{z}}$, and does not induce a mean flow. Therefore in the base state the velocity and pressure fields in the suspension are given by: $\boldsymbol{u}(\boldsymbol{x}) = \boldsymbol{0}$, and $p(\boldsymbol{x}) = p_0 - F(z - \beta z^2/2)$. The stratified density field is advected downwards as follows:

$$c(\boldsymbol{x}, \boldsymbol{p}, t) = n\Psi(\boldsymbol{p}) \left[1 - \beta\left(z - \hat{\boldsymbol{z}} \cdot \boldsymbol{U}_s(\boldsymbol{p})t\right)\right], \tag{4.25}$$

which is an exact solution of the conservation equation (4.19). Note in particular that because particles with different orientations sediment at different speeds, the orientation distribution at a given vertical station will evolve in time.

To investigate the stability of the suspension, we consider a weak perturbation with respect to the base state:

$$c(\boldsymbol{x}, \boldsymbol{p}, t) = n\Psi(\boldsymbol{p}) \left[1 - \beta\left(z - \hat{\boldsymbol{z}} \cdot \boldsymbol{U}_s(\boldsymbol{p})t\right)\right] + \epsilon c'(\boldsymbol{x}, \boldsymbol{p}, t), \tag{4.26}$$

where $|\epsilon| \ll 1$ and $|c'(\boldsymbol{x}, \boldsymbol{p}, t)| \sim O(n/4\pi)$. This perturbation induces a weak disturbance flow: $\boldsymbol{u}(\boldsymbol{x}) = \epsilon\boldsymbol{u}'(\boldsymbol{x})$ (with an associated pressure perturbation $p = \epsilon p'$), which in turn causes the rotation of the particles at the angular velocity $\dot{\boldsymbol{p}} = \epsilon\dot{\boldsymbol{p}}'$. Substituting the perturbed density field Equation (4.26) into the conservation equation (4.19), and identifying terms of order ϵ yields the following linearized equation for the density fluctuations:

$$
\begin{aligned}
\frac{\partial c'}{\partial t} \quad &+ \quad n\Psi(\boldsymbol{p})\left[1 - \beta\left(z - \hat{\boldsymbol{z}} \cdot \boldsymbol{U}_s(\boldsymbol{p})t\right)\right]\boldsymbol{\nabla_p} \cdot \dot{\boldsymbol{p}}' + n\dot{\boldsymbol{p}}' \cdot \boldsymbol{\nabla_p}\left\{\Psi(\boldsymbol{p})\left[1 - \beta\left(z - \hat{\boldsymbol{z}} \cdot \boldsymbol{U}_s(\boldsymbol{p})t\right)\right]\right\} \\
&+ \quad \boldsymbol{U}_s \cdot \boldsymbol{\nabla_x} c' - \beta n\Psi(\boldsymbol{p})\hat{\boldsymbol{z}} \cdot \boldsymbol{u}' - \boldsymbol{\nabla_x} \cdot \left(\mathbf{D} \cdot \boldsymbol{\nabla_x} c'\right) = 0, \tag{4.27}
\end{aligned}
$$

where we made use of the incompressibility condition $\boldsymbol{\nabla} \cdot \boldsymbol{u}' = 0$. In Equation (4.27) the disturbance velocity field $\boldsymbol{u}'$ and angular velocity $\dot{\boldsymbol{p}}'$ still satisfy Equations (4.22) and (4.23), respectively, with primed variables. Note in particular that the coefficients in Equation (4.27) are time-dependent, which is a consequence of having a time-dependent base

state (Equation (4.25)). In general such a stability problem could be solved using Floquet theory [51]. Here we limit ourselves to the case of short times and weak density gradients, i.e. we restrict our analysis to length and time scales that satisfy the following condition: $|z - \hat{\boldsymbol{z}} \cdot \boldsymbol{U}_s(\boldsymbol{p})t| \ll \beta^{-1}$. In particular, the characteristic wavelength of the instability should remain smaller than the stratification length scale β^{-1}, and our results will only be valid over time scales shorter than the characteristic time $(\beta\lambda_0 F)^{-1}$ for a particle to sediment over the stratification length β^{-1}. As we shall see in the numerical simulations of Section 4.3.4, the stratification length β^{-1} in the bulk of the suspensions typically remains of the order of the height of the simulation box or larger (except near the very end of the simulations), in which case both conditions are indeed satisfied. Under these assumptions, the linearized conservation equation simplifies to the following equation, in which the coefficients no longer depend on time:

$$\frac{\partial c'}{\partial t} + n\Psi(\boldsymbol{p})\boldsymbol{\nabla_p}\cdot\dot{\boldsymbol{p}}' + n\dot{\boldsymbol{p}}'\cdot\boldsymbol{\nabla_p}\Psi(\boldsymbol{p}) + \boldsymbol{U}_s\cdot\boldsymbol{\nabla_x}c' - \beta n\Psi(\boldsymbol{p})\hat{\boldsymbol{z}}\cdot\boldsymbol{u}' - \boldsymbol{\nabla_x}\cdot\left(\mathbf{D}\cdot\boldsymbol{\nabla_x}c'\right) = 0. \quad (4.28)$$

Dispersion relation

To achieve analytical progress, we consider the evolution of a density perturbation written as a plane wave of wavevector $\boldsymbol{k}$ and complex frequency $\omega \equiv \omega_{\mathrm{R}} + \mathrm{i}\omega_{\mathrm{I}}$:

$$c'(\boldsymbol{x}, \boldsymbol{p}) = \tilde{c}(\boldsymbol{k}, \boldsymbol{p}, \omega)\exp\mathrm{i}\left(\boldsymbol{k}\cdot\boldsymbol{x} - \omega t\right). \quad (4.29)$$

We wish to determine the dispersion relation $\omega(\boldsymbol{k})$ allowing for such modes to satisfy the linearized conservation equation (4.28), and more specifically to identify the wavevectors $\boldsymbol{k}$ leading to positive growth rates, i.e. positive values of the imaginary part ω_{I} of the frequency.

By linearity of the Stokes equations (4.22), the disturbance velocity induced by the density perturbation Equation (4.29) can also be written as a plane wave of the same wavevector and frequency: $\boldsymbol{u}'(\boldsymbol{x}) = \tilde{\boldsymbol{u}}(\boldsymbol{k}, \omega)\exp\mathrm{i}\left(\boldsymbol{k}\cdot\boldsymbol{x} - \omega t\right)$, where the Fourier coefficient

$\tilde{\boldsymbol{u}}(\boldsymbol{k}, \omega)$ is obtained analytically as [81]:

$$\tilde{\boldsymbol{u}}(\boldsymbol{k}, \omega) = \frac{1}{\mu k^2} \left(\mathbf{I} - \hat{\boldsymbol{k}}\hat{\boldsymbol{k}} \right) \cdot \boldsymbol{F} \int \tilde{c}(\boldsymbol{k}, \boldsymbol{p}, \omega) \mathrm{d}\boldsymbol{p}, \qquad (4.30)$$

where we use the notation $\hat{\boldsymbol{k}} \equiv \boldsymbol{k}/|\boldsymbol{k}|$. Substituting this expression into Jeffery's equation (4.23) allows us to calculate the Fourier coefficient $\dot{\tilde{\boldsymbol{p}}}(\boldsymbol{k}, \boldsymbol{p}, \omega)$ of the angular velocity, as well as its orientational divergence:

$$\dot{\tilde{\boldsymbol{p}}}(\boldsymbol{k}, \boldsymbol{p}, \omega) = \frac{\mathrm{i}}{2\mu k^2} \left(\mathbf{I} - \boldsymbol{pp} \right) \cdot \left[(\gamma + 1)(\boldsymbol{p} \cdot \boldsymbol{k})\mathbf{I} + (\gamma - 1)\boldsymbol{kp} \right] \cdot \left(\mathbf{I} - \hat{\boldsymbol{k}}\hat{\boldsymbol{k}} \right) \cdot \boldsymbol{F} \int \tilde{c} \mathrm{d}\boldsymbol{p}, \quad (4.31)$$

$$\boldsymbol{\nabla}_{\boldsymbol{p}} \cdot \dot{\tilde{\boldsymbol{p}}}(\boldsymbol{k}, \boldsymbol{p}, \omega) = -\frac{3\mathrm{i}\gamma}{\mu k^2} \left(\boldsymbol{p} \cdot \boldsymbol{k} \right) \boldsymbol{p} \cdot \left(\mathbf{I} - \hat{\boldsymbol{k}}\hat{\boldsymbol{k}} \right) \cdot \boldsymbol{F} \int \tilde{c} \mathrm{d}\boldsymbol{p}. \qquad (4.32)$$

Using Equations (4.29)–(4.32) for the Fourier coefficients of the concentration fluctuations, disturbance velocity, and angular velocity, we find that the linearized conservation equation (4.28) becomes:

$$(\mathrm{i}\boldsymbol{k} \cdot \boldsymbol{U}_s - \mathrm{i}\omega + \boldsymbol{k} \cdot \mathbf{D} \cdot \boldsymbol{k}) \, \tilde{c} - \frac{n\Psi(\boldsymbol{p})}{\mu k^2} \left[\beta\hat{\boldsymbol{z}} + 3\mathrm{i}\gamma \left(\boldsymbol{p} \cdot \boldsymbol{k} \right) \boldsymbol{p} \right] \cdot \left(\mathbf{I} - \hat{\boldsymbol{k}}\hat{\boldsymbol{k}} \right) \cdot \boldsymbol{F} \int \tilde{c} \mathrm{d}\boldsymbol{p}$$

$$+\frac{\mathrm{i}n}{2\mu k^2} \boldsymbol{\nabla}_{\boldsymbol{p}} \Psi(\boldsymbol{p}) \cdot (\mathbf{I} - \boldsymbol{pp}) \cdot \left[(\gamma + 1)(\boldsymbol{p} \cdot \boldsymbol{k})\mathbf{I} + (\gamma - 1)\boldsymbol{kp} \right] \cdot \left(\mathbf{I} - \hat{\boldsymbol{k}}\hat{\boldsymbol{k}} \right) \cdot \boldsymbol{F} \int \tilde{c} \mathrm{d}\boldsymbol{p} = 0.$$

$$(4.33)$$

Following Koch & Shaqfeh [102], we divide Equation (4.33) by $(\mathrm{i}\boldsymbol{k} \cdot \boldsymbol{U}_s - \mathrm{i}\omega + \boldsymbol{k} \cdot \mathbf{D} \cdot \boldsymbol{k})$ and integrate over orientation space. We also introduce the following dimensionless variables:

$$\boldsymbol{k}^* = \boldsymbol{k} \left(\frac{\mu\lambda_1}{n} \right)^{1/2}, \quad \omega^* = \omega \left(\frac{\mu}{n\lambda_1 F^2} \right)^{1/2}, \quad \lambda = \frac{\lambda_0}{\lambda_1},$$

$$\beta^* = \beta \left(\frac{\mu\lambda_1}{n} \right)^{1/2}, \quad \mathbf{D}^* = \mathbf{D} \left(\frac{n}{\mu\lambda_1^3 F^2} \right)^{1/2}. \qquad (4.34)$$

After simplifications, we arrive at the following dimensionless dispersion relation, which is

an equation for $\omega^*(\boldsymbol{k}^*)$:

$$1 + \frac{1}{k^{*2}} \int \Psi(\boldsymbol{p}) \left[\frac{\beta^* \hat{\boldsymbol{z}} + 3\mathrm{i}\gamma \left(\boldsymbol{p} \cdot \boldsymbol{k}^*\right) \boldsymbol{p}}{\mathrm{i}\boldsymbol{k}^* \cdot \boldsymbol{U}_s^* - \mathrm{i}\omega^* + \boldsymbol{k}^* \cdot \mathbf{D}^* \cdot \boldsymbol{k}^*} \right] \cdot \left(\mathbf{I} - \hat{\boldsymbol{k}}\hat{\boldsymbol{k}} \right) \cdot \hat{\boldsymbol{z}} \mathrm{d}\boldsymbol{p} \qquad (4.35)$$

$$-\frac{\mathrm{i}}{2k^{*2}} \int \boldsymbol{\nabla}_{\boldsymbol{p}} \Psi(\boldsymbol{p}) \cdot (\mathbf{I} - \boldsymbol{pp}) \cdot \left[\frac{(\gamma+1)(\boldsymbol{p} \cdot \boldsymbol{k}^*)\mathbf{I} + (\gamma-1)\boldsymbol{k^*p}^*}{\mathrm{i}\boldsymbol{k}^* \cdot \boldsymbol{U}_s^* - \mathrm{i}\omega^* + \boldsymbol{k}^* \cdot \mathbf{D}^* \cdot \boldsymbol{k}} \right] \cdot \left(\mathbf{I} - \hat{\boldsymbol{k}}\hat{\boldsymbol{k}} \right) \cdot \hat{\boldsymbol{z}} \mathrm{d}\boldsymbol{p} = 0,$$

where the dimensionless sedimentation velocity is given by: $\boldsymbol{U}_s^*(\boldsymbol{p}) = -(\lambda\mathbf{I} + \boldsymbol{pp}) \cdot \hat{\boldsymbol{z}}$. The original dispersion relation of Koch & Shaqfeh [102] can be recovered by neglecting stratification and center-of-mass dispersion ($\beta^* = 0$ and $\mathbf{D}^* = \mathbf{0}$), and by considering the case of an isotropic orientation distribution: $\Psi(\boldsymbol{p}) = (4\pi)^{-1}$.

A general solution of Equation (4.35) is not easily obtained. In the present work we limit our discussion to the case of horizontal waves, for which $\boldsymbol{k} \cdot \hat{\boldsymbol{z}} = 0$. These waves were indeed shown by Koch & Shaqfeh to be the most unstable in the isotropic homogeneous case [102]. We first investigate the case of isotropic suspensions, for which the dispersion relation greatly simplifies, and then discuss the effect of an anisotropic orientation distribution.

Isotropic case

In the case of a horizontal wave with an isotropic orientation distribution, the dispersion relation Equation (4.35) simplifies as follows:

$$1 + \frac{1}{4\pi k^{*2}} \int \left[\frac{\mathrm{i}\beta^* - 3\gamma \left(\boldsymbol{p} \cdot \boldsymbol{k}^*\right) \left(\boldsymbol{p} \cdot \hat{\boldsymbol{z}}\right)}{\left(\boldsymbol{p} \cdot \boldsymbol{k}^*\right) \left(\boldsymbol{p} \cdot \hat{\boldsymbol{z}}\right) + \omega^* + \mathrm{i}k^{*2}D_\perp^*} \right] \mathrm{d}\boldsymbol{p} = 0. \qquad (4.36)$$

We expect the complex frequency ω^* to be pure imaginary: solutions with $\omega_\mathrm{R}^* > 0$ would indeed correspond to traveling or standing waves in the direction of $\boldsymbol{k}^*$, which are not physical when $\boldsymbol{k}^*$ points in the horizontal direction. We therefore look for solutions written as $\omega^* = \mathrm{i}\omega_\mathrm{I}^*$, and solve Equation (4.36) numerically using quadrature and a bisection algorithm. Figure 4.14 shows the calculated normalized growth rate (or imaginary part ω_I^* of the complex frequency) for the most unstable modes at the given value of $D_\perp^* = 0.02$ and for various values of β^*. In the absence of stratification ($\beta^* = 0$), the growth rate
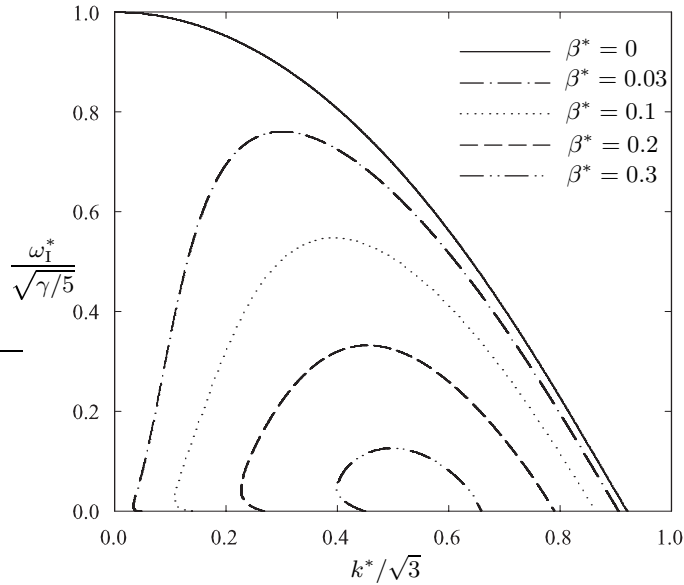
Figure 4.14: Growth rate (imaginary part ω_I^* of the complex frequency) as a function of wavenumber for a horizontal wave ($\boldsymbol{k} \cdot \hat{\boldsymbol{z}} = 0$), and for a dimensionless center-of-mass diffusivity of $D_\perp^* = 0.02$. The various curves corresponds to different levels of stratification. The growth rates were computed by numerical solution of the dispersion relation Equation (4.36) using a bisection algorithm.

is found to be greatest at zero wavenumber. This is analogous to the result of Koch & Shaqfeh [102], with the difference that center-of-mass dispersion now causes a more rapid decay of the growth rate at high wavenumbers. A similar stabilizing effect from center-of-mass dispersion will be observed in Chapter 5 in the case of sedimenting deformable particles [159]. Adding stratification ($\beta^* > 0$) however results in a qualitatively different picture: the shortest wavenumbers ($k^* \gtrsim 0$) are stabilized, and a maximum growth rate is observed at a finite positive wavenumber. As stratification becomes stronger, i.e. as β^* increases, the most unstable wavenumber increases while the maximum growth rate decreases. Beyond a certain level of stratification the instability is suppressed. As seen in Figure 4.14, some values of k^* yield two pure imaginary roots for ω^*, in which case the largest growth rate is expected to dominate.

The effects of stratification and center-of-mass dispersion on the stability are illustrated in more detail in Figure 4.15, showing the range of unstable wavenumbers as a function of
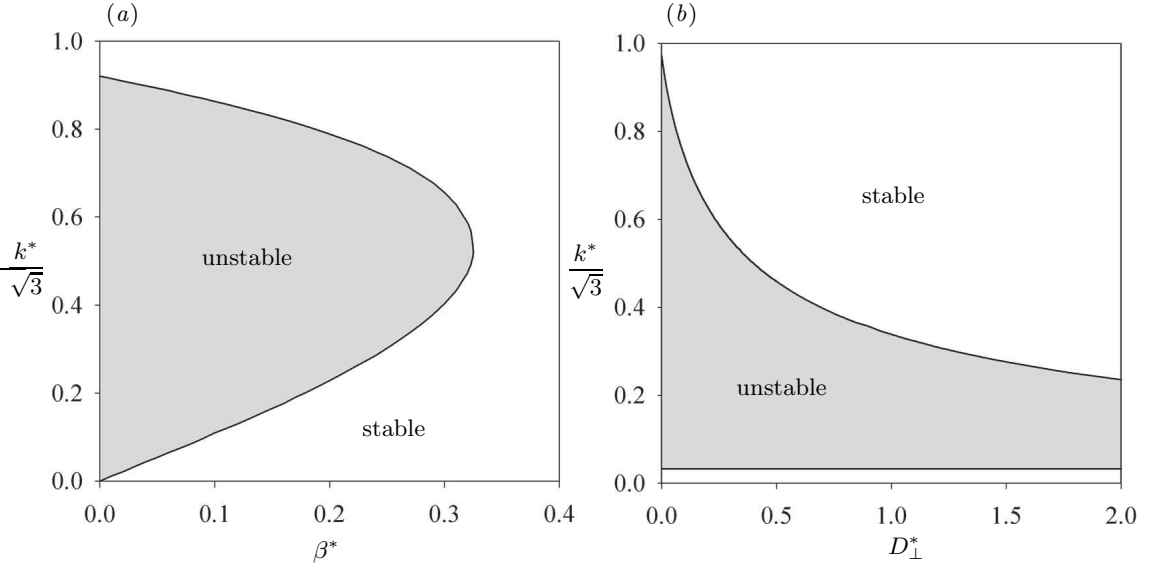
Figure 4.15: Range of unstable wavenumbers as a function of (a) the stratification parameter β^* (for a constant dispersion coefficient of $D_\perp^* = 0.02$), and of (b) the dispersion coefficient $D_\perp^*$ (for a stratification parameter of $\beta^* = 0.03$).

β^* and $D_\perp^*$. Figure 4.15(a) confirms the stabilizing effect of stratification: as β^* increases the range of unstable wavenumbers shrinks. Beyond $\beta^* \approx 0.32$ all wavenumbers become stable, where this value of β^* depends on the value chosen for the dispersion coefficient $D_\perp^*$. In addition, a stronger center-of-mass dispersion is also shown to reduce the range of unstable wavenumbers (Figure 4.15(b)). Dispersion however predominantly affects high wavenumbers, and is less efficient than stratification at suppressing the instability.

Additional insight can be gained into the respective leading-order effects of stratification and dispersion by seeking perturbation solutions in the limit of long waves ($k^* \ll 1$). When stratification is present ($\beta^* > 0$), the leading terms in an expansion of the dispersion relation Equation (4.36) for small $|\boldsymbol{k}^*|$ are found to be:

$$\omega^* + \mathrm{i}\frac{\beta^*}{k^{*2}} + O(1/k^*) = 0, \tag{4.37}$$

hence the growth rate: $\omega_\mathrm{I}^* = -\beta^*/k^{*2} + O(1/k^*)$. The main effect of stratification is therefore to damp the fluctuations at low wavenumbers (or long wavelengths), in agreement

with the numerical solution shown in Figure 4.14.

On the other hand, in the absence of stratification ($\beta^* = 0$), we find that expanding Equation (4.36) in the limit of small $|\boldsymbol{k}^*|$ yields the following algebraic equation:

$$\omega^{*4} + \frac{\gamma}{5}\omega^{*2} - \mathrm{i}\frac{2\gamma D_\perp^*}{5}k^{*2}\omega^* + \frac{\gamma}{35}k^{*2} + O(k^{*3}) = 0. \tag{4.38}$$

A solution of Equation (4.38) is obtained as a perturbation expansion: $\omega^* = \omega_0 + \omega_1 k^* + \omega_2 k^{*2} + O(k^{*3})$. After manipulation, the growth rate or imaginary part of the complex frequency is found as:

$$\omega_\mathrm{I}^* = \pm\left(\frac{\gamma}{5}\right)^{1/2} - k^{*2}\left[D_\perp^* \pm \frac{1}{70}\left(\frac{5}{\gamma}\right)^{3/2}\right] + O(k^{*3}). \tag{4.39}$$

The leading-order effect of center-of-mass dispersion on the concentration fluctuations is to damp the growth rate at high wavenumbers as $-k^{*2}D_\perp^*$. A similar effect will be found in Section 5.2 in the case of sedimenting deformable particles. However, center-of-mass dispersion is not the only mechanism resulting in damping at high wavenumbers: even in the absence of dispersion, ω_I^* decays with k^* in agreement with the original stability analysis of Koch & Shaqfeh [102]. One should also note that the two scalings for the leading-order effects of stratification ($\omega_\mathrm{I}^* \sim -\beta^*/k^{*2}$) and of diffusion ($\omega_\mathrm{I}^* \sim -D_\perp^* k^{*2}$), which were obtained here in the limit of $k^* \ll 1$, are in fact valid for arbitrary k^* as can easily be shown from the linearized conservation equation (4.33): this will justify the use of these expressions in Section 4.3.3 when deriving a scaling for the most unstable mode in a stratified suspension.

Anisotropic case

Experiments [84] and numerical simulations [122, 32, 108, 157, 159, 187] (including those of Chapter 3 and Section 4.2.6) both show that sedimenting rods tend to align in the direction of gravity as a result of the vertical shear between the dense clusters and clarified regions. It is therefore useful to investigate how the instability is modified when the orientation distribution is anisotropic. Here, we limit ourselves to distributions that are axisymmetric

with respect to the direction of gravity, i.e. $\Psi(\boldsymbol{p}) = \Psi(\alpha)$ where $\alpha = \boldsymbol{p}\cdot\hat{\boldsymbol{z}}$. In that particular case, the gradient of Ψ appearing in the dispersion relation becomes:

$$\boldsymbol{\nabla}_{\boldsymbol{p}}\Psi(\boldsymbol{p}) = \frac{\mathrm{d}\Psi}{\mathrm{d}\alpha}\left(\mathsf{I} - \boldsymbol{p}\boldsymbol{p}\right)\cdot\hat{\boldsymbol{z}}, \tag{4.40}$$

which greatly simplifies the evaluation of the second integral in Equation (4.35). The dispersion relation Equation (4.35) was solved numerically for an Onsager orientation distribution [144], in which the degree of anisotropy is parameterized by a scalar m:

$$\Psi(\alpha) = \frac{m\cosh(m\alpha)}{4\pi\sinh(m)}, \tag{4.41}$$

The isotropic distribution is recovered when $m = 0$, while $m \to \infty$ corresponds to a fully aligned suspension. The solutions for the growth rates of horizontal waves for various values of m are shown in Figure 4.16. In Figure 4.16(a), both stratification and diffusion are neglected ($\beta^* = 0$, $D_{\perp}^* = 0$), which allows us to isolate the effects of anisotropy. In particular, we observe that anisotropy tends to reduce the growth rates at all wavelengths. This stabilizing effect is easily understood: vertically aligned rods have very weak horizontal velocities, which hinders their lateral migration and thereby reduces their ability to form clusters. Note that in very anisotropic suspensions ($m \geq 4.75$ approximately), the longest modes are no longer the most unstable, and a maximum growth rate appears at a finite wavenumber. This suggests that anisotropy could in principle result in a wavenumber selection: no such effect was however observed in simulations, where the orientation distribution quickly adjusts to the flow conditions. When both stratification and diffusion are present (Figure 4.16(b)), a wavenumber selection is expected for all values of m for the reasons discussed in Section 4.3.2, and the effect of particle alignment is to reduce the growth rates at all wavenumbers.

The largest unstable wavenumber in the absence of stratification and of diffusion can be obtained analytically by setting $\omega^* \equiv 0$ in Equation (4.35) and solving for k^*. The result is found to be:

$$k_{max}^* = \left[3\gamma + \int\left(\gamma\alpha + \frac{\gamma+1}{2\alpha}\right)\frac{\mathrm{d}\Psi}{\mathrm{d}\alpha}\mathrm{d}\boldsymbol{p}\right]^{1/2}, \tag{4.42}$$
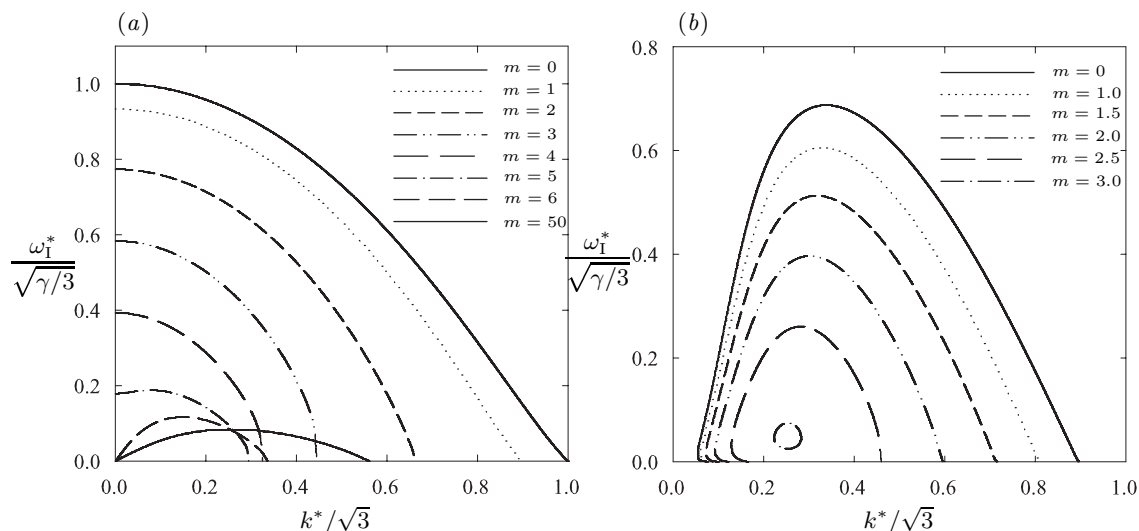
Figure 4.16: Growth rate (imaginary part ω_I^* of the complex frequency) as a function of wavenumber for a horizontal wave ($\boldsymbol{k} \cdot \hat{\boldsymbol{z}} = 0$) in anisotropic suspensions. The various curves corresponds to different degrees of anisotropy, parameterized by the coefficient m in the Onsager distribution Equation (4.41). The growth rates were computed by numerical solution of the dispersion relation Equation (4.35) using a bisection algorithm. In plot (a) stratification and diffusion are neglected ($\beta^* = 0$, $D_\perp^* = 0$); in plot (b) they are set to $\beta^* = 0.05$, $D_\perp^* = 0.02$.

and the range $[0, k_{max}^*]$ of unstable wavenumbers is shown in Figure 4.17 for Onsager distributions as a function of the parameter m. As expected from Figure 4.17, the effect of anisotropy is to shrink the range of unstable wavenumbers. Note however that the range is not reduced monotonically: the initial decay is followed by a small increase and a saturation, also visible in Figure 4.16(a). In very anisotropic suspensions there always remains a finite range of unstable modes; the corresponding growth rates however keep decreasing with m, and in the limit of perfect alignment ($m = \infty$) the suspension is neutrally stable.

As we have accomplished for the isotropic case, we can also obtain the behavior at low-wavenumbers by seeking a perturbation solution to the dispersion relation. When stratification is included ($\beta^* > 0$), the result of Equation (4.37) remains unchanged to the
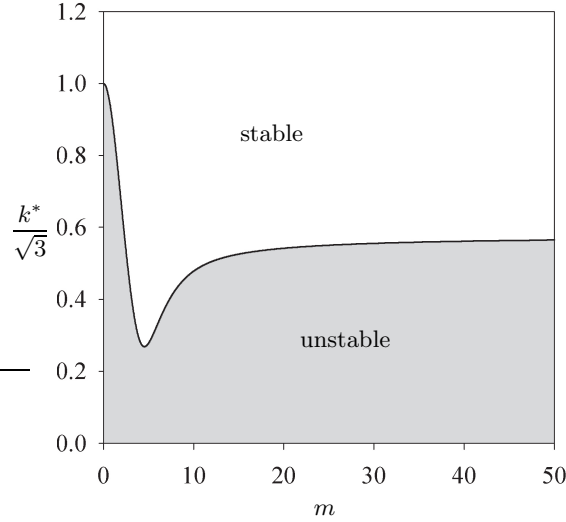
Figure 4.17: Range of unstable wavenumbers for a horizontal wave in an anisotropic suspension as a function of the Onsager parameter m (Equation (4.41)). Both stratification and diffusion are neglected ($\beta^* = 0$, $D_\perp^* = 0$).

order retained in the expansion:

$$\omega_I^* = -\frac{\beta^*}{k^{*2}} \int \Psi(\alpha) \mathrm{d}\boldsymbol{p} + O(1/k^*) = -\frac{\beta^*}{k^{*2}} + O(1/k^*). \tag{4.43}$$

The effects of anisotropy become clearer in the absence of stratification ($\beta^* = 0$). An expansion of Equation (4.35) for a horizontal wave in the limit of $|\boldsymbol{k}^*| \ll 1$ indeed yields the following algebraic equation:

$$\omega^{*4} + a(\Psi)\omega^{*2} - 2\,\mathrm{i}D_\perp^* a(\Psi)k^{*2}\omega^* + b(\Psi)k^{*2} + O(k^{*3}) = 0, \tag{4.44}$$

which is very similar to Equation (4.38) for the isotropic case, but where the coefficients $a(\Psi)$ and $b(\Psi)$ now depend on the orientation distribution. More precisely, a and b can be expressed in terms of moments of the orientation vector $\boldsymbol{p}$. Introduce the following notations:

$$\mathsf{M}_i = \int \Psi(\alpha) \underbrace{\boldsymbol{p} \dots \boldsymbol{p}}_{i\,\text{times}} \mathrm{d}\boldsymbol{p}, \quad \mathsf{N}_i = \int \frac{\mathrm{d}\Psi}{\mathrm{d}\alpha} \underbrace{\boldsymbol{p} \dots \boldsymbol{p}}_{i\,\text{times}} \mathrm{d}\boldsymbol{p}, \tag{4.45}$$
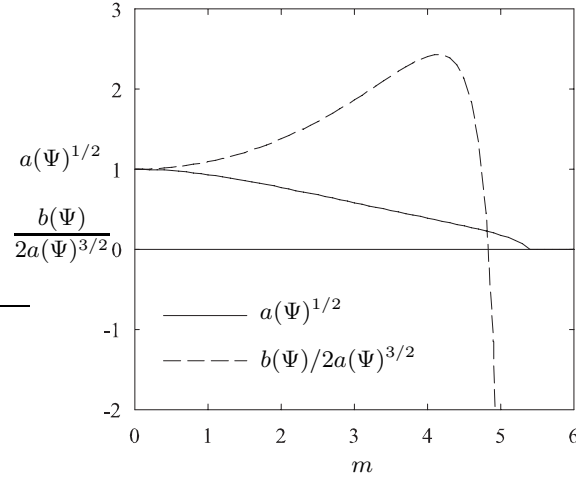
Figure 4.18: Coefficients $a(\Psi)^{1/2}$ and $b(\Psi)/2a(\Psi)^{3/2}$ in the long-wave expansion Equation (4.49) for an Onsager orientation distribution (Equation (4.41)) as a function of the parameter m. Both coefficients are normalized by their value at $m = 0$ (isotropic limit).

and:

$$\hat{\boldsymbol{k}}^{(i)}\hat{\boldsymbol{z}}^{(j)} = \underbrace{\hat{\boldsymbol{k}}\ldots\hat{\boldsymbol{k}}}_{i\,\text{times}}\underbrace{\hat{\boldsymbol{z}}\ldots\hat{\boldsymbol{z}}}_{j\,\text{times}}. \tag{4.46}$$

The scalar coefficients a and b are found as:

$$a(\Psi) = 3\gamma\mathbf{M}_4 : \left(\hat{\boldsymbol{k}}^{(2)}\hat{\boldsymbol{z}}^{(2)}\right) - \frac{\gamma+1}{2}\mathbf{N}_3 : \left(\hat{\boldsymbol{k}}^{(2)}\hat{\boldsymbol{z}}\right) + \gamma\mathbf{N}_5 : \left(\hat{\boldsymbol{k}}^{(2)}\hat{\boldsymbol{z}}^{(3)}\right), \tag{4.47}$$

$$b(\Psi) = 3\gamma\mathbf{M}_8 : \left(\hat{\boldsymbol{k}}^{(4)}\hat{\boldsymbol{z}}^{(4)}\right) - \frac{\gamma+1}{2}\mathbf{N}_7 : \left(\hat{\boldsymbol{k}}^{(4)}\hat{\boldsymbol{z}}^{(3)}\right) + \gamma\mathbf{N}_9 : \left(\hat{\boldsymbol{k}}^{(4)}\hat{\boldsymbol{z}}^{(5)}\right), \tag{4.48}$$

where the symbol $:$ denotes the scalar product between the tensors on each side.

The solution of Equation (4.44) for $k^* \ll 1$ can be shown to be pure imaginary with imaginary part:

$$\omega_{\mathrm{I}}^* = \pm a(\Psi)^{1/2} - k^{*2}\left[D_{\perp}^* \pm \frac{b(\Psi)}{2a(\Psi)^{3/2}}\right] + O(k^{*3}). \tag{4.49}$$

This solution is similar to Equation (4.39) for the isotropic case. In particular, an interesting observation is that the leading order effect of diffusion is unaffected by the orientation

distribution. The two coefficients $a(\Psi)^{1/2}$ and $b(\Psi)/2a(\Psi)^{3/2}$ now depend on the orientation distribution as expected from Figure 4.16, and are plotted in Figure 4.18 for the Onsager distribution of Equation (4.41) as a function of m. As expected from Figure 4.16, $a(\Psi)^{1/2}$ decreases as m increases and becomes zero for $m \geq 5.5$ approximately, confirming that a strongly aligned suspension is stable at zero-wavenumber. The second derivative of $\omega^*(k^*)$ at $k^* = 0$, which is related to $b(\Psi)/2a(\Psi)^{3/2}$, is also observed to change sign at a finite value of m, in agreement with the observations made earlier on Figure 4.16.

4.3.3 Scaling analysis

The analysis of the previous section has shown that the growth of concentration fluctuations can be damped at low wavenumbers by stratification and at high wavenumbers by center-of-mass dispersion. The wavenumber for the most unstable mode in a stratified suspension can therefore be determined by balancing these two effects (Equations (4.37)–(4.39)):

$$-\frac{\beta^*}{k^{*2}} \sim -k^{*2} \left[D_\perp^* + \frac{1}{70} \left(\frac{5}{\gamma} \right)^{3/2} \right]. \tag{4.50}$$

The hydrodynamic diffusivity $D_\perp^*$ models the randomizing effect of velocity fluctuations arising in the suspension over long times, and is expected to be a function of the suspension structure and concentration. Its scaling with the wavenumber k^* and with the volume fraction ϕ must therefore be determined. Since the velocity fluctuations which result in hydrodynamic dispersion are driven by concentration fluctuations occurring over length scales of the order of k^{-1}, we expect the dimensional diffusivity to scale as $D_\perp \sim \Delta U k^{-1}$, where ΔU is the magnitude of the velocity fluctuations. In turn, ΔU is determined by balancing the gravity force and the Stokes drag acting on a typical concentration fluctuation of size k^{-1}: $\Delta N V_p \Delta \rho g \sim \mu k^{-1} \Delta U$, where ΔN is the excess number of particles in the concentration fluctuation [34, 87]. Since concentration fluctuations in the suspension grow as a result of the instability, their magnitude ΔN evolves in time and is unknown *a priori*. Let us consider the onset of the instability in a random suspension, which is described by Poisson statistics: $\Delta N \sim \sqrt{\phi k^{-3}/V_p}$. This assumption, whose validity will

have to be assessed, results in the following scaling for the magnitude of the velocity fluctuations and for the diffusivity: $\Delta U \sim U_0(kl)^{-1/2}\phi^{1/2}$, and $D_\perp \sim U_0 l(kl)^{-3/2}\phi^{1/2}$, where $U_0 = \Delta\rho V_p g/\mu l$ is the scale for the sedimentation velocity of an isolated particle of characteristic size l.

This scaling for the hydrodynamic diffusivity can be substituted into Equation (4.50). When center-of-mass diffusion is the dominant mechanism for damping at high wavenumbers $(D_\perp^* \gg (5/\gamma)^{3/2}/70)$, we obtain the following scaling for the most unstable wavenumber:

$$kl \sim (\beta l)^{2/5}\phi^{1/5}. \tag{4.51}$$

On the other hand, if center-of-mass diffusion is negligible $(D_\perp^* \ll (5/\gamma)^{3/2}/70)$, a different scaling is expected:

$$kl \sim (\beta l)^{1/4}\phi^{3/8}. \tag{4.52}$$

Equivalently, the characteristic size of the density fluctuations in the suspension will be given by: $\xi = k^{-1}$. Note that in both Equation (4.51) and Equation (4.52) the proportionality constant may depend on the particle aspect ratio. These predictions will be tested against simulation data in Section 4.3.4, where we will see that good agreement with Equation (4.51) is observed, suggesting that hydrodynamic dispersion is in practice the main mechanism for the damping of high-wavenumber fluctuations.

Interestingly, the first scaling for ξ (Equation (4.51)) is the same as that found by Mucha *et al.* [132, 186] for the correlation length in a stratified suspension of sedimenting spheres. In that particular case, the physical mechanism that they proposed to obtain the scaling goes as follows. As in the previous discussion, a concentration fluctuation of characteristic size ξ, which has a magnitude of $\Delta\phi \sim (\phi l^3/\xi^3)^{1/2}$ for Poissonian statistics, creates a velocity fluctuation of scale $\Delta U \sim U_0(\xi/l)^{1/2}\phi^{1/2}$ as it sediments. This velocity fluctuation, however, only occurs if there is a true density mismatch with the surrounding fluid, i.e. if the size of the concentration fluctuation remains below the length scale over which stratification changes the background volume fraction ϕ by $\Delta\phi$. This length scale is given by $\Delta\phi/(\beta\phi)$. The maximum value for the correlation length therefore satisfies

$\xi \sim (\phi l^3/\xi^3)^{1/2}/(\beta\phi)$, from which the scaling of Equation (4.51) is easily obtained.

In the case of sedimenting spheroids, a qualitatively similar mechanism can be expected. A cluster of particles, which has a certain density mismatch with the surrounding fluid, can only travel a certain distance in a stably stratified suspension until the mismatch becomes negligible. The fact that the scaling we obtained in Equation (4.51) is the same as for sedimenting spheres is a direct consequence of the assumption made above of Poissonian statistics over the length scale of the fluctuations. This assumption is justified at the onset of the instability when the arrangement of the particles is random, and suggests that initially at least the growth of the concentration fluctuations is directly governed by the velocity fluctuations. At later times however, the statistics clearly will depart from Poissonian owing to the clustering of the particles: the validity of Equation (4.51) may then become questionable, and will need to be tested against simulations.

4.3.4 Numerical simulations

Fluctuations in stably stratified suspensions

Using the simulation method of Section 4.2.1, we first test the conclusions of the stability analysis of Section 4.3.2 by performing simulations of suspensions in which a vertical density gradient is imposed in the initial configuration. As a measure of the characteristic size of the structures that develop in the suspension, we use the correlation length ξ defined as the position of the first minimum in the autocorrelation function $C_{zz}(x)$ of the vertical fluid velocity component in the horizontal direction:

$$C_{zz}(x) = \int u_z(x')u_z(x' + x)\mathrm{d}x'. \tag{4.53}$$

In Section 4.2.4, we showed indeed that the velocity field decorrelates in the horizontal direction over a distance of the order of the size of the clusters in the suspension, since these entrain the fluid with them and are surrounded by backflow regions. This measure has also been used successfully in experiments to estimate the size of the clusters in fiber suspensions [126, 127]. To isolate the effects of the initial stratification, ξ is measured at
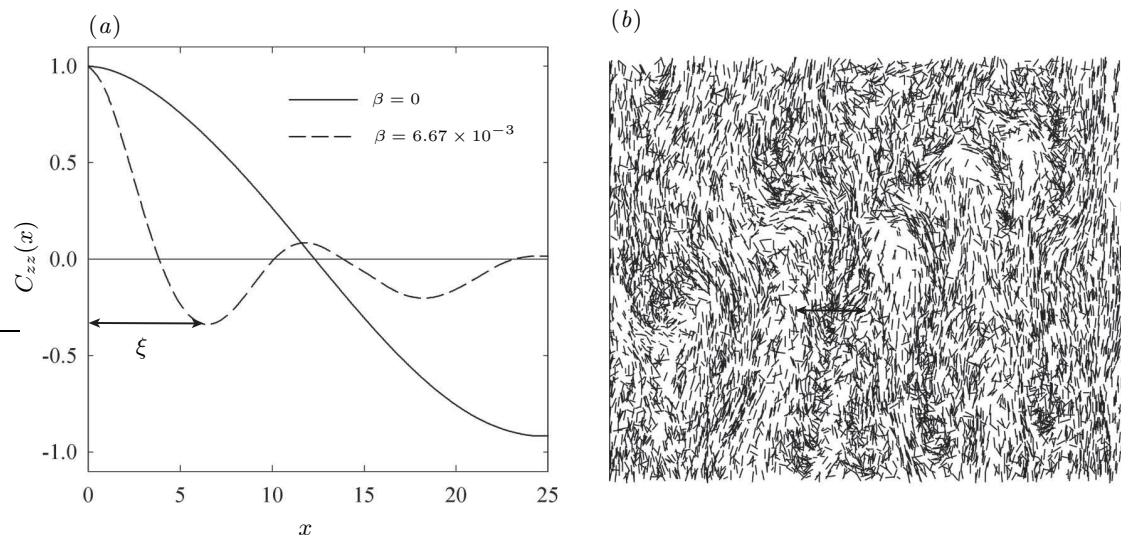
Figure 4.19: (*a*) Autocorrelation length $C_{zz}(x)$ in the horizontal direction of the vertical disturbance fluid velocity, in a suspension of 257,831 spheroids of aspect ratio $A = 15$ in a box of dimensions $L_x = 50$, $L_y = 20$, $L_z = 300$ (volume fraction $\phi = 0.2\%$), measured at $t = 15$ near the peak of the fluctuations, with and without stratification. The correlation length ξ is measured as the position of the first minimum. (*b*) Visualization of the suspension of (*a*) at $t = 15$ in the stratified case ($\beta = 6.67\times10^{-3}$), where a wavenumber selection is observed. The arrow represents the correlation length measured in (*a*).

time $t = 15$ shortly after the start of the simulations, which corresponds approximately to the occurrence of the peak in the velocity fluctuations (cf. Figure 4.8(*b*)): this time is short enough for the stratification to remain roughly constant, but sufficiently long for the inhomogeneities to start forming in the suspension.

Typical velocity autocorrelation functions in non-stratified and stratified suspensions are shown in Figure 4.19(*a*). In the absence of stratification ($\beta = 0$), the velocity field decorrelates over half a box width ($\xi = L_x/2$), indicating the formation of a single streamer spanning the full width of the box. This agrees qualitatively with experimental observations [126] and the simulations of Section 4.2 in homogeneous suspensions shortly after the start of sedimentation, and is also predicted by the original stability analysis of Koch & Shaqfeh [102] for a homogeneous base state, in which the longest wavelength dominates. The behavior is quite different, however, when stratification is imposed: when
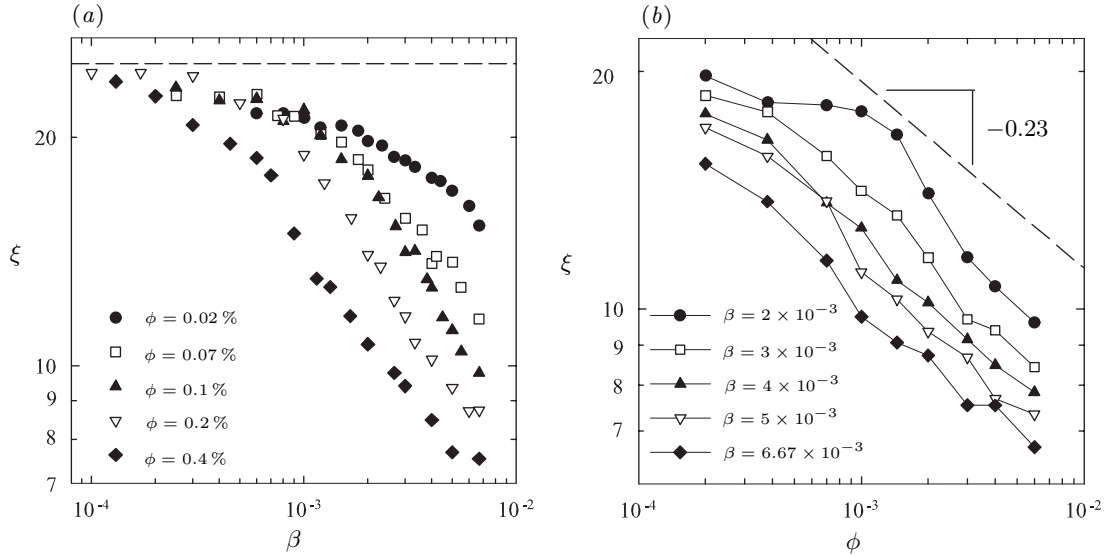
Figure 4.20: Correlation length ξ in the horizontal direction, measured as the first minimum in the autocorrelation function of the vertical fluid velocity component (cf. Figure 4.7), as a function of: (a) the stratification parameter β in the suspension, and (b) the local volume fraction ϕ. The stratification was imposed in the initial particle distributions, and the correlation length was measured at $t = 15$ near the center of the box. The simulations were run in a box of dimensions $L_x = 50$, $L_y = 20$, $L_z = 300$, and are for spheroids of aspect ratio $A = 15$. Each point on the graphs is an average over 20 to 30 simulations. The dependence of ξ on the volume fraction ϕ is well approximated by a power law with exponent ≈ -0.23.

$\beta = 6.67 \times 10^{-3}$ in Figure 4.19(a), the correlation length is found to be much shorter, of the order of a few particle lengths. Figure 4.19(b) shows the corresponding particle distribution, on which the correlation length ξ is denoted by an arrow: the particle distribution indeed presents several distinct clusters in the lateral direction, the characteristic size of which is of the order of ξ. These observations confirm the stabilizing influence of stratification and its role in selecting the size or wavelength of the inhomogeneities in the suspension.

The effects of the density gradient β on the wavelength of the instability are shown more quantitatively in Figure 4.20(a), where the correlation length ξ is plotted vs. β for various volume fractions ϕ. In very weakly stratified suspensions ($\beta \sim 10^{-4}$), the correlation length saturates at approximately half a box width, showing that the wavelength is selected by
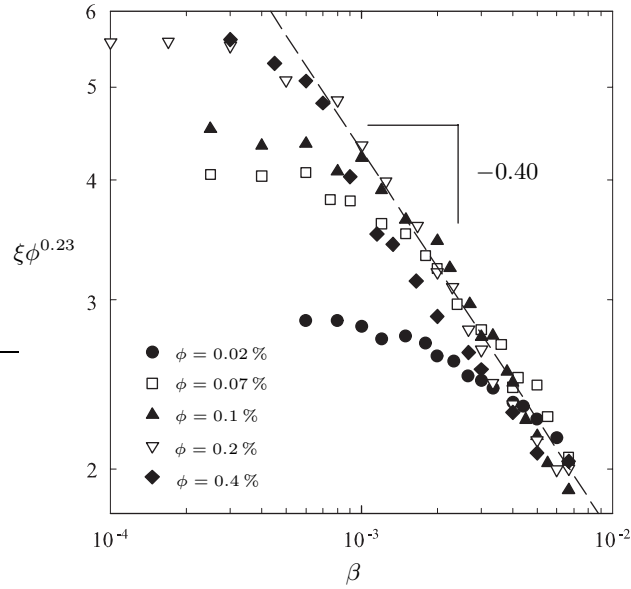
Figure 4.21: Correlation length ξ in the horizontal direction, scaled by $\phi^{-0.23}$, as a function of the stratification parameter β at various volume fractions. The data are the same as in Figure 4.20(a). At high values of β the curves asymptote to a power law with exponent ≈ -0.40.

the size of the container. When β increases, ξ is found to decrease, yielding cluster sizes that are controlled by stratification and do not depend on the container dimensions. At a given value of β, the correlation length is observed to be larger in more dilute suspensions.

The dependence on concentration is shown more precisely in Figure 4.20(b), where ξ is shown as a function of ϕ for a few given values of β. The correlation length indeed decreases with increasing volume fraction, and the decay is well described by the following power law: $\xi \sim \phi^{-0.23}$. The data of Figure 4.20(a) rescaled with $\phi^{-0.23}$ are shown in Figure 4.21, where the curves corresponding to various volume fractions are observed to collapse onto a single straight line on a log-log plot, with departures at small values of β owing to box-size effects. We therefore find the following scaling for the correlation length when box-size effects are negligible (i.e. when $\xi < L_x/2$):

$$\xi \approx C\beta^{-0.40}\phi^{-0.23}, \tag{4.54}$$

where the dimensionless constant C is of the order of 0.3.

The exponents found in Equation (4.54) are in good agreement with the theoretical prediction of Equation (4.51), but do not agree with the other proposed scaling (Equation 4.52): this suggests as explained in Section 4.3.3 that center-of-mass dispersion is the main mechanism for damping at high wavenumbers. Small departures are expected to occur for a variety of reasons. Most importantly, the theoretical scaling was derived based on the assumption that the particle distribution on the length scale of the fluctuations is Poissonian. While this is strictly true at $t = 0$, the distribution then evolves as a result of the instability, leading to stronger density fluctuations and a possibly different scaling for the hydrodynamic diffusivity. The good agreement between simulations and theory suggests that these effects are weak, at least initially. Finite-box effects are also likely to influence the results from the simulations, in particular in the more dilute cases or when the stratification is very weak: this is for instance clear at the low volume fraction of $\phi = 0.02\,\%$ in Figures 4.20(a) and 4.21, where the exponent of -0.40 for the dependence on β is never fully reached.

Wavenumber selection process

In initially well-mixed suspensions, the stratification at $t = 0$ is negligible: the onset of the instability is therefore governed by the analysis of Koch & Shaqfeh [102], and characterized by the formation of a large-scale streamer spanning the width of the container [126, 159]. Stratification however is known to develop (cf. Figure 4.3), and may subsequently have an effect on the wavelength of the instability. The evolution of the vertical concentration profile in a typical simulation is shown in Figure 4.22. At $t = 0$, the concentration is uniform, but a significant gradient in the vertical direction is observed to appear as the sedimentation progresses. First, the interface between the bulk of the suspension and the clear fluid spreads in time, resulting in the formation of a broad suspension front: this phenomenon can be attributed in part to the difference in the sedimentation rates of spheroids with different orientations. In addition, the bulk of the suspension also becomes stratified, with particles accumulating near the bottom of the container: while the precise
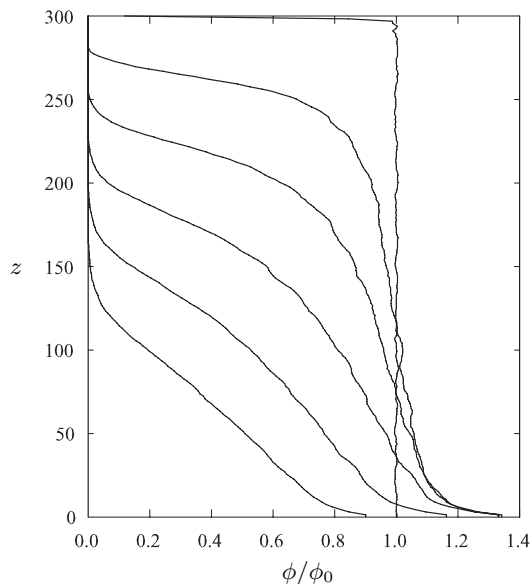
Figure 4.22: Evolution of the vertical concentration profile with time in a suspension of 257,831 spheroids of aspect ratio $A = 15$ in a box of dimensions $L_x = 50$, $L_y = 20$, $L_z = 300$ (volume fraction $\phi_0 = 0.2\%$). The different curves correspond to the times: $t = 2, 40, 80, 120, 160, 200$, and are averaged over 20 simulations. The local volume fraction ϕ is normalized by the bulk value ϕ_0 at $t = 0$.

mechanism for this effect deserves further consideration, it is likely to be due to the formation of clusters in the suspension, which settle at a higher speed than particles in the clarified regions. At later times, the concentration gradients in the suspension front and in the bulk become comparable, resulting in an almost linear concentration profile in the vertical direction.

The concentration fluctuations are described more quantitatively in Figure 4.23, which shows the evolution of the stratification parameter β and of the local volume fraction ϕ at a given vertical station during the sedimentation. Figure 4.23(a) confirms that the stratification, which is initially negligible ($\beta \approx 0$), becomes significant with values of β reaching 0.03 at $t = 200$. Note that such gradients are much stronger than those investigated in Section 4.3.4, where the largest value for β did not exceed 0.01: significant effects on the wavelength of the instability can therefore be anticipated. The local concentration at a given height in the container also decreases in time, as shown in Figure 4.23(b). In
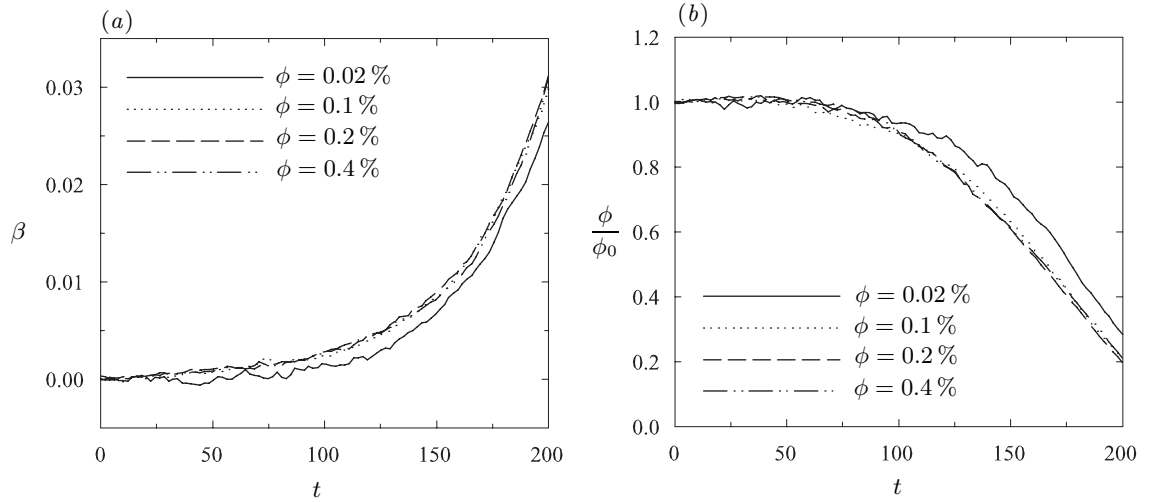
Figure 4.23: Time evolution of (a) the stratification parameter β, and (b) the normalized volume fraction ϕ/ϕ_0, over the course of a simulation. The simulations are for spheroids of aspect ratio $A = 15$ and were performed in a box of dimensions $L_x = 50$, $L_y = 20$, $L_z = 300$. Both β and ϕ/ϕ_0 were measured at a height of $z = 100$ in the container. The curves are averaged over 20 simulations.

particular, the simulations show that the decay begins quite early (before the approach of the sedimentation front), and is therefore at first a consequence of the stratification in the bulk. Note however that very near the bottom of the container the concentration first increases, as can be seen in Figure 4.22.

Figure 4.24(a) illustrates the wavenumber selection process of the concentration instability. The correlation length ξ in the horizontal direction during sedimentation, measured at the same height in the container as β and ϕ in Figure 4.23, is plotted vs. time. The trends observed agree with previous observations [126, 159]: initially the correlation length is of the order of the box width ($\xi \approx L_x/2$), after which it undergoes a transition to a much shorter value of the order of a few particle lengths ($\xi \approx 8$ to 12 in Figure 4.24). While Figure 4.24(a) suggests a saturation at long times, no true steady state is observed and ξ continues to decay until the end of settling. The very slow decay of ξ, however, may explain why the microstructure in our previous simulations on smaller systems appeared to reach a steady state (cf. Section 4.2.3). The influence of concentration is also shown in
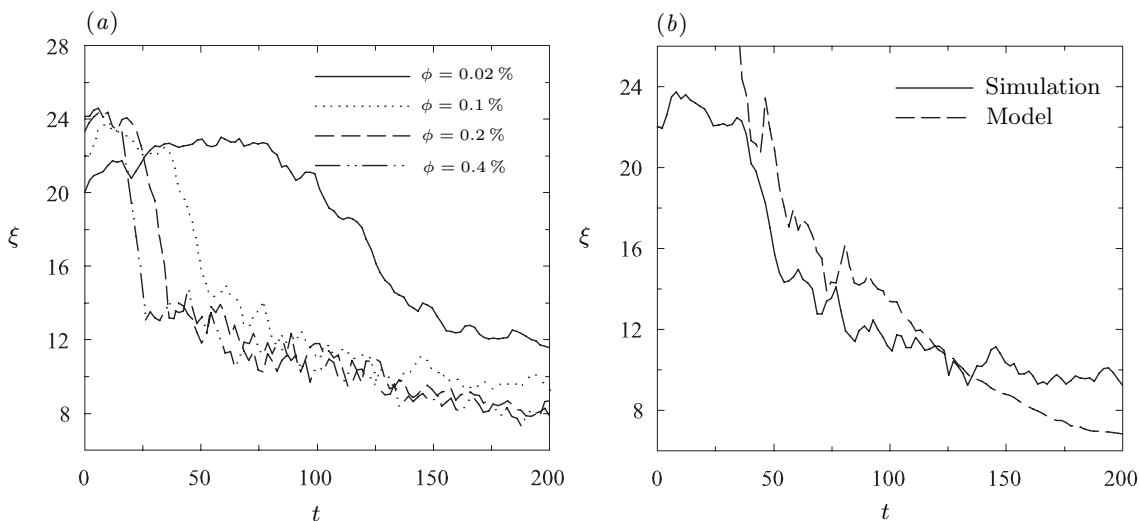
Figure 4.24: (a) Time evolution of the correlation length ξ in the horizontal direction. The simulations are for spheroids of aspect ratio $A = 15$ and were performed in a box of dimensions $L_x = 50$, $L_y = 20$, $L_z = 300$. The correlation length was measured at a height of $z = 100$ in the container. The curves are averaged over 20 simulations. (b) Comparison between the correlation length measured in the simulations (in the case $\phi_0 = 0.1\%$), and the prediction of Equation (4.54), in which the data of Figure 10 were used for the local evolution of β and ϕ.

Figure 4.24, where we see that the transition from a single streamer to multiple clusters occurs more rapidly in the concentrated suspensions, where the final correlation length is also typically shorter. The effects of concentration are nonetheless quite weak, except in the most dilute case ($\phi = 0.02\%$), where the transition to small-scale structures occurs at a significantly later time.

To quantitatively assess the role played by stratification in the evolution of the correlation length shown in Figure 4.24(a), we compare in Figure 4.24(b) the measured correlation length to that predicted by the scaling of Equation (4.54), in which we use the data of Figure 4.23 for the evolution of the stratification parameter β and of the local volume fraction ϕ. While the model does not reproduce the saturation at half a box width at short times, which is a finite-box effect, it does capture the subsequent time decay of the correlation length. The predicted decay is slightly faster than observed in the simulations,

yet the measured and predicted correlation lengths never differ by more than approximately 20 %. This agreement is suprisingly good in the light of the approximations made in Section 4.3.3 when deriving the scaling, and strongly suggests that the wavenumber selection is controlled by stratification at least in these simulations. An important remark is that the initial decay of ξ occurs quite early in Figure 4.24(a) (between $t = 50$ and 75 for both the measured and predicted curves), at a time when the stratification in the suspension is still very weak as seen in Figure 4.23(a) ($\beta \approx 2 \times 10^{-3}$): this demonstrates that relatively weak density gradients can have sizeable effects on the wavenumber selection of the instability. Note that a similar remark had been made by Mucha *et al.* regarding the effect of stratification on the correlation length in sphere suspensions [132].

The theoretical scaling for the correlation length also allows us to understand several of the features observed in Figure 4.24(a). In particular, since the stratification parameter β is sensibly the same at all volume fractions (Figure 4.24(a)), the main effect of volume fraction on the wavenumber selection occurs through the scaling with ϕ in Equation (4.54): we can therefore expect the correlation length to be larger in more dilute suspensions, and hence the transition from a box-dependent streamer to multiple clusters to occur at a later time, as indeed observed in the simulation data. The saturation of ξ near the end the sedimentation process can also be explained: whereas the vertical density gradient (or stratification parameter β) keeps increasing in time (Figure 4.23(a)), the local volume fraction, which is initially constant, drops considerably as the front approaches (Figure 4.23(b)): the competing effects of increasing stratification and decreasing volume fraction may therefore be responsible for the saturation of ξ, according to Equation (4.54).

4.4 Concluding remarks

We have used a combination of large-scale numerical simulations and theory to study the sedimentation of orientable particles such as rigid spheroids. Our analysis focused on the concentration fluctuations and the microstructure in very dilute suspensions of realistic sizes. The concentration instability in suspensions of spheroids was captured in our

simulations, and we observed that the no-flux boundary condition imposed at the bottom of the container has a strong impact on the structure of the suspension and can lead to a wavenumber selection for the concentration fluctuations. This result differs qualitatively from previous computational studies of periodic systems, including that of Chapter 3, in which the longest wavelength set by the width of the container always dominates. Our simulations suggest that horizontal container boundaries provide a mechanism for the decay or break-up of these long-wavelength fluctuations, down to the selected wavelength of the instability. Results for the velocity and orientation statistics were also presented and showed good agreement with the published experiments of Herzhaft & Guazzelli [84]; in particular these statistics were found not to depend upon the size and aspect ratio of the sedimenting system, unlike in previous simulations with periodic boundary conditions (Sections 3.5.3 and 3.5.4).

To elucidate the mechanism leading to the wavenumber selection, we revisited the linear stability analysis of Koch & Shaqfeh [102] by including the effects of stratification and dispersion. Our analysis demonstrated that stratification provides a mechanism for damping of the fluctuations at low wavenumbers, while high-wavenumber fluctuations are suppressed by hydrodynamic dispersion. The balance of these two effects therefore results in a selection of a most unstable mode at a finite wavenumber. Based on the results of the stability analysis, we were able to derive the following scaling for the characteristic size of the fluctuations: $\xi/l \sim (\beta l)^{-2/5} \phi^{-1/5}$. This scaling, which is the same as that previously obtained for the size of the fluctuations in sphere suspensions [132, 186], is based on an assumption of Poissonian statistics over the length scale of the fluctuations, and is therefore only rigorous at the onset of the instability. Simulations were performed in which a density gradient was imposed at $t = 0$, and showed good agreement with the predicted scaling. In initially well-mixed suspensions, we observed that the continuous decay of the wavelength of the fluctuations is also described reasonably well by the same model.

While the present work demonstrates that an accurate description of the concentration instability should take stratification into account, it is by no means a proof that

the wavenumber selection in a real system is only governed by the mechanisms described herein. In particular, other effects which have not been accounted for in our analysis are likely to play a role as well. One such effect is hydrodynamic screening by the container side walls, which is a consequence of the no-slip boundary condition on solid boundaries and is not captured by the tangential flow boundary condition used in our simulations. As described previously by Brenner in the case of spheres [28], no-slip walls provide an additional cutoff for the hydrodynamic interaction between the suspended particles, which become negligible beyond distances of the order of the shortest wall separation distance. Other effects may also arise owing to close particle interactions, which were neglected in our theory and simulations. In suspensions of spheroids, lubrication forces and excluded volume can lead to entanglements whose effects are not described by far-field hydrodynamics. These interactions, which may play a role inside the dense clusters and certainly become important in more concentrated suspensions, may affect the typical size of the clusters, as well as statistical properties such as the orientation distributions and the mean velocity. The resulting entanglements are likely to reinforce the fluctuations over short-distances, which will lead to stronger departures from Poisson statistics.

One remaining question which we have not resolved is the exact process leading to the formation of the vertical density gradients in the suspension. While the broadening of the front at the top of the suspension can be understood from the differential settling of particles with different orientations, the reason for the formation of gradients in the bulk of the suspension is not clear. Models have been proposed previously to describe stratification in sphere suspensions [131, 132], and were based on solutions of a convective-diffusion equation for the particle phase, in which closure approximations were used for hydrodynamic diffusivities. One could envisage developing a similar framework in the case of anisotropic particles; yet the presence of clusters in the suspension, which settle at higher rates than the remainder of the particles, would have to be considered. Since the size of these clusters may itself be controlled by stratification, a coupled model for the vertical density profile and for the microstructure will almost certainly be required.

Chapter 5

The dilute sedimentation of deformable particles

5.1 Introduction

The sedimentation of orientable particles was shown in Chapters 3 and 4 to be characterized by a concentration instability, which arises as a result of the coupling between the orientation of the particles and the disturbance flow in the fluid. Deformable particles, such as drops, bubbles, elastic particles or flexible polymers, can have similar dynamic behavior as orientable particles, as deformable particles may also become anisotropic under flow and therefore also be subject to an instability. This was first suggested by Manga & Stone [124], who pointed out that the deformation of rising bubbles as a result of hydrodynamic interactions should result in a migration towards the regions of high density. They illustrated this mechanism using a similar picture as in Koch & Shaqfeh [102], but made no further attempt to study the instability. In spite of the clear analogy between the two situations, the instability for drops, if it exists, is slightly more complex than that characterizing orientable particles as the deformations leading to the lateral migration are themselves induced by the density fluctuations through the disturbance field. To our knowledge the instability for drops has never been reported in an experiment, but a

few computational studies seem to confirm its existence. Zinchenko & Davis [199, 200] performed boundary integral simulations of concentrated suspensions of deformable drops under sedimentation. Starting from random configurations of spherical drops, they observed that the drops acquired prolate shapes and oriented in the direction of gravity, resulting in an increase of the sedimentation rate. Again clustering was reported, but no detailed study of the suspension structure was undertaken.

In this Chapter, we wish to further investigate the sedimentation of deformable particles in the case where the suspension is very dilute. First, we develop a model for such suspensions based on small deformation theory in Section 5.2, and show using a linear stability analysis that an instability similar to that observed for spheroids indeed exists for deformable particles. We then adapt the method of Section 4.2.1 to the case of slightly deformable particles, and present simulation results in Section 5.4.

5.2 Theoretical analysis

In this section we develop a model for suspensions of deformable particles under sedimentation and investigate the stability of the suspension to fluctuations in concentration. As will become apparent, the formalism is quite similar to that presented in Section 4.3.2 for suspensions of spheroids, although significant differences exist. We first explain the micromechanical model used to describe the particle deformations and hydrodynamic interactions in Section 5.2.1, then define a convective-diffusive equation for the concentration field in a suspension of such particles in Section 5.2.2, and perform a linear stability analysis based on this continuum model in Section 5.2.3.

5.2.1 Micromechanical model

The particles we consider here are isotropic in the absence of flow, and by deformation we mean departure from isotropy. In particular, the particles need not be technically spherical, and we will explain in Section 5.3 that the arguments developed here can apply for instance to flexible polymers with strong internal Brownian motion. We make the

fundamental assumption that particle deformations remain small, and are entirely deter-
mined by the local rate of strain $\mathbf{E} = \left[\boldsymbol{\nabla u} + (\boldsymbol{\nabla u})^T \right] / 2$ with no regard for the history of
the flow and of particle position. This implicitly assumes that the particle shape adjusts
instantaneously on the flow time scale, or in other words that the characteristic time for
the shape relaxation (which is determined by properties such as surface tension for a drop,
membrane elasticity for a capsule, or internal Brownian motion for a flexible polymer)
is much less than the characteristic time scale of the flow (which is set by the balance
between the gravity force on the density fluctuations and viscous dissipation); this condi-
tion will be justified and made more quantitative in Section 5.3. Under this assumption
the mobility $\mathbf{M}(\mathbf{E})$ of a particle can be expanded in a Taylor series with respect to the
undeformed configuration, leading to the following approximation:

$$\mathbf{M}(\mathbf{E}) \approx M_0(\mathbf{I} + \tau_s \mathbf{E} + ...), \tag{5.1}$$

where $M_0 \mathbf{I}$ is the (isotropic) mobility of the undeformed particle, and τ_s is a characteristic
time defining the response of the mobility to a weak flow field and is a property of the
particle. The condition on the flow strength can be written as:

$$\epsilon = \tau_s \dot{\gamma} \ll 1 \tag{5.2}$$

where $\dot{\gamma}$ is the effective characteristic shear rate of the disturbance flow imposed by the
density fluctuations.

The center-of-mass velocity $\boldsymbol{U}_\alpha$ of a particle α located at position $\boldsymbol{x}_\alpha$ in a suspension is
then given by the sum of the sedimentation velocity of the particle and of the disturbance
velocity in the fluid induced by the motion of the other particles:

$$\boldsymbol{U}_\alpha = \boldsymbol{U}_s + \boldsymbol{u}(\boldsymbol{x}_\alpha). \tag{5.3}$$

The sedimentation velocity can be written as $\boldsymbol{U}_s = \mathbf{M}(\mathbf{E}) \cdot \boldsymbol{F}$, where $\mathbf{M}(\mathbf{E})$ is given by
Equation (5.1) evaluated at position $\boldsymbol{x}_\alpha$, and $\boldsymbol{F} = \Delta \rho V_p \boldsymbol{g}$ is the gravity force on the

particle. To leading order the disturbance velocity $\boldsymbol{u}$ induced by the other particles in the suspension satisfies the Stokes equations:

$$-\nabla^2 \boldsymbol{u} + \boldsymbol{\nabla} p = \boldsymbol{F} \sum_{\beta \neq \alpha} \delta(\boldsymbol{x}_\beta - \boldsymbol{x}), \quad \boldsymbol{\nabla} \cdot \boldsymbol{u} = 0, \tag{5.4}$$

where $\delta(\boldsymbol{x})$ is the three-dimensional Dirac delta function, and the sum is over all particles in the suspension other than α. The only disturbance of a given particle on the fluid is therefore taken to be a point force, which is a valid approximation if the suspension is dilute. This corresponds to the leading order term in the multipole expansion of Section 2.3, and in a more accurate model higher force moments may be taken into account.

5.2.2 Continuum limit

Based on the above model for particle deformations, a conservation equation can be written for the evolution of the concentration of particles in a suspension. Under the assumption discussed previously concerning the instantaneous relaxation of particle configurations, only one particle shape can exist at a given position and at a given time, which allows one to define the variable $c(\boldsymbol{x}, t)$ as the concentration of particles at position $\boldsymbol{x}$ at time t. More precisely, the number of particles in an infinitesimal volume $\mathrm{d}\boldsymbol{x}$ surrounding the point $\boldsymbol{x}$ is given by $c(\boldsymbol{x}, t)\mathrm{d}\boldsymbol{x}$. $c(\boldsymbol{x}, t)$ is normalized by setting its mean value over the entire domain equal to the average number density n:

$$\frac{1}{V} \int_V c(\boldsymbol{x}, t)\mathrm{d}\boldsymbol{x} = n. \tag{5.5}$$

Using a different normalization, $c(\boldsymbol{x}, t)$ can also be interpreted as the probability density of finding a particle at position $\boldsymbol{x}$ and time t. $c(\boldsymbol{x}, t)$ satisfies the following conservation equation:

$$\frac{\partial c}{\partial t} + \boldsymbol{\nabla} \cdot (\boldsymbol{U} c) - \boldsymbol{\nabla} \cdot (\mathbf{D} \boldsymbol{\nabla} c) = 0, \tag{5.6}$$

in which the rate of change of concentration at a given point is balanced by convective and diffusive fluxes. $\boldsymbol{U}$ is the center-of-mass velocity of a particle at position $\boldsymbol{x}$, and is again

given by Equation (5.3). The disturbance velocity $\boldsymbol{u}$ now satisfies a continuum equivalent of Equation (5.4), in which we include a body force proportional to the local number density:

$$-\nabla^2\boldsymbol{u} + \boldsymbol{\nabla}p = \boldsymbol{F}c(\boldsymbol{x},t), \quad \boldsymbol{\nabla}\cdot\boldsymbol{u} = 0. \tag{5.7}$$

The diffusion term in the conservation equation may have several origins. If the particles are small enough, Brownian diffusion will arise from the thermal fluctuations in the solvent, leading to a diffusivity tensor given by the Stokes-Einstein relation: $\mathbf{D} = kT\mathbf{M}$, which may be anisotropic as the particles are allowed to deform. For the time being we will assume that the center-of-mass diffusion due to Brownian motion is negligible. Even in the absence of Brownian diffusion, hydrodynamic dispersion due to the random fluctuations in the disturbance velocity field will result in an effective diffusivity (e.g. [77, 104, 138]), which is unknown *a priori* and is difficult to predict as it may evolve during the settling of the suspension. The details of this process are discussed more precisely in Section 5.4.5, where our simulation results indeed show proof of a diffusive motion at long times. As in Section 4.3.2, we will assume that the hydrodynamic diffusivity is anisotropic and can be written in the general form:

$$\mathbf{D} = D_\parallel\hat{\boldsymbol{z}}\hat{\boldsymbol{z}} + D_\perp(\mathbf{I} - \hat{\boldsymbol{z}}\hat{\boldsymbol{z}}), \tag{5.8}$$

where $D_\parallel$ and $D_\perp$ denote the diffusivities in the directions parallel and perpendicular to gravity respectively, and $\hat{\boldsymbol{z}}$ is a unit vector in the vertical direction.

5.2.3   Linear stability analysis

We now have all the ingredients to perform a linear stability analysis. The base state of the system corresponds to the absence of density fluctuations: $c(\boldsymbol{x},t) = n$, where n is the number density. In that case the disturbance velocity is zero everywhere ($\boldsymbol{u}(\boldsymbol{x}) = 0$), the particles are all isotropic, and a mean pressure gradient in the vertical direction balances the gravity force on the suspension: $\boldsymbol{\nabla}p = \boldsymbol{F}n$. Consider now a small perturbation in

particle density:

$$c(\boldsymbol{x}, t) = n + c'(\boldsymbol{x}, t), \tag{5.9}$$

resulting in a small velocity disturbance $\boldsymbol{u}(\boldsymbol{x}) = \boldsymbol{u}'(\boldsymbol{x})$, and a small deformation of the particles through the disturbance rate of strain and the linearized mobility Equation (5.1). Substituting these perturbations into the conservation equation for the particle concentration and neglecting nonlinear products of perturbations leads to the following linearized equation for the concentration fluctuations:

$$\frac{\partial c'}{\partial t} + M_0 \boldsymbol{F} \cdot \boldsymbol{\nabla} c' + n \boldsymbol{\nabla} \cdot \left(\boldsymbol{u}' + \tau_s M_0 \mathsf{E}' \boldsymbol{F} \right) - \boldsymbol{\nabla} \cdot (\mathsf{D} \boldsymbol{\nabla} c') = 0. \tag{5.10}$$

Assume a normal mode perturbation of a given wavevector $\boldsymbol{k}$:

$$c'(\boldsymbol{x}, t) = \tilde{c}(\boldsymbol{k}) \exp \mathrm{i}(\boldsymbol{k} \cdot \boldsymbol{x} - \omega t). \tag{5.11}$$

The resulting disturbance velocity can be written: $\boldsymbol{u}'(\boldsymbol{x}, t) = \tilde{\boldsymbol{u}}(\boldsymbol{k}) \exp \mathrm{i}(\boldsymbol{k} \cdot \boldsymbol{x} - \omega t)$ where the Fourier coefficient $\tilde{\boldsymbol{u}}(\boldsymbol{k})$ was calculated analytically by Hasimoto [81] (cf. Appendix A):

$$\tilde{\boldsymbol{u}}(\boldsymbol{k}) = \frac{1}{\mu k^2} \left(\mathsf{I} - \frac{\boldsymbol{k}\boldsymbol{k}}{k^2} \right) \cdot \boldsymbol{F} \tilde{c}(\boldsymbol{k}). \tag{5.12}$$

Noting that $\tilde{\mathsf{E}}'(\boldsymbol{k}) = \mathrm{i}(\tilde{\boldsymbol{u}}'\boldsymbol{k} + \boldsymbol{k}\tilde{\boldsymbol{u}}')/2$, and that $\boldsymbol{k} \cdot \tilde{\boldsymbol{u}}' = 0$ from continuity, Equation (5.10) simplifies to:

$$-\mathrm{i}\omega\tilde{c} + \mathrm{i}M_0\boldsymbol{F} \cdot \boldsymbol{k}\tilde{c} - \frac{\tau_s n M_0}{2\mu} \boldsymbol{F} \cdot \left(\mathsf{I} - \frac{\boldsymbol{k}\boldsymbol{k}}{k^2} \right) \cdot \boldsymbol{F}\tilde{c} + \boldsymbol{k} \cdot \mathsf{D} \cdot \boldsymbol{k}\tilde{c} = 0. \tag{5.13}$$

Denote by θ the angle between the wavevector $\boldsymbol{k}$ and the direction of gravity: $\boldsymbol{k} \cdot \hat{\boldsymbol{z}} = k \cos \theta$, and let $\boldsymbol{F} = F\hat{\boldsymbol{z}}$. After manipulation we can solve for the wave frequency ω as a function of the magnitude k and orientation θ of the wavevector:

$$\omega = M_0 F k \cos \theta + \mathrm{i} \left[\frac{\tau_s n M_0 F^2}{2\mu} \sin^2 \theta - k^2 \left(D_{\parallel} \cos^2 \theta + D_{\perp} \sin^2 \theta \right) \right]. \tag{5.14}$$
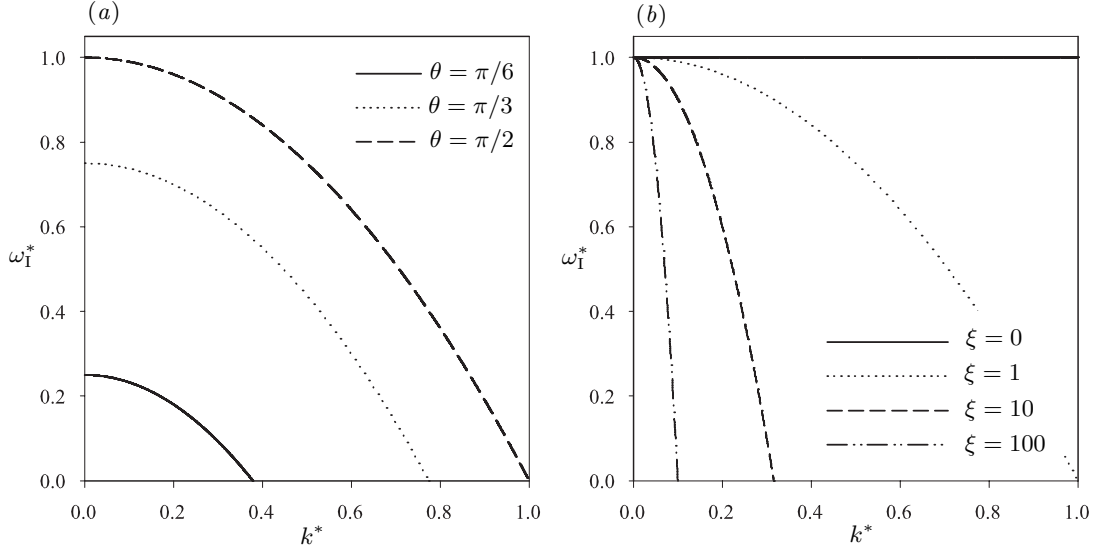
Figure 5.1: Growth rate as a function of the magnitude of the wavenumber: in dimensionless variables, $\omega_I^* = \sin^2\theta - \xi(k^*)^2(D_\parallel/D_\perp \cos^2\theta + \sin^2\theta)$, where ξ is a dimensionless diffusion constant (Equation (5.17)). For both plots the ratio $D_\parallel/D_\perp$ of the diffusivities was chosen equal to 2. Plot (a) shows the influence of the orientation angle θ of the wavevector with respect to the direction of gravity, at $\xi = 1$. Plot (b) shows the influence of the diffusion coefficient ξ for a horizontal wave $(\theta = \pi/2)$.

The frequency ω has a real part $\omega_R = M_0 F k \cos\theta = U_0 k \cos\theta$, which is non-zero for wavevectors with a vertical component i.e. for density fluctuations in the vertical direction, and corresponds to traveling waves with a wave speed equal to the sedimentation velocity; such waves do not either grow or decay. More interestingly the imaginary part of the frequency

$$\omega_I = \frac{\tau_s n M_0 F^2}{2\mu} \sin^2\theta - k^2 \left(D_\parallel \cos^2\theta + D_\perp \sin^2\theta\right) \tag{5.15}$$

is non-zero and positive at low wavenumbers for wavevectors with a horizontal component, provided that the constant τ_s is positive (which, as we argue in Section 5.3, is the case in many situations). Low-wavenumber fluctuations in the horizontal direction will therefore amplify, and the growth rate is plotted vs. k for different values of the wave orientation θ and of the diffusivities $D_\perp$ and $D_\parallel$ in Figure 5.1, in which the following dimensionless variables are used:

$$\omega_{\mathrm{I}}^* = \omega_I \times \left[\frac{\tau_s n M_0 F^2}{2\mu} \right]^{-1} \quad \text{and} \quad k^* = k \times n^{-1/3}, \tag{5.16}$$

and where we introduce a dimensionless diffusion coefficient

$$\xi = \frac{2\mu D_\perp}{\tau_s n^{1/3} M_0 F^2} \tag{5.17}$$

comparing the effects of diffusion and of the lateral convection due to deformations.

In the absence of hydrodynamic dispersion Equation (5.15) and Figure 5.1(b) show that the growth rate is independent of the wavenumber, i.e. in the linear regime all fluctuations grow at the same pace. This peculiar behavior is a consequence of the linear dependence of the mobility correction on the disturbance rate of strain and of the slow decay of the disturbance velocity in sedimenting suspensions, both of which result in a migration flux scaling as $1/k$, and in a growth rate independent of k. The damping of the fluctuations shown in Figure 5.1 is therefore purely a consequence of hydrodynamic dispersion: at a value of $\xi = 1$ diffusion dominates deformation-induced lateral migration over length scales on the order of the mean interparticle distance, hence the negative growth rates observed beyond $k^* = 1$. This mechanism is to be contrasted with the damping observed by Koch & Shaqfeh [102] in the case of orientable rigid spheroids, where diffusion had been neglected. For the sedimentation of rigid spheroids the decay at high wavenumbers is a consequence of the non-instantaneous relaxation of the particle orientation, whose characteristic time can be on the same order as the time for the spheroid to migrate over one wavelength at high enough wavenumbers. An equivalent way of looking at it is to recognize that the dispersion in orientation due to the initial random configuration leads to an effective dispersion of the center-of-mass motion, qualitatively similar to the Taylor dispersion for Brownian systems [27]. Introducing shape history effects (i.e. non-instantaneous shape relaxation) into our model would provide an additional mechanism for damping similar to the dispersion in orientation for rigid spheroids; however as we will observe for droplets in Section 5.3.1, including shape history would typically lead to $O(\epsilon^2)$ corrections in weak flows. It should also be noted that the continuum model developed here is not valid for fluctuations over length scales that are shorter than the interparticle distance, and the

results described above are expected to break down at sufficiently high wavenumbers.

Note that the present analysis has assumed that the background concentration is uniform (as in the analysis of Koch & Shaqfeh [102]), although we showed in the case of spheroids in Section 4.3.2 that including stratification can lead to qualitatively different results, and in particular to a wavenumber selection. As we shall see in Section 5.4.2, stratification is also quite significant in sedimenting suspensions of deformable particles (cf. Figure 5.4), and its effects should therefore be considered. As in Section 4.3.2 for spheroids, the analysis described above is easily repeated for fluctuations with respect to a linearly stratified concentration field:

$$c(\boldsymbol{x}, t) = n(1 - \beta z) + c'(\boldsymbol{x}, t). \tag{5.18}$$

The dispersion relation in this case is easily obtained, and only the final result is quoted here. The complex frequency for the normal mode of Equation (5.11) is found to have the following real and imaginary parts:

$$\omega_{\mathrm{R}} = M_0 F k \cos\theta - \frac{\beta n \tau_s M_0 F^2}{2\mu k} \cos\theta \sin^2\theta, \tag{5.19}$$

$$\omega_{\mathrm{I}} = \frac{\tau_s n M_0 F^2}{2\mu} \sin^2\theta - \frac{\beta n F}{\mu k^2} \sin^2\theta - k^2 \left(D_{\parallel} \cos^2\theta + D_{\perp} \sin^2\theta \right). \tag{5.20}$$

The real part ω_{R} still corresponds to traveling waves. The imaginary part ω_{I}, or growth rate, is now found to be damped by stratification at low wavenumbers, as shown by the second term on the right-hand side of Equation (5.20), which is to be compared to Equation (4.37) in the case of rigid spheroids. In particular, the balance of diffusion and stratification will once more result in a maximum growth rate at a finite wavenumber. This most unstable wavenumber can again be estimated by balancing the second and third terms in Equation (5.20). Using the scaling obtained in Section 4.3.3 for hydrodynamic diffusivities: $D_{\parallel,\perp} \sim U_0 a (ka)^{-3/2} \phi^{1/2}$ where a is the characteristic particle radius and ϕ is the local volume fraction, we obtain the same scaling as in the case of spheroids for the most unstable wavenumber:

$$ka \sim (\beta a)^{2/5} \phi^{1/5}. \tag{5.21}$$

5.3 Examples of deformable particles

The previous model, for all its simplicity, is based on two strong assumptions whose applicability may not seem obvious: first, that the particle shape relaxes instantaneously on the flow time scale; and second, that in weak flows the mobility of a slightly deformed particle can be written as a linear function of the local rate of strain with a positive constant of proportionality. In this section we discuss in turn the small deformation of viscous drops, elastic microcapsules and flexible polymers, and show that all three of these satisfy both assumptions in the limit of weak flows.

5.3.1 Viscous drops

The small deformation of a viscous drop in a linear flow field was first studied by Taylor [184, 185] and later generalized by Cox [44] and Frankel & Acrivos [68]. At zero Reynolds number the deformation is a function of two dimensionless groups, namely the viscosity ratio $\lambda = \mu/\mu_0$ and the capillary number $Ca = \mu\dot{\gamma}a/\sigma$, where $\dot{\gamma}$ is the characteristic shear rate of the imposed flow field, a is the radius of the undeformed drop and σ is the surface tension. The capillary number compares the effect of the flow, which tends to stretch the drop along its extensional axis, to the restoring effect of surface tension, which tries to minimize the interfacial energy by maintaining a spherical shape. In the limit of weak flows ($Ca \ll 1$), the drop is found to deform into an ellipsoid whose surface is defined by:

$$r = a\left(1 + 3\,Ca\,\boldsymbol{n}\cdot\mathbf{A}\cdot\boldsymbol{n}\right) + O(Ca^2), \tag{5.22}$$

where $\boldsymbol{n}$ is a radial unit vector and $\mathbf{A}$ is a symmetric and traceless second-order tensor satisfying the following evolution equation:

$$Ca\left(\frac{\partial \mathbf{A}}{\partial t} - \boldsymbol{\Omega}\cdot\mathbf{A} + \mathbf{A}\cdot\boldsymbol{\Omega}\right) = a_0\mathbf{E} + a_1\mathbf{A} + O(Ca), \tag{5.23}$$

with $a_0 = 5/(6\lambda+9)$ and $a_1 = -40(\lambda+1)/\left[(2\lambda+3)(19\lambda+16)\right]$. $\boldsymbol{\Omega}$ and $\mathbf{E}$ are respectively the rate of rotation and rate of strain of the imposed flow; in Equation (5.23) lengths have

been non-dimensionalized by the drop radius a, and time by the inverse of the effective characteristic shear rate $\dot{\gamma}^{-1}$. At zeroth order in the capillary number, Equation (5.23) leads to:

$$\mathbf{A} = -\frac{a_0}{a_1}\mathbf{E} = \frac{8(19\lambda + 16)}{3(\lambda + 1)}\mathbf{E} + O(Ca), \tag{5.24}$$

showing that the drop shape is only dependent upon the local rate of strain and not on the shape history (i.e. it relaxes instantaneously). Equation (5.22) then becomes:

$$r = a\left(1 + \frac{8(19\lambda + 16)}{\lambda + 1}\,Ca\,\boldsymbol{n}\cdot\mathbf{E}\cdot\boldsymbol{n}\right) + O(Ca^2). \tag{5.25}$$

The drop shape is therefore ellipsoidal, its principal axes are aligned with the principal axes of the local rate of strain, and it is stretched in the direction of flow extension. The sedimentation velocity of such a deformed drop placed in a gravity field was calculated by Haber & Hetsroni [76] using expansions in spherical harmonics, and more recently by Manga & Stone [123] by application of the reciprocal theorem for Stokes flow. Both indeed find a correction to the sedimentation velocity which is linear in the rate of strain $\mathbf{E}$ for small deformations. The result from Haber & Hetsroni [76] can be written as:

$$\mathbf{M}(\mathbf{E}) = M_0\left(\mathbf{I} + \frac{(19\lambda + 16)(3\lambda^2 + 3\lambda + 4)}{40(2 + 3\lambda)(1 + \lambda)^2}\,Ca\,\mathbf{E} + O(Ca^2)\right), \tag{5.26}$$

where $M_0 = (1 + \lambda)/2(2 + 3\lambda)\pi\mu a$ is the mobility of a spherical drop. Equation (5.26) is indeed identical to Equation (5.1) with a positive constant τ_s.

5.3.2   Elastic microcapsules

Barthès-Biesel [9] and Barthès-Biesel & Rallison [10] developed a similar small deformation theory for elastic microcapsules, which are particles consisting of an elastic membrane enclosing a drop of fluid. In this case the dimensionless parameters are the viscosity ratio λ, and the ratio $\epsilon = \mu\dot{\gamma}a/Eh$ of the viscous stresses in the fluid to elastic tensions in the membrane, where E denotes the elastic modulus of the membrane material and h its thickness. In weak flows ($\epsilon \ll 1$) the shape is again found to be ellipsoidal, and to leading

order in ϵ the equation of the surface is obtained to be [10]:

$$r = a\left(1 + f\epsilon \boldsymbol{n} \cdot \mathbf{E} \cdot \boldsymbol{n}\right) + O(\epsilon^2), \tag{5.27}$$

where f is a function of the material properties of the membrane; for an incompressible isotropic material in the small deformation regime $f = 25/2$.

The mobility of an ellipsoidal capsule is simply the mobility of a solid ellipsoid, which is known exactly [79]. In the case of small deformations the mobility can be expanded in a Taylor series with respect to the spherical shape, and is found to be:

$$\mathbf{M}(\mathbf{E}) = M_0\left(\mathbf{I} + \frac{f\epsilon}{5}\mathbf{E} + O(\epsilon^2)\right), \tag{5.28}$$

where $M_0 = 1/6\pi\mu a$ is the mobility of a solid sphere.

5.3.3 Flexible polymers

The applicability of the model to flexible polymers is less evident. In the absence of flow a polymer molecule relaxes to a statistically isotropic coiled state as a result of internal Brownian motion. The application of a weak flow will lead to a small departure from this isotropic state, provided that the molecule can sample its configuration space sufficiently fast on the flow time scale, i.e. that its relaxation time is much faster than the inverse $\dot{\gamma}^{-1}$ of the effective flow shear rate. The configuration of the molecule is then well represented by the average second moment of its end-to-end vector: $\mathbf{Q} = \langle \boldsymbol{RR} \rangle$, and its mobility can be written in the general form:

$$\mathbf{M} = m\mathbf{I} + m'\mathbf{Q}. \tag{5.29}$$

In the simplest case of a linear spring law, the configuration tensor $\mathbf{Q}$ satisfies the following evolution equation [18]:

$$Wi\left(\frac{\mathrm{d}}{\mathrm{d}t}\mathbf{Q} - \boldsymbol{\nabla u} \cdot \mathbf{Q} - \mathbf{Q} \cdot \boldsymbol{\nabla u}^{\mathrm{T}}\right) + \mathbf{Q} - \frac{kT}{H}\mathbf{I} = 0. \tag{5.30}$$

In Equation (5.30) Wi is the effective Weissenberg number defined as the ratio of the relaxation time of the molecule to the characteristic flow time scale $\dot{\gamma}^{-1}$, kT is the thermal energy of the solvent, and H is the spring constant. For weak flows ($Wi \ll 1$) the configuration tensor can be solved for as a perturbation expansion in powers of the Weissenberg number: $\mathbf{Q} = \mathbf{Q}^{(0)} + Wi\,\mathbf{Q}^{(1)} + O(Wi^2)$, yielding:

$$\mathbf{Q} = \frac{kT}{H}\left(\mathbf{I} + Wi\left(\boldsymbol{\nabla}\boldsymbol{u} + \boldsymbol{\nabla}\boldsymbol{u}^{\mathrm{T}}\right)\right) + O(Wi^2). \tag{5.31}$$

The mobility of the molecule Equation (5.29) then becomes:

$$\mathbf{M}(\mathbf{E}) = \left(m + m'\frac{kT}{H}\right)\mathbf{I} + 2m'\frac{kT}{H}\,Wi\,\mathbf{E} + O(Wi^2) \tag{5.32}$$

and is again in the form of Equation (5.1).

5.4   Numerical simulations

5.4.1   Simulation method for deformable particles

The simulation method described in Section 4.2.1 for spheroids is easily adapted to the case of deformable particles, using the model of Section 5.2.1. The motion of a particle α is described by the following dynamic equation:

$$\dot{\boldsymbol{x}}_\alpha = \mathbf{M}(\boldsymbol{x}_\alpha) \cdot \boldsymbol{F} + \boldsymbol{u}(\boldsymbol{x}_\alpha), \tag{5.33}$$

in which the linearized mobility of Equation (5.1) is used:

$$\mathbf{M}(\boldsymbol{x}_\alpha) = M_0\left(\mathbf{I} + \tau_s \mathbf{E}(\boldsymbol{x}_\alpha)\right). \tag{5.34}$$

Hydrodynamic interactions are again captured through the disturbance velocity field $\boldsymbol{u}$ which is obtained as a solution of the Stokes equations (4.5) with the same body force field Equation (4.8) as in the case of spheroids. $\boldsymbol{u}$ is used to infer the disturbance rate of strain $\mathbf{E}$ at the particle positions, which appears in the particle mobility Equation (5.34). The

Stokes equations are again solved spectrally on a grid as explained in Section 4.2.1. The particle positions are advanced using a fourth-order Runge-Kutta time-marching scheme. Unless noted otherwise the results shown are for non-periodic systems with slip boundary conditions.

In the following discussion the results are made dimensionless using the characteristic radius a of an undeformed particle, the sedimentation velocity $U_0 = M_0F$ of an isolated particle, and the characteristic time a/U_0 for an isolated particle to sediment over its radius. A precise non-dimensionalization of the equations yields two dimensionless groups (in addition to the volume fraction ϕ): a deformation parameter $\epsilon = \tau_s U_0/a$, which characterizes the effect of the flow on the shape deformation (in the case of droplets ϵ is essentially the Bond number or capillary number based on the shear rate induced by the sedimentation of a drop, modified to include the function of the viscosity ratio in Equation 5.26), and a resistance parameter $r = \Delta\rho V_p g/\mu U_0 a$, which takes on the value of 6π for a solid particle and of $2\pi(2 + 3\lambda)/(1 + \lambda)$ for a viscous droplet. Most of the results presented below are for a deformation parameter of $\epsilon = 0.5$ (which as we verify in Section 5.4.3 does indeed lead to small deformations at the volume fractions considered in this work), and a resistance parameter of $r = 15$, corresponding approximately to a drop with a viscosity ratio of 1. For the sake of comparison a few results are also shown for spherical particles, obtained by setting the deformation parameter ϵ to zero.

5.4.2 Concentration fluctuations and microstructure

The same type of analysis as in the sedimentation of spheroids can be carried out for deformable particles. Figure 5.2 shows the evolution of a few Fourier coefficients of the concentration field in non-periodic and periodic systems. Initially all Fourier modes are equally important. In the periodic case (Figure 5.2(b)) no significant growth is observed up until 1000 time units, after which all four modes start growing. As in the case of spheroids and as predicted by the linear stability analysis (Equation (5.15) and Figure 5.1) the longest mode $\boldsymbol{k} = (1, 0, 0)$ set by the width of the box dominates; the growth is exponential and does not seem to saturate. As expected the non-periodic case is quite
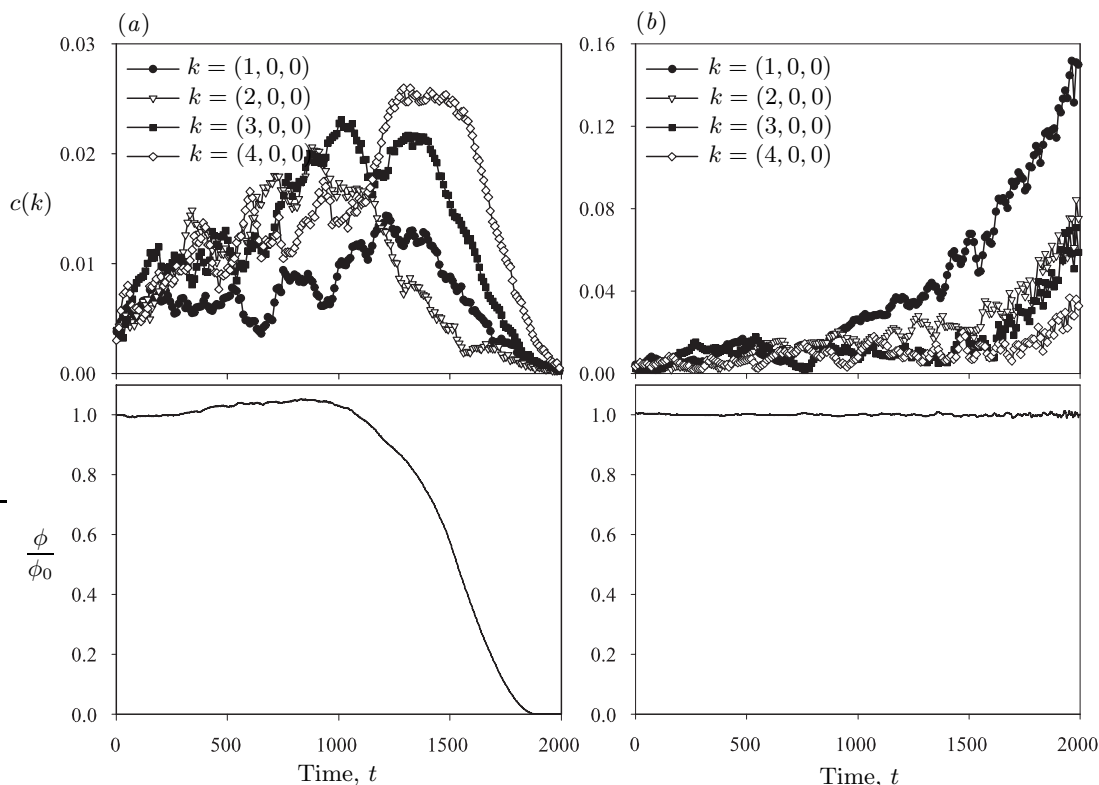
Figure 5.2: Time evolution of the Fourier coefficients of the concentration for a simulation of 158,239 deformable particles in a box of dimensions $L_x = 390$, $L_y = 390$ and $L_z = 2200$ (volume fraction $\phi = 0.2$ %), in both (a) non-periodic and (b) periodic boundary conditions. The results shown are for $\epsilon = 0.5$ and $r = 15$. The spectra were calculated over a subsection of the container: $250 < z < 650$, and were averaged over four runs. The bottom plots show the evolution of the mean volume fraction in the section in which the spectra were obtained.

different. The fluctuations are typically much weaker and the longest mode is not the strongest. Figure 5.2(a) shows that all modes initially grow at the same pace. The longest modes $\boldsymbol{k} = (1, 0, 0)$ and $\boldsymbol{k} = (2, 0, 0)$ however stop growing, giving way progressively to the growth of the shorter modes $\boldsymbol{k} = (3, 0, 0)$ and $\boldsymbol{k} = (4, 0, 0)$ which dominate up until the arrival of the suspension front (bottom plot) and the decay of the fluctuations.

As in the case of spheroids, Figure 5.2 suggests that the presence of walls and the possibility of stratification provide a mechanism for the break-up of the longest modes into fluctuations at shorter wavelengths, which are then observed to dominate the spectrum.

In spite of the strong similarity between the sedimentation of orientable and deformable particles, the two situations also present some differences. In the case of deformable particles the growth is much more progressive and slow: the peak of the fluctuations occurs quite late during the sedimentation process. For spheroids however the growth of the fluctuations was rapid initially, after which it was found to saturate in non-periodic systems and to slow down in periodic systems (Figure 4.2). This qualitative difference can be explained in the following way. In the case of spheroids we saw in Figure 4.10 that the fluctuations in the fluid result in a very quick alignment of the particles in the direction of gravity. Once most particles are aligned migration becomes rather difficult, as the lateral velocity of an almost vertical spheroid is weak: further clustering is therefore limited. In the case of deformable particles however, the stretching of the particles occurs along the axis of flow extension which is at $45°$ in shear flow, and migration is therefore quite easy even though the deformations may be small. Moreover as we will show in Section 5.4.3 deformations become larger with time, allowing for a steady increase of the concentration fluctuations, whereas for spheroids the orientation distribution quickly reaches a steady state. This explains why the instability takes a longer time to develop, and similar observations will be made on the mean velocity and velocity fluctuations in Section 5.4.4.

Figure 5.3 shows the pair distribution function and the structure factor in the lateral direction at $t = 0$ and $t = 1200$, for both deformable particles ($\epsilon = 0.5$) and isotropic particles such as rigid spheres ($\epsilon = 0$). At $t = 0$ the pair distribution is uniform in both cases, and no clear peak is present in the structure factor. In the case of deformable particles $g(x)$ progressively develops oscillations and a peak near $x = 0$; while these are not as pronounced as in Figure 4.4 for spheroids, the data of Figure 5.3 are less noisy and the oscillations clearer. These oscillations result in a sharp peak in the structure factor at $t = 1200$, which is located near $k = 3$. A similar structure as for spheroids is therefore present in the suspension, with denser regions or clusters alternating in the lateral direction with clear fluid. The evolution of the structure factor with time (not shown), also suggests that the formation of this structure is the consequence of the break-up of long wavelength
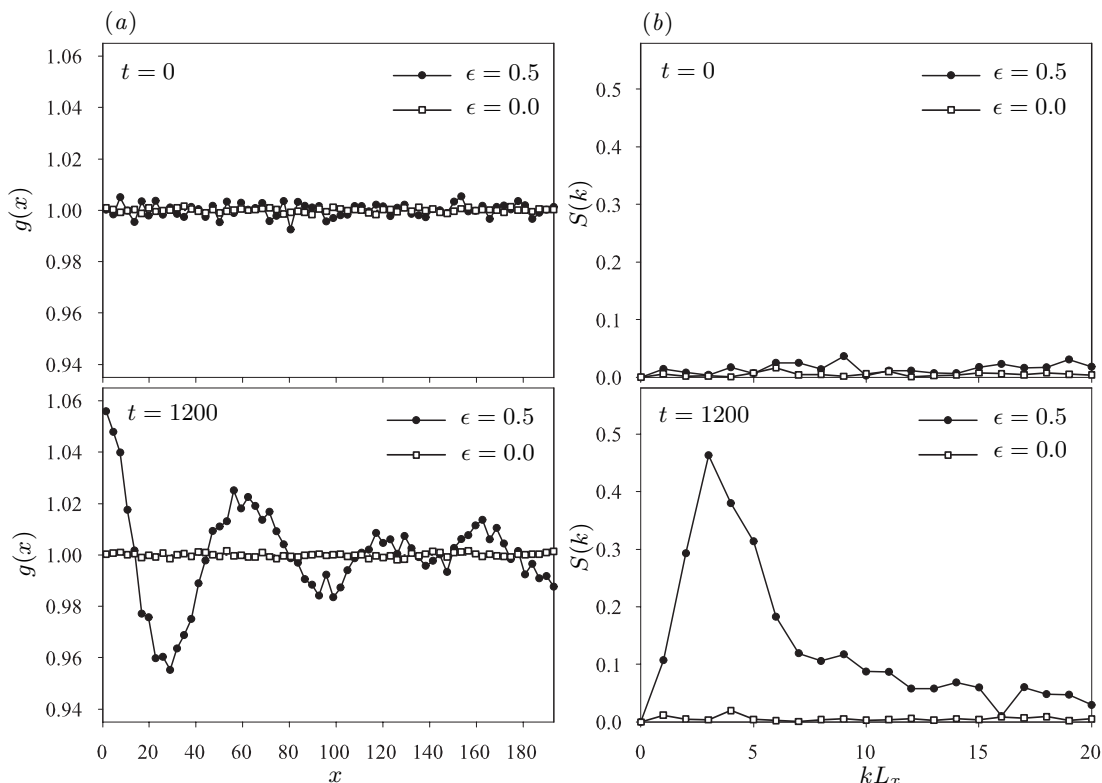
Figure 5.3: (a) Pair distribution function and (b) structure factor at $t = 0$ and $t = 1200$ for a simulation of 148,349 particles in a box of dimensions $L_x = 390$, $L_y = 145$ and $L_z = 2200$ (volume fraction $\phi = 0.5\ \%$). The plots show results for both deformable particles ($\epsilon = 0.5$) and isotropic particles such as rigid spheres ($\epsilon = 0$), at the same resistance parameter of $r = 15$.

fluctuations. In the case of undeformed isotropic particles ($\epsilon = 0$) no clear evolution of the pair distribution function or structure factor can be seen, and the fluctuations at $t = 1200$ remain negligible. This confirms the central role of shape anisotropy in the concentration instability observed in suspensions of either spheroids or deformable particles.

Results on the stratification are also shown in Figure 5.4 for both deformable and isotropic particles. The deformable case (Figure 5.4(a)) is qualitatively similar to the case of spheroids shown in Figures 4.3 and 4.22. In particular, a broad suspension front is observed to form between the bulk of the suspension and the clear fluid at the top; concentrations exceeding the bulk average are also observed near the bottom of the box as
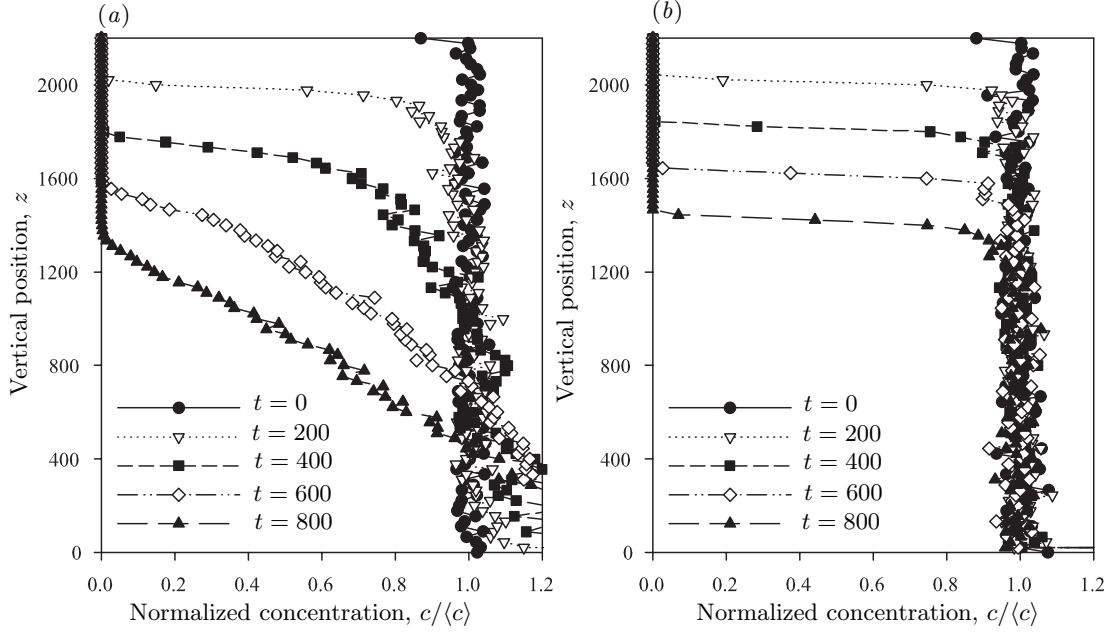
Figure 5.4: Cross-section averaged concentration profile in the vertical direction at various times during the sedimentation of suspensions of (a) deformable particles ($\epsilon = 0.5$), and (b) isotropic particles ($\epsilon = 0$). The results are for a resistance parameter of $r = 15$ and were obtained in suspensions of 148,349 particles in a box of dimensions $L_x = 390$, $L_y = 145$, $L_z = 2200$ (volume fraction $\phi = 0.5$ %). The concentration profile is normalized by its average value $\langle c \rangle$.

a result of clustering. As in the case of spheroids, this strong stratification is a consequence of the anisotropic mobility of the particles, which acts like a polydispersity, and of the segregation of the clusters near the bottom of the container. Note that neither of these effects is present in the case of isotropic particles (Figure 5.4(b)), where the interface between the suspension and the clear fluid is sharp and does not shown any significant broadening, and where the concentration in the suspension remains uniform in the vertical direction and equal to the mean bulk value.

5.4.3   Particle deformation

It is important to verify *a posteriori* that the deformation of the particles in the simulations remains small. As the particle shape or configuration is not explicitly calculated in the
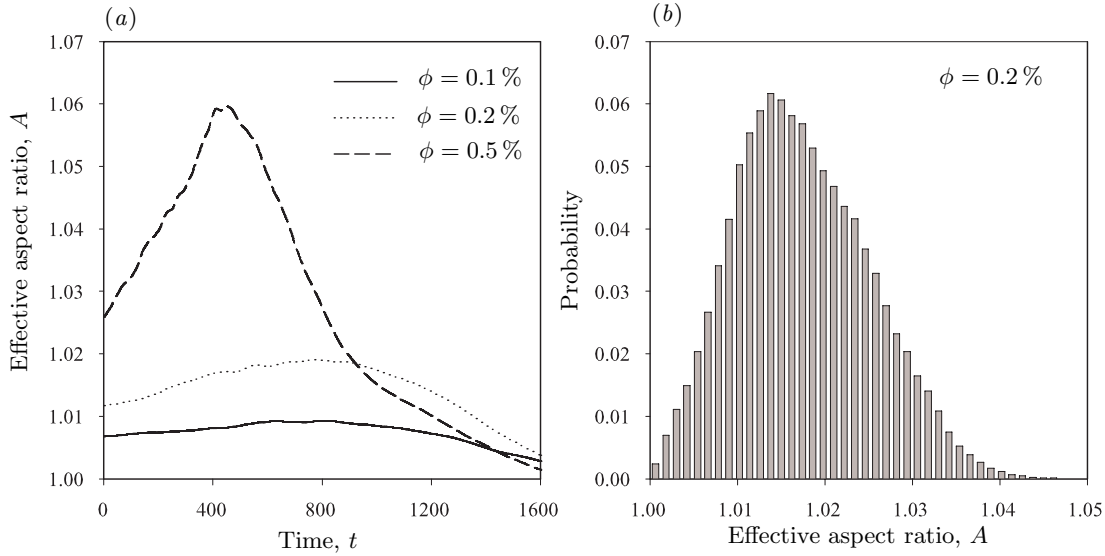
Figure 5.5: (*a*) Time evolution of the mean effective aspect ratio A at different volume fractions, and (*b*) distribution of the effective aspect ratio at a volume fraction of $\phi = 0.2\,\%$. The simulations are for $\epsilon = 0.5$ and $r = 15$ and were performed in a box of dimensions $L_x = 390$, $L_y = 145$, $L_z = 2200$. The results were obtained in a subsection of the box: $550 < z < 850$, and are averaged over ten runs.

simulation method, but only its mobility, we define an effective aspect ratio A as the ratio of the largest to the smallest of the eigenvalues of the mobility tensor. This ratio, which is 1 for a spherical particle but would approach 2 for a very slender particle, is indeed a measure of the anisotropy. Figure 5.5(*a*) shows the evolution of A at various volume fractions, for a deformation parameter ϵ of 0.5. All three curves present an initial increase of the effective aspect ratio as a result of the instability, followed by a decrease as the front approaches and as the fluctuations decay in the suspension. At low volume fractions ($\phi = 0.1\,\%$) the particles remain very close to isotropic, with a mean aspect ratio of less than 1.01. Deformations become more significant at higher concentrations as a result of the stronger velocity fluctuations; nevertheless the mean aspect ratio does not exceed 1.06 even at the highest volume fraction of 0.5 %, therefore validating our small deformation assumption. A typical distribution for the aspect ratio is shown in Figure 5.5(*b*) at $\phi = 0.2$ %: while the mean value falls slightly below 1.02, aspect ratios

in the suspension range from 1 up to nearly 1.05. This shape polydispersity is a natural consequence of the inhomogeneous flow field: the particles located in regions of strong shear typically undergo stronger deformations than those located near the local extrema of the disturbance velocity.

Note that larger deformations may have been expected given the value chosen for the deformation parameter ($\epsilon = 0.5$). This is a consequence of the length scale used in the definition of ϵ (the particle radius a), which can differ significantly from the characteristic length scale l_c over which the velocity fluctuations occur in the suspension. Typically the disturbance velocity varies over distances that are much larger than a (up to the width L of the container during the initial instants), leading to velocity gradients scaling with U_0/l_c. A more appropriate deformation parameter would be $\epsilon = \tau_s U_0/l_c$; however the fact that l_c is unknown *a priori* and evolves during the sedimentation process makes this definition awkward.

5.4.4   Velocity statistics

As in the case of spheroids, the particle deformations and the clustering have a strong impact on the sedimentation rate and the velocity fluctuations. This is illustrated in Figures 5.6 and 5.7, where results for deformable ($\epsilon = 0.5$) and isotropic ($\epsilon = 0$) particles are compared at various volume fractions. The mean sedimentation speed in both cases is shown in Figure 5.6. In the case of deformable particles Figure 5.6(a) shows a slow and steady increase of the mean sedimentation speed beyond the velocity of 1 of an isolated isotropic particle; this enhancement of the velocity is to be contrasted with the results of Figure 5.6(b) in the absence of deformations, where the mean velocity is approximately constant and equal to 1 at all three volume fractions. Note that in reality a dependence on volume fraction will be observed in suspensions of spherical particles, as fluid backflow results in velocity hindrance [13]; this effect however, which is a consequence of the finite volume of the particles, cannot be captured at the point force level used in our simulations. While the velocity increase in Figure 5.6(a) is quite weak at low volume fractions (due
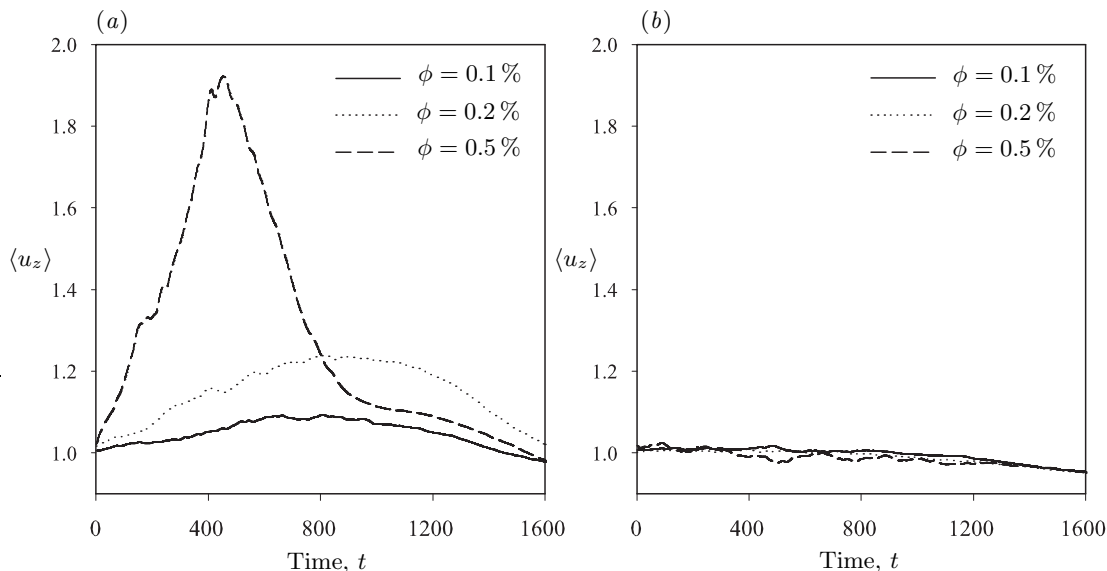
Figure 5.6: Mean sedimentation velocity $\langle u_z \rangle$ in suspensions of (a) deformable particles ($\epsilon = 0.5$), and (b) isotropic particles ($\epsilon = 0$) for a resistance parameter of $r = 15$ and at various volume fractions. The simulations were performed in a box of dimensions $L_x = 390$, $L_y = 145$, $L_z = 2200$. The results were obtained in a subsection of the box: $550 < z < 850$, and are averaged over ten runs.

to the small deformations resulting in a weak instability), it becomes quite significant at $\phi = 0.5$ % where the mean velocity reaches a peak value beyond 1.9. This very drastic increase is mainly a consequence of the clustering, as the particle mobility at $\phi = 0.5$ % was shown in Figure 5.5 to differ by less than 10 % from the isotropic mobility. Again the velocities are observed to decay as the front gets nearer and as the concentration fluctuations become weaker.

The very high value for the sedimentation speed at $\phi = 0.5$ % may seem surprising when compared to the case of prolate spheroids where the peak velocity was also slightly slightly less than 2 at the same volume fraction (Figure 4.8). This can be understood in the light of the comments made in Section 5.4.2: in the case of spheroids the strong and rapid alignment in the vertical direction somewhat hinders the lateral migration of the particles after a short initial time. For deformable particles however, the steady increase
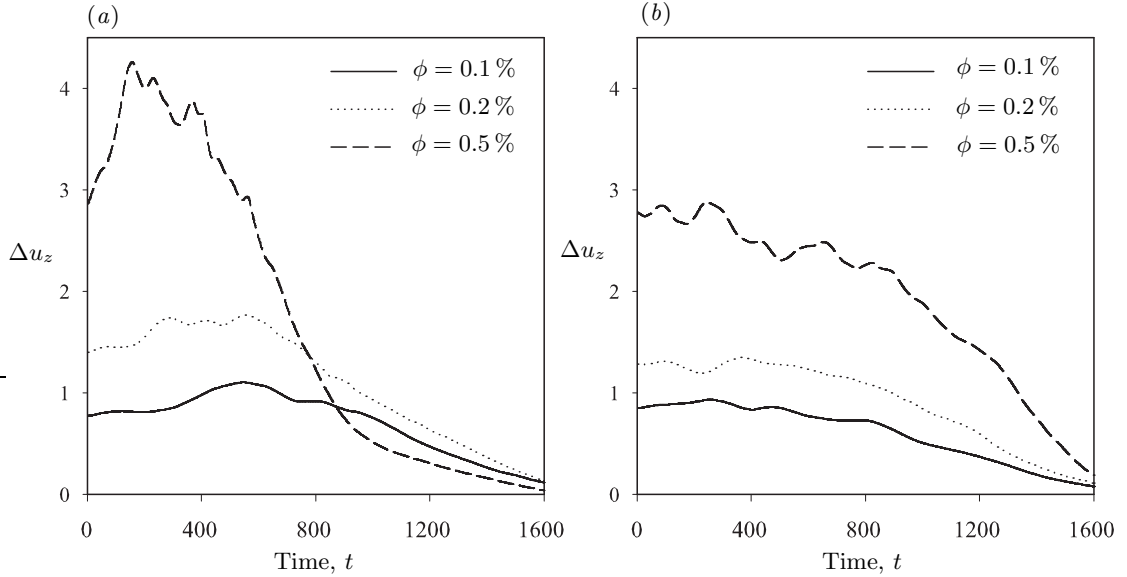
Figure 5.7: Velocity fluctuations Δu_z in the z-direction in suspensions of (a) deformable particles ($\epsilon = 0.5$), and (b) isotropic particles ($\epsilon = 0$) for a resistance parameter of $r = 15$ and at various volume fractions. The simulations were performed in a box of dimensions $L_x = 390$, $L_y = 145$, $L_z = 2200$. The results were obtained in a subsection of the box: $550 < z < 850$, and are averaged over ten runs.

in the effective aspect ratio and the orientation of the particles along the direction of flow extension result in a prolonged clustering and in the steady increase of the mean velocity.

The velocity fluctuations in the vertical direction are shown in Figure 5.7. While Figure 5.7(b) shows a decay of the fluctuations in the case of isotropic particles, confirming observations made in previous studies (e.g. [20, 132]), the instability in the deformable case causes an initial increase in the fluctuations, followed by a steady decrease towards zero; no steady state is reached. The initial increase, which is a result of the deformations and of the clustering, leads to very strong fluctuations at the highest volume fraction of $\phi = 0.5$ %, where they reach up to 4 times the sedimentation speed of an isotropic particle. The subsequent decay of the fluctuations also appears to be somewhat faster with deformable particles, a possible consequence of the strong stratification that is observed to develop in the suspension [120].
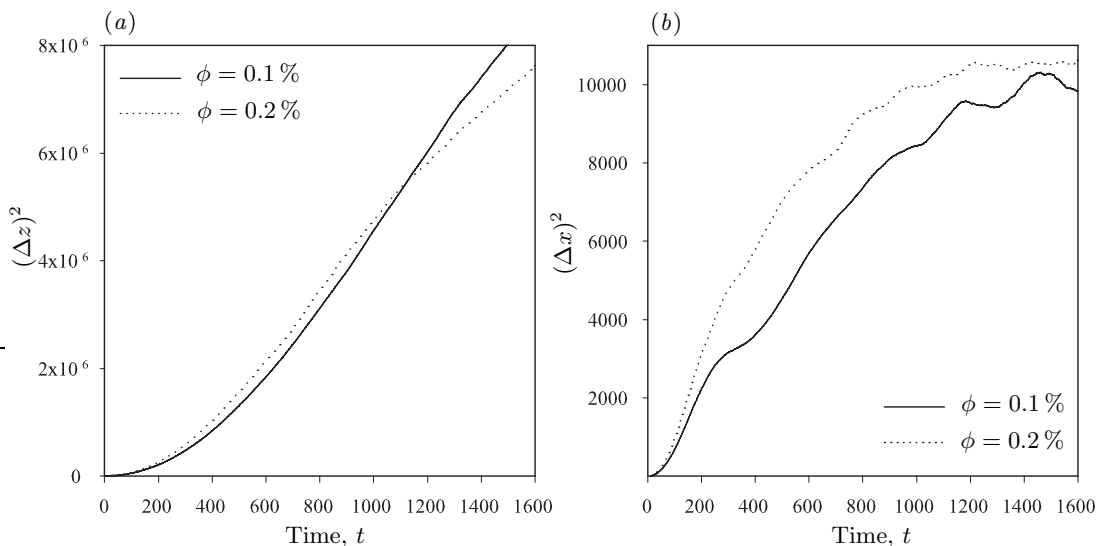
Figure 5.8: Mean squared displacement (a) in the z-direction and (b) in the x-direction at various volume fractions. The simulations are for $\epsilon = 0.5$ and $r = 15$ and were performed in a box of dimensions $L_x = 390$, $L_y = 145$, $L_z = 2200$; the results are averaged over three runs. For plot (a) the displacements were measured with respect to the mean motion of the entire suspension.

5.4.5   Hydrodynamic dispersion

The decay of high-wavenumber fluctuations in the stability analysis of Section 5.2.3 was attributed to hydrodynamic dispersion. As we previously mentioned, it is an established result that particles in sedimenting suspensions undergo a diffusive motion at long times relative to the mean settling motion and as a result of random fluctuations in the velocity field. In an attempt to understand the qualitative influence of the concentration fluctuations on hydrodynamic dispersion, mean-squared displacement curves were calculated and are shown in Figure 5.8. All curves have a zero derivative at $t = 0$ and show a convective behavior at short times: $(\Delta x)^2 \sim t^2$, $(\Delta z)^2 \sim t^2$. The slopes progressively stop increasing and a transition to a different regime occurs. The motion in the vertical direction becomes clearly diffusive, as suggested by the nearly constant slope in Figure 5.8(a): $(\Delta z)^2 \sim D_{\parallel}t$. While confirming the diffusive nature of the particle motions, Figure 5.8(a) should not be expected to produce quantitative results for the diffusivity, since close particle interactions

and short-scale variations of the velocity field, both of which play an important part in the diffusion process, have been completely neglected in the simulations.

Interestingly, diffusion is much less clear in the lateral direction (Figure 5.8(b)), in which the mean-squared displacement slowly saturates to a constant value. This saturation could have several origins: in particular lateral displacements are limited owing to the finite extent of the simulation box. It is also possible that the arrangement of the particles into dense clusters confines the lateral diffusion to the extent of one streamer; this seems to be supported by the steady state value of $\Delta x \approx 100$ in Figure 5.8(b), which is on the order of one fourth of a box width. A more precise investigation is needed to confirm this hypothesis.

5.5 Concluding remarks

A simple model was developed for sedimenting suspensions of deformable particles, which is equally applicable to viscous droplets, elastic microcapsules or flexible polymers. Under the assumptions that the flow-induced deformations are small and that the relaxation of the particle shape or configuration occurs instantaneously on the flow time scale, we were able to perform a linear stability analysis and to prove that such suspensions are unconditionally unstable to horizontal density fluctuations. The analysis, based on a dilute assumption in an unbounded domain, shows that in the absence of center-of-mass dispersion all wavenumbers are equally unstable. Hydrodynamic dispersion is predicted to damp fluctuations at high wavenumbers, while low-wavenumber fluctuations are damped by stratification: the combination of these two effects results in a wavenumber selection.

Point-particle simulations were also performed for deformable particles, confirming the mechanism for the instability. Density fluctuations in the particle distribution are observed to grow in time as a result of the deformation of the particles, which leads to a lateral migration; the growth of the fluctuations is typically slower but more steady than in suspensions of spheroids. The simulation results manifest a qualitatively similar mechanism for the wavenumber selection: while the longest wavelength grows without bound in

periodic systems, this mode is observed to break-up in non-periodic geometries, resulting in the formation of distinct clusters separated by clarified regions in the lateral direction. The instability for deformable particles also causes an increase in the mean sedimentation velocity, and our simulations suggest that quite small departures from isotropy can have very strong effects. To our knowledge no experimental data are available for comparison, but we hope that the present observations will spur additional interest into this problem.

As in the case of rigid spheroids studied in Chapter 4, a number of effects have been neglected. Most importantly, the small deformation approximation is likely to apply only in very dilute suspensions. In more concentrated systems the effects of short-range interactions, which will depend on the precise nature of the particles, may become significant. The previous work by Zinchenko & Davis [199, 200] addressed the case of very concentrated emulsions ($\phi \approx 0.5$): the non-local nature of the flow and the lubrication interactions between neighboring drops result in complex drop deformations that cannot be adequately captured by the small deformation model used in our work. In emulsions the concentration instability may also enhance drop coalescence and therefore increase polydispersity; coalescence during sedimentation, which was previously studied using population dynamics (e.g. [124, 193]), could be incorporated into our simulations using similar phenomenological collision models.

Chapter 6

Hydrodynamic interactions in the induced-charge electrophoresis of colloidal rod dispersions

6.1 Introduction

The manipulation of small particles suspended in a liquid is a challenging task, with applications in fields as diverse as separation science, analytical chemistry, microfluidics, or microrheology. A simple and widely used strategy for controlling particle motions consists of utilizing externally applied electric fields, which under certain conditions can cause particle migration and reorientation. The basic mechanism for this electrophoretic motion has been described extensively, and falls into the broad category of linear electrokinetic phenomena [163, 153, 85, 91]. A uniformly charged surface in an electrolyte attracts a cloud of counterions, which accumulate near the surface, resulting in the formation of an electrical double layer (EDL). The application of a steady electric field exerts a net force on the excess counterions, which migrate along the local electric field lines and drag the fluid with them. Near a fixed surface such as a channel wall, this effective body force inside the EDL drives an electroosmotic flow in the fluid bulk. In the case of a freely suspended

particle such as a colloid or macromolecule, electrophoretic migration occurs.

When the characteristic thickness λ_D of the EDL is much less than the characteristic radius of curvature of the particle, and if the applied field is sufficiently weak for surface conduction to be negligible, a boundary layer analysis of the electrokinetic and flow equations shows that to a good approximation the effects of the body force on the charge cloud can be captured by an effective slip velocity $\boldsymbol{u}_s$ at the outer edge of the EDL, given by the Helmholtz-Smoluchowski equation:

$$\boldsymbol{u}_s = -\frac{\varepsilon\zeta}{\mu}\boldsymbol{E}_s, \tag{6.1}$$

where ε and μ are the permittivity and viscosity of the fluid, respectively, and $\boldsymbol{E}_s$ is the value of the electric field at the edge of the EDL, where it is tangential to the local surface. The parameter ζ, called zeta-potential, is the electric potential drop across the double layer, and is considered a material property. The Helmholtz-Smoluchowski equation (6.1) can be used as a boundary condition for the flow equations outside of the charge cloud. For a freely suspended spherical particle this slip boundary condition was shown by Smoluchowski [174] and Henry [82] to yield the following translational velocity in an applied field $\boldsymbol{E}_\infty$:

$$\boldsymbol{U} = \frac{\varepsilon\zeta}{\mu}\boldsymbol{E}_\infty. \tag{6.2}$$

This classical result, which assumes a spherical shape, uniform charge density, absence of polarization, thin electrical double layer and weak applied field, was later generalized to more complex situations. First Morrison [130] proved that the same result holds for any particle shape under the same assumptions, and that the torque on a non-spherical particle is zero. O'Brien [142] and O'Brien & Ward [143] considered the effects of surface conduction, which results from charge build-up in some regions of the EDL and can be significant when the applied field is not weak or as the zeta-potential increases. Ion transport within the EDL was also addressed by Solomentsev, Pawar & Anderson [177], who also accounted for a non-uniform surface charge density. Solomentsev & Anderson [176] studied the effects of nonhomogeneous electric fields, and showed that electric field gradients cause rotation, while second gradients contribute to translation without rotation.

A variety of nonspherical particle shapes have also been considered, including spheroids [143, 59, 176], disks [169], rod-like particles [78, 36], and slender-bodies [175, 168].

While many investigations have addressed the case of particles with a fixed possibly nonuniform charge density, we focus in this Chapter on particles that can acquire a surface charge by polarization. Typical examples include polarizable dielectric particles and metallic colloids, which recently have found applications in analytical chemistry and biological assays (e.g. [136, 192]). The behavior of polarizable colloids in an electric field was previously studied in a series of papers by Dukhin and coworkers [70, 53, 52], the results of which were later summarized by Murtsovkin [133]. As explained in these papers, the polarization of a suspended sphere due to an applied electric field results in the formation of a dipolar charge cloud similar to the electrical double layer of classical electrophoresis, the effects of which can be modeled by an effective nonuniform zeta-potential. The action of the electric field on this charge cloud in turn drives a non-linear electrophoretic flow around the particle: this flow, which has a quadrupolar structure, does not lead to a net particle motion in the case of a sphere, but can create relative motions between nearby particles as a result of hydrodynamic interactions. Experimental observations of this induced flow were reported by Gamayunov, Mantrov & Murtsovkin [69] and recently by Levitan *et al.* [116].

The general framework for the modeling of these flows was laid out in detail in the context of fixed electrodes in microfluidic devices by Bazant & Squires [16, 178], who named the phenomenon induced-charge electroosmosis. The terminology of induced-charge electrophoresis was also proposed in the case of freely-suspended particles. More recently, Squires & Bazant [179] considered a variety of situations where broken symmetries in induced-charge electrophoresis (such as shape anisotropy, non-uniform surface properties, or non-uniform applied fields) can result in particle motions. An important conclusion of their work is that shape anisotropy can yield quite different behaviors than in the case of perfectly spherical particles: departures from sphericity indeed result in the rotation and alignment of the particle in the direction of the electric field, while shape asymmetry can lead to the migration of a particle carrying no net charge. Some of these effects were also

described recently by Yariv [197], who derived general formulae for the linear and angular velocities of a particle of arbitrary shape. The effects of induced-charge electrophoresis on the motion of rodlike particles was also recently considered by Rose *et al.* [152], who developed analytical single particle models for both thin and thick double layers, and obtained good agreement with experiments on metallic cylindrical colloids.

In this Chapter we focus on the effects of hydrodynamic interactions on the particle dynamics in suspensions of infinitely polarizable slender rods undergoing induced-charge electrophoresis. In particular, we wish to determine how the induced electrophoretic flows on the particle surfaces influence statistical properties such as orientation probabilities, pair probabilities, and hydrodynamic diffusivities in suspensions of hydrodynamically interacting particles. We start by considering the case of a single particle in Section 6.2, where we modify the slender-body formulation of Section 2.4 to capture the effects of the induced-charge electrophoresis on both the particle dynamics and the surrounding fluid flow. This new slender-body model combined with the method of reflections is used to investigate pair interactions in suspensions of aligned rods in Section 6.3. To obtain more quantitative information on the behavior of systems of many particles, we describe in Section 6.4 a method for the simulation of periodic systems of interacting rods that accounts for induced-charge electrophoresis, far-field and near-field hydrodynamic interactions, and Brownian motion. Simulation results are presented for both non-Brownian and Brownian suspensions in Section 6.5, where orientation probabilities, pair probabilities, and hydrodynamic dispersion are all discussed in detail. A summary and concluding remarks are given in Section 6.6.

6.2 Induced-charge electrophoresis of a polarizable rod

The basic theory and formalism for induced-charge electrokinetic phenomena were discussed in detail in the case of an infinite cylinder by Squires & Bazant [178], who also justifield them using an asymptotic analysis. In Section 6.2.1 we present an extension of their theory to the case of a polarizable rodlike particle, which for simplicity we take to
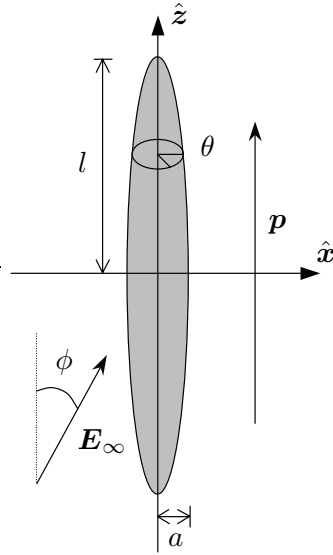
Figure 6.1: Problem geometry: the major axis of the spheroid, denoted by a unit vector $\boldsymbol{p}$, is assumed to be aligned in the z-direction, and forms an angle ϕ with respect to the direction of the applied electric field $\boldsymbol{E}_\infty$: $\boldsymbol{E}_\infty \cdot \boldsymbol{p} = E_\infty \cos\phi$. The azimuthal angle in the (x, y)-plane is denoted by θ.

be a spheroid. The limit of high aspect ratio, which is examined in Section 6.2.2 and Section 6.2.3, will yield results that are independent of the exact shape of the particle. Focus is placed on the derivation of a simple model that encompasses the electrophoretic motion of the particle while capturing the induced hydrodynamic interactions.

6.2.1 Basic theory

Consider a conducting polarizable spheroid in an electrolyte, to which an electric field $\boldsymbol{E}_\infty$ is applied as shown in Figure 6.1. We define a coordinate system such that the major axis of the spheroid, whose direction is given by a unit vector $\boldsymbol{p}$, lies along the z-direction, and without loss of generality we can assume that both vectors $\boldsymbol{E}_\infty$ and $\boldsymbol{p}$ lie in the (x, z)-plane and form an angle ϕ: $\boldsymbol{E}_\infty \cdot \boldsymbol{p} = E_\infty \cos\phi$. Let $2l$ and $2a$ be the lengths of the major and minor axes of the spheroid, respectively. We denote by A the particle aspect ratio, and by α its inverse, which will prove to be a useful quantity in the following discussion:

$$A = \alpha^{-1} = l/a. \tag{6.3}$$

We also introduce an abscissa $s \in [-l, l]$ along the axis of the particle and a cylindrical coordinate system (r, θ, z) where $r^2 = x^2 + y^2$ and θ is the azimuthal angle in the (x, y)-plane, and let $\boldsymbol{x} = r\hat{\boldsymbol{r}} + z\hat{\boldsymbol{z}}$ denote a general position vector. With these definitions the equation for the surface ∂S of the spheroid can be written as:

$$\frac{x^2 + y^2}{a^2} + \frac{z^2}{l^2} = \frac{r^2}{a^2} + \frac{z^2}{l^2} = 1. \tag{6.4}$$

Electric problem

When placed in a uniform electric field, a conducting particle modifies the field in such as way that the field lines intersect its surface at right angles. In a net neutral medium, the electric potential Φ therefore satisfies Laplace's equation:

$$\nabla^2 \Phi = 0, \tag{6.5}$$

subject to the conducting boundary conditions:

$$\begin{cases} \Phi(\boldsymbol{x}) = \Phi_s & \text{as } \boldsymbol{x} \in \partial S, \\ \boldsymbol{\nabla}\Phi(\boldsymbol{x}) \to -\boldsymbol{E}_\infty & \text{as } |\boldsymbol{x}| \to \infty, \end{cases} \tag{6.6}$$

where Φ_s is the uniform potential of the particle. As argued however by Squires & Bazant [178], this configuration is not stable as the electric field in the electrolyte results in the migration of ions along the field lines with a current $\boldsymbol{J} = \sigma\boldsymbol{E}$ (where σ is the conductivity of the solution). These ions accumulate on the surface of the particle which itself polarizes, resulting in the formation of a dipolar charge cloud similar in nature to the electrical double layer of classical electroosmosis. The double layer, which is net neutral, has the effect of repelling the electric field lines so that at steady state the particle and its EDL behave like an insulator.

In the following discussion we make the assumptions of thin EDL and weak applied fields. The first assumption states that the characteristic thickness λ_D of the double layer is much less than the characteristic radius of curvature of the particle:

$$\frac{\lambda_D}{a} \ll 1. \tag{6.7}$$

For a symmetric electrolyte the thickness λ_D, or Debye screening length, is defined as:

$$\lambda_D \equiv \sqrt{\frac{\varepsilon kT}{2n_0(ze)^2}}, \tag{6.8}$$

where ε is the electric permittivity of the electrolyte, k is Boltzman's constant, T is the absolute temperature, n_0 is the ionic concentration in the bulk of the electrolyte, and ze is the charge of a single ion. Under the thin EDL assumption a boundary layer approximation can be used to derive new boundary conditions for the electric field that apply at the edge of the EDL. Note that the thin EDL assumption is rather severe in the case of slender particles addressed here, since the particle thickness a can be quite small: it is likely therefore to apply only at relatively high salt concentrations, for which the Debye screening length is very small, or for mesoscopic or macroscopic particles, whose thickness a remains relatively large. In other cases the effects of finite EDL thickness are likely to come into play, and would require a different treatment. Finally, the weak applied field condition, or Debye-Hückel approximation, can be stated as $E_\infty a \ll kT/ze$ and ensures that surface conduction can be neglected.

Under these assumptions the boundary conditions Equation (6.6) can be replaced by the following insulating boundary conditions:

$$\begin{cases} \boldsymbol{n} \cdot \boldsymbol{\nabla}\Phi(\boldsymbol{x}) = 0 & \text{as } \boldsymbol{x} \in \partial S, \\ \boldsymbol{\nabla}\Phi(\boldsymbol{x}) \to -\boldsymbol{E}_\infty & \text{as } |\boldsymbol{x}| \to \infty, \end{cases} \tag{6.9}$$

where $\boldsymbol{n}$ is a unit outward normal on the particle surface. Equation (6.9) technically applies at the outer edge of the boundary layer, but can be safely enforced on the particle surface as we assumed that the Debye length is much less than the radius of the particle. This boundary condition, which can be justifield by matched asymptotics [178], results in electric field lines that are everywhere tangential to the particle surface.

Equations (6.5) and (6.9) for a spheroid admit an analytical solution, which can be obtained by the method of singularities [39, 40, 78]. The electric field outside of the

spheroid is sought as that due to a line distribution of potential dipoles along the focal
axis:

$$\boldsymbol{E}(\boldsymbol{x}) = \left\{ \mathbf{I} + \int_{-c}^{c} \left(c^2 - s^2\right) \left[\beta_\parallel \boldsymbol{D}\left(\boldsymbol{x} - s\hat{\boldsymbol{z}}; \hat{\boldsymbol{z}}\right) \hat{\boldsymbol{z}} + \beta_\perp \boldsymbol{D}\left(\boldsymbol{x} - s\hat{\boldsymbol{z}}; \hat{\boldsymbol{x}}\right) \hat{\boldsymbol{x}} \right] \mathrm{d}s \right\} \cdot \boldsymbol{E}_\infty. \quad (6.10)$$

$c = (l^2 - a^2)^{1/2}$ is the half-focal length of the spheroid, and $\boldsymbol{D}(\boldsymbol{x}; \boldsymbol{a})$ is the field induced
by a three-dimensional potential dipole of strength $\boldsymbol{a}$:

$$\boldsymbol{D}(\boldsymbol{x}; \boldsymbol{a}) = \boldsymbol{\nabla} \left(\boldsymbol{\nabla} \cdot \frac{\boldsymbol{a}}{x} \right) = -\frac{\boldsymbol{a}}{x^3} + 3\frac{(\boldsymbol{a} \cdot \boldsymbol{x})\boldsymbol{x}}{x^5}. \quad (6.11)$$

Equation (6.10) satisfies Laplace's equation by construction. The integral can be computed
analytically [40], and enforcing the boundary condition at the surface ($\boldsymbol{n} \cdot \boldsymbol{E}(\boldsymbol{x}) = 0$) allows
one to solve for the constants $\beta_\parallel$ and $\beta_\perp$:

$$\beta_\parallel = \alpha^2 \left[-4(1 - \alpha^2)^{1/2} + 2\alpha^2 \log \left(\frac{1 + (1 - \alpha^2)^{1/2}}{1 - (1 - \alpha^2)^{1/2}} \right) \right]^{-1}, \quad (6.12)$$

$$\beta_\perp = \alpha^2 \left[2(1 - \alpha^2)^{1/2} - 4(1 - \alpha^2)^{3/2} - 2\alpha^2 \log \left(\frac{1 + (1 - \alpha^2)^{1/2}}{1 - (1 - \alpha^2)^{1/2}} \right) \right]^{-1}. \quad (6.13)$$

After manipulation, the electric field and potential on the surface of the spheroid are found
to be:

$$\boldsymbol{E}_s = (\mathbf{I} - \boldsymbol{n}\boldsymbol{n}) \cdot \mathbf{G} \cdot \boldsymbol{E}_\infty, \quad (6.14)$$

$$\Phi_s = -\boldsymbol{x} \cdot \mathbf{G} \cdot \boldsymbol{E}_\infty. \quad (6.15)$$

$\mathbf{G}$ is the following geometric tensor:

$$\mathbf{G} = G_\parallel \hat{\boldsymbol{z}}\hat{\boldsymbol{z}} + G_\perp (\mathbf{I} - \hat{\boldsymbol{z}}\hat{\boldsymbol{z}}), \quad (6.16)$$

with

$$G_\parallel = -4\frac{(1 - \alpha^2)^{3/2}}{\alpha^2}\beta_\parallel, \quad G_\perp = -4\frac{(1 - \alpha^2)^{3/2}}{\alpha^2}\beta_\perp. \quad (6.17)$$

Equations (6.12)–(6.17) are equivalent to those given by Stratton [183] and Fair & Ander-
son [59], which were obtained using ellipsoidal harmonics. Figure 6.2 shows typical field
lines in the (x, z)-plane calculated for various orientations of the electric field. Note that

$\phi = 0$ $\phi = \pi/4$ $\phi = \pi/2$
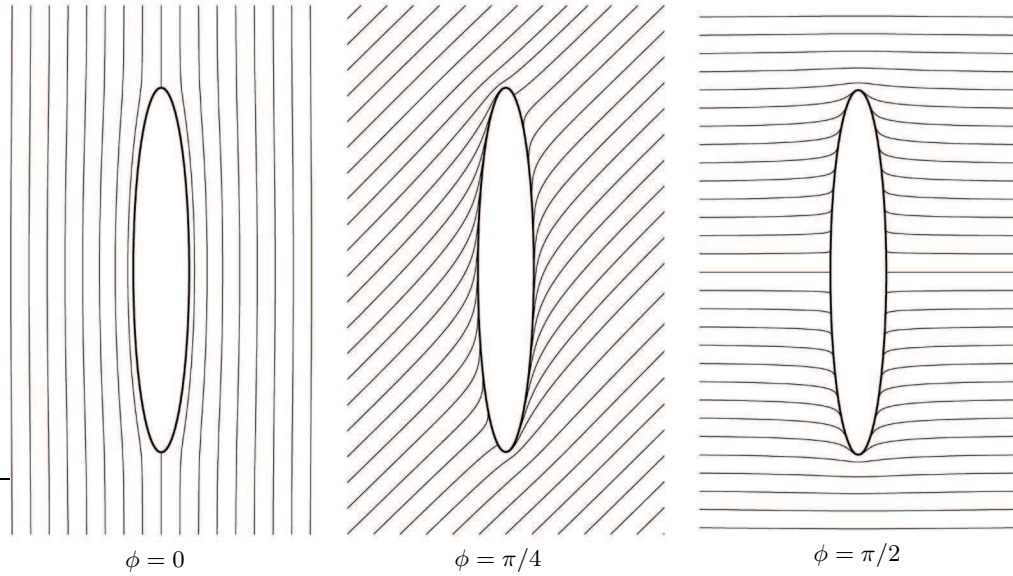
Figure 6.2: Electric field lines around a non-conducting spheroid of aspect ratio $A = 6.5$ for various orientations ϕ of the electric field, calculated from Equation (6.10). In three dimensions the deflection of the streamlines occurs over lengths scales of the order of the particle radius a, and the disturbance to the imposed field is very weak.

these field lines differ substantially from those obtained in two dimensions, by conformal mapping for instance, especially when the field is not aligned with the direction of the major axis: the deflection of the field lines in Figure 6.2 is quite weak and the electric field only differs from its value at infinity in a thin layer near the surface of the spheroid. This comes from the fact that the geometry is three-dimensional and a significant azimuthal field exists when $\phi \neq 0$, so that the deflection of the field lines occurs on length scales of the order of the spheroid thickness $2a$. Equations (6.10)–(6.11) also show that the electric field disturbance decays quite rapidly as $1/|\boldsymbol{x}|^3$ (vs. $1/|\boldsymbol{x}|^2$ in two dimensions), and Taylor expansions of $\beta_\parallel$ and $\beta_\perp$ as $\alpha \to 0$ show that both of these coefficients scale as α^2:

$$\boldsymbol{E}(\boldsymbol{x}) - \boldsymbol{E}_\infty \sim E_\infty \alpha^2 \frac{l^3}{|\boldsymbol{x}|^3}. \tag{6.18}$$

The perturbation to the imposed uniform electric field in the case of slender particles is therefore very weak, and we can safely expect electric interactions between particles in a

dilute suspension to be negligible. This is to be contrasted to the flow disturbance due to the induced-charge electrophoresis, which as we show in Section 6.2.2 decays more slowly as $1/|\boldsymbol{x}|^2$, and scales with the large dimension $2l$ of the particle.

Slip velocity and flow problem

The electric potential at the outer edge of the electrical double layer is equivalent to an induced zeta-potential, which varies along the surface of the particle and scales linearly with the imposed field. Following Squires & Bazant [178, 179], we can write the total zeta-potential on the surface as:

$$\zeta(\boldsymbol{x}) = \Phi_0 - \Phi_s(\boldsymbol{x}) = \Phi_0 + \boldsymbol{x} \cdot \mathsf{G} \cdot \boldsymbol{E}_\infty \quad \text{for } \boldsymbol{x} \in \partial S, \tag{6.19}$$

where the constant potential Φ_0 is determined to ensure that the area average of $\zeta(\boldsymbol{x})$ yields the native potential ζ_0 of the particle surface, which is assumed to be uniform:

$$\frac{1}{S} \int_{\partial S} \zeta(\boldsymbol{x}) \mathrm{d}S = \zeta_0 \quad \text{i.e.} \quad \Phi_0 = \zeta_0 + \frac{1}{S} \int_{\partial S} \Phi_s(\boldsymbol{x}) \mathrm{d}S, \tag{6.20}$$

where S denotes the surface area of the spheroid. Note that for the surface potential of Equation (6.15) the constant potential Φ_0 is simply the native zeta-potential: $\Phi_0 = \zeta_0$. The non-uniform zeta-potential Equation (6.19), along with the expression for the tangential component of the electric field (Equation 6.14), can be substituted into the Helmholtz-Smoluchowski equation (6.1) for the electrophoretic slip velocity on the surface of the particle, yielding:

$$\boldsymbol{u}_s(\boldsymbol{x}) = -\frac{\varepsilon\zeta}{\mu}\boldsymbol{E}_s = -\frac{\varepsilon}{\mu}\left(\zeta_0 + \boldsymbol{x} \cdot \mathsf{G} \cdot \boldsymbol{E}_\infty\right) \times \left[(\mathsf{I} - \boldsymbol{n}\boldsymbol{n}) \cdot \mathsf{G} \cdot \boldsymbol{E}_\infty\right]. \tag{6.21}$$

This slip velocity contains a linear contribution $-\varepsilon\zeta_0\boldsymbol{E}_s/\mu$, which is due to the native zeta-potential and corresponds to classical electrophoresis [59], and a quadratic contribution $-\varepsilon(\boldsymbol{x} \cdot \mathsf{G} \cdot \boldsymbol{E}_\infty)\boldsymbol{E}_s/\mu$, which is induced by the polarization and is responsible for induced-charge electrophoresis.

Fair & Anderson [59] made use of the Lorentz reciprocal theorem to derive the linear and angular velocities of a spheroid undergoing phoretic motion in Stokes flow with an arbitrary slip velocity:

$$\boldsymbol{U} = -\left(3V_p\right)^{-1} \iint_{\partial S} (\boldsymbol{n} \cdot \boldsymbol{x}) \boldsymbol{v}_s(\boldsymbol{x}) \mathrm{d}S, \tag{6.22}$$

$$\boldsymbol{\Omega} = -(2V_p)^{-1} \left[l^{-2}\boldsymbol{pp} + (a^2 + l^2)^{-1} \left(\mathsf{I} - \boldsymbol{pp}\right) \right] \cdot \iint_{\partial S} (\boldsymbol{n} \cdot \boldsymbol{x}) \boldsymbol{x} \times \boldsymbol{v}_s(\boldsymbol{x}) \mathrm{d}S, \tag{6.23}$$

where $V_p = 4\pi l a^2 / 3$ is the volume of the spheroid. Equations (6.22)–(6.23) are a special case of the more general expressions found by Yariv [197]. In particular, it should be noted that the motion of the particle is interfacially driven and does not directly result from the electric forces on the particle, which are screened by opposing forces on the counterions inside the EDL. Rather, the translation and rotation are consequences of the slip velocity at the particle surface, which is a kinematic boundary condition resulting from the balance between electric forces and viscous forces resulting from the motion of the counterions [5].

It can be shown that the linear part of the slip velocity leads to translation of the particle without rotation as in classical electrophoresis, while the quadratic part does not cause translation but results in a rotation that tends to align the particle in the direction of the electric field, in agreement with previous studies [16, 197, 179, 152]. As noted by Bazant & Squires [16], Yariv [197], and Squires & Bazant [179], the absence of a translational induced-charge electrophoretic velocity is a consequence of the fore-aft symmetry of the particle: an asymmetric particle would feel a quadratic translational velocity that quite interestingly would not change sign upon reversal of the electric field. In the remainder of the paper we will focus on the induced-charge effects and therefore discard the linear term in the slip velocity ($\zeta_0 \equiv 0$), as it has been studied extensively in the past (e.g. [59, 175]).

In addition to causing rotation, the slip velocity also drives a disturbance flow in the surrounding fluid. The induced velocity can be obtained as a solution of the Stokes equations:

$$-\mu \nabla^2 \boldsymbol{u} + \boldsymbol{\nabla} p = \boldsymbol{0}, \quad \boldsymbol{\nabla} \cdot \boldsymbol{u} = 0, \tag{6.24}$$

subject to the boundary conditions:

$$\begin{cases} \boldsymbol{u}(\boldsymbol{x}) = \boldsymbol{U} + \boldsymbol{\Omega} \times \boldsymbol{x} + \boldsymbol{u}_s(\boldsymbol{x}) & \text{as } \boldsymbol{x} \in \partial S, \\ \boldsymbol{u}(\boldsymbol{x}) \to \boldsymbol{0} & \text{as } |\boldsymbol{x}| \to \infty. \end{cases} \tag{6.25}$$

Once again, the slip boundary condition in Equation (6.25) applies at the outer edge of the electrical double layer, but can be enforced on the particle surface in the thin EDL limit. Except in a few special cases such as a perfect sphere or an infinite cylinder [178] as well as slightly deformed spheres [179], the complexity of the slip velocity Equation (6.21), which depends on both coordinates z and θ on the surface of the particle, precludes one from solving Equations (6.24)–(6.25) analytically. Numerical solutions could be obtained using boundary integral methods, such as that described by Youngren & Acrivos [198], which are easily modifield to allow a slip boundary condition. Such methods however are costly and would only allow the calculation of the flow around a few particles. As we show in the next section, the case of high-aspect ratio particles ($A = \alpha^{-1} \gg 1$) is amenable to an approximate solution based on slender-body theory.

6.2.2 Slender-body formulation

The slender-body theory for Stokes flow introduced in Section 2.4, which approximates the velocity disturbance induced by a particle whose length is much greater than its radius by a line distribution of point force singularities along the particle axis, can be modifield in the case where a slip velocity exists at the particle surface. Its application to electrophoresis was described by Solomentsev & Anderson [175]; recently Sellier [168] considered the more general case of a body of non-uniform zeta-potential and non-circular cross-section in an axisymmetric electric field. Batchelor's result (Equation (2.23)), modifield to include a slip boundary condition on the particle surface by Solomentsev & Anderson [175], relates the linear and angular velocities of the particle to the imposed fluid velocity $\boldsymbol{u}'$ (which may include the velocity disturbance in the fluid due to other particles), slip velocity $\boldsymbol{u}_s$, and line distribution of point forces $\boldsymbol{f}(s)$ in the following way:

$$\dot{\boldsymbol{x}} + s\dot{\boldsymbol{p}} + \tilde{\boldsymbol{u}}_s(s) - \boldsymbol{u}'(\boldsymbol{x} + s\boldsymbol{p}) = \frac{\log 2A}{4\pi\mu} (\mathbf{I} + \boldsymbol{pp}) \cdot \boldsymbol{f}(s) + O(|\boldsymbol{f}|/\mu), \tag{6.26}$$

where $\boldsymbol{x}$ denotes the position of the particle center of mass, and where we introduced the circumferential average $\tilde{\boldsymbol{u}}_s(s)$ of the slip velocity [175]:

$$\tilde{\boldsymbol{u}}_s(s) = \frac{1}{2\pi} \int_0^{2\pi} \boldsymbol{u}_s(s, \theta) \mathrm{d}\theta. \tag{6.27}$$

Note that this model, which describes the disturbance flow around the particle as that induced by a line distribution of point forces only, neglects the effects of particle thickness on the flow, and is therefore only valid for very slender particles. To account for the thickness of the particle, distributions of higher-order singularities (typically potential dipoles), would have to be included in the formulation, as previously done for instance by Claeys & Brady [42] in their Stokesian dynamics simulations of rigid spheroids. These additional singularities however would all contribute to higher-order terms in Equation (6.26).

Equations (2.24)–(2.25) for the linear and angular velocity, obtained by integration of Equation (6.26), now become:

$$\dot{\boldsymbol{x}} = \frac{1}{2l} \int_{-l}^{l} \left[\boldsymbol{u}'(\boldsymbol{x} + s\boldsymbol{p}) - \tilde{\boldsymbol{u}}_s(s) \right] \mathrm{d}s + \frac{\log 2A}{8\pi\mu l} (\mathbf{I} + \boldsymbol{pp}) \cdot \boldsymbol{F}^{(0)}, \tag{6.28}$$

$$\dot{\boldsymbol{p}} = \frac{3}{2l^3} (\mathbf{I} - \boldsymbol{pp}) \cdot \int_{-l}^{l} s \left[\boldsymbol{u}'(\boldsymbol{x} + s\boldsymbol{p}) - \tilde{\boldsymbol{u}}_s(s) \right] \mathrm{d}s + \frac{3\log 2A}{8\pi\mu l^3} (\mathbf{I} - \boldsymbol{pp}) \cdot \boldsymbol{F}^{(1)}, \tag{6.29}$$

where $\boldsymbol{F}^{(0)}$ and $\boldsymbol{F}^{(1)}$ again denote the zeroth and first moments of the force distribution along the rod axis:

$$\boldsymbol{F}^{(0)} = \int_{-l}^{l} \boldsymbol{f}(s) \mathrm{d}s, \quad \boldsymbol{F}^{(1)} = \int_{-l}^{l} s\boldsymbol{f}(s) \mathrm{d}s. \tag{6.30}$$

In addition to yielding simple expressions for the motion of the particle, this formulation also allows an easy calculation of the disturbance flow induced by the particle, using the convolution of Equation (2.22) where the line distribution of point forces $\boldsymbol{f}(s)$ is known from inverting Equation (6.26):

$$\boldsymbol{f}(s) = \frac{4\pi\mu}{\log 2A} \left(\mathbf{I} - \frac{1}{2}\boldsymbol{pp} \right) \cdot \left[\boldsymbol{U} + s\boldsymbol{\Omega} \times \boldsymbol{p} + \tilde{\boldsymbol{u}}_s(s) - \boldsymbol{u}'(\boldsymbol{x} + s\boldsymbol{p}) \right]. \tag{6.31}$$
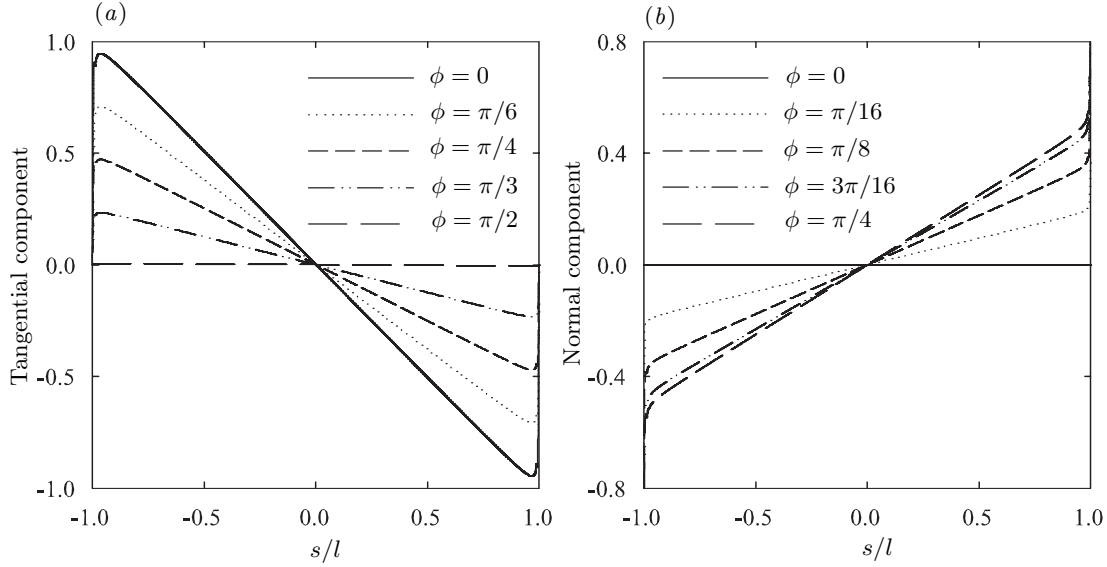
Figure 6.3: Tangential and normal components (with respect to the orientation vector $\boldsymbol{p}$) of the dimensionless circumferentially averaged slip velocity $\tilde{\boldsymbol{u}}_s(s)/(\varepsilon E_\infty^2/\mu)$, for various orientations ϕ of the electric field.

6.2.3 Slip velocity linearization

The previous discussion showed that the induced-charge electrophoretic motion of a slender-body, along with the associated disturbance velocity field in the fluid, are entirely determined by the circumferentially averaged slip velocity $\tilde{\boldsymbol{u}}_s$, which can be obtained by averaging Equation (6.21) over the azimuthal direction. Its tangential and normal components with respect to the orientation vector $\boldsymbol{p}$ are:

$$\boldsymbol{p}\boldsymbol{p} \cdot \tilde{\boldsymbol{u}}_s(s) = -\frac{\varepsilon E_\infty^2}{\mu} s G_\parallel^2 \cos^2\phi \left[1 - \frac{2\alpha^2 s^2 + \alpha^2(1-s^2)(G_\perp/G_\parallel)^2 \tan^2\phi}{2(1-s^2+\alpha^2 s^2)} \right] \hat{\boldsymbol{z}}, \quad (6.32)$$

$$(\mathbf{I} - \boldsymbol{p}\boldsymbol{p}) \cdot \tilde{\boldsymbol{u}}_s(s) = \frac{\varepsilon E_\infty^2}{\mu} s G_\perp G_\parallel \cos\phi \sin\phi \left[1 - \frac{(1+\alpha^2)(1-s^2)}{2(1-s^2+\alpha^2 s^2)} \right] \hat{\boldsymbol{x}}. \quad (6.33)$$

These components are plotted in dimensionless form in Figure 6.3 for an aspect ratio of $\alpha^{-1} = 20$ and for various orientations ϕ of the electric field. Figure 6.3 shows that both components vary almost linearly along the axis of the particle, the only significant

departure occurring near the ends. This is also confirmed by an expansion of Equations (6.32)–(6.33) as $\alpha \to 0$, and justifies the following linearization of the slip velocity for high aspect ratio particles:

$$\boldsymbol{pp} \cdot \tilde{\boldsymbol{u}}_s(s) \approx -\frac{\varepsilon E_\infty^2}{\mu} s G_\parallel^2 \cos^2 \phi \, \hat{\boldsymbol{z}}, \tag{6.34}$$

$$(\boldsymbol{\mathsf{I}} - \boldsymbol{pp}) \cdot \tilde{\boldsymbol{u}}_s(s) \approx \frac{\varepsilon E_\infty^2}{2\mu} s G_\perp G_\parallel \cos \phi \sin \phi \, \hat{\boldsymbol{x}}, \tag{6.35}$$

where in each case the error in the linearization is of order $O(\alpha^2)$. Equations (6.34)–(6.35) are conveniently recast in a frame-independent manner:

$$\tilde{\boldsymbol{u}}_s(s) \approx -\frac{\varepsilon}{\mu} s \left(\boldsymbol{p} \cdot \tilde{\boldsymbol{E}}_\infty \right) \tilde{\boldsymbol{E}}_\infty + O(\alpha^2), \tag{6.36}$$

where we have introduced the following notation:

$$\tilde{\boldsymbol{E}}_\infty = \left[G_\parallel \boldsymbol{pp} + \frac{1}{2} G_\perp (\boldsymbol{\mathsf{I}} - \boldsymbol{pp}) \right] \cdot \boldsymbol{E}_\infty. \tag{6.37}$$

Note that in the limit of high aspect ratio ($\alpha^{-1} \gg 1$) we have $\tilde{\boldsymbol{E}}_\infty \approx \boldsymbol{E}_\infty$.

From the discussion of Section 6.2.2 on slender-body theory, we infer that the induced translational velocity is zero: $\dot{\boldsymbol{x}}_s = \boldsymbol{0}$. The normal component of the slip contributes to an angular velocity:

$$\dot{\boldsymbol{p}}_s = \frac{\varepsilon}{\mu} (\boldsymbol{\mathsf{I}} - \boldsymbol{pp}) \cdot \tilde{\boldsymbol{E}}_\infty \left(\boldsymbol{p} \cdot \tilde{\boldsymbol{E}}_\infty \right). \tag{6.38}$$

The force distribution along the particle axis is linear and is given by:

$$\boldsymbol{f}(s) = -\frac{2\pi\varepsilon s}{\log 2A} \boldsymbol{p} \left(\boldsymbol{p} \cdot \tilde{\boldsymbol{E}}_\infty \right)^2. \tag{6.39}$$

Equation (2.22) can then be used to evaluate the velocity disturbance in the fluid.

It is enlightening for the purpose of understanding hydrodynamic interactions between suspended particles to investigate the far-field behavior of the velocity disturbance. The asymptotic behavior as $|\boldsymbol{x}|/l \to \infty$ can be obtained by performing a multipole expansion about the center of the particle, in which it is straightforward to see that the linear force distribution only contributes to the first force moment, or force dipole (cf. Section 2.3). This was pointed out by Batchelor [12], who observed that a linear force distribution on

a slender-body results in stresslet and rotlet flows in the far field. In the case of interest here, the rotlet flow is zero since induced-charge electrophoresis creates no torque and the force distribution Equation (6.39) is tangential to the rod axis. The stresslet disturbance flow $\boldsymbol{u}'_S$ can be shown to be:

$$\boldsymbol{u}'_S(\boldsymbol{x}) = -3\frac{(\boldsymbol{x} \cdot \mathbf{S} \cdot \boldsymbol{x})\,\boldsymbol{x}}{8\pi\mu|\boldsymbol{x}|^5}, \tag{6.40}$$

where the second-order traceless tensor $\mathbf{S}$ is given by:

$$\mathbf{S} = \frac{4\pi\varepsilon l^3}{3\log 2A}\left(\boldsymbol{p} \cdot \tilde{\boldsymbol{E}}_\infty\right)^2\left(\boldsymbol{p}\boldsymbol{p} - \frac{\mathbf{I}}{3}\right). \tag{6.41}$$

An important conclusion of this analysis is the far-field decay as $1/|\boldsymbol{x}|^2$ and scaling with $(\log 2A)^{-1}$ of the velocity disturbance, as shown by Equations (6.40)–(6.41). In particular, this can be compared to the decay of the electric field perturbation as $1/|\boldsymbol{x}|^3$, which furthermore scales with A^{-2} (Section 6.2.1): this remark will justify neglecting electric interactions between particles compared to hydrodynamic interactions in the subsequent discussion. Note that electric interactions may still become significant when two particles get very close to one another. In that case electric field gradients may indeed result in dielectrophoretic effects, which are not included in the present discussion: additional work will be required to determine the precise importance of these effects.

6.2.4   Electrorotational torque

In addition to the angular velocity $\dot{\boldsymbol{p}}_s$ induced by the slip velocity on the particle surface, rotation also occurs as a result of the interaction between the applied electric field and the dipole moment of the disturbance potential $\Phi(\boldsymbol{x}) - \Phi_\infty$, which creates an electrorotational torque (e.g. [98, 78, 179]). More precisely, a multipole expansion of the disturbance potential around the center of the rod can be written as:

$$\Phi(\boldsymbol{x}) + \boldsymbol{E}_\infty \cdot \boldsymbol{x} \approx \frac{1}{4\pi\varepsilon}\frac{\boldsymbol{d} \cdot \boldsymbol{x}}{|\boldsymbol{x}|^3} + ... \tag{6.42}$$

where the dipole strength $\boldsymbol{d}$ is easily obtained from Equation (6.10) as:

$$\boldsymbol{d} = -4\pi\varepsilon \int_{-c}^{c} (c^2 - s^2) \left(\beta_\parallel \hat{\boldsymbol{z}}\hat{\boldsymbol{z}} + \beta_\perp \hat{\boldsymbol{x}}\hat{\boldsymbol{x}}\right) \cdot \boldsymbol{E}_\infty \mathrm{d}s = \frac{8}{3}\pi\varepsilon l^3 \alpha^2 \tilde{\boldsymbol{E}}_\infty. \tag{6.43}$$

A similar expression was previously obtained by Han & Yang [78]. The dipole moment $\boldsymbol{d}$ results in an electrorotational torque on the rod given by $\boldsymbol{T}_e = \boldsymbol{d} \times \boldsymbol{E}_\infty$ (or equivalently a first force moment $\boldsymbol{F}_e^{(1)}$ satisfying: $(\mathsf{I} - \boldsymbol{pp}) \cdot \boldsymbol{F}_e^{(1)} = \boldsymbol{p} \times \boldsymbol{T}^e$), and yields the following angular velocity:

$$\dot{\boldsymbol{p}}_e = \frac{3\log 2A}{8\pi\mu l^3}(\mathsf{I} - \boldsymbol{pp}) \cdot \boldsymbol{F}_e^{(1)} = \frac{\varepsilon \log 2A}{\mu A^2}\boldsymbol{p} \times \left(\tilde{\boldsymbol{E}}_\infty \times \boldsymbol{E}_\infty\right), \tag{6.44}$$

which also contributes to the alignment of the rod in the direction of the field. Note however that this angular velocity is weaker than that induced by the slip velocity (Equation 6.38) by a factor of $\log 2A/A^2 \approx 0.01$ for $A = 20$. The electrorotational torque, which could easily be carried along, will therefore be neglected in the remainder of the paper.

6.3 Pair interactions

Substantial information about the macroscopic behavior of a suspension can be gained by a detailed understanding of pair interactions. In the following we use the results of the single particle model of Section 6.2 to derive expressions for the relative motion between two rods undergoing induced-charge electrophoresis. A detailed model based on interactions between slender-bodies is used to calculate the relative velocity in Section 6.3.1; asymptotic expressions for this velocity are also obtained in Appendix D by the method of reflections [101]. We then apply the results of Section 6.3.1 to evaluate the pair distribution function in a dilute suspension of aligned rods in Section 6.3.2.

6.3.1 Relative velocity

As depicted in Figure 6.4, we consider two rodlike particles, which for simplicity we take to be aligned in the direction of the electric field: $\boldsymbol{p}_1 = \boldsymbol{p}_2 = \boldsymbol{p}$. This assumption is
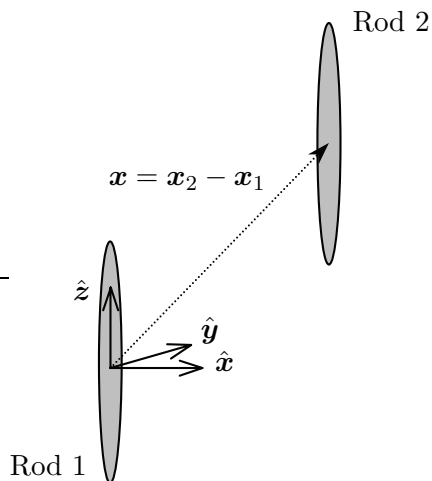
Figure 6.4: Particle pair considered in the analytical model of Section 6.3. For simplicity, the two rods are assumed to remain parallel and aligned in the direction of the electric field.

reasonable as we showed that the electric field causes the particles to reorient; even in Brownian suspensions good alignment can be observed at sufficiently high Péclet number (cf. Section 6.5.2). Let $\boldsymbol{x} = \boldsymbol{x}_2 - \boldsymbol{x}_1$ be the separation vector between the particle centers: we wish to determine the relative velocity $\boldsymbol{U} = \dot{\boldsymbol{x}}$ as a function of $\boldsymbol{x}$. In this problem the particles, which are assumed to be aligned with the field, are force-free and torque-free (although this fact will further discussed below): their only motion is therefore due to the velocity disturbance in the fluid, which is determined by the force distributions along the particle axes (Equation 2.22). Following the discussion of Section 2.4.3, we linearize these distributions. For a force- and torque-free rod, the linear distribution is simply given by (Section 2.4.3):

$$\boldsymbol{f}_\alpha(s_\alpha) = \frac{3}{2l^3} s_\alpha \mathscr{S}_\alpha \boldsymbol{p}, \tag{6.45}$$

where $\alpha = 1, 2$. The scalar stresslet (Equation (2.33)) is now given by:

$$\mathscr{S}_\alpha = -\frac{2\pi\mu}{\log 2A} \int_{-l}^{l} s_\alpha \boldsymbol{p} \cdot [\boldsymbol{u}'_\alpha(\boldsymbol{x}_\alpha + s_\alpha \boldsymbol{p}) - \tilde{\boldsymbol{u}}^s_\alpha(s_\alpha)] \mathrm{d}s_\alpha, \tag{6.46}$$

where $\boldsymbol{u}'_\alpha$ is the velocity disturbance created by the force distribution of rod $\beta \neq \alpha$. Recognizing that $\tilde{\boldsymbol{u}}^s_\alpha$ and $\boldsymbol{u}'_\alpha$ are given by Equations (6.36) and (2.22) respectively, an equation can be derived that relates the two stresslets $\mathscr{S}_\alpha$ and $\mathscr{S}_\beta$:

$$\mathscr{S}_\alpha = -\frac{4\pi\varepsilon l^3}{3\log 2A}G_\parallel^2 E_\infty^2 - \frac{3\mathscr{S}_\beta}{8l^3\log 2A}\iint_{-l}^{l}\boldsymbol{p}\cdot\mathsf{K}(\boldsymbol{x}+(s_\alpha-s_\beta)\boldsymbol{p})\cdot\boldsymbol{p}s_\alpha s_\beta\mathrm{d}s_\alpha\mathrm{d}s_\alpha, \quad (6.47)$$

where K is again the Oseen-Burgers tensor (Equation (2.8)). The first term on the right-hand side of Equation (6.47) is created by the slip velocity on rod α, and is to be compared to Equation (6.41). The second term however, which is linear in $\mathscr{S}_\beta$, is an induced stresslet which captures the effects of infinite reflections between the two rods. By symmetry it is possible to see that the two stresslets are equal: $\mathscr{S}_\alpha = \mathscr{S}_\beta = \mathscr{S}$; they can be easily obtained from Equation (6.47) as:

$$\mathscr{S} = -\frac{32\pi\varepsilon G_\parallel^2 E_\infty^2 l^3}{24\log 2A + 9H}, \quad \text{with} \quad H = \frac{1}{l^3}\iint_{-l}^{l}\boldsymbol{p}\cdot\mathsf{K}(\boldsymbol{x}+(s_2-s_1)\boldsymbol{p})\cdot\boldsymbol{p}s_1 s_2\mathrm{d}s_1\mathrm{d}s_2. \quad (6.48)$$

Equations (6.28) and (2.22) then yield the relative velocity:

$$\boldsymbol{U} = \dot{\boldsymbol{x}}_2 - \dot{\boldsymbol{x}}_1 = \frac{3\mathscr{S}}{16\pi\mu l^4}\iint_{-l}^{l}\mathsf{K}(\boldsymbol{x}+(s_2-s_1)\boldsymbol{p})\cdot\boldsymbol{p}s_1\mathrm{d}s_1\mathrm{d}s_2. \quad (6.49)$$

This expression is to be compared to the asymptotic result derived by the method of reflections and by multipole expansions in Appendix D. Using Equations (6.48)–(6.49), in which the double integrals can be evaluated numerically, we calculated the relative velocity $\boldsymbol{U}$ for various separation vectors $\boldsymbol{x}$. The results are summarized in Figure 6.5(a), which shows contours of $\dot{x} = (\boldsymbol{U}\cdot\boldsymbol{x})/|\boldsymbol{x}|$ in the plane containing the two rods. In particular, we observe that depending on the separation vector the rods are either attracted or repelled. For separation vectors $\boldsymbol{x}$ that form an angle of less than approximately $55°$ with the electric field, attraction is observed, while repulsion occurs for other orientations. The strongest attraction, as indicated by the white region, occurs when the two rods are side by side and offset by about half a particle length. The presence of distinct regions of attraction and repulsion suggest that pairing may occur: this will be confirmed in the
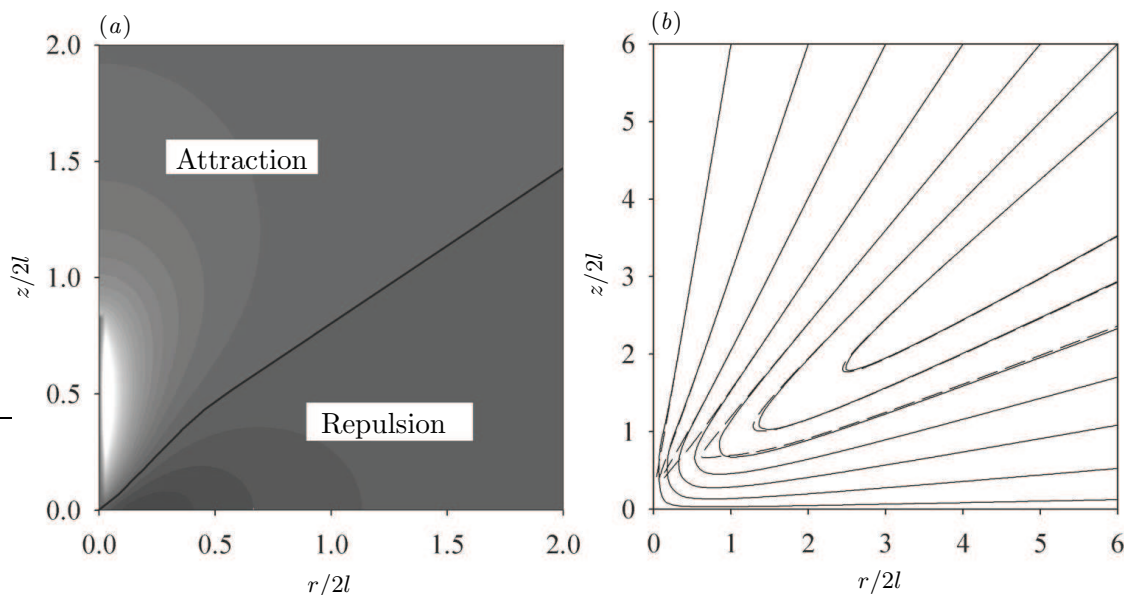
Figure 6.5: (a) Contours of the relative velocity magnitude $\dot{x} = (\boldsymbol{U} \cdot \boldsymbol{x})/|\boldsymbol{x}|$ between two parallel rods of aspect ratio $A = 20$. The interaction between the particles transitions from being repulsive (dark gray) to attractive (light gray to white) when the direction of the separation vector $\boldsymbol{x}$ changes from perpendicular to parallel to the electric field; the neutral line where $\dot{x} = 0$ is drawn in black. The strongest attraction (white) occurs when the two rods are side by side with an offset of about half a particle length. (b) Relative trajectories in the reference frame of one of the two rods, calculated using the slender-body formulation of Equation (6.49) (full lines), and using the method of reflections as shown in Appendix D (Equation D.17, dashed lines). Both methods yield indistinguishable results outside of a radius of approximately three rod lengths, but the asymptotic result fails at shorter distances.

next section where we calculate the pair distribution function in a dilute suspension, as well as in the more detailed simulations that we describe in Section 6.4 and Section 6.5. Figure 6.5(b) also shows relative trajectories in the reference frame of one of the two rods, calculated using both Equation (6.49) and the far-field approximation obtained in Appendix D by the method of reflections (Equation D.17). In particular, a comparison of the two methods shows that the method of reflections provides accurate results outside of a radius of approximately three rod lengths, but fails at closer distances.

A few comments on the limitations of our model are in order. The two assumptions that the rods are both torque-free and aligned in the direction of the field are rigorously

incompatible: hydrodynamic interactions indeed would cause slight rotations even in the presence of the electric field (cf. Appendix D), that could only be prevented by application of an external torque. However, departures from the exact alignment are typically very weak even when the rods are nearby (cf. Figure 6.11(d) for instance), so that the error incurred by either neglecting rotations or neglecting the torque required to keep the rods aligned can be expected to be small. Other effects that have been left out and may play a role are close particle interactions such as excluded volume and lubrication: these are likely to influence velocities and trajectories in the near-field, and will be accounted for in Section 6.4 and Section 6.5.

6.3.2 Pair distribution function

Our knowledge of the relative velocity between two rods (Equation 6.49) can be used to evaluate the pair distribution function in a dilute suspension. In the dilute regime pair interactions are most frequent, so that following Batchelor & Green [14] we can define $P(\boldsymbol{x}_0 + \boldsymbol{x}|\boldsymbol{x}_0; t)$ as the probability density function at time t for finding a rod at position $\boldsymbol{x}_0 + \boldsymbol{x}$ knowing that a rod is located in $\boldsymbol{x}_0$, where once again all rods are assumed to remain aligned in the direction of the field. Outside of the region of excluded volume, P can be normalized as:

$$P(\boldsymbol{x}_0 + \boldsymbol{x}|\boldsymbol{x}_0; t) = np\left(\boldsymbol{x}/2l; t\right), \tag{6.50}$$

where n is the number density in the suspension, and p tends to 1 as $|\boldsymbol{x}|/2l \rightarrow \infty$. In the absence of Brownian motion, p satisfies the following conservation equation:

$$\frac{\partial p}{\partial t} + \boldsymbol{\nabla} \cdot (\boldsymbol{U}p) = 0, \tag{6.51}$$

which at steady state reduces to:

$$\boldsymbol{U} \cdot \boldsymbol{\nabla}(\log p) = -\boldsymbol{\nabla} \cdot \boldsymbol{U}. \tag{6.52}$$

In Equations (6.51) and (6.52), $\boldsymbol{U}$ is the relative velocity between two rods separated by $\boldsymbol{x}$, and is given by Equation (6.49). In particular, the expression found for $\boldsymbol{U}$ has a non-zero

divergence:

$$\boldsymbol{\nabla} \cdot \boldsymbol{U} = \frac{3}{16\pi\mu l^4}\boldsymbol{\nabla}\mathscr{S} \cdot \iint_{-l}^{l} \mathsf{K}(\boldsymbol{x} + (s_2 - s_1)\boldsymbol{p}) \cdot \boldsymbol{p}s_1\mathrm{d}s_1\mathrm{d}s_2 \neq 0, \qquad (6.53)$$

which is a consequence of accounting for multiple reflections between the two rods in Equation (6.47). Integrating Equation (6.52) analytically is not tractable in general, although we show in Appendix D that an asymptotic solution can be obtained in the far-field. However the method of characteristics can be employed to obtain a numerical solution, by simultaneously integrating the two following equations:

$$\frac{\mathrm{d}\boldsymbol{x}}{\mathrm{d}t} = \boldsymbol{U}(\boldsymbol{x}), \qquad (6.54)$$

$$\frac{\mathrm{d}}{\mathrm{d}t}(\log p) = -\boldsymbol{\nabla} \cdot \boldsymbol{U}(\boldsymbol{x}), \qquad (6.55)$$

subject to the boundary condition $p(\boldsymbol{x}) \to 1$ as $|\boldsymbol{x}| \to \infty$. These equations were integrated numerically using a fourth-order Runge-Kutta time-marching scheme, along with a 50-point Gauss-Legendre quadrature for the double integrals in the expressions for the velocity. The results for rods of aspect ratio $A = 20$ are shown in Figure 6.6, in which the value of p was set to zero along the segment $[0, 1]$ of the z-axis to reproduce the effects of excluded volume. The pair distribution of Figure 6.6 presents several interesting features. In particular the presence of a sharp peak (white region) shows that there is a high probability of finding two particles next to one another, with an offset of slightly more than half a rod length, i.e. that particle pairings can be expected in a suspension. Conversely, the black region near the origin corresponds to a depletion, and suggests that it is highly unlikely for two particles to remain aligned side by side, as could have been expected from the relative velocity field of Figure 6.5. Once again, the pair distribution of Figure 6.6 can only be taken as qualitative owing to the limitations mentioned above; in particular close particle interactions will affect the shapes of the pairing and depletion regions as shown in Section 6.5.
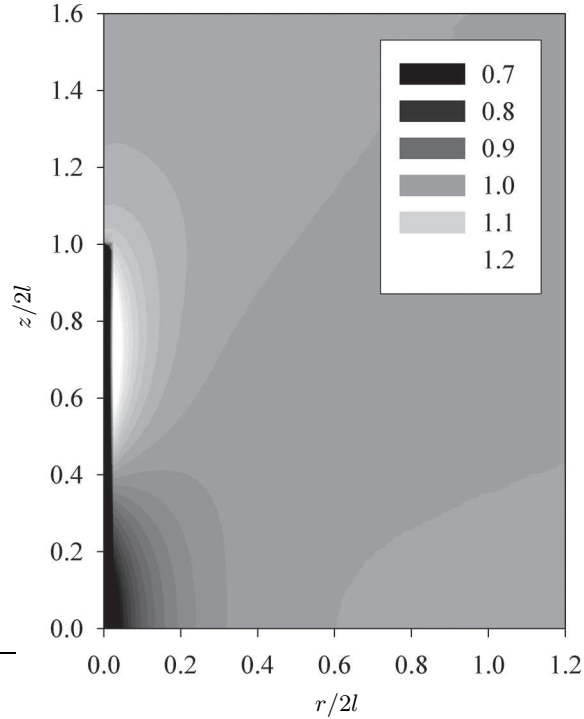
Figure 6.6: Pair distribution function $p(r/2l, z/2l)$ in a dilute suspension of rods of aspect ratio $A = 20$, obtained by numerically solving the conservation equation (6.52) using the method of characteristics (Equations (6.54)–(6.55)). The distribution function is normalized so that it tends to 1 far from the origin. The value of p was set to zero along the segment $[0, 1]$ of the z-axis to reproduce the effects of excluded volume.

6.4 Simulation method

In this section we describe a method for the simulation of high-aspect ratio rodlike particles undergoing induced-charge electrophoresis, which includes both far-field hydrodynamic interactions and near-field lubrication forces, as well as Brownian motion. The method, which is based on the algorithm described in Chapter 3 for the sedimentation of fibers, can be viewed as an extension of the two-particle model of Section 6.3 to larger assemblies of particles. Brownian motion is included in a self-consistent manner using a spectral approximation of the mobility square-root first suggested by Fixman [66], in a similar way as has been done in Stokesian dynamics simulations by Banchio & Brady [8].

6.4.1   Mathematical formulation

Equations of motion

We consider a periodic system of N rods of aspect ratio A in a box of dimensions $L_x \times L_y \times L_z$. We denote by $\boldsymbol{x}_\alpha$ and $\boldsymbol{p}_\alpha$ the position and orientation vectors of a given rod $\alpha = 1, ..., N$. Equations of motion for $\boldsymbol{x}_\alpha$ and $\boldsymbol{p}_\alpha$ are obtained from the slender-body formulation of Section 6.2.2:

$$\dot{\boldsymbol{x}}_\alpha = \int_{-1/2}^{1/2} \boldsymbol{u}'_\alpha \mathrm{d}s_\alpha + (\mathsf{I} + \boldsymbol{p}_\alpha \boldsymbol{p}_\alpha) \cdot \boldsymbol{F}_\alpha^{(0)}, \tag{6.56}$$

$$\dot{\boldsymbol{p}}_\alpha = 12\,(\mathsf{I} - \boldsymbol{p}_\alpha \boldsymbol{p}_\alpha) \cdot \int_{-1/2}^{1/2} s\left[\boldsymbol{u}'_\alpha - Pe\,\tilde{\boldsymbol{u}}_\alpha^s\right]\mathrm{d}s_\alpha + 12\,\,(\mathsf{I} - \boldsymbol{p}_\alpha \boldsymbol{p}_\alpha) \cdot \boldsymbol{F}_\alpha^{(1)}. \tag{6.57}$$

where $\boldsymbol{F}_\alpha^{(0)}$ and $\boldsymbol{F}_\alpha^{(1)}$ denote the zeroth and first moments of the force distribution along the rod of interest, respectively. In this section and for all Brownian simulations, equations are made dimensionless by the following length, time and velocity scales:

$$l_c = 2l, \quad t_c = \frac{32\pi\mu l^3}{kT\log 2A}, \quad u_c = \frac{l_c}{t_c} = \frac{kT\log 2A}{16\pi\mu l^2}. \tag{6.58}$$

The thermal time scale t_c can be viewed as the characteristic time for a rod to diffuse over a distance equal to its length under the action of Brownian motion. In the case of non-Brownian systems discussed in Section 6.5.1, we shall use the electroviscous time, or characteristic time for fluid advection along the length of a rod under the action of the slip:

$$t_c = \frac{\mu}{\varepsilon E_\infty^2}, \quad u_c = \frac{l_c}{t_c} = \frac{2\varepsilon E_\infty^2 l}{\mu}. \tag{6.59}$$

The equations for the non-Brownian case can easily be obtained by setting the Brownian forces and torques to zero and changing the non-dimensionalization.

In Equations (6.56)–(6.57), $\boldsymbol{u}'_\alpha$ is the velocity disturbance induced by rods $\beta \neq \alpha$ and evaluated at position $\boldsymbol{x}_\alpha + s_\alpha \boldsymbol{p}_\alpha$ along the rod axis; its calculation proceeds as in Section 3.2.3 using the periodic Green's function for Stokes flow (Appendix A). The dimensionless slip velocity $\tilde{\boldsymbol{u}}_\alpha^s$ is obtained from Equation (6.36) as:

$$\tilde{\boldsymbol{u}}_\alpha^s(s_\alpha, \boldsymbol{p}_\alpha) = -s_\alpha \left(\boldsymbol{p}_\alpha \cdot \boldsymbol{e}_\alpha\right) \boldsymbol{e}_\alpha, \tag{6.60}$$

where $\boldsymbol{e}_\alpha$ corresponds to $\tilde{\boldsymbol{E}}_\infty$ after non-dimensionalization:

$$\boldsymbol{e}_\alpha = \left[G_\parallel \boldsymbol{p}_\alpha \boldsymbol{p}_\alpha + \frac{1}{2} G_\perp \left(\mathbf{I} - \boldsymbol{p}_\alpha \boldsymbol{p}_\alpha\right)\right] \cdot \hat{\boldsymbol{z}}, \tag{6.61}$$

and where we have chosen the z-direction as the direction of the electric field. The strength of the electric field is captured by the Péclet number Pe in Equation (6.57), which compares the magnitude of the slip velocity to the thermal velocity scale u_c:

$$Pe = \frac{2\varepsilon l E_\infty^2 / \mu}{u_c} = \frac{32\pi \varepsilon l^3 E_\infty^2}{kT \log 2A}. \tag{6.62}$$

A rotational Péclet number based on the rotary diffusivity of the rods and on the angular velocity induced by induced-charge electrophoresis can also be defined, and will prove more useful in Section 6.5.2 when discussing orientation distributions:

$$Pe_r = \frac{\varepsilon E_\infty^2 \mu}{D_r} = \frac{8\pi \varepsilon l^3 E_\infty^2}{3kT \log 2A} = \frac{Pe}{12}. \tag{6.63}$$

Neglecting the electrorotational torque as justifield in Section 6.2.4, the external forces and torques on the rods will include contributions from lubrication and contacts, as well as Brownian motion:

$$\boldsymbol{F}_\alpha^{(0)} = \boldsymbol{F}_\alpha^{(0),l} + \boldsymbol{F}_\alpha^{(0),c} + \boldsymbol{F}_\alpha^{(0),b}, \quad \boldsymbol{F}_\alpha^{(1)} = \boldsymbol{F}_\alpha^{(1),l} + \boldsymbol{F}_\alpha^{(1),c} + \boldsymbol{F}_\alpha^{(1),b}. \tag{6.64}$$

The lubrication and contact forces and torques are implemented in the same way as in Section 3.2.2. The Brownian forces and torques, which model thermal fluctuations of the solvent molecules, will be discussed in detail in Section 6.4.2.

Hydrodynamic interactions

Hydrodynamic interactions between rods are captured through the disturbance velocity in Equations (6.56)–(6.57), which is obtained as:

$$\boldsymbol{u}'_\alpha(\boldsymbol{x}_\alpha + s_\alpha \boldsymbol{p}_\alpha) = \frac{1}{2\log 2A} \sum_{\beta=1}^{N} \int_{-1/2}^{1/2} \mathbf{J}(\boldsymbol{x}_\alpha + s_\alpha \boldsymbol{p}_\alpha - \boldsymbol{x}_\beta - s_\beta \boldsymbol{p}_\beta) \cdot \boldsymbol{f}_\beta(s_\beta) \mathrm{d}s_\beta. \qquad (6.65)$$

The convolution kernel $\mathbf{J}$ is again the appropriate Green's function for Stokes flow. Here we use the periodic Green's function $\mathbf{K}_p$ derived in Appendix A, modifield as in Equation (3.9) by removing the Oseen-Burgers tensor when $\beta = \alpha$. The calculation of the sums in Equation (6.65) is performed using the smooth particle-mesh algorithm of Chapter 3, to which the reader is referred for more details.

As described in Sections 2.4.3 and 3.2.4, we linearize the force distribution using Legendre polynomials as follows:

$$\boldsymbol{f}_\alpha(s_\alpha) = \boldsymbol{F}_\alpha^{(0)} + 12\,s_\alpha \left[(\mathbf{I} - \boldsymbol{p}_\alpha \boldsymbol{p}_\alpha) \cdot \boldsymbol{F}_\alpha^{(1)} + \mathscr{S}_\alpha \boldsymbol{p}_\alpha \right], \qquad (6.66)$$

in which the scalar stresslet $\mathscr{S}_\alpha$ is now defined in dimensionless form as:

$$\mathscr{S}_\alpha = -\frac{1}{2} \int_{-1/2}^{1/2} s_\alpha \boldsymbol{p}_\alpha \cdot \left[\boldsymbol{u}'_\alpha(\boldsymbol{x}_\alpha + s_\alpha \boldsymbol{p}_\alpha) - Pe\, \tilde{\boldsymbol{u}}_\alpha^s(s_\alpha) \right] \mathrm{d}s_\alpha. \qquad (6.67)$$

The method of solution then proceeds as follows. Equations (6.60) and (6.65), when substituted into the definition of the stresslet equation (6.67), allow one to write a linear system for the stresslets $\mathscr{S}_\alpha$ ($\alpha = 1, ..., N$), and for the magnitudes of the lubrication forces. This linear system is inverted using a preconditioned generalized minimum residual iterative method (cf. Section 3.4). Once stresslets and lubrication forces are known, the dynamic equations (6.56)–(6.57) are used to integrate the position and orientation of the rod forward in time, using the midpoint algorithm of Section 6.4.3.

The calculation of the linear and angular velocities from the knowledge of the forces and torques on the particles corresponds to the so-called mobility problem (e.g. [25]). Let $\mathscr{U} = [\dot{\boldsymbol{x}}_\alpha, \dot{\boldsymbol{p}}_\alpha]^T$ denote the generalized velocity vector that contains the linear and angular velocities of all the rods, and $\mathscr{F} = [\boldsymbol{F}_\alpha^{(0)}, \boldsymbol{F}_\alpha^{(1)}]^T$ the generalized force vector that contains all the forces and first force moments of non-hydrodynamic nature (i.e. excluding lubrication). The method described above allows the calculation of $\mathscr{U}$ knowing $\mathscr{F}$, which we can write symbolically as [33]:

$$\mathscr{U} = \mathscr{U}^s + \mathscr{M} \cdot \mathscr{F}, \tag{6.68}$$

where $\mathscr{U}^s$ is induced by the electrophoretic slip velocity, and $\mathscr{M}$ is the grand mobility operator. This operator, which is a function of the particle configurations and solvent viscosity only, accounts for far-field hydrodynamics up to the stresslet term and for near-field lubrication. In particular, the method described here does not explicitly compute the coefficients of matrix $\mathscr{M}$, but rather allows the efficient evaluation of the action of $\mathscr{M}$ on a given force vector $\mathscr{F}$ using the SPME algorithm (Chapter 3).

6.4.2   Brownian forces: Fixman's method

The Brownian forces and torques appearing in Equation (6.64) are random variables that model the thermal collisions between the solvent molecules and the particles, and must be calculated to satisfy certain statistical properties (e.g. [33]). Denoting by $\langle \cdot \rangle$ the ensemble average, we require in particular that the generalized Brownian force vector $\mathscr{F}^b$ have zero mean at any given time:

$$\langle \mathscr{F}^b(t) \rangle = 0, \tag{6.69}$$

and that its variance satisfy the fluctuation-dissipation theorem from statistical mechanics (e.g. [50]):

$$\langle \mathscr{F}^b(t) \otimes \mathscr{F}^b(t') \rangle = 2 \, \delta(t - t') \, \mathscr{M}^{-1}, \tag{6.70}$$

where $\delta(t)$ is the Dirac delta function, and $\mathscr{M}$ is the grand mobility operator introduced in Section 6.4.1. The conditions (6.69)–(6.70) can be satisfield in a number of ways. In a computer simulation where time is discretized, the generalized Brownian force vector over a step of length Δt is typically calculated as [24]:

$$\mathscr{F}^b = \sqrt{\frac{2}{\Delta t}} \, \mathscr{B} \cdot \mathscr{W}, \tag{6.71}$$

where the matrix $\mathscr{B}$ can be obtained as either the square root or the Cholesky decomposition of the inverse mobility: $\mathscr{B} \cdot \mathscr{B} = \mathscr{M}^{-1}$ or $\mathscr{B} \cdot \mathscr{B}^T = \mathscr{M}^{-1}$, and where $\mathscr{W}$ is a vector of length $6N$ containing random numbers from a Gaussian distribution with zero mean and unit variance.

Calculating the square root or the Cholesky decomposition of $\mathscr{M}^{-1}$, in addition to being computationally prohibitive with a cost of $O(N^3)$, also requires knowledge of the coefficients of the grand mobility. As discussed in Chapter 3 and in Section 6.4.1, such knowledge cannot be obtained when using the SPME algorithm owing to the fast Fourier transforms which circumvent the direct calculation of $\mathscr{M}$. A solution to this problem consists of using a spectral approximation of the matrix square root, based on Chebyshev polynomials. This method, termed Fixman's method after its first application to hydrodynamic interactions inside polymer chains by Fixman [66], was more recently used in bead-spring simulations of polymers by Jendrejack *et al.* [94], and in Stokesian dynamics simulations of colloidal sphere dispersions by Banchio & Brady [8]. If we denote by $[\lambda_{\min}, \lambda_{\max}]$ the range of the eigenvalues of the grand mobility, we can find an approximation to the inverse square root valid over that range on the basis of Chebyshev polynomials:

$$x^{-1/2} \approx \sum_{i=1}^{n_p} a_i P_i(x). \tag{6.72}$$

The Chebyshev polynomials P_i are calculated by recursion:

$$P_0(\tilde{x}) = 1, \quad P_1(\tilde{x}) = \tilde{x}, \quad P_{i+1}(\tilde{x}) = 2\tilde{x}P_i(\tilde{x}) - P_{i-1}(\tilde{x}), \tag{6.73}$$

where $\tilde{x} \in [-1, 1]$ is a shifted coordinate:

$$\tilde{x} = \frac{2x}{\lambda_{\max} - \lambda_{\min}} - \frac{\lambda_{\max} + \lambda_{\min}}{\lambda_{\max} - \lambda_{\min}}. \tag{6.74}$$

The Chebyshev coefficients a_i, which decay exponentially, can be calculated using a fast cosine transform algorithm [35]. If Equation (6.72) is uniformly valid over the range of the eigenvalues, by transformation to the basis of the eigenvectors of $\mathscr{M}$ it is easy to see that the following approximation is also valid for the mobility:

$$\mathscr{B} \cdot \mathscr{W} = \mathscr{M}^{-1/2} \cdot \mathscr{W} \approx \sum_{i=1}^{n_p} a_i P_i(\mathscr{M}) \cdot \mathscr{W}, \tag{6.75}$$

for any vector $\mathscr{W}$. The evaluation of the right-hand side in Equation (6.75) using the recursion formulae for the Chebyshev polynomials now only requires the action of the grand

mobility operator on given vectors, and can therefore be performed with our algorithm.

As noted by Butler & Shaqfeh [33], the grand mobility matrix defined in Section 6.4.1 is not positive definite: some of its eigenvalues can be shown to be zero owing to the restriction that the orientation vectors $\boldsymbol{p}_\alpha$ must remain normalized. This prevents the calculation of the inverse square root using the method described above, as no valid polynomial approximation to $x^{-1/2}$ can be found over an interval of the type $[0, \lambda_{\mathrm{max}}]$. Butler & Shaqfeh [33] however remarked that $\mathscr{M}$ can be decomposed as:

$$\mathscr{M} = \mathscr{K} \cdot \mathscr{M}' \cdot \mathscr{K} \quad \text{with} \quad \mathscr{K} = \begin{bmatrix} \mathsf{I} & \mathbf{0} \\ \mathbf{0} & \mathsf{I} - \boldsymbol{p}_\alpha \boldsymbol{p}_\alpha \end{bmatrix}, \tag{6.76}$$

where each block in $\mathscr{K}$ has size $3N \times 3N$. In Equation (6.76) the matrix $\mathscr{M}'$ is now positive definite, so that Fixman's method can be applied. A generalized Brownian force vector that satisfies the fluctuation-dissipation theorem is then constructed as follows:

$$\mathscr{F}^b = \sqrt{\frac{2}{\Delta t}} \, \mathscr{K} \cdot \mathscr{B}' \cdot \mathscr{W}, \quad \text{where} \quad \mathscr{B}' = (\mathscr{M}')^{-1/2}. \tag{6.77}$$

In our computer implementation we truncate the polynomial expansions so as to maintain an accuracy of approximately three significant figures. The range of the eigenvalues of the grand mobility, which determines the convergence of the expansions, is calculated using an iterative method. As its determination can be quite costly, the range is only updated when the particle configurations have changed significantly. Larger errors (accuracy of two significant figures) are sometimes tolerated when two particles become very close to one another, as lubrication interactions result in a very stiff grand mobility, for which the convergence of the expansion is slow.

6.4.3 Time integration: midpoint algorithm

As recommended by Grassia, Hinch & Nitsche [72] for the integration of Langevin equations with configuration-dependent mobilities, we use the second-order midpoint algorithm of Fixman [65] to advance particle configurations in time. If we let $\mathscr{R}_n = [\boldsymbol{x}_\alpha^n, \boldsymbol{p}_\alpha^n]^T$ denote the generalized configuration vector that contains all the rod positions and orientations

at time t_n, the configuration $\mathscr{R}_{n+1}$ at time $t_{n+1} = t_n + \Delta t$ is obtained by a two-step procedure:

$$\mathscr{R}_* = \mathscr{R}_n + \frac{1}{2}\left[\mathscr{U}_n^s + \mathscr{M}_n \cdot \left(\mathscr{F}_n^c + \mathscr{F}_n^b\right)\right]\Delta t, \tag{6.78}$$

$$\mathscr{R}_{n+1} = \mathscr{R}_* + \left[\mathscr{U}_*^s + \mathscr{M}_* \cdot \left(\mathscr{F}_*^c + \mathscr{F}_n^b\right)\right]\Delta t, \tag{6.79}$$

where $\mathscr{U}^s$ is the generalized velocity vector containing the angular velocities from induced-charge electrophoresis (e.g. Equation (6.57)), and where all hydrodynamic interactions (including lubrication) are contained in the grand mobility. Most importantly, the Brownian forces $\mathscr{F}^b$, which are obtained using the method discussed in Section 6.4.2, are not updated during the second step (Equation (6.79)): this allows to reproduce the drift term $(\boldsymbol{\nabla}\cdot\mathscr{M})\Delta t$ that arises in Langevin equations with configuration-dependent mobilities, and which one would need to include explicitly in a first-order integration scheme [56, 65, 72].

6.5   Results and discussion

We start by describing results for non-Brownian suspensions (infinite Péclet number limit) in Section 6.5.1, in which the effects of induced-charge electrophoresis on the dynamics can be isolated; Brownian motion is then discussed in Section 6.5.2. The non-Brownian results were typically obtained in suspensions of 400 rods, whereas smaller systems of 60 to 100 rods were used in the Brownian case. In all simulations 8 quadrature points were used along the rod lengths.

6.5.1   Infinite Péclet number

Particle distributions and pair probabilities

A typical particle distribution at infinite Péclet number is shown in Figure 6.11(d) at steady state, where we see that all particles are very well aligned in the direction of the electric field (z-direction). This alignment occurs rapidly with a characteristic time of the order of the electroviscous time as soon as the field is turned on, and remains very
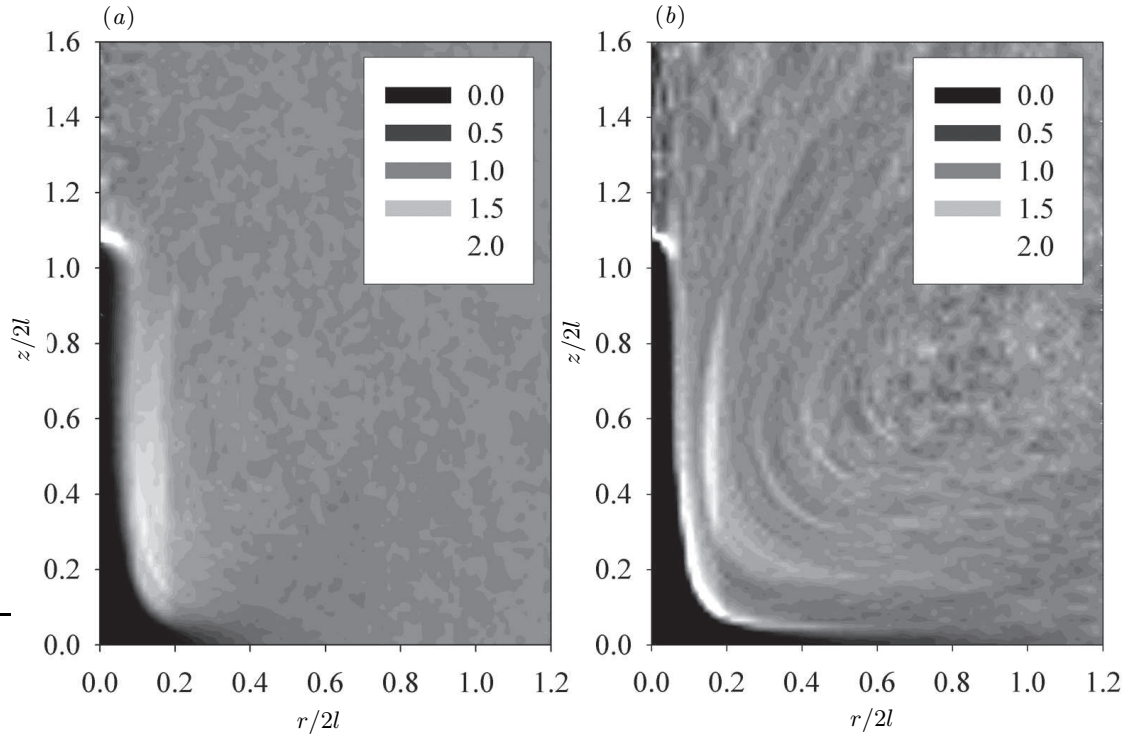
Figure 6.7: Pair distributions in a suspension of 400 rods of aspect ratio $A = 10$ at infinite Péclet number, at an effective volume fraction of (a) $nl^3 = 0.1$, and (b) $nl^3 = 0.01$. The black region along the vertical axis is due to excluded volume, while the white patches around it show proof of particle pairing.

strong, with some fluctuations occurring as a result of particle-particle interactions. These fluctuations are more frequent in more concentrated suspensions, but for all concentrations investigated the second moment $\langle p_z p_z \rangle$ of the z-component of orientation vector typically remained above 0.99.

Once the particles are aligned, hydrodynamic interactions result in relative motions with no average suspension velocity, which lead to a subtle rearrangement of the particle distributions. In particular, snapshots of the suspensions show the presence of particle pairs, which would be unlikely in a random suspension. More precisely, these pairing events consist of the following steps: two particles are attracted from their ends, slide along one another until they become side by side, then separate in the lateral direction.

These dynamics confirm the analysis of pair interactions carried out in Section 6.3, where we identifield regions of attraction and repulsion.

While these pairing events are typically transient, they are frequent enough to modify the pair distribution function in the suspension. This is illustrated in Figure 6.7, which shows the pair distribution function $p(r, z)$ (in cylindrical coordinates) at two effective volume fractions nl^3 (where n is the number density and l the rod half-length), where p is normalized so that it tends towards 1 at infinity. Figure 6.7 can be compared to Figure 6.6, which had been obtained by numerically solving the conservation equation for the pair probabilities. While both figures differ in details, the qualitative features are similar. The region of excluded volume is located along the z-axis since the rods are aligned in the direction of the electric field, and is colored in black in Figure 6.7. As expected its length is approximately one rod length, and its width is of the order of a rod diameter (in fact slightly less as orientation fluctuations often occur when rods are close to one another). A very steep gradient is then observed near the tip and on the side of the excluded volume region, where two sharp peaks are observed and are the consequence of the pairings described above: the peak at the tip corresponds to rods being attracted head-on, while the peak on the side corresponds to interactions with a slight offset. A depletion region is also observed along the horizontal axis ($z = 0$), where the black region of excluded volume is seen to extend radially: this depletion is the consequence of the repulsion that occurs when two rods are aligned side by side. Further away from the excluded volume region $p(r, z)$ quickly becomes uniform in all directions and reaches its asymptotic value of 1. Interestingly $p(r, z)$ is qualitatively the same at both concentrations ($nl^3 = 0.1$ and 0.01), and in particular pairing is still observed to occur even in quite dilute systems.

Hydrodynamic dispersion

The superposition of all the relative motions between the rods can be expected to lead to a diffusive behavior at long times. This is indeed confirmed by considering mean square displacement curves, as shown in Figure 6.8. Initially the mean square displacements
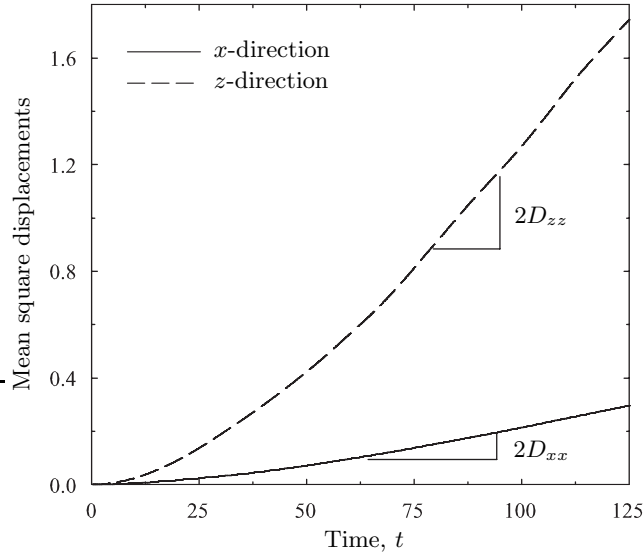
Figure 6.8: Mean square displacements $\langle (x - x_0)^2 \rangle$ and $\langle (z - z_0)^2 \rangle$ in the x- and z-directions as a function of time, in a suspension of 400 rods of aspect ratio $A = 20$ at an effective volume fraction of $nl^3 = 1$. The initial quadratic (convective) growth gives way to a diffusive regime, from which hydrodynamic dispersion coefficients can be inferred: $\langle (x - x_0)^2 \rangle \sim 2D_{xx}t$, $\langle (z - z_0)^2 \rangle \sim 2D_{zz}t$.

are observed to grow quadratically, corresponding to a convective regime. However after several particle-particle interactions the motions decorrelate in time, resulting in a linear growth characteristic of diffusive processes. Hydrodynamic dispersion is a common phenomenon in non-Brownian particulate suspensions, and in particular has been well characterized in sedimentation (e.g. [77, 138]) as well as simple linear flows (e.g. [172]). While in these instances dispersion occurs relative to a mean convective motion such as settling under gravity or shear flow, the dispersion observed in Figure 6.8 is atypical as the mean motion of the suspension is zero.

Curves such as those of Figure 6.8 can be used to calculate effective dispersion coefficients. More precisely we define a hydrodynamic diffusion tensor **D** as:

$$\mathbf{D} = \lim_{t \to \infty} \frac{1}{2} \frac{\mathrm{d}}{\mathrm{d}t} \langle (\boldsymbol{x}(t) - \boldsymbol{x}_0)(\boldsymbol{x}(t) - \boldsymbol{x}_0) \rangle. \tag{6.80}$$

As is obvious from Figure 6.8 the tensor **D** is anisotropic, and for symmetry reasons $D_{xx} =$
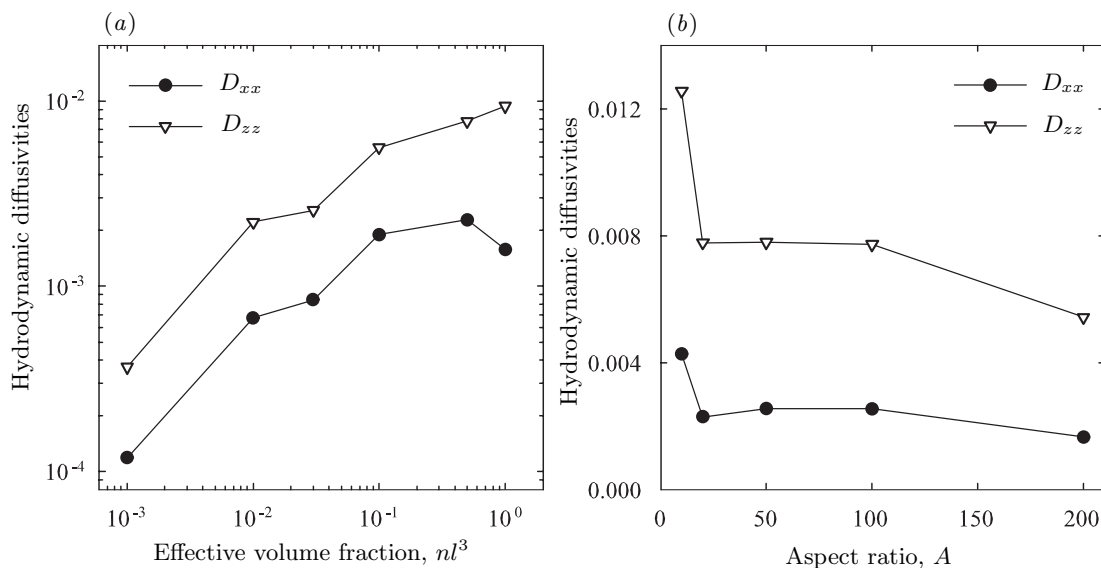
Figure 6.9: Hydrodynamic diffusivities at infinite Péclet number in the directions parallel (z-direction) and perpendicular (x-direction) to the electric field, as a function of (a) the effective volume fraction nl^3 for rods of aspect ratio $A = 20$, and (b) the rod aspect ratio A at $nl^3 = 0.1$. The results were obtained in suspensions of 400 rods.

D_{yy}. Simulations also show that off-diagonal components are zero: $D_{ij} = 0$ for $i \neq j$. Numerical results for D_{xx} and D_{zz} at various concentrations and aspect ratios are shown in Figure 6.9, where **D** is made dimensionless by $\varepsilon E_\infty^2 l^2 / \mu$. The dependence on the effective volume fraction nl^3 is shown in Figure 6.9(a), where we see that the diffusivities increase with the concentration, as a result of stronger hydrodynamic interactions. The ratio D_{zz}/D_{xx} of the diffusivities parallel and perpendicular to the direction of the electric field is roughly equal to 3.5 and approximately constant over three decades of concentration. The dependence on the rod aspect ratio is shown in Figure 6.9(b). It is observed to be rather weak except at very low values of A, at which the validity of the slender-body approximation used in the simulations becomes questionable. As A increases the diffusivities decrease slightly at a fixed nl^3: hydrodynamic interactions indeed become weaker at very high aspect ratio, as can seen for instance from Equation (6.48).
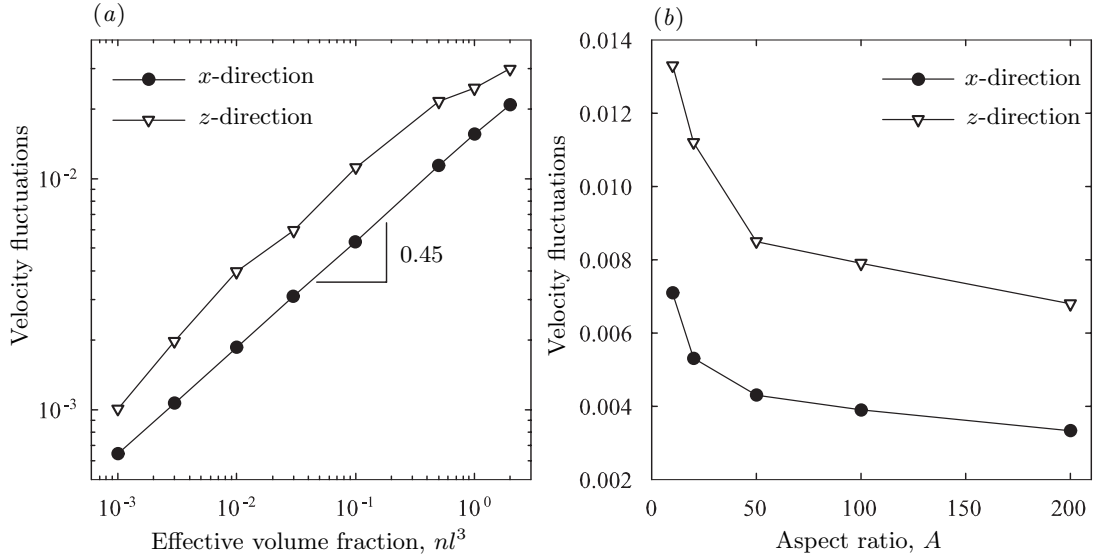
Figure 6.10: Velocity fluctuations (standard deviation of the rod velocities) at infinite Péclet number in the directions parallel (z-direction) and perpendicular (x-direction) to the electric field, as a function of (a) the effective volume fraction nl^3 for rods of aspect ratio $A = 20$, and (b) the rod aspect ratio A at $nl^3 = 0.1$. The results were obtained in suspensions of 400 rods.

Velocity statistics

We also characterize the velocity fluctuations in the suspension, which are another conse-
quence of the relative motions between the rods. Figure 6.10 shows the standard deviations
Δu_x and Δu_z of the rod velocities in the x- and z-directions at various concentrations and
rod aspect ratios. Note that these are typically very weak in the dilute regime, because of
the relatively rapid decay as $1/r^2$ of the interactions (compared to $1/r$ in sedimentation
for instance, where very strong fluctuations arise). As shown in Figure 6.10(a) the velocity
fluctuations increase with concentration according to a power law:

$$\Delta u_x, \Delta u_z \sim \frac{2l\varepsilon E_\infty^2}{\mu} \left(nl^3\right)^{0.45}, \tag{6.81}$$

and the ratio of the fluctuations parallel and perpendicular to the direction of the electric
field is again approximately constant and equal to: $\Delta u_z/\Delta u_x \approx 1.8$, which is of the order

of the square root of the ratio of the diffusivities. As in the case of the diffusivities, Figure 6.10(b) shows that the dependence of velocity fluctuations on the rod aspect ratio is weak, except at very low values of A.

6.5.2   Finite Péclet number

Orientation statistics

We now consider the effects of Brownian motion, which introduces both rotational and translational diffusion. Typical particle distributions at various values of the rotational Péclet number (i.e. for various electric field strengths) are shown in Figure 6.11. When no field is applied ($Pe_r = 0$), the rods assume random positions and orientations, and as the Péclet number increases the alignment of the rods in the direction of the field becomes stronger. As already discussed in Section 6.5.1, the alignment is almost perfect in the infinite Péclet number limit where Brownian motion is negligible.

The dependence of the orientation of the rods on the electric field strength is made more quantitative in Figure 6.12, which shows simulated orientation distributions $\Psi(\phi)$ at various values of Pe, where ϕ denotes the angle between the directions of the electric field and of the rods, and where the following normalization was used:

$$\int_0^\pi \Psi(\phi)\sin\phi\,\mathrm{d}\phi = 1. \tag{6.82}$$

Figure 6.12 also compares the simulation results to an analytical solution for the orientation distribution in the limit of infinite dilution. Indeed, if the effects of hydrodynamic interactions on orientations can be neglected, the probability density function $\Psi(\boldsymbol{p})$ for the orientation vector $\boldsymbol{p}$ of a given rod satisfies the following Fokker-Planck equation [50]:

$$\frac{\partial\Psi}{\partial t} + \boldsymbol{\nabla_p}\cdot(\dot{\boldsymbol{p}}\Psi) - \boldsymbol{\nabla_p}\cdot(D_r\boldsymbol{\nabla_p}\Psi) = 0, \tag{6.83}$$

where $\boldsymbol{\nabla_p}$ is the differential operator in orientational space [3]. $\dot{\boldsymbol{p}}$ denotes the rotational velocity of the rod induced by the electric field and is given by Equations (6.29) and (6.57),
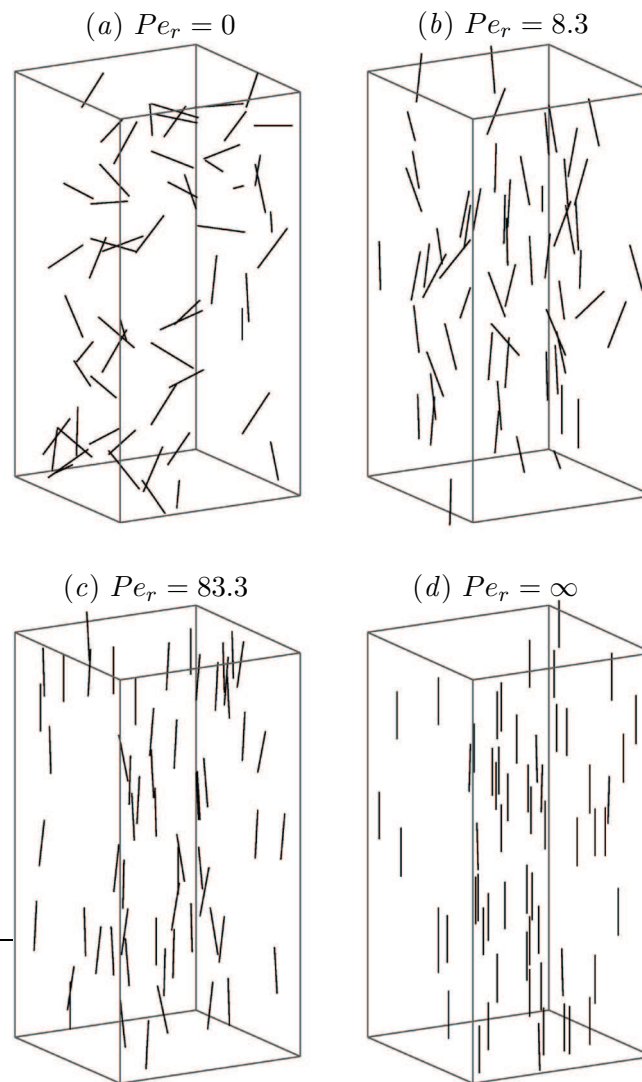
Figure 6.11: Typical particle distributions at steady state in suspensions of 60 rods of aspect ratio $A = 20$, at an effective volume fraction of $nl^3 = 0.05$, and at various electric field strengths, defined by the rotational Péclet number: (a) $Pe_r = 0$ (no electric field), (b) $Pe_r = 8.3$, (c) $Pe_r = 83.3$, and (d) $Pe_r = \infty$ (no Brownian motion).
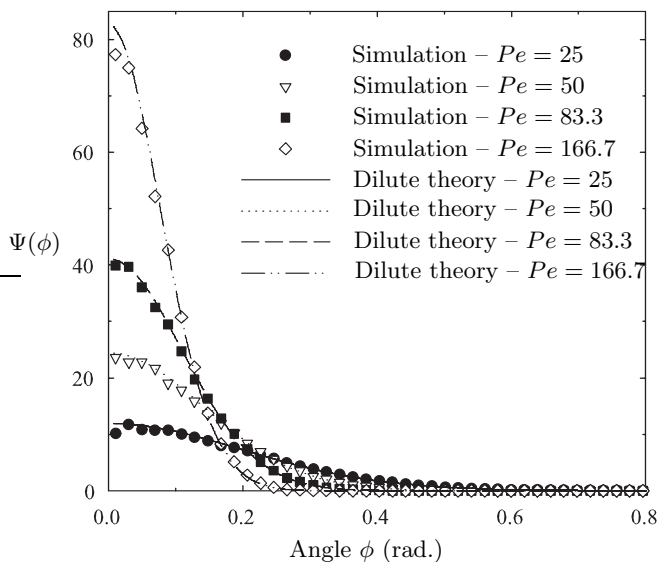
Figure 6.12: Orientation distributions $\Psi(\phi)$ at various Péclet numbers in suspensions of rods of aspect ratio $A = 20$ at an effective volume fraction of $nl^3 = 0.05$, obtained from simulations (symbols) and from the dilute theory of Equation (6.85) (lines).

and $D_r = 3kT \log 2A/8\pi\mu l^3$ is the Brownian rotational diffusivity of the rod. At steady state the distribution only depends on the angle ϕ, and Equation (6.83) reduces to:

$$\frac{\partial}{\partial\phi}\left(\frac{\varepsilon}{4\mu}G_\perp G_\parallel E_\infty^2 \sin 2\phi\, \Psi(\phi)\right) + \frac{3kT\log 2A}{8\pi\mu l^3}\frac{\partial^2}{\partial\phi^2}\Psi(\phi) = 0, \qquad (6.84)$$

the solution of which is a Boltzmann distribution:

$$\Psi(\phi) = C\exp\left(\frac{Pe_r}{8}\, G_\parallel G_\perp \cos 2\phi\right). \qquad (6.85)$$

The constant C is easily determined to satisfy the normalization condition of Equation (6.82). As shown in Figure 6.12, the orientation distributions present a peak near $\phi = 0$, which becomes sharper and sharper as the electric field increases. Excellent agreement between the simulated results and the exact solution for infinite dilution is observed at the concentration shown, although larger departures can be expected at higher concentrations.
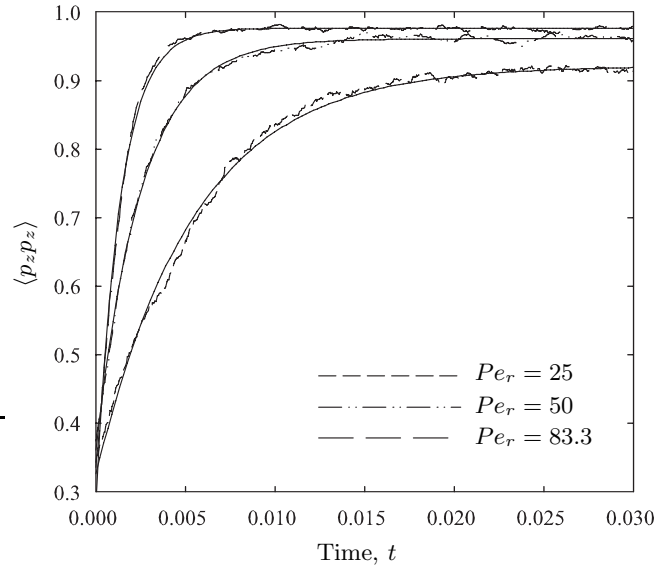
Figure 6.13: Evolution of the second moment $\langle p_z p_z \rangle$ of the z-component of the rod orientation vectors after application of an electric field in Brownian suspensions of rods of aspect ratio $A = 20$ at an effective volume fraction of $nl^3 = 0.05$. The plot shows both simulations data (dashed lines) and exponential fits (full lines) at various electric field strengths.

The evolution to steady state for the orientation distributions is illustrated in Figure 6.13, which shows the time evolution of the second moment $\langle p_z p_z \rangle$ of the z-component of the rod orientation vectors, where the electric field is suddenly applied at $t = 0$. Initially the rod orientations are random owing to Brownian motion, hence the value of 1/3; as time goes on the rods align with the field, resulting in the steady increase of $\langle p_z p_z \rangle$. A plateau is finally reached, the value of which indicates the degree of alignment in the suspension. As already observed in Figure 6.12, the alignment is stronger at high Péclet numbers. The characteristic time for the alignment also depends on the electric field strength, and is observed to be shorter at high Péclet numbers.

Pair probabilities

We also discuss the effects of Brownian motion on the particle pairing previously described in Section 6.5.1. Figure 6.14 shows simulated pair distribution functions in Brownian
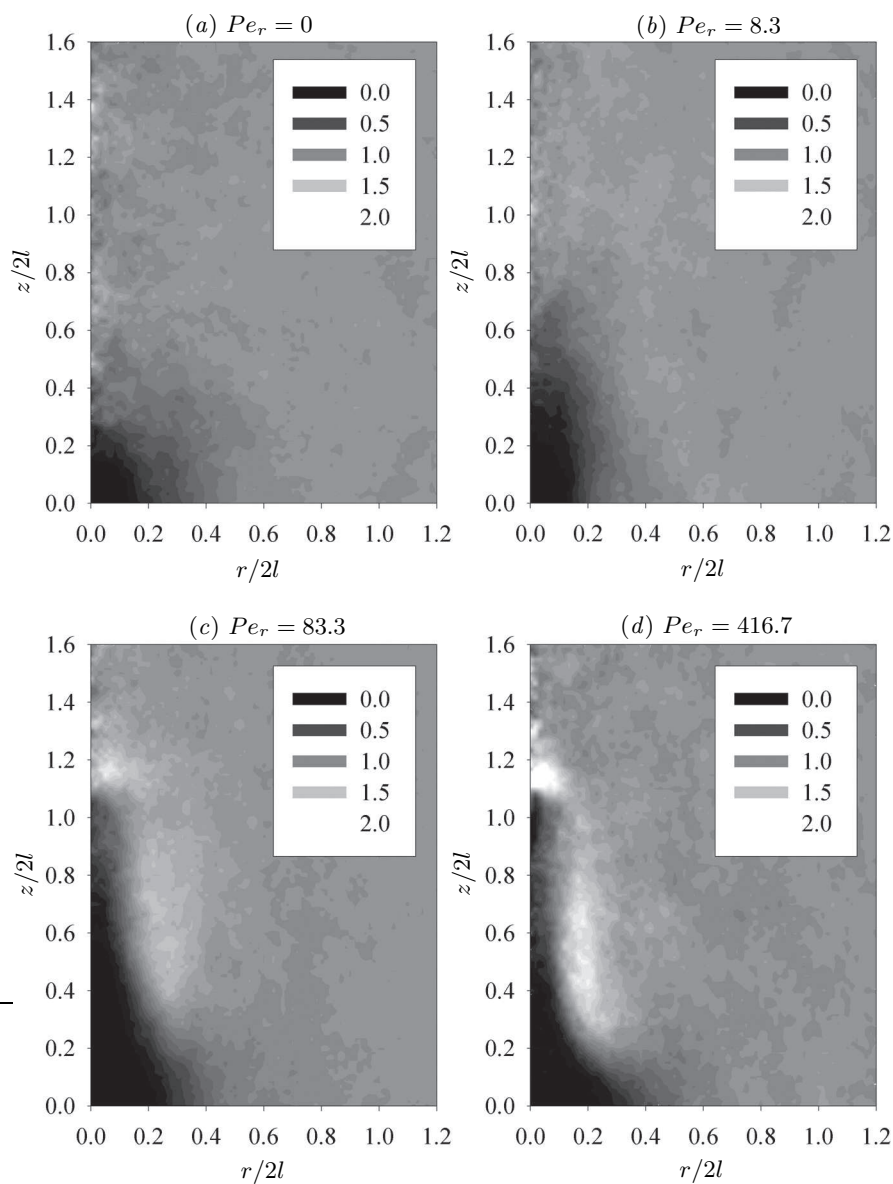
Figure 6.14: Pair distributions in Brownian suspensions of 60 rods of aspect ratio $A = 10$ at an effective volume fraction of $nl^3 = 0.1$, and at various electric field strengths, defined by the rotational Péclet number: (a) $Pe_r = 0$ (no electric field), (b) $Pe_r = 8.3$, (c) $Pe_r = 83.3$, and (d) $Pe_r = 416.7$.

suspensions at the same aspect ratio and concentration as in Figure 6.7(a), for various values of the Péclet number. When no field is applied ($Pe_r = 0$), the rods assume random orientations and positions resulting in the isotropic pair distribution of Figure 6.14(a): a depleted region of spherical shape and characteristic size l exists near the origin due to excluded volume, beyond which the pair distribution rapidly reaches its asymptotic value of 1. When a moderate field is applied (e.g. $Pe_r = 8.3$, Figure 6.14(b)), the depletion region is distorted and stretches in the direction of the field, as a result of the alignment of the rods; yet the pair distribution remains qualitatively very similar to the case $Pe = 0$, and in particular no pairing is observed. Pairing only appears at much higher values of the Péclet number, as shown in Figures 6.14(c) and (d): beyond $Pe_r = 83.3$, peaks in the pair distributions surround the tip of the depletion region, which is now much narrower. At $Pe_r = 416.7$ the effects of Brownian diffusion become negligible and the pair distribution is qualitatively similar to the non-Brownian case of Figure 6.7.

6.6 Concluding remarks

We presented a study of the behavior of dispersions of infinitely polarizable slender rods in an electric field, with and without Brownian motion. We first derived a simple model for particle motions and interactions, based on the thin double layer approximation and on slender-body theory, and valid for high aspect ratio particles. In particular, we showed that the effects of the nonlinear induced-charge electrophoretic flows on the particle surfaces can be modeled by a linear slip velocity along the rod axes, which causes the alignment of the rods in the direction of the electric field and induces linear distributions of point force singularities. These distributions of point forces drive stresslet disturbance flows in the surrounding fluid, resulting in hydrodynamic interactions. We then applied this slender-body model to study the relative motions of two suspended rods: approximate expressions were calculated for the relative velocity between two aligned rods, and a semi-analytical solution was obtained for the pair distribution function in a dilute dispersion. The presence of a peak in the pair distribution function suggests that particle pairing can

be expected as result of the relative motions.

More detailed information on the particle dynamics was then obtained using numerical simulations. We described a simulation method based on interactions between slender-bodies, which includes both far-field and near-field hydrodynamic interactions as well as Brownian motion. Simulations at infinite Péclet number (negligible Brownian motion) confirmed the existence of pairing, and qualitative agreement was obtained between the semi-analytical and simulated pair distribution functions. The superposition of the disturbance flows induced by the rods was also shown to result in a diffusive motion at long times, and hydrodynamic dispersion coefficients were calculated. Finally the effects of Brownian diffusion were discussed, and we showed that both particle alignment and pairing are made weaker by Brownian motion.

The results discussed in this Chapter have implications for colloid science and microfluidics, where electric fields are commonly used to control the orientation of anisotropic particles (e.g. [78, 191]). While previous studies have focused on the determination of the rotational motion of the particles overlooking hydrodynamic interactions, this work demonstrates that the latter can be relevant even in the case of uncharged particles, as relative motions created by the induced-charge electrophoresis can lead to a non-random, possibly non-uniform microstructure.

Our discussion has focused on neutrally buoyant particles in the bulk of a suspension, an ideal situation which allowed us to isolate the effects of induced-charge electrophoresis, but which may seldom occur in practical situations. In particular, metallic colloids are typically non-neutrally buoyant, and settling under gravity may lead to interesting phenomena. We observed in Chapters 3 and 4 that sedimenting suspensions of anisotropic particles such as rods and disks undergo a concentration instability, by which a well-mixed suspension develops inhomogeneities as a result of the coupling between the translational and rotational motions of the particles: both induced-charge electrophoresis and Brownian diffusion will disrupt this coupling and may prevent the instability from developing. The effects of confinement may also be significant in some applications, notably in microfluidic devices: interactions with solid boundaries are therefore worthy of interest as well.

Chapter 7

The shear-induced migration of short-chain polymers in parabolic channel flow

7.1 Introduction

The recent advent of microfluidics as a tool for the miniaturization of chemical and biological assays has spurred a renewed interest in the behavior of macromolecules and colloids in confinement. Interactions with boundaries and the short-scale variations of fluid flows in such environments indeed result in unusual dynamics (e.g. [95, 37]), many aspects of which remain poorly understood. One phenomenon of interest, addressed in this paper, is the cross-streamline migration of polymeric molecules in inhomogeneous flows, which has implications for the effective rheology and transport of flowing polymer solutions. Numerous studies have addressed this problem in the past (cf. the review by Agarwal *et al.* [4]), yet often disagree on issues as fundamental as the direction of migration. A wide variety of physical mechanisms, such as wall exclusion, configuration-dependent diffusivities or hydrodynamic interactions (HI), may contribute to the phenomenon, thereby making general predictions difficult to formulate.

The case of long-chain flexible polymers such as DNA molecules has received much attention recently, both in experiments [37, 63] and computer simulations [95, 97, 37, 189, 190]. The consensus from these studies is that flexible polymers in a pressure-driven channel flow migrate away from the walls toward the centerline, leading to the formation of a depletion layer, whose characteristic thickness greatly exceeds the radius of gyration of a single molecule. Graham and coworkers proposed a theoretical model explaining the migration as a consequence of hydrodynamic interactions between the walls and the entropic force dipole exerted by a stretched polymer on the fluid, leading to a deterministic drift away from the walls [97, 121]. As higher shear rates result in stronger molecular stretching, the drift is expected to increase with flow strength, as indeed observed experimentally [63] and in numerical simulations [97].

Experimental evidence of depletion layers in flowing solutions of rigid and semi-flexible polymers has also been reported [6]. Yet in these systems the depletion layer thickness, which also increases with shear rate, typically remains of the order of the radius of gyration of a molecule. Models for rigid polymers have focused on steric exclusion with the walls [6, 48, 164]. While neglecting wall hydrodynamic interactions, these studies were reasonably successful at explaining experimental observations, including the thickening of the depletion in strong flows, which may be a consequence of more frequent collisions with the walls owing to an increased rate of molecular tumbling.

The precise effects of wall hydrodynamic interactions and the applicability of the entropic dipole model of Ma & Graham [121] in the case of less flexible polymers therefore deserve closer attention. In this Chapter, we employ Brownian dynamics simulations to address these issues. A Kuhn step level polymer model is described in Section 7.2, which is based on the slender-body theory described in Section 2.4: it allows the simulation of a short chain of a few persistence lengths and includes multibody hydrodynamic interactions between the chain segments and the channel walls. Results are discussed in Section 7.3, where we emphasize the effect of flexibility. A summary and concluding remarks are given in Section 7.4.
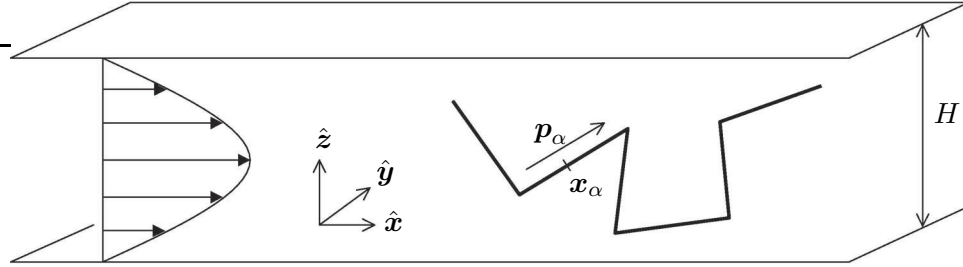
Figure 7.1: Problem geometry: we consider the pressure-driven flow of a dilute polymer solution between two infinite flat plates. A polymer molecule is modeled as a chain of freely-jointed hydrodynamically interacting Brownian rods

7.2 Model and numerical implementation

We consider the pressure-driven flow of a dilute polymer solution between two infinite flat plates separated by a distance H (Figure 7.1). A polymer molecule is modeled as a chain composed of N freely-jointed rigid rods of length L and aspect ratio A, as previously done by Nyland *et al.* [141], Ådland & Mikkelsen [2], and most recently Butler & Shaqfeh [33]. As the method we employ is similar in many respects to those used in Chapters 3 and 6, it is only outlined here. The spatial configuration of a given rod α is determined by the position $\boldsymbol{x}_\alpha$ of its center of mass and by a unit vector $\boldsymbol{p}_\alpha$ aligned with its major axis. The motion of each rod is described using slender-body theory for Stokes flow of Section 2.4, which relates the linear and angular velocities of the rod to the fluid velocity $\boldsymbol{u}(\boldsymbol{x})$ and to a line distribution $\boldsymbol{f}_\alpha$ of point force singularities along the rod axis [12]:

$$\dot{\boldsymbol{x}}_\alpha + s_\alpha \dot{\boldsymbol{p}}_\alpha - \boldsymbol{u}(\boldsymbol{x}_\alpha + s_\alpha \boldsymbol{p}_\alpha) = (\mathsf{I} + \boldsymbol{p}_\alpha \boldsymbol{p}_\alpha) \cdot \boldsymbol{f}_\alpha(s_\alpha), \tag{7.1}$$

where s_α denotes a linear coordinate along the axis of the rod of interest, with origin the center of the rod. Equation (7.1), in which terms of order $(\log 2A)^{-1}$ have been neglected, is an asymptotic approximation valid for high aspect ratios $(A \gg 1)$. In the present discussion lengths and times are made dimensionless using the characteristic scales $l_c = L$ and $t_c = 4\pi\mu L^3/kT \log 2A$, where μ and kT are the viscosity and thermal energy of the solvent, respectively. The linear and angular velocities of the rod are obtained by

integration of Equation (7.1) (cf. Section 2.4.2):

$$\dot{\boldsymbol{x}}_\alpha = \int_{-1/2}^{1/2} \boldsymbol{u}(\boldsymbol{x}_\alpha + s_\alpha \boldsymbol{p}_\alpha) \mathrm{d}s_\alpha + (\mathsf{I} + \boldsymbol{p}_\alpha \boldsymbol{p}_\alpha) \cdot \boldsymbol{F}_\alpha^{(0)}, \tag{7.2}$$

$$\dot{\boldsymbol{p}}_\alpha = 12\,(\mathsf{I} - \boldsymbol{p}_\alpha \boldsymbol{p}_\alpha) \cdot \int_{-1/2}^{1/2} s_\alpha \boldsymbol{u}(\boldsymbol{x}_\alpha + s_\alpha \boldsymbol{p}_\alpha) \mathrm{d}s_\alpha + 12\,(\mathsf{I} - \boldsymbol{p}_\alpha \boldsymbol{p}_\alpha) \cdot \boldsymbol{F}_\alpha^{(1)}, \tag{7.3}$$

where $\boldsymbol{F}_\alpha^{(0)}$ and $\boldsymbol{F}_\alpha^{(1)}$ denote the zeroth and first moments of the force distribution along the rod axis, and are related to the total external force and torque on the rod.

Hydrodynamic interactions between rods and with the walls are captured through the fluid velocity $\boldsymbol{u}$ in Equations (7.1) through (7.3), which is the sum of the imposed pressure driven flow $\boldsymbol{u}_\infty$ and the disturbance velocities induced by the other rods in the polymer chain, and by the presence of the walls. For example, along rod α, $\boldsymbol{u}$ becomes:

$$\boldsymbol{u}(\boldsymbol{x}) = \boldsymbol{u}_\infty(\boldsymbol{x}) + \frac{1}{2\log 2A} \sum_{\beta=1}^{N} \int_{-1/2}^{1/2} \mathsf{J}^W(\boldsymbol{x}; \boldsymbol{x}_\beta + s_\beta \boldsymbol{p}_\beta) \cdot \boldsymbol{f}_\beta(s_\beta) \mathrm{d}s_\beta, \tag{7.4}$$

where $\mathsf{J}^W(\boldsymbol{x}; \boldsymbol{x}_0)$ denotes the Green's function for Stokes flow in the geometry of interest, from which the Oseen-Burgers tensor is subtracted when $\beta = \alpha$. In this work the exact Green's function between two infinite flat plates, as first determined by Liron & Mochon [117], was implemented in its regularized form as described by Staben *et al.* [180]. In the case of a pressure-driven flow between two flat plates, the imposed fluid velocity is:

$$\boldsymbol{u}_\infty(\boldsymbol{x}) = Pe\,\frac{z}{L}\left(1 - \frac{z}{H}\right)\hat{\boldsymbol{x}}, \quad \text{where} \quad Pe = \dot{\gamma}_w \times t_c. \tag{7.5}$$

The Péclet number Pe, which measures the relative effects of the imposed flow and of thermal diffusion on the dynamics of a chain segment, is defined as the product of the wall shear rate $\dot{\gamma}_w = 6U_0/H$ (where U_0 is the cross-sectional average fluid velocity) and the characteristic thermal time scale t_c defined above.

Equations (7.1)–(7.4) constitute an integral system for the force distributions along the chain segments. As in the previous Chapters, we solve this system approximately

by expanding the force distribution along each rod in Legendre polynomials and only retaining the first two terms (cf. Section 2.4.3):

$$\boldsymbol{f}_\alpha(s_\alpha) \approx \boldsymbol{F}_\alpha^{(0)} + 12s_\alpha \left[\mathscr{S}_\alpha \boldsymbol{p}_\alpha + (\boldsymbol{I} - \boldsymbol{p}_\alpha \boldsymbol{p}_\alpha) \cdot \boldsymbol{F}_\alpha^{(1)} \right]. \tag{7.6}$$

We have introduced the stresslet $\mathscr{S}_\alpha$ on rod α, which is a scalar quantity arising from the inability of the rod to stretch or compress along its major axis:

$$\mathscr{S}_\alpha = -\frac{1}{2} \int_{-1/2}^{1/2} s_\alpha \boldsymbol{p}_\alpha \cdot \boldsymbol{u}(\boldsymbol{x}_\alpha + s_\alpha \boldsymbol{p}_\alpha) \mathrm{d}s_\alpha. \tag{7.7}$$

The linearization Equation (7.6) reduces the integral system for the force distributions to an $N \times N$ linear system for the stresslets on the chain segments, which is easily inverted by Gaussian elimination. Once the stresslets are known they can be substituted into the linearized force distribution Equation (7.6), which itself is used to obtain the disturbance velocity Equation (7.4). The rod motions are then inferred using Equations (7.2)–(7.3). The method thus described allows for the calculation of the rod velocities in terms of the imposed flow velocity and of the external force and torque on each rod, which can be written symbolically as:

$$\dot{\mathscr{R}} = \dot{\mathscr{R}}_\infty + \mathscr{M}(\mathscr{R}) \cdot \mathscr{F}, \tag{7.8}$$

where $\mathscr{R}$ denotes a generalized position vector containing the center-of-mass positions and orientations of all the rods, and $\mathscr{F}$ is a generalized force vector containing the zeroth and first force moments on each rod. The tensor $\mathscr{M}$ is the grand mobility operator, which accounts for hydrodynamic interactions between rods and with the walls up to the stresslet term.

In this work the rods are subjected to constraint forces, excluded volume forces, and Brownian forces, all of which are discussed in detail by Butler & Shaqfeh [33]. The constraint forces $\mathscr{F}^c$ are required to maintain the integrity of the chain, and are calculated using the method of Lagrange multipliers to satisfy the constraint that adjacent chain segments must remain linked. Excluded volume interactions are captured through strong and

short-ranged repulsive forces $\mathscr{F}^e$, which prevent overlap between chain segments and with the channel walls. Finally the Brownian forces $\mathscr{F}^b$ model collisions between the solvent molecules and the chain, and are stochastic variables that must satisfy the fluctuation-dissipation theorem that we introduced in Section 6.4.2:

$$\langle \mathscr{F}^b(t) \rangle = 0, \quad \langle \mathscr{F}^b(t) \otimes \mathscr{F}^b(t') \rangle = 2\delta(t - t')\mathscr{M}^{-1}, \tag{7.9}$$

where $\langle \cdot \rangle$ denotes the ensemble average, and $\delta(t)$ is the Dirac delta function. They are calculated in a classic manner as:

$$\mathscr{F}^b = \sqrt{\frac{2}{\Delta t}}\mathscr{B} \cdot \mathscr{W}, \tag{7.10}$$

where Δt is the time step, $\mathscr{B}$ satisfies $\mathscr{B} \cdot \mathscr{B}^T = \mathscr{M}^{-1}$ and is obtained by Cholesky decomposition of the inverse of the grand mobility matrix, and $\mathscr{W}$ is a vector of length $6N$ containing random numbers from a Gaussian distribution with zero mean and unit variance. Note that instead of using a Cholesky decomposition, one may have applied the more efficient Fixman's method which we described and implemented in Section 6.4.2. Finally, the stochastic motion of the chain inside the gap is integrated in time using Fixman's midpoint algorithm [65], which is appropriate for Brownian systems with configuration-dependent diffusivities [72].

7.3 Results and discussion

In the following discussion, length are conveniently expressed in terms of the bulk radius of gyration, which is defined as:

$$R_g^2 = \langle \frac{1}{N} \sum_{i=1}^{N+1} (\boldsymbol{x}_i - \langle \boldsymbol{x} \rangle)^2 \rangle, \tag{7.11}$$

where $\boldsymbol{x}_i$, $i = 1, ..., N + 1$ denote the position of the rods ends, and $\langle \boldsymbol{x} \rangle$ denotes the chain center of mass. In the following we make use of the bulk value of R_g, measured
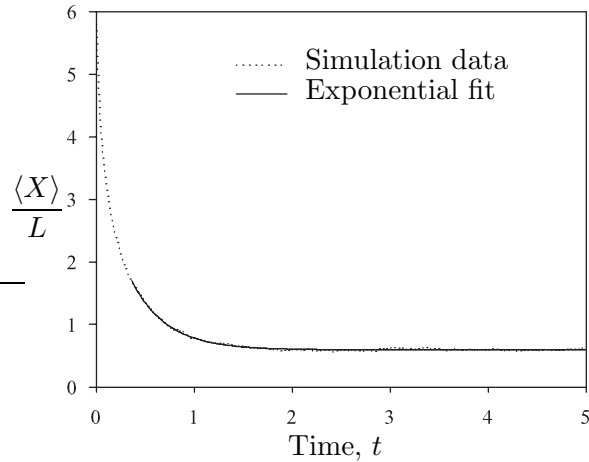
Figure 7.2: Determination of the polymer relaxation time, in the case $N = 6$: an ensemble of initially straight chains is allowed to relax, and the longest relaxation time τ is obtained by fitting a decaying exponential to the last 30 % of extension: $\langle X \rangle / L = A \exp(-t/\tau) + B$.

for a chain at equilibrium in an infinite fluid. We shall also express flow strengths in terms of the Weissenberg number Wi, or ratio of the longest bulk relaxation time τ of the chain to the characteristic time scale of the flow (defined as the inverse of the wall shear rate): $Wi = \dot{\gamma}_w \tau$. The longest bulk relaxation time is obtained by letting an ensemble of initially straight chains relax in an infinite fluid, and by fitting a decaying exponential to the last 30 % of extension: $\langle X \rangle / L = A \exp(-t/\tau) + B$ (cf. Figure 7.2). Equivalently, the Weissenberg number is given by the product of the Péclet number and the dimensionless chain relaxation time. Note that in very confined geometries, both the radius of gyration and the relaxation time can be impacted by the presence of walls, the effects of which is are to decrease R_g and slow down relaxation [30, 7, 194, 195, 95, 96]. However these effects only become significant when $H < R_g$: for the cases investigated here where H is significantly larger than the radius of gyration, both R_g and τ are unaffected by confinement and we can therefore use their bulk values.

Typical concentration profiles across the gap are shown in Figure 7.3(*a*) for a chain composed of $N = 6$ segments and for various flow strengths in a channel of width $H = 8R_g$. The profiles, which are qualitatively similar to those obtained previously by other authors
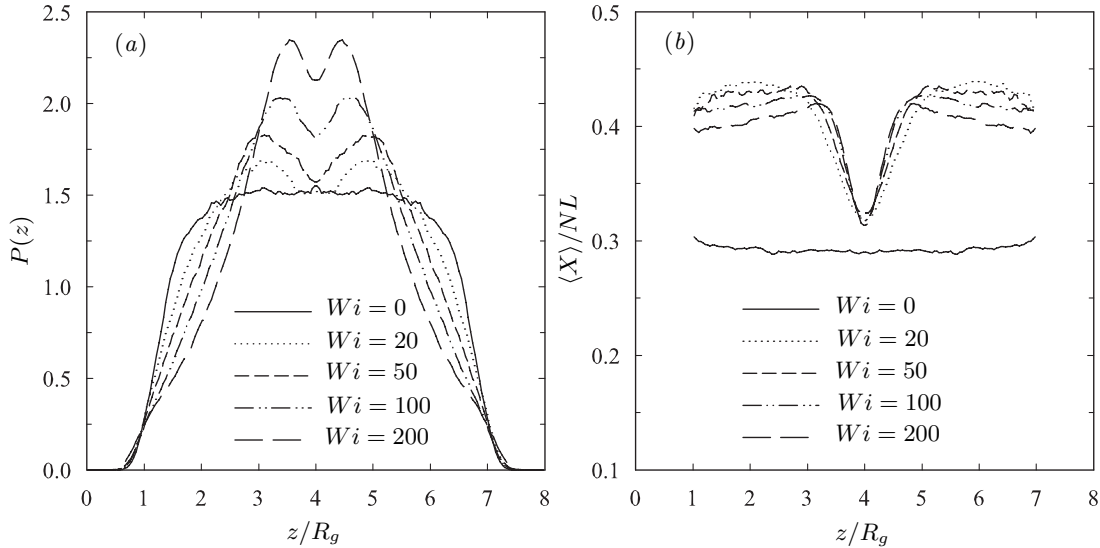
Figure 7.3: (a) Center-of-mass concentration profile and (b) average normalized stretch in the flow direction in a channel of width $H = 8R_g$ at various flow strengths, for a molecule composed of $N = 6$ segments of aspect ratio $A = 10$.

in the case of much longer chains [95, 97, 189, 190], present several interesting features. A clear depletion layer is observed in the vicinity of the walls. While this depletion layer exists even in the absence of flow ($Wi = 0$), where its thickness is of the order of one radius of gyration, it is shown to grow as Wi increases, resulting in fairly peaked distributions in strong flows. The profiles for $Wi > 0$ also exhibit a slight depletion at the centerline, which is a consequence of the gradient in the cross-streamline center-of-mass diffusivity resulting from the nonuniform stretching of the chain in the inhomogeneous shear. This nonuniform stretching is illustrated in Figure 7.3(b), showing the average molecular stretch $\langle X \rangle$ in the flow direction, normalized by the chain contour length NL. While the stretch profile is uniform in the absence of flow, significant variations of $\langle X \rangle$ across the gap are visible when flow is applied, with markedly stronger molecular stretch near the walls than near the centerline owing to the variations in shear rate. Interestingly, the dependence of $\langle X \rangle$ on the flow strength is rather weak when $Wi > 0$, a possible consequence of hydrodynamic interaction with the walls as further discussed below.
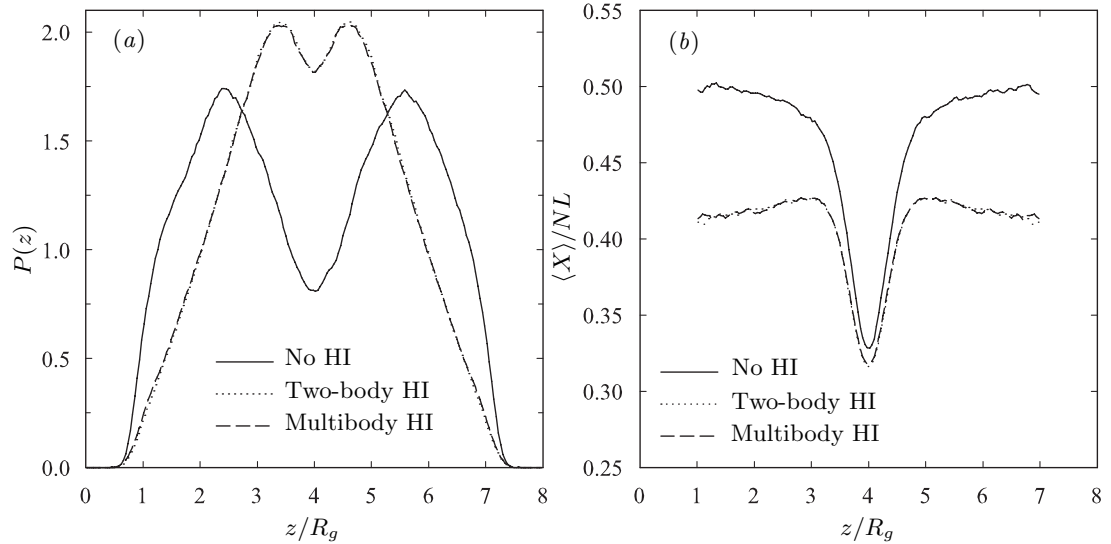
Figure 7.4: Influence of hydrodynamic interactions on (a) the center-of-mass concentration profile and (b) the average normalized stretch for a molecule composed of $N = 6$ segments of aspect ratio $A = 10$, in a channel of width $H = 8R_g$ at $Wi = 100$. The different curves show different levels of modeling: no hydrodynamic interactions, two-body hydrodynamic interactions, and multibody hydrodynamic interactions at the stresslet level.

To confirm the role of hydrodynamic interactions in the migration of the chains to-ward the centerline, simulations were performed in which the interactions were completely turned off, corresponding to a freely-draining chain with anisotropic drag. The results are summarized in Figure 7.4, showing concentration profiles and average stretch profiles with and without HI. The figure also shows profiles with a different level of modeling, in which the stresslet on each rod (Equation 7.7) was calculated based on $\boldsymbol{u}_\infty$ only: in that case each segment feels the disturbance velocity induced by the other segments placed in the imposed field $\boldsymbol{u}_\infty$ (including the associated wall disturbance), but the multiple reflections between the segments are not included (two-body HI). While the profiles corresponding to the two levels of modeling for HI cannot be distinguished, completely neglecting hydro-dynamic interactions yields qualitatively different results, with a very strong depletion at the channel centerline and no clear migration away from the walls (other than that due to excluded volume): in that case the depletion at the centerline is a consequence of the anisotropic drag on the chain segments, which results in a gradient in cross-streamline
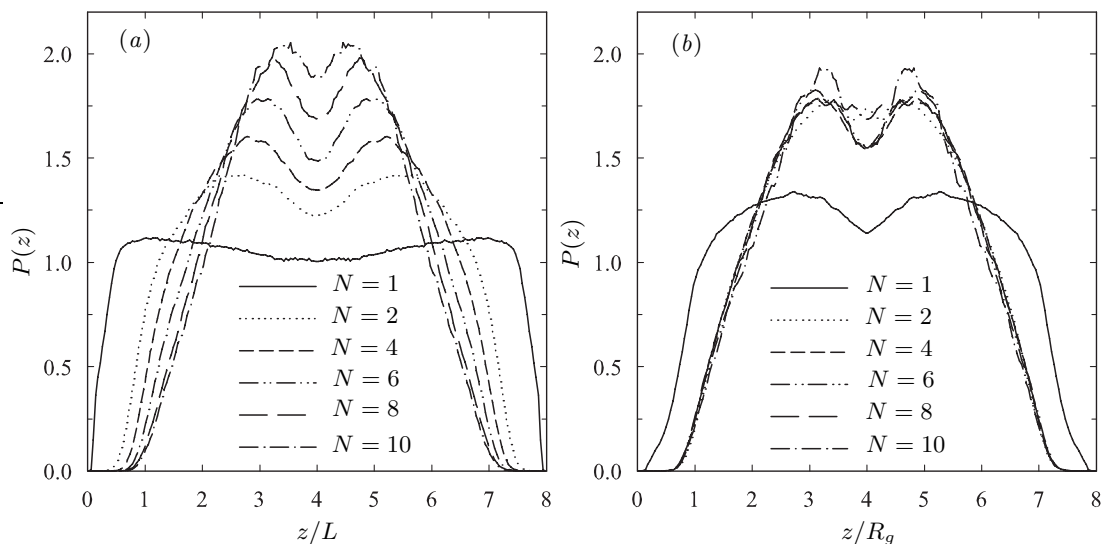
Figure 7.5: Concentration profiles for various chain lengths N when: (a) the Péclet number Pe and ratio H/L of the channel width to the Kuhn step length are held constant ($Pe = 100$, $H/L = 8$); (b) the Weissenberg number Wi and ratio H/R_g of the channel width to the bulk radius of gyration are held constant ($Wi = 50$, $H/R_g = 8$).

diffusivity qualitatively similar to that observed for a single Brownian rod [139, 164]. This is in qualitative agreement with the previous observations of Jendrejack *et al.* [97] for bead-spring chains, and confirms the importance of wall hydrodynamic interactions in the description of channel flows of flexible molecules. The effects of HI on molecular stretch are also visible in Figure 7.4(b), where it appears that hydrodynamic interactions reduce the ability for the chain to stretch in the vicinity of the walls. Note that this effect has also been observed in experiments [63], and may explain the weak dependence of molecular stretch on flow strength observed in Figure 7.3(b).

Figure 7.5 illustrates the influence of chain flexibility (measured by the number of Kuhn steps N) on the cross-streamline migration. In Figure 7.5(a) the Péclet number Pe and the ratio H/L of the channel width to the Kuhn step length are held constant: in this situation longer chains migrate much more strongly away from the walls than shorter ones, as exemplified by the very flat and very peaked profiles for $N = 1$ and $N = 10$ respectively. In this sense chain flexibility appears to facilitate migration, a consequence
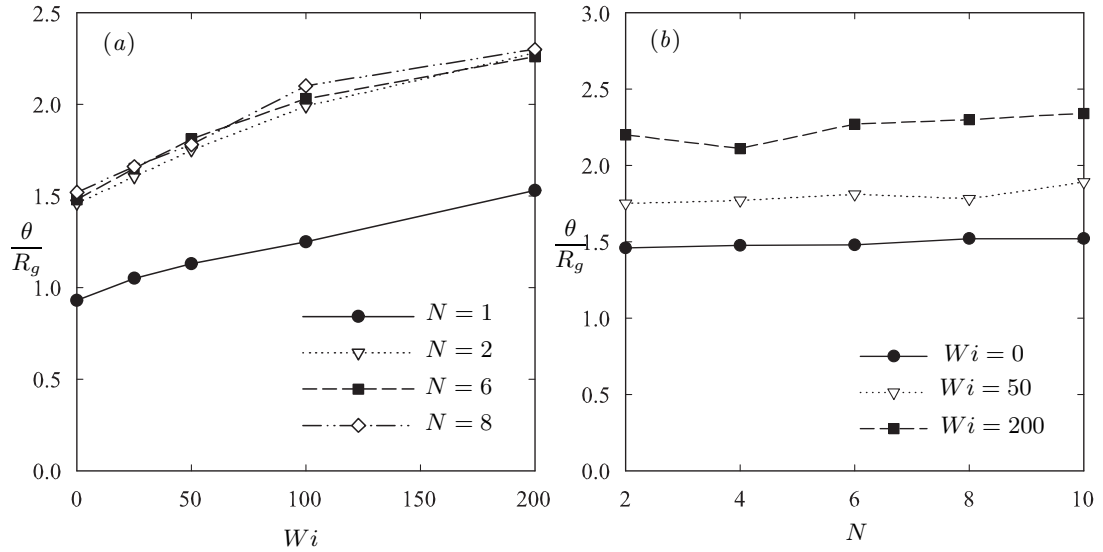
Figure 7.6: Depletion layer thickness θ (measured as the distance from the wall where the concentration reaches its mean value) as a function of: (a) the flow strength (or Weissenberg number Wi), and (b) the chain length N, for molecules composed of N segments of aspect ratio $A = 10$ in a channel of width $H = 8R_g$.

of the entropic force dipole exerted on the fluid [121], which is stronger in longer chains but nonexistent in the limit of a fully rigid rod ($N = 1$), where the only force dipole on the fluid is deterministic and due to the stresslet induced by the imposed shear rate. Most interestingly, the concentration profiles for the chain lengths $N \geq 2$ are observed to collapse onto a single curve when the Weissenberg number Wi and the ratio H/R_g of the channel width to the bulk radius of gyration are held constant, as shown in Figure 7.5(b) for $Wi = 50$ and $H = 8R_g$. Note that a similar collapse is also observed at other values of the Weissenberg number. This suggests in particular that Wi and H/R_g, rather than Pe and H/L, are the appropriate dimensionless groups for quantifying the effects of flow strength and channel width on the shear-induced migration. The fully rigid case ($N = 1$) however differs qualitatively, as shown in Figure 7.5(b): it is characterized by a much weaker migration (the mechanism for which is discussed below), and by a fairly strong depletion at the centerline as result of the gradient in center-of-mass diffusivity induced by the differential alignment of the rod across the channel width [139, 164].

Some of the observations mentioned above are summarized in Figure 7.6, showing the effects of flow strength and chain flexibility on the thickness θ of the wall depletion layer, defined as the position away from the walls where the concentration profile reaches its mean value. Figure 7.6(a) illustrates the thickening of the depletion layer with flow strength: θ/R_g is observed to increase from a value of approximately 1.5 in the absence of flow ($Wi = 0$) up to approximately 2.3 at $Wi = 200$ (for flexible chains $N \geq 2$). Again when θ is scaled by R_g the dependence on chain length is negligible, as the depletion layer thicknesses for $N = 2$, 6, and 8 collapse onto a single master curve. The insensitivity of the depletion layer thickness upon chain length is also illustrated in Figure 7.6(b), where it is observed that for a given flow strength θ/R_g does not depend on N over the range $N = 2$ to 10. Figure 7.6(a) also confirms the significantly different behavior of fully rigid chains ($N = 1$), for which depletions layers are much thinner than for flexible chains; yet a thickening of θ/R_g with flow strength is also observed.

The case of a fully rigid polymer ($N = 1$) was shown to differ qualitatively from the flexible case and therefore deserves further attention. Unlike a flexible chain which relaxes by entropic recoil, a rodlike polymer relaxes by randomization of its orientation. The mechanism for shear-induced migration proposed by Jendrejack *et al.* [97] and Ma & Graham [121] for flexible polymers, based on the entropic force dipole exerted by a chain on the fluid as it tries to recoil while being stretched by flow, therefore does not trivially carry over to rodlike polymers. Owing to its resistance to stretching, a rigid rod in a non-uniform flow also exerts a force dipole on the fluid, the magnitude of which is the stresslet $\mathscr{S}$ defined in Equation (7.7). While $\mathscr{S}$ clearly scales with flow strength, its sign and magnitude both depend on the orientation of the rod relative to the imposed flow, which itself is determined by the balance between fluid flow and thermal diffusion.

These considerations can be made more quantitative using similar arguments as in Ma & Graham [121]. The force dipole $\mathbf{D}$ on a freely-suspended rod with orientation $\boldsymbol{p}$ in the pressure-driven flow Equation (7.5) is given in dimensionless variables by:

$$\mathbf{D} = \mathscr{S} \left(\boldsymbol{pp} - \frac{\mathsf{I}}{3} \right) \approx \frac{1}{24} p_x p_z \dot{\gamma}(z) \left(\boldsymbol{pp} - \frac{\mathsf{I}}{3} \right), \tag{7.12}$$

where $\mathscr{S}$ is the stresslet on the rod, and $\dot{\gamma}(z) = \partial u_\infty/\partial z = Pe(1 - 2z/H)/L$ is the local shear rate. The rightmost expression in Equation (7.12) is the leading-order term in an expansion of Equation (7.7). As shown by Smart & Leighton [173], a force dipole **D** in the vicinity of a no-slip wall is subject to a drift velocity as a result of hydrodynamic interactions:

$$\boldsymbol{U}^D = -\frac{3}{8h^2 \log 2A}\left(\mathbf{I} + \frac{1}{2}\boldsymbol{nn}\right) \cdot \mathbf{D} \cdot \boldsymbol{n}, \tag{7.13}$$

where $\boldsymbol{n}$ is a unit vector normal to the plane of the wall and h is the distance from the wall. Substituting (7.12) into (7.13), and superimposing the effects of both walls (an approximation valid for large gaps $H/L \gg 1$), we find that the cross-streamline drift velocity of the rigid rod is to leading order:

$$U_z^D = -\frac{\dot{\gamma}(z)}{128 \log 2A}f(\phi)\left[\frac{1}{z^2} - \frac{1}{(H-z)^2}\right], \tag{7.14}$$

where $f(\phi)$ is a function of the projected angle ϕ of the rod orientation vector $\boldsymbol{p}$ onto the (x, z)-plane and measured with respect to the x-axis: $f(\phi) = \cos\phi\sin\phi(3\sin^2\phi - 1)$. Note that a more accurate albeit less intuitive expression for U_z^D accounting for multipole reflections between the rod and the two walls is easily derived using the slender-body theory described in §7.2.

Equation (7.14) shows that the rod can migrate either toward or away from the walls depending on the sign of $f(\phi)$, which is plotted on Figure 7.7(a). We see that both signs are possible depending on the value of the projected angle. In a sufficiently strong shear flow a rod will spend most of its time almost aligned in the flow direction ($\phi \gtrsim 0$), leading to a migration away from the walls ($f(\phi) \geq 0$ for $0 \leq \phi \leq 35°$). Note however that $f(0) = 0$, so that a very strong flow, while leading to large values of the shear rate $\dot{\gamma}(z)$ in Equation (7.14) for U_z^D, will also result in a very strong alignment of the rod for which $\langle f(\phi)\rangle$ may be small: the overall effect on the migration is therefore a subtle interplay between the magnitude of the dipole induced on the rod and the orientation of the rod with respect to the flow. The precise effect of flow strength is illustrated in Figure 7.7(b), showing the mean cross-streamline drift velocity $\langle U_z^D\rangle$ as a function
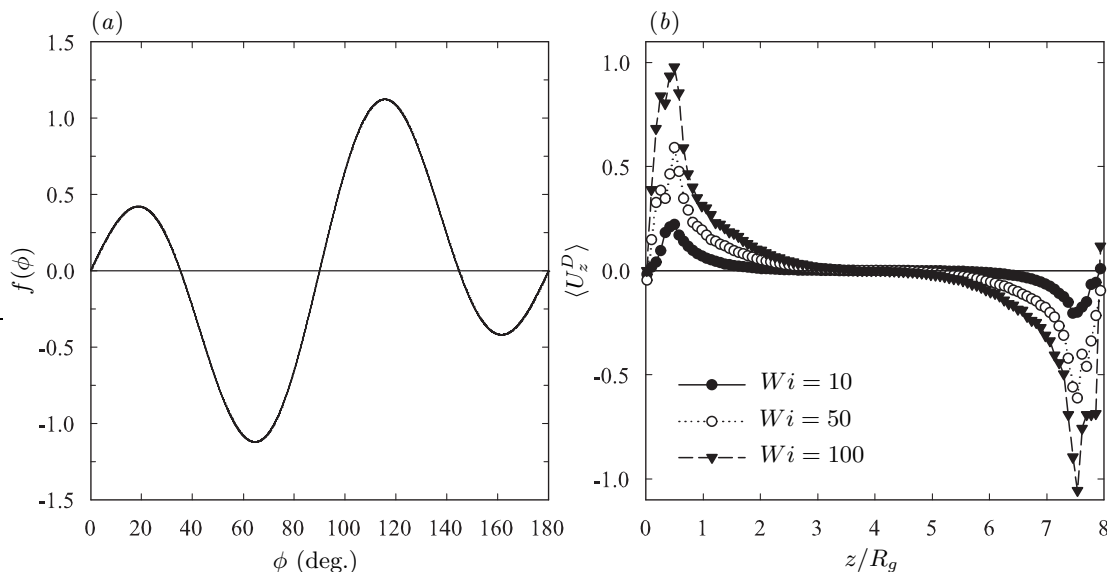
Figure 7.7: (*a*) Dependence $f(\phi)$ of the cross-streamline drift velocity U_z^D upon the projected angle ϕ of a rigid rod in the (x, z)-plane: $f(\phi) = \cos\phi\sin\phi(3\sin^2\phi - 1)$. (*b*) Profile of the mean cross-streamline drift velocity $\langle U_z^D \rangle$ for a rod of aspect ratio $A = 10$ in a channel of width $H = 8R_g$, at various flow strengths, obtained from simulations.

of position and for various values of the Weissenberg number, obtained using the full slender-body theory of §7.2 and calculated numerically over the course of the simulations. In particular, migration away from the walls is observed, and the magnitude of the drift increases with flow strength. Figure 7.7(*b*) also shows that the drift velocity is quite weak in the bulk of the channel, which may explain the relatively weak migration observed in Figure 7.5.

7.4 Concluding remarks

We have performed Brownian dynamics simulations of short-chain polymers in the pressure-driven flow between two infinite flat plates, in which we modeled a polymer molecule as a chain of freely-jointed hydrodynamically interacting Brownian rods. Our simulations showed that cross-streamline migration toward the channel centerline occurs as a result of hydrodynamic interaction of the polymer with the wall. While flexible chains of various

lengths $(2 \leq N \leq 10)$ all behave in a similar fashion for given values of the Weissenberg number Wi and of H/R_g, the ratio of the channel width to the bulk radius of gyration, fully rigid polymers $(N = 1)$ are observed to undergo a much weaker migration, the mechanism for which differs qualitatively and is based on a coupling between the stresslet induced by the flow on the rod, the orientation of the rod as determined by the balance of flow and thermal fluctuations, and hydrodynamic interactions with the walls.

Chapter 8

Conclusions and directions for future work

In this work, we have considered a number of problems in which complex dynamics arise in a particulate suspension or polymer solution as a consequence of the long-ranged hydrodynamic interactions between the suspended particles. In particular, our aim was to understand how particle shape or deformability modify these dynamics and in some instances result in new phenomena that are otherwise unobserved in suspensions of rigid isotropic particles. The approach followed here has consisted of investigating a few model problems with the aim of identifying the relevant physical mechanisms. Yet all of the problems described herein have broader implications for numerous physical phenomena or technological applications involving complex fluids.

In Chapters 3, 4 and 5, we developed efficient computer algorithms to simulate the inhomogeneous sedimentation in dispersions of rigid anistropic particles (such as fibers and spheroids) and deformable particles (such as viscous droplets, elastic microcapsules and flexible polymers). Our simulations were successful at capturing the concentration instability that occurs in these systems, and we performed a detailed investigation of the suspension microstructure and of the large-scale collective dynamics that result from the instability. Results on statistical properties such as the mean sedimentation speed,

velocity fluctuations and orientation distributions were also reported, and the effects of the instability on these quantities were discussed. By combining the simulation results with theoretical analyses and scaling arguments, we were able to describe a likely mechanism for the instability and determine a number of parameters affecting the wavenumber selection.

In Chapter 6, we focused on electrokinetically-driven hydrodynamic interactions in suspensions of polarizable particles. Previous investigations of these interactions had been very limited, and our study provided the first detailed description of this phenomenon in the case of rodlike particles. In particular, we demonstrated using theory and numerical simulations that the induced-charge electrophoretic flows that are driven at the particle surfaces when polarizable particles are placed in an electric field result in relative motions and pairing dynamics. The effects of these interactions in suspensions of both non-Brownian and Brownian particles were discussed, and results were presented for pair probabilities, hydrodynamic dispersion coefficients, velocity fluctuations, and orientation distributions.

Finally in Chapter 7, we investigated the effects of flexibility and of wall hydrodynamic interactions on the dynamics of short-chain flexible polymers in a pressure-driven channel flow. While this problem had recently been addressed in the case of long-chain polymers such as DNA, much less was known on the precise effects of flexibility when the chain length is a few random-walk steps. Using a detailed model for hydrodynamic interactions between the chain segments and channel walls, we performed Brownian dynamics simulations and showed that shear-induced migration away from the solid boundaries still occurs even for very short chains. We also discussed the case of fully rigid polymers, in which case a slightly different mechanism for migration was proposed.

For all of these problems, numerical simulations have proven a tremendous ally for the modeling the complex effects arising from multibody hydrodynamic interactions. The long-ranged nature of these interactions, which often act on length scales comparable to the system size, indeed defies simple analytical models. In fact, the work described here has shown the need for sophisticated algorithms if systems of realistic sizes are to be accurately simulated: much work therefore remains to be done as we attempt to simulate

yet larger and more complex systems. Several areas of complex fluid dynamics are yet to be fully understood, and we describe a few of these below.

- **Concentrated systems**: The problems described in this work all involved suspensions that were dilute, so that relatively simple models based on far-field descriptions of hydrodynamic interactions were often sufficient to capture the dynamics of interest. In fact, the simulation method used in Chapters 4 and 5 completely neglected short-range interactions, and yet yielded good comparisons with the experimental data. In many instances more concentrated suspensions are important: in these cases small-scale variations of the velocity fields, contacts or other close interactions may play a significant part in the dynamics. The modeling of these effects is typically quite difficult, and only a few successful attempts have been made. The Stokesian dynamics method introduced in Section 1.2.4 allows the simulation of concentrated suspensions of spheres, with volume fractions approaching the maximum random packing limit; its application remains however quite costly, especially for colloidal suspensions, and is therefore limited to systems of a few thousands of particles in fairly simple geometries. Other approaches for concentrated systems consist of neglecting far-field hydrodynamic interactions altogether by invoking screening by the surrounding particles, an approximation that may need to be quantified.

- **Confined systems**: Recent applications involving complex fluids in small scale systems such as micro- and nanofluidic devices have exposed the need for more efficient models to capture dynamics in strongly confined systems. Interactions with the boundaries, whether steric or hydrodynamic, as well as the short-scale variations of fluid flows in these devices indeed result in unexpected dynamics, one example of which was described in Chapter 7. Current methods to self-consistently simulate confined systems, such as those listed in Section 2.5, are not generally useful: while the Green's function method described in Chapter 7 is only easily applied in very simple geometries, more general methods based on the boundary integral equation are hardly practical owing to their very high cost.

- *Inertial effects*: In this work, we have only considered flows in which both fluid and particle inertia could be neglected with respect to viscous effects ($Re, St \to 0$). In the large-scale suspensions that arise for instance in environmental systems as well as in some industrial applications, fluid and/or particle inertia may become significant and lead to additional effects that cannot be anticipated using the methods presented here. Methods based on the boundary integral equation or multipole expansion do not easily carry over to the inertial regime, as the nonlinearity of the Navier-Stokes equations precludes the use of Green's functions. Yet other methods, similar in essence to that described in Section 4 and based on momentum coupling between the Navier-Stokes equations and Newton's equation of motion using distributed force fields can be used for flows at finite Stokes or Reynolds number (e.g. [22, 23, 31]): these methods have yet to be generally applied.

- *Complex physics*: The greatest challenge of complex fluid dynamics today may reside in the description of systems involving multiple physical phenomena, such as electric, thermal, chemical or mechanical phenomena. Such systems arise commonly in micro- and nanofluidic devices, where the short length and time scales involved often result in the interplay of various effects; such is also the case in numerous bio-physical systems. The difficulty in tackling these problems is twofold. On the one hand, a precise understanding of the basic physical phenomena and their coupling is in most cases still lacking. For instance electrokinetic phenomena, which result from the dynamics of diffuse ions in solution, are traditionally described using continuum models: these models however are observed to break down in some instances where discrete ion effects become significant (e.g. steric effects inside electrical double layers). On the other hand, the numerical simulation of these phenomena offers new challenges owing to the large number of degrees of freedom and of the highly nonlinear coupling between the various effects. Much work therefore remains be to done before an accurate understanding of many of these systems is achieved.

Appendix A

Periodic fundamental solution and Ewald summation formula

A.1   Periodic fundamental solution

This section derives the periodic fundamental solution of the Stokes equations, which was first obtained by Hasimoto [81]. The derivation presented here is similar to that of Hasimoto, although other approaches are possible. Pozrikidis [148] gives a comprehensive review of both two- and three-dimensional solutions, for singly, doubly and triply periodic arrays.

Consider the flow past a three-dimensional periodic array of point forces $\boldsymbol{F}$ applied at positions:

$$\boldsymbol{r}_n = n_1\boldsymbol{a}_1 + n_2\boldsymbol{a}_2 + n_3\boldsymbol{a}_3, \tag{A.1}$$

where $\boldsymbol{a}_1$, $\boldsymbol{a}_2$, $\boldsymbol{a}_3$ are the lattice unit vectors and $n_1, n_2, n_3 \in \mathbb{Z}$. Let τ_0 denote the volume of the unit cell: $\tau_0 = \boldsymbol{a}_1 \cdot (\boldsymbol{a}_2 \times \boldsymbol{a}_3)$. The Stokes equations take on the following form:

$$\mu\boldsymbol{\nabla}^2\boldsymbol{u} = \boldsymbol{\nabla}p + \boldsymbol{F}\sum_n \delta(\boldsymbol{r} - \boldsymbol{r}_n) \quad \text{and} \quad \boldsymbol{\nabla}\cdot\boldsymbol{u} = 0, \tag{A.2}$$

where $\delta(\boldsymbol{r} - \boldsymbol{r}_n)$ is the three-dimensional Dirac delta function.

The flow field is expected to be periodic, and therefore we can expand $\boldsymbol{u}$ and $-\boldsymbol{\nabla}p$ in Fourier series as follows:

$$\boldsymbol{u} = \sum_{\boldsymbol{k}} \boldsymbol{u}_{\boldsymbol{k}} \mathrm{e}^{-2\pi \mathrm{i}\boldsymbol{k}\cdot\boldsymbol{r}} \tag{A.3}$$

$$-\boldsymbol{\nabla}p = \sum_{\boldsymbol{k}} \boldsymbol{P}_{\boldsymbol{k}} \mathrm{e}^{-2\pi \mathrm{i}\boldsymbol{k}\cdot\boldsymbol{r}} \tag{A.4}$$

The vectors $\boldsymbol{k}$ are the reciprocal lattice vectors: $\boldsymbol{k} = n_1\boldsymbol{b}_1 + n_2\boldsymbol{b}_2 + n_3\boldsymbol{b}_3$ and satisfy: $\boldsymbol{k}\cdot\boldsymbol{a}_j = n_j$ for $j = 1,2,3$. The basis vectors $\boldsymbol{b}_1$, $\boldsymbol{b}_2$, $\boldsymbol{b}_3$ in the reciprocal lattice can be found to be:

$$\boldsymbol{b}_1 = \frac{\boldsymbol{a}_2 \times \boldsymbol{a}_3}{\tau_0}, \quad \boldsymbol{b}_2 = \frac{\boldsymbol{a}_3 \times \boldsymbol{a}_1}{\tau_0}, \quad \boldsymbol{b}_3 = \frac{\boldsymbol{a}_1 \times \boldsymbol{a}_2}{\tau_0} \tag{A.5}$$

When the original lattice is orthogonal, $\boldsymbol{b}_j$ is equal to $\boldsymbol{a}_j$ rescaled by the unit volume τ_0.

We have the following representation for the three-dimensional periodic Dirac delta function:

$$\sum_{n} \delta(\boldsymbol{r} - \boldsymbol{r}_n) = \frac{1}{\tau_0} \sum_{\boldsymbol{k}} \mathrm{e}^{-2\pi \mathrm{i}\boldsymbol{k}\cdot\boldsymbol{r}}, \tag{A.6}$$

which can be derived by expanding the left-hand side in Fourier series:

$$\sum_{n} \delta(\boldsymbol{r} - \boldsymbol{r}_n) = \sum_{\boldsymbol{k}} c_{\boldsymbol{k}} \mathrm{e}^{-2\pi \mathrm{i}\boldsymbol{k}\cdot\boldsymbol{r}}, \tag{A.7}$$

and solving for the Fourier coefficient as follows:

$$c_{\boldsymbol{k}} = \frac{1}{\tau_0} \int_{\tau_0} \sum_{n} \delta(\boldsymbol{r} - \boldsymbol{r}_n) \mathrm{e}^{2\pi \mathrm{i}\boldsymbol{k}\cdot\boldsymbol{r}} \mathrm{d}V = \frac{1}{\tau_0} \int_{\tau_0} \delta(r) \mathrm{e}^{2\pi \mathrm{i}\boldsymbol{k}\cdot\boldsymbol{r}} \mathrm{d}V = \frac{1}{\tau_0}. \tag{A.8}$$

Substituting (A.3), (A.4) and (A.6) into the momentum equation gives:

$$\mu\boldsymbol{\nabla}^2 \left(\sum_{\boldsymbol{k}} \boldsymbol{u}_{\boldsymbol{k}} \mathrm{e}^{-2\pi \mathrm{i}\boldsymbol{k}\cdot\boldsymbol{r}} \right) = -\sum_{\boldsymbol{k}} \boldsymbol{P}_{\boldsymbol{k}} \mathrm{e}^{-2\pi \mathrm{i}\boldsymbol{k}\cdot\boldsymbol{r}} + \frac{\boldsymbol{F}}{\tau_0} \sum_{\boldsymbol{k}} \mathrm{e}^{-2\pi \mathrm{i}\boldsymbol{k}\cdot\boldsymbol{r}} \tag{A.9}$$

from which we easily obtain:

$$-4\pi^2\mu k^2 \boldsymbol{u_k} = -\boldsymbol{P_k} + \frac{\boldsymbol{F}}{\tau_0}, \quad \forall \boldsymbol{k} = n_1\boldsymbol{b_1} + n_2\boldsymbol{b_2} + n_3\boldsymbol{b_3}. \tag{A.10}$$

We wish to solve for the Fourier coefficients of the velocity $\boldsymbol{u_k}$ and pressure gradient $\boldsymbol{P_k}$. First observe that (A.10) for $\boldsymbol{k} = \boldsymbol{0}$ gives:

$$\boldsymbol{P_0} = \frac{\boldsymbol{F}}{\tau_0}, \tag{A.11}$$

meaning that the force exerted by the particles on the fluid is balanced by a mean pressure gradient.

The continuity equation also leads to:

$$\boldsymbol{\nabla} \cdot \left(\sum_{\boldsymbol{k}} \boldsymbol{u_k} e^{-2\pi i \boldsymbol{k} \cdot \boldsymbol{r}} \right) = \sum_{\boldsymbol{k}} \boldsymbol{k} \cdot \boldsymbol{u_k} e^{-2\pi i \boldsymbol{k} \cdot \boldsymbol{r}} = 0 \tag{A.12}$$

and hence $\boldsymbol{k} \cdot \boldsymbol{u_k} = 0$ for all $\boldsymbol{k}$. Thus taking the dot product of (A.10) with $\boldsymbol{k}$ allows one to eliminate $\boldsymbol{u_k}$ and gives:

$$\boldsymbol{k} \cdot \boldsymbol{P_k} = \frac{\boldsymbol{k} \cdot \boldsymbol{F}}{\tau_0}. \tag{A.13}$$

Taking the curl of (A.4) also shows easily that $\boldsymbol{P_k} \times \boldsymbol{k} = \boldsymbol{0}$. This shows that $\boldsymbol{P_k}$ is colinear with $\boldsymbol{k}$ and therefore:

$$\boldsymbol{P_k} = \frac{(\boldsymbol{P_k} \cdot \boldsymbol{k})\boldsymbol{k}}{k^2} = \frac{(\boldsymbol{k} \cdot \boldsymbol{F})\boldsymbol{k}}{\tau_0 k^2}, \quad \forall \boldsymbol{k} \neq \boldsymbol{0}. \tag{A.14}$$

Having found the Fourier coefficients for the pressure gradient, we can substitute (A.14) back into (A.10) to find those for the velocity:

$$\boldsymbol{u_k} = \frac{1}{4\pi^2\mu\tau_0} \left(\frac{\boldsymbol{k}\boldsymbol{k}}{k^4} - \frac{\mathsf{I}}{k^2} \right) \cdot \boldsymbol{F}, \quad \forall \boldsymbol{k} \neq \boldsymbol{0}. \tag{A.15}$$

We have determined the Fourier coefficients of the velocity and pressure gradient of

the fluid, which can now be expressed as:

$$\boldsymbol{u} \; = \; \boldsymbol{u}_0 - \frac{1}{4\pi\mu}\left[S^1 - \boldsymbol{\nabla}(\boldsymbol{\nabla}S^2)\right]\boldsymbol{F}, \tag{A.16}$$

$$-\boldsymbol{\nabla}p \; = \; \frac{\boldsymbol{F}}{\tau_0} - \frac{1}{4\pi}\boldsymbol{\nabla}(\boldsymbol{\nabla}S^1)\boldsymbol{F}, \tag{A.17}$$

where S^1 and S^2 are the following sums:

$$S^1 \; = \; \frac{1}{\pi\tau_0}\sum_{\boldsymbol{k}\neq\boldsymbol{0}}\frac{\mathrm{e}^{-2\pi\mathrm{i}\boldsymbol{k}\cdot\boldsymbol{r}}}{k^2}, \tag{A.18}$$

$$S^2 \; = \; -\frac{1}{4\pi^3\tau_0}\sum_{\boldsymbol{k}\neq\boldsymbol{0}}\frac{\mathrm{e}^{-2\pi\mathrm{i}\boldsymbol{k}\cdot\boldsymbol{r}}}{k^4}. \tag{A.19}$$

Equations (A.16)–(A.17) are an exact solution to the Stokes equations. Yet the Fourier sums S^1 and S^2 still decay quite slowly as $1/k^2$ and $1/k^4$, making their direct calculation impractical. Next, we derive the Ewald summation formula, which allows the transformation of S^1 and S^2 into exponentially convergent sums.

A.2   Ewald summation formula

The starting point for the transformation consists of using the following integral representation for $1/k^{2m}$, valid for any integer $m > 0$:

$$\frac{1}{k^{2m}} = \frac{\pi^m}{\Gamma(m)}\int_0^\infty \mathrm{e}^{-\pi k^2\beta}\beta^{m-1}\mathrm{d}\beta, \tag{A.20}$$

where $\Gamma(m)$ is the complete Γ-function. We wish to evaluate sums of the form:

$$\sigma_m = \sum_{\boldsymbol{k}\neq\boldsymbol{0}}\frac{\mathrm{e}^{-2\pi\mathrm{i}\boldsymbol{k}\cdot\boldsymbol{r}}}{k^{2m}}, \tag{A.21}$$

from which $S^1 = \sigma_1/\pi\tau_0$ and $S^2 = -\sigma_2/4\pi^3\tau_0$. Using Equation (A.20) we find:

$$\sigma_m = \frac{\pi^m}{\Gamma(m)}\sum_{\boldsymbol{k}\neq\boldsymbol{0}}\int_0^\infty \mathrm{e}^{-\pi k^2\beta-2\pi\mathrm{i}\boldsymbol{k}\cdot\boldsymbol{r}}\beta^{m-1}\mathrm{d}\beta. \tag{A.22}$$

Split the integral with respect to β into two parts by introducing a parameter $\alpha \in [0, \infty]$ called Ewald coefficient, and apply Ewald's θ-transformation formula

$$\sum_{\boldsymbol{k}} \mathrm{e}^{-\pi k^2 \beta - 2\pi \mathrm{i} \boldsymbol{k} \cdot \boldsymbol{r}} = \frac{\tau_0}{\beta^{3/2}} \sum_n \mathrm{e}^{-\pi (\boldsymbol{r} - \boldsymbol{r}_n)^2 / \beta} \tag{A.23}$$

to the integral from 0 to α. We obtain:

$$\begin{aligned}
\sum_{\boldsymbol{k} \neq \boldsymbol{0}} \int_0^\infty \mathrm{e}^{\pi k^2 \beta - 2\pi \mathrm{i} \boldsymbol{k} \cdot \boldsymbol{r}} \beta^{m-1} \mathrm{d}\beta &= \int_0^\alpha \left[\frac{\tau_0}{\beta^{3/2}} \sum_n \mathrm{e}^{-\pi (\boldsymbol{r} - \boldsymbol{r}_n)^2 / \beta} - 1 \right] \beta^{m-1} \mathrm{d}\beta \\
&\quad + \sum_{\boldsymbol{k} \neq \boldsymbol{0}} \int_\alpha^\infty \mathrm{e}^{-\pi k^2 \beta - 2\pi \mathrm{i} \boldsymbol{k} \cdot \boldsymbol{r}} \beta^{m-1} \mathrm{d}\beta,
\end{aligned} \tag{A.24}$$

in which the -1 in the first term on the right-hand side comes from the term $\boldsymbol{k} = \boldsymbol{0}$ in the sums. Changing the integration variable to $\xi = \alpha / \beta$ in the first integral, and to $\xi = \beta / \alpha$ in the second integral, we obtain the following expression for σ_m:

$$\begin{aligned}
\sigma_m &= \frac{\pi^m \alpha^m}{\Gamma(m)} \left[\frac{\tau_0}{\alpha^{3/2}} \sum_n \int_1^\infty \mathrm{e}^{-\frac{\pi (\boldsymbol{r} - \boldsymbol{r}_n)^2 \xi}{\alpha}} \xi^{-m+1/2} \mathrm{d}\xi - \frac{1}{m} \right. \\
&\quad \left. + \sum_{\boldsymbol{k} \neq \boldsymbol{0}} \mathrm{e}^{-2\pi \mathrm{i} \boldsymbol{k} \cdot \boldsymbol{r}} \int_1^\infty \mathrm{e}^{-\pi \alpha k^2 \xi} \xi^{m-1} \mathrm{d}\xi \right].
\end{aligned} \tag{A.25}$$

Introducing the incomplete Γ-functions $\phi_\nu(x) = \int_1^\infty \xi^\nu \mathrm{e}^{-x\xi} \mathrm{d}\xi$, this simplifies to:

$$\sigma_m = \frac{\pi^m \alpha^m}{\Gamma(m)} \left[\frac{\tau_0}{\alpha^{3/2}} \sum_n \phi_{-m+\frac{1}{2}} \left(\frac{\pi (\boldsymbol{r} - \boldsymbol{r})^2}{\alpha} \right) - \frac{1}{m} + \sum_{\boldsymbol{k} \neq \boldsymbol{0}} \mathrm{e}^{-2\pi \mathrm{i} \boldsymbol{k} \cdot \boldsymbol{r}} \phi_{m-1}(\pi \alpha k^2) \right]. \tag{A.26}$$

The incomplete Γ-functions are calculated by application of the following recursion formula: $x\phi_\nu = \mathrm{e}^{-x} + \nu \phi_{\nu-1}$. In particular:

$$\phi_0(x) = \frac{\mathrm{e}^{-x}}{x}, \quad \text{and} \quad \phi_{-1/2}(x) = \sqrt{\frac{\pi}{x}} \mathrm{erfc}(\sqrt{x}). \tag{A.27}$$

Appendix B

Cardinal B-spline interpolation

B.1 General properties of Cardinal B-splines

This appendix presents a few basic results on the Cardinal B-splines used for the interpolation in the SPME algorithm of Chapter 3. A similar, somewhat more detailed discussion can be found in Essmann et al. [57], or in Schoenberg [165].

A Cardinal spline of order p is a function defined over the set of real numbers $\mathbb{R}$, of class C^{p-2} (i.e. $p-2$ times continuously differentiable), and such that its restriction to any interval $[m, m+1)$ for any integer m is a polynomial of degree less than or equal to $p-1$. The set of Cardinal splines of order p is denoted S_p and is easily shown to be a vector space. Quite obviously, S_p is stable by integer translation, i.e. if $f(u)$ is in S_p, so is $f(u-m)$ for any integer m. A linear basis for this vector space is provided by the Cardinal B-splines, which are defined as follows. For any real number $u \in \mathbb{R}$, introduce the notations $u_+ = \max(u, 0) = (u + |u|)/2$, and $u_+^p = (u_+)^p$. Define the following function over $\mathbb{R}$:

$$M_p(u) = \frac{1}{(p-1)!} \sum_{k=0}^{p} (-1)^k \frac{p!}{k!(p-k)!} (u-k)_+^{p-1}, \qquad u \in \mathbb{R}. \tag{B.1}$$

It can be shown that $M_p(u)$ is a Cardinal spline, and that the set of its integer translates $M_p(u-m)$, called Cardinal B-splines, forms a basis of S_p. This means in particular that

225

any function $f(u)$ in S_p can be written uniquely as:

$$f(u) = \sum_{m=-\infty}^{+\infty} c_m M_p(u - m).$$ (B.2)

The function $M_p(u)$ can be shown to have the following interesting properties:

1. $M_p(u) > 0$ for $u \in (0, p)$, and $M_p(u) = 0$ otherwise. In particular, this shows that all the p-th order Cardinal B-splines have compact support of length $p + 1$.

2. $M_p(u)$ is symmetric with respect to the center of its support: $M_p(p - u) = M_p(u)$.

3. The Cardinal B-splines sum up to 1: $\displaystyle\sum_{m=-\infty}^{+\infty} M_p(u - m) = 1$.

4. The p-th order B-splines can be obtained from the lower-order B-splines by a recursion formula:
$$M_p(u) = \frac{u}{p-1} M_{p-1}(u) + \frac{p - u}{p - 1} M_{p-1}(u - 1).$$ (B.3)

   In practice Equation (B.3) is used to compute the Cardinal B-splines, rather than the definition Equation (B.1).

5. The derivatives of the B-splines can be obtained from lower-order B-splines:

$$\frac{\mathrm{d}}{\mathrm{d}u} M_p(u) = M_{p-1}(u) + M_{p-1}(u - 1).$$ (B.4)

A list of the Cardinal B-splines of orders 1 through 7 can be found in Deserno and Holm [49].

B.2   Interpolation of complex exponentials

Let us now proceed to show how the Cardinal B-splines can be used to interpolate complex exponentials. Consider the complex-valued function $g(u) = \exp\left(2\pi \mathrm{i} k u / K\right)$, where u is a real number, and k and K are fixed integers. To alleviate the notations we will set

$z = \exp(2\pi \mathrm{i} k/K)$, so that now $g(u) = z^u$ where z is some fixed complex number. Quite obviously, we have the property that $g(u+1) = zg(u)$. We wish to interpolate the function g by a p-th order spline $g_p \in S_p$ which satisfies the same property: $g_p(u+1) = zg_p(u)$. Since $g_p(u)$ is a Cardinal spline, it can be decomposed on the basis of B-splines:

$$g_p(u) = \sum_{m=-\infty}^{+\infty} c_m M_p(u - m), \tag{B.5}$$

and also:

$$g_p(u+1) = \sum_{m=-\infty}^{+\infty} c_m M_p(u + 1 - m) = \sum_{m=-\infty}^{+\infty} c_{m+1} M_p(u - m). \tag{B.6}$$

Invoking the uniqueness of the decompositions Equations (B.5) and (B.6), we must have $c_{m+1} = zc_m$ for all integers m for the property $g_p(u+1) = zg_p(u)$ to be satisfied. A simple recursion leads to $c_m = z^m c_0$ for all integers m, and hence:

$$g_p(u) = c_0 \Phi_p(u) \quad \text{where} \quad \Phi_p(u) = \sum_{m=-\infty}^{+\infty} z^m M_p(u - m). \tag{B.7}$$

If $\Phi_p(0)$ is non-zero, we can choose the coefficient c_0 to be $1/\Phi_p(0)$. Then we have by construction $g_p(0) = 1$, and $g_p(m) = zg_p(m-1)$ for any integer m, so that by simple recursion $g_p(m) = z^m g_p(0) = z^m$. It can be shown that the only case where $\Phi_p(0) = 0$ is when p is odd and $2|k| = K$. In all other cases we have constructed a p-th order spline which interpolates the function $g(u)$ at all the integers. Recalling the original definition of z, and defining:

$$b(k) = \frac{1}{\Phi_p(0)} = \frac{\exp\left(2\pi \mathrm{i}\dfrac{k}{K}(p-1)\right)}{\displaystyle\sum_{m=0}^{p-2} M_p(m+1)\exp\left(2\pi \mathrm{i}\dfrac{km}{K}\right)}, \tag{B.8}$$

we obtain:

$$\exp\left(2\pi \mathrm{i}\frac{ku}{K}\right) \simeq b(k) \sum_{m=-\infty}^{\infty} M_p(u - m)\exp\left(2\pi \mathrm{i}\frac{km}{K}\right). \tag{B.9}$$

The error in the approximation Equation (B.9) can be shown to be bounded by $(2|k|/K)^p$.

Appendix C

Numerical accuracy of the slip solutions

The solution of the Stokes equations described in Section 4.2.1 is based on a few approximations, the effects of which are investigated in this Appendix. First we study the effects of the tangential flow boundary condition at the container walls in Section C.1, where we provide a comparison to a more accurate solution satisfying the no-slip boundary condition on two of the vertical walls. The effects of the grid resolution (number of Fourier modes) are then discussed in Section C.2.

C.1 Effect of the tangential flow boundary condition

The simulations of Chapter 4 have shown the importance of the no-flux boundary condition for the fluid of the bottom of the container, which is responsible for large-scale recirculation and appears to play a central role in the wavenumber selection of the concentration instability. While the no-flux condition is crucial at the bottom wall, previous investigations have suggested that the no-slip boundary condition on the container side walls may play a part in the damping of the velocity fluctuations (e.g. [28, 132]). The Green's function for Stokes flow is indeed strongly affected in confined geometries, where

Time	Window	Slip		No-slip	
		$\langle u_z \rangle$	Δu_z	$\langle u_z \rangle$	Δu_z
$t = 0$	$0 < z < 180$	0.79	1.20	0.78	0.59
	$45 < z < 67.5$	0.83	1.17	0.79	0.61
$t = 20$	$0 < z < 180$	1.38	2.43	1.18	1.12
	$45 < z < 67.5$	1.52	3.09	1.21	1.19
$t = 40$	$0 < z < 180$	1.18	1.35	1.03	0.87
	$45 < z < 67.5$	1.21	1.60	1.11	0.98
$t = 60$	$0 < z < 180$	1.15	1.20	1.05	0.89
	$45 < z < 67.5$	1.13	1.47	1.05	0.85
$t = 80$	$0 < z < 180$	1.06	0.85	1.06	0.80
	$45 < z < 67.5$	1.10	0.91	1.07	0.80

Table C.1: Influence of the flow boundary condition on the container side walls. Average sedimentation velocities $\langle u_z \rangle$ and velocity fluctuations in the vertical direction Δu_z were evaluated for a set of particle configurations corresponding to various stages during sedimentation ($t = 0$ to 80), using the tangential flow boundary condition described in Section 4.2.1 ('slip'), and the Green's function of Mucha *et al.* [132], which satisfies the no-slip boundary condition on two of the side walls ('no-slip'). The particle configurations used were obtained from a full simulation using the tangential flow boundary condition, in a suspension of 29,702 spheroids of aspect ratio $A = 15$ in a box of dimensions $L_x = 32$, $L_y = 12$, $L_z = 180$ (volume fraction $\phi = 0.1$ %). The statistics were calculated in two different windows: $0 < z < 180$ (entire container), and $45 < z < 67.5$ (same window as in Figure 4.8).

hydrodynamic interactions decay faster and are effectively screened over distances of the order of the shortest wall separation.

While the Green's function for Stokes flow between two parallel walls is known [117, 17, 180, 99]), no analytical form exists in the case of finite containers such as the ones considered in this work. For the purpose of comparison with the slip solution used in our work, we implemented the Green's function proposed by Mucha *et al.* [132], which satisfies the no-slip boundary condition on two of the side walls (typically the two closest ones) and a tangential flow boundary condition on the remaining walls. This Green's function uses expansions in Fourier series in the two directions parallel to the no-slip walls, which are typically truncated at a finite number of modes; yet the absence of periodicity in the third

direction precludes the use of fast Fourier transforms as for the slip solution, resulting in a higher computational cost for the evaluation of hydrodynamic interactions. The reader is referred to the appendix of Mucha *et al.* [132] for a detailed discussion of the no-slip solution.

Results of the comparison are summarized in Table C.1, where we show the effects of the boundary condition on the mean velocity and velocity fluctuations. These two quantities were calculated with either of the two Green's functions for a series of particle configurations corresponding to various stages of the sedimentation in a suspension of spheroids. While the mean velocities are quite similar in both cases (albeit somewhat higher with slip boundaries), Table C.1 shows that velocity fluctuations are systematically overestimated when slip is allowed, by up to a factor of 2 at the peak of the fluctuations. This result, which supports the previous conclusions of Brenner [28] and Mucha *et al.* [132], also explains some of the differences noted in Section 4.2.5 between our simulation results and the experimental data of Herzhaft & Guazzelli [84].

C.2   Effect of the grid resolution

The effects of the grid resolution (i.e. number of Fourier modes) on the sedimentation statistics were also investigated. The results of this study are summarized in Table C.2, which reports velocity statistics obtained using three different grid resolutions. Note that in the method described in Sections 4.2.1 and 4.2.1, an increase in the number of Fourier modes also results in the reduction of the extent of the force assignment function, so that in the limit of an infinite number of modes the exact solution for a point force (Dirac delta function) should be recovered. As shown in Table C.2, the effect of the grid resolution on the mean sedimentation velocity are negligible. The velocity fluctuations however are affected more strongly, and are observed to decrease as the number of modes increases; significant errors can be expected using very coarse grids. In the simulations described in Chapters 4 and 5 we typically used on the order of 32 modes in the horizontal directions and 128 modes in the vertical direction.

		Number of Fourier modes					
		$16 \times 16 \times 64$		$32 \times 16 \times 128$		$64 \times 32 \times 256$	
Time	Window	$\langle u_z \rangle$	Δu_z	$\langle u_z \rangle$	Δu_z	$\langle u_z \rangle$	Δu_z
$t = 0$	$0 < z < 180$	0.81	1.82	0.79	1.20	0.77	0.99
	$45 < z < 67.5$	0.84	1.85	0.83	1.17	0.81	0.92
$t = 20$	$0 < z < 180$	1.36	2.98	1.38	2.43	1.38	2.22
	$45 < z < 67.5$	1.54	3.75	1.52	3.09	1.52	2.89
$t = 40$	$0 < z < 180$	1.09	1.93	1.18	1.35	1.21	1.19
	$45 < z < 67.5$	1.17	2.31	1.21	1.60	1.31	1.51
$t = 60$	$0 < z < 180$	1.06	1.60	1.15	1.20	1.22	1.32
	$45 < z < 67.5$	1.16	1.83	1.13	1.47	1.18	1.45
$t = 80$	$0 < z < 180$	0.96	1.13	1.06	0.85	1.18	0.98
	$45 < z < 67.5$	1.03	1.21	1.10	0.91	1.20	1.03

Table C.2: Influence of the grid resolution on the accuracy of the Stokes flow solution. Average sedimentation velocities $\langle u_z \rangle$ and velocity fluctuations in the vertical direction Δu_z were evaluated for a set of particle configurations corresponding to various stages during sedimentation ($t = 0$ to 80), for various grid resolutions (i.e. numbers of Fourier modes). The same particle configurations were used as in Table C.1, and the statistics were calculated in two different windows: $0 < z < 180$ (entire container), and $45 < z < 67.5$ (same window as in figure 4.8).

Appendix D

Pair interactions by the method of reflections

This Appendix uses the method of reflections [101] combined with multipole expansions to analytically derive an asymptotic expression for the relative motion between two aligned rods as a series in powers of $l/|\boldsymbol{x}|$. Note that a similar series can also be obtained by expanding Equations (6.47)–(6.49); however the method of reflections provides an intuitive justification for these equations, and does not make any assumptions on the linearity or direction of the force distributions along the rods.

D.1 Zeroth-order velocity

We consider the situation of Figure 6.4 where the two rods are aligned in the direction of the electric field and the first rod is located at the origin. The first step of the method of reflections consists of determining the linear velocity of the second rod placed in the electrophoretic disturbance field that the first rod would create if it were by itself. This disturbance field is that induced by the linear force distribution of Equation (6.39), which for an aligned rod simplifies to:

$$\boldsymbol{f}_1^{(0)}(s_1) = -\frac{2\pi\varepsilon s_1}{\log 2\gamma} G_\parallel^2 E_\infty^2 \boldsymbol{p}.$$

(D.1)

From Equation (2.22) the disturbance velocity at an arbitrary position $\boldsymbol{x}$ is:

$$\boldsymbol{u}_1^{(0)}(\boldsymbol{x}) = \frac{1}{8\pi\mu} \int_{-l}^{l} \mathsf{K}(\boldsymbol{x} - s_1\boldsymbol{p}) \cdot \boldsymbol{f}_1^{(0)}(s_1)\mathrm{d}s_1. \tag{D.2}$$

Expanding $\mathsf{K}(\boldsymbol{x} - s_1\boldsymbol{p})$ in a Taylor series around $s_1 = 0$, and substituting Equation (D.1) for the force distribution, we can express the disturbance velocity as:

$$\boldsymbol{u}_1^{(0)}(\boldsymbol{x}) = \frac{\varepsilon G_\parallel^2 E_\infty^2}{4\mu \log 2\gamma} \left[\frac{2l^3}{3} \boldsymbol{p} \cdot \boldsymbol{\nabla}\mathsf{K}(\boldsymbol{x}) + \frac{l^5}{15} \boldsymbol{ppp} : \boldsymbol{\nabla}\boldsymbol{\nabla}\boldsymbol{\nabla}\mathsf{K}(\boldsymbol{x}) \right] \cdot \boldsymbol{p} + O(|\boldsymbol{x}|^{-6}). \tag{D.3}$$

Note that only odd derivatives appear in the expansion due to the linearity of the force distribution. Using the notation $\cos\Theta = (\boldsymbol{x} \cdot \boldsymbol{p})/|\boldsymbol{x}|$, evaluation of the derivatives yields:

$$\boldsymbol{p} \cdot \boldsymbol{\nabla}\mathsf{K}(\boldsymbol{x}) \cdot \boldsymbol{p} = \left(1 - 3\cos^2\Theta\right) \frac{\boldsymbol{x}}{|\boldsymbol{x}|^3}, \tag{D.4}$$

$$\begin{aligned} \boldsymbol{ppp} : \boldsymbol{\nabla}\boldsymbol{\nabla}\boldsymbol{\nabla}\mathsf{K}(\boldsymbol{x}) \cdot \boldsymbol{p} &= \left(-9 + 90\cos^2\Theta - 105\cos^4\Theta\right) \frac{\boldsymbol{x}}{|\boldsymbol{x}|^5} \\ &\quad + \left(-18\cos\Theta + 30\cos^3\Theta\right) \frac{\boldsymbol{p}}{|\boldsymbol{x}|^4}. \end{aligned} \tag{D.5}$$

The translational velocity of the second rod placed in the disturbance field $\boldsymbol{u}_1^{(0)}$ is then given by Equation (6.28):

$$\boldsymbol{U}_2^{(0)} = \frac{1}{2l} \int_{-l}^{l} \boldsymbol{u}_1^{(0)}(\boldsymbol{x}_2 + s_2\boldsymbol{p})\mathrm{d}s_2. \tag{D.6}$$

This time, expanding $\boldsymbol{u}_1^{(0)}(\boldsymbol{x}_2 + s_2\boldsymbol{p})$ in a Taylor series about $s_2 = 0$, we find:

$$\boldsymbol{U}_2^{(0)} = \boldsymbol{u}_1^{(0)}(\boldsymbol{x}_2) + \frac{l^2}{6} \boldsymbol{pp} : \boldsymbol{\nabla}\boldsymbol{\nabla}\boldsymbol{u}_1^{(0)}(\boldsymbol{x}_2) + O(|\boldsymbol{x}_2|^{-6}). \tag{D.7}$$

Substituting the expression found for $\boldsymbol{u}_1^{(0)}$ (Equation D.3), we obtain the velocity of the second rod as:

$$\begin{aligned} \boldsymbol{U}_2^{(0)} &= \frac{\varepsilon G_\parallel^2 E_\infty^2 l}{6\mu \log 2\gamma} \left[\left(1 - 3\cos^2\Theta\right) \frac{\boldsymbol{x}l^2}{|\boldsymbol{x}|^3} + \frac{4}{5} \left(-3 + 30\cos^2\Theta - 35\cos^4\Theta\right) \frac{\boldsymbol{x}l^4}{|\boldsymbol{x}|^5} \right. \\ &\quad \left. + \frac{4}{5} \left(-6\cos\Theta + 10\cos^3\Theta\right) \frac{\boldsymbol{p}l^4}{|\boldsymbol{x}|^4} \right] + O(|\boldsymbol{x}|^{-6}), \end{aligned} \tag{D.8}$$

where we used $x_2 = x$. Similarly, $u_1^{(0)}$ induces a rotation of the second rod at an angular velocity given by Equation (6.29):

$$\mathbf{\Omega}_2^{(0)} = \frac{3}{2l^3} \int_{-l}^{l} s_2 \boldsymbol{p} \times \boldsymbol{u}_1^{(0)}(\boldsymbol{x}_2 + s_2 \boldsymbol{p}) \mathrm{d}s_2, \tag{D.9}$$

or, upon expansion of $\boldsymbol{u}_1^{(0)}(\boldsymbol{x}_2 + s_2 \boldsymbol{p})$ about $s_2 = 0$:

$$\mathbf{\Omega}_2^{(0)} = \boldsymbol{p} \times \left(\boldsymbol{p} \cdot \boldsymbol{\nabla} \boldsymbol{u}_1^{(0)}(\boldsymbol{x}_2) + \frac{l^2}{10} \boldsymbol{ppp} : \boldsymbol{\nabla}\boldsymbol{\nabla}\boldsymbol{\nabla} \boldsymbol{u}_1^{(0)}(\boldsymbol{x}_2) \right) + O(|\boldsymbol{x}_2|^{-6}). \tag{D.10}$$

All calculations done, the zeroth-order angular velocity is found to be:

$$\mathbf{\Omega}_2^{(0)} = \frac{\varepsilon G_{\parallel}^2 E_{\infty}^2 l}{2\mu \log 2\gamma} \left[\left(-3 \cos \Theta + 15 \cos^3 \Theta \right) \frac{\boldsymbol{p} \times \boldsymbol{x} l^3}{|\boldsymbol{x}|^4} \right. \tag{D.11}$$
$$\left. + 15 \left(15 \cos \Theta - 70 \cos^3 \Theta + 63 \cos^5 \Theta \right) \frac{\boldsymbol{p} \times \boldsymbol{x} l^5}{|\boldsymbol{x}|^6} \right] + O(|\boldsymbol{x}|^{-6}).$$

For obvious symmetry reasons, the velocity of the first rod induced by the electrophoretic flow on the second rod is the opposite of Equation (D.8), while both angular velocities are the same.

D.2 First reflection

In addition to causing the motion of the second rod, the zeroth-order disturbance $\boldsymbol{u}_1^{(0)}$ created by the first rod also induces a force distribution along the second rod, given by Equation (6.31):

$$\boldsymbol{f}_2^{(1)}(s_2) = \frac{4\pi\mu}{\log 2\gamma} \left(\mathbf{I} - \frac{1}{2}\boldsymbol{pp} \right) \cdot \left[\boldsymbol{U}_2^{(0)} + s_2 \mathbf{\Omega}_2^{(0)} \times \boldsymbol{p} - \boldsymbol{u}_1^{(0)}(\boldsymbol{x}_2 + s_2 \boldsymbol{p}) \right], \tag{D.12}$$

which creates the following disturbance flow:

$$\boldsymbol{u}_2^{(1)}(\boldsymbol{x}) = \frac{1}{8\pi\mu} \int_{-l}^{l} \mathbf{K}(\boldsymbol{x} - \boldsymbol{x}_2 - s_2 \boldsymbol{p}) \cdot \boldsymbol{f}_2^{(1)}(s_2) \mathrm{d}s_2. \tag{D.13}$$

Expanding both $\mathbf{K}(\boldsymbol{x} - \boldsymbol{x}_2 - s_2 \boldsymbol{p})$ and $\boldsymbol{u}_1^{(0)}(\boldsymbol{x}_2 + s_2 \boldsymbol{p})$ in Taylor series about $s_2 = 0$ yields:

$$\boldsymbol{u}_2^{(1)}(\boldsymbol{x}) = -\frac{l^3}{2 \log 2\gamma} \boldsymbol{p} \cdot \boldsymbol{\nabla}\mathbf{K}(\boldsymbol{x} - \boldsymbol{x}_2) \cdot \left. \frac{\partial \boldsymbol{f}_2^{(1)}(s_2)}{\partial s_2} \right|_{s_2=0} + O(|\boldsymbol{x} - \boldsymbol{x}_2|^{-6}), \tag{D.14}$$

which convects the first rod at a velocity:

$$\boldsymbol{U}_1^{(1)} = \frac{1}{2l} \int_{-l}^{l} \boldsymbol{u}_2^{(1)}(\boldsymbol{x}_1 + s_1\boldsymbol{p})\mathrm{d}s_1 = \boldsymbol{u}_2^{(1)}(\boldsymbol{x}_1) + O(|\boldsymbol{x}_1 - \boldsymbol{x}_2|^{-6}). \tag{D.15}$$

The derivatives in Equation (D.14) can be calculated, and recalling that $\boldsymbol{x}_2 - \boldsymbol{x}_1 = \boldsymbol{x}$ we find that the first reflection of the electrophoretic velocity from the second rod back to the first rod results in the following velocity:

$$\boldsymbol{U}^{(1)} = \frac{\varepsilon G_\parallel^2 E_\infty^2 l}{18\mu(\log 2\gamma)^2} \left(1 - 15\cos^2\Theta + 51\cos^4\Theta - 45\cos^6\Theta\right) \frac{\boldsymbol{x}l^5}{|\boldsymbol{x}|^6} + O(|\boldsymbol{x}|^{-6}). \tag{D.16}$$

For symmetry reasons the first reflection on the second rod leads to $\boldsymbol{U}_2^{(1)} = -\boldsymbol{U}_1^{(1)}$. Note that the reflected disturbance flow Equation (D.13) also induces an additional angular velocity on the first rod, which scales as $O(|\boldsymbol{x}|^{-6})$ and therefore is not computed here.

D.3 Relative motion to order $|\boldsymbol{x}|^{-6}$

Realizing that the relative velocity between the two rods is equal to $\boldsymbol{U} = 2\boldsymbol{U}_2$, the above derivations provide an asymptotic expansion for the relative velocity:

$$\boldsymbol{U} = \boldsymbol{U}^{(0)} + \boldsymbol{U}^{(1)} + O(|\boldsymbol{x}|^{-6}), \tag{D.17}$$

where:

$$\boldsymbol{U}^{(0)} = \frac{\varepsilon G_\parallel^2 E_\infty^2 l}{3\mu\log 2\gamma} \left[\left(1 - 3\cos^2\Theta\right) \frac{\boldsymbol{x}l^2}{|\boldsymbol{x}|^3} + \frac{4}{5}\left(-3 + 30\cos^2\Theta - 35\cos^4\Theta\right) \frac{\boldsymbol{x}l^4}{|\boldsymbol{x}|^5} \right.$$
$$\left. + \frac{4}{5}\left(-6\cos\Theta + 10\cos^3\Theta\right) \frac{\boldsymbol{p}l^4}{|\boldsymbol{x}|^4} \right], \tag{D.18}$$

$$\boldsymbol{U}^{(1)} = \frac{\varepsilon G_\parallel^2 E_\infty^2 l}{9\mu(\log 2\gamma)^2} \left(1 - 15\cos^2\Theta + 51\cos^4\Theta - 45\cos^6\Theta\right) \frac{\boldsymbol{x}l^5}{|\boldsymbol{x}|^6}. \tag{D.19}$$

Both rods also rotate at the same angular velocity:

$$\boldsymbol{\Omega} = \frac{\varepsilon G_\parallel^2 E_\infty^2 l}{2\mu\log 2\gamma} \left[\left(-3\cos\Theta + 15\cos^3\Theta\right) \frac{\boldsymbol{p} \times \boldsymbol{x}l^3}{|\boldsymbol{x}|^4} \right.$$
$$\left. + 15\left(15\cos\Theta - 70\cos^3\Theta + 63\cos^5\Theta\right) \frac{\boldsymbol{p} \times \boldsymbol{x}l^5}{|\boldsymbol{x}|^6} \right] + O(|\boldsymbol{x}|^{-6}). \tag{D.20}$$

Higher terms in the expansions could be obtained by considering further reflections of the disturbance field and keeping additional terms in the multipole expansions. Importantly, one should note that the angular velocity is non-zero, and two rods initially aligned with the electric field will not remain so. The assumption of alignment with the field made in Section 6.3.1 is therefore not exact; yet simulations show that departures from the perfect alignment are typically quite weak. Note also that the exact same asymptotic expression for the relative velocity could have been obtained by expanding Equation (6.49) in a Taylor series; higher order terms however would differ, as the method of reflections can account for nonlinear force distributions, unlike the slender-body model of Section 6.3.1 (cf. Equation (6.45)).

D.4   Asymptotic form of the pair distribution function

Equation (6.52) for the pair distribution $p(\boldsymbol{x})$ can be solved analytically in the far-field. Indeed, the leading-order term in $\boldsymbol{U}$ is radial, as shown in Equation (D.18), so that in spherical coordinates (ρ, Θ) (where $\rho = |\boldsymbol{x}|$ and $\cos \Theta = (\boldsymbol{x} \cdot \boldsymbol{p})/|\boldsymbol{x}|$) Equation (6.52) simplifies to:

$$\frac{\varepsilon G_\parallel^2 E_\infty^2 l}{3\mu \log 2\gamma} \left(1 - 3\cos^2 \Theta\right) \frac{1}{\rho^2} \frac{\partial}{\partial \rho} (\log p) = -\boldsymbol{\nabla} \cdot \boldsymbol{U}. \tag{D.21}$$

It is easy to see that $\boldsymbol{U}^{(0)}$ is divergence-free, and that the leading order term in the divergence is therefore $\boldsymbol{\nabla} \cdot \boldsymbol{U}^{(1)}$. Calculating the leading order term in $\boldsymbol{\nabla} \cdot \boldsymbol{U}^{(1)}$ and integrating Equation (D.21) subject to the boundary condition $p(\rho, \Theta) \to 1$ as $\rho \to \infty$ yields:

$$p(\rho, \Theta) = \exp \left(-\frac{(1 - 12\cos^2 \Theta + 15\cos^4 \Theta)l^3}{6 \log 2\gamma \rho^3} \right), \tag{D.22}$$

using Equation (D.19) from the method of reflections. In particular, $p(\rho, \Theta)$ tends to 1 exponentially as $\rho \to \infty$.

Bibliography

[1] Acrivos, A., Jeffrey, D. J. & Saville, D. A. 1990 Particle migration in suspensions by thermocapillary and electrophoretic motion. *J. Fluid Mech.* **212**, 95–110.

[2] Ådland, H. M. & Mikkelsen, A. 2004 Brownian dynamics simulations of needle chains and nugget chain polymer models — rigid contraint conditions versus infinitely stiff springs. *J. Chem. Phys.* **120**, 9848–9858.

[3] Advani, S. & Tucker, C. 1987 The use of tensors to describe and predict fiber orientation in short fiber composites. *J. Rheol.* **31**, 751–784.

[4] Agarwal, U. S., Dutta, A. & Mashelkar, R. A. 1994 Migration of macromolecules under flow: the physical origin and engineering implications. *Chem. Eng. Sci.* **11**, 1693–1717.

[5] Anderson, J. L. 1989 Colloid transport by interfacial forces. *Ann. Rev. Fluid Mech.* **21**, 61–99.

[6] Ausserré, D., Edwards, J., Lecourtier, J., Hervet, H. & Rondelez, F. 1991 Hydrodynamic thickening of depletion layers in colloidal solutions. *Europhys. Lett.* **14**, 33–38.

[7] Bakajin, O. B., Duke, T. A. J., Chou, C. F., Chan, S. S., Austin, R. H. & Cox, E. C. 1998 Electrohydrodynamic stretching of DNA in confined environments. *Phys. Rev. Lett.* **80**, 2737–2740.

[8] BANCHIO, A. J. & BRADY, J. F. 2003 Accelerated Stokesian Dynamics: Brownian motion. *J. Chem. Phys.* **118**, 10323–10332.

[9] BARTHÈS-BIESEL, D. 1980 Motion of a spherical microcapsule freely suspended in a linear shear flow. *J. Fluid Mech.* **100**, 831–853.

[10] BARTHÈS-BIESEL, D. & RALLISON, J. M. 1981 The time-dependent deformation of a capsule freely suspended in a linear shear flow. *J. Fluid Mech.* **113**, 251–267.

[11] BATCHELOR, G. K. 1967 *An Introduction to Fluid Dynamics,* Cambridge University Press.

[12] BATCHELOR, G. K. 1970 Slender-body theory for particles of arbitrary cross-section in Stokes flow. *J. Fluid Mech.* **44**, 419–440.

[13] BATCHELOR, G. K. 1972 Sedimentation of a dilute dispersion of spheres. *J. Fluid Mech.* **52**, 245–268.

[14] BATCHELOR, G. K. & GREEN, J. T. 1972 The determination of the bulk stress in a suspension of spherical particles to order c^2. *J. Fluid Mech.* **56**, 401–427.

[15] BATCHELOR, G. K. 1974 Transport properties of two-phase materials with random structure. *Ann. Rev. Fluid Mech.* **6**, 227–256.

[16] BAZANT, M. Z. & SQUIRES, T. M. 2004 Induced-charge electrokinetic phenomena: Theory and microfluidic applications. *Phys. Rev. Lett.* **92**, 066101.

[17] BHATTACHARYA, S. & BŁAWZDZIEWICZ J. 2002 Image system for Stokes-flow singularity between two parallel planar walls. *J. Math. Phys.* **43**, 5720–5731.

[18] BIRD, H. B., CURTISS, C. F., ARMSTRONG, R. C. & HASSAGER, O. 1987 *Dynamic of Polymeric Liquids,* Wiley Interscience.

[19] BLAKE, J. R. 1971 A note on the image system for a stokeslet in a no-slip boundary. *Proc. Camb. Phil. Soc.* **70**, 303–310.

[20] BERGOUGNOUX, L., GHICINI, S., GUAZZELLI, É. & HINCH, J. 2003 Spreading fronts and fluctuations in sedimentation. *Phys. Fluids* **15**, 1875–1887.

[21] BOEK, E. S., COVENEY, P. V., LEKKERKERKER, H. N. W. & VAN DER SCHOOT, P. 1997 Simulating the rheology of dense colloidal suspensions using dissipative particle dynamics. *Phys. Rev.* E **55**, 3124–3133.

[22] BOSSE, T., KLEISER, L., HÄRTEL, C. & MEIBURG, E. 2005 Numerical simulation of finite Reynolds number suspension drops settling under gravity. *Phys. Fluids* **17**, 037101.

[23] BOSSE, T., KLEISER, L. & MEIBURG, E. 2006 Small particles in homogeneous turbulence: Settling velocity enhancement by two-way coupling. *Phys. Fluids* **18**, 027102.

[24] BOSSIS, G. & BRADY, J. F. 1987 Self-diffusion of Brownian particles in concentrated suspensions under shear. *J. Chem. Phys.* **87**, 5437–5448.

[25] BRADY, J. F. & BOSSIS, G. 1988 Stokesian Dynamics. *Ann. Rev. Fluid Mech.* **20**, 111–157.

[26] BRADY, J. F., PHILLIPS, R. J., LESTER, J. C. & BOSSIS, G. 1988 Dynamic simulation of hydrodynamically interacting suspensions. *J. Fluid Mech.* **195**, 257–280.

[27] BRENNER, H. 1979 Taylor dispersion in systems of sedimenting nonspherical Brownian particles. I. Homogeneous, centrosymmetric, axisymmetric particles. *J. Colloid Interface Sci.* **71**, 189–208.

[28] BRENNER, M. P. 1999 Screening mechanisms in sedimentation. *Phys. Fluids* **11**, 754–772.

[29] BRETHERTON, F. P. 1962 The motion of rigid particles in a shear flow at low Reynolds number. *J. Fluid Mech.* **14**, 284–304.

[30] Brochard, F. & de Gennes, P. G. 1977 Dynamics of confined polymer chains. *J. Chem. Phys.* **67**, 52–56.

[31] Burton, T. M. & Eaton, J. K. 2005 Fully resolved simulations of particle-turbulence interactions. *J. Fluid Mech.* **545**, 67–111.

[32] Butler, J. E. & Shaqfeh, E. S. G. 2002 Dynamic simulations of the inhomogeneous sedimentation of rigid fibres. *J. Fluid Mech.* **468**, 205–237.

[33] Butler, J. E. & Shaqfeh, E. S. G. 2005 Brownian dynamics simulations of a flexible polymer chain which includes continuous resistance and multibody hydrodynamic interactions. *J. Chem. Phys.* **122**, 014901.

[34] Caflisch, R. E. & Luke, J. H. C. 1985 Variance in the sedimentation speed of a suspension. *Phys. Fluids* **28**, 759–760.

[35] Canuto, C., Hussaini, M. Y., Quarteroni, A. & Zang, T. A. 1988 *Spectral Methods in Fluid Dynamics*, Springer.

[36] Chen, S. B. & Koch, D. L. 1996 Electrophoresis and sedimentation of charged fibers. *J. Colloid Interface Sci.* **180**, 466–477.

[37] Chen, Y.-L., Graham, M. D., de Pablo, J. J., Randall, G. C., Gupta, M. & Doyle, P. S. 2005 Conformation and dynamics of single DNA molecules in parallel-plate slit geometry. *Phys. Rev.* E **70**, 060901.

[38] Chun, B. & Ladd, A. J. C. 2006 Inertial migration of neutrally buoyant particles in a square duct: An investigation of multiple equilibrium positions. *Phys. Fluids* **18**, 031704.

[39] Chwang, A. T. & Wu, T. Y. 1974 A note of potential flow involving prolate spheroids. *Schiffstech.* **21**, 19–31.

[40] Chwang, A. T. & Wu, T. Y. 1975 Hydromechanics of low-Reynolds-number flow. Part 2. Singularity method for Stokes flow. *J. Fluid Mech.* **67**, 787–815.

[41] CLAEYS, I. L. & BRADY, J. F. 1989 Lubrication singularities of the grand resistance tensor for two arbitrary particles. *PhysicoChem. Hydrodyn.* **11**, 261–293.

[42] CLAEYS, I. L. & BRADY, J. F. 1993 Suspensions of prolate spheroids in Stokes flow. Part 1. Dynamics of a finite number of particles in an unbounded fluid. *J. Fluid Mech.* **251**, 411–442.

[43] COULIETTE, C. & POZRIKIDIS, C. 1998 Motion of liquid drops through tubes. *J. Fluid Mech.* **358**, 1–28.

[44] COX, R. G. 1969 The deformation of a drop in a general time-dependent fluid flow. *J. Fluid Mech.* **37**, 601–623.

[45] COX, R. G. 1970 The motion of long slender bodies in a viscous fluid. Part 1. General Theory. *J. Fluid Mech.* **44**, 791–810.

[46] DAVIS, R. H. & ACRIVOS, A. 1985 Sedimentation of noncolloidal particles at low Reynolds numbers *Ann. Rev. Fluid Mech.* **17**, 91–118.

[47] DE GENNES, P. G. 1974 Coil-stretch transition of dilute flexible polymers under ultrahigh velocity gradients. *J. Chem. Phys.* **60**, 5030–5042.

[48] DE PABLO, J. J., ÖTTINGER, H. C. & RABIN, Y. 1992 Hydrodynamic changes of the depletion layer of dilute polymer solutions near a wall. *AIChE J.* **38**, 273–283.

[49] DESERNO M. & HOLM, C. 1998 How to mesh up Ewald sums. I. A theoretical and numerical comparison of various particle mesh routines. *J. Chem. Phys.* **109**, 7678–7693.

[50] DOI, M. & EDWARDS, S. F. 1986 *The Theory of Polymer Dynamics*, Oxford University Press.

[51] DRAZIN, P. G. & REID, W. H. 1981 *Hydrodynamic Stability*, Cambridge University Press.

[52] DUKHIN, A. S. 1986 Pair interaction of particles in electric field. 3. Hydrodynamic interaction of ideally polarizable metal particles and dead biological cells. *Colloid J. USSR* **48**, 376–381.

[53] DUKHIN, A. S. & MURTSOVKIN, V. A. 1986 Pair interaction of particles in electric field. 2. Influence of polarization of double layer of dielectric particles on their hydrodynamic interaction in a stationary electric field. *Colloid J. USSR* **48**, 203–209.

[54] DURBIN, P. A. & PETTERSSON REIF, B. A. 2001 *Statistical Theory and Modeling for Turbulent Flows*, Wiley.

[55] DURLOFSKY, L. J. & BRADY, J. F. 1989 Dynamic simulation of bounded suspensions of hydrodynamically interacting particles. *J. Fluid Mech.* **200**, 39–67.

[56] ERMAK, D. L. & MCCAMMON, J. A. 1978 Brownian dynamics with hydrodynamic interaction. *J. Chem. Phys.* **69**, 1352–1360.

[57] ESSMANN, U., PERERA, L., BERKOWITZ, M. L., DARDEN, T., LEE H. & PEDERSEN, L. G. 1995 A smooth particle mesh Ewald method. *J. Chem. Phys.* **103**, 8577–8593.

[58] EWALD, P. P. 1921 Die Berechnung optischer und elektrostatischer Gitterpotentiale. *Ann. Phys.* **64**, 253–287.

[59] FAIR, M. C. & ANDERSON, J. L. 1989 Electrophoresis of nonuniformly charged ellipsoidal particles. *J. Colloid Interface Sci.* **127**, 388–400.

[60] FAN, X., PHAN-THIEN, N. & ZHENG, R. 1998 A direct simulation of fibre suspensions. *J. Non-Newtonian Fluid Mech.* **74**, 113–135.

[61] FAN, X., PHAN-THIEN, N., YONG, N. T., WU, X. & XU, D. 2003 Microchannel flow of a macromolecular suspension. *Phys. Fluids* **15**, 11–21.

[62] FAN, X., PHAN-THIEN, N., CHEN, S., WU, X. & YONG, T. N. 2006 Simulating flow of DNA suspension using dissipative particle dynamics *Phys. Fluids* **18**, 063102.

[63] FANG, L., HU, H. & LARSON, R. G. 2005 DNA configurations and concentration in shearing flow near a glass surface in a microchannel. *J. Rheol.* **127**, 127–138.

[64] FEUILLEBOIS, F. 1984 Sedimentation in a dispersion with vertical inhomogeneities. *J. Fluid Mech.* **139**, 145–171.

[65] FIXMAN, M. 1978 Simulation of polymer dynamics. I. General theory. *J. Chem. Phys.* **69**, 1527–1537.

[66] FIXMAN, M. 1986 Construction of Langevin forces in the simulation of hydrodynamic interaction. *Macromolecules* **19**, 1204–1207.

[67] FRANK, M., ANDERSON, D., WEEKS, E. R. & MORRIS, J. F. 2003 Particle migration in pressure-driven flow of a Brownian suspension. *J. Fluid Mech.* **493**, 363–378.

[68] FRANKEL, N. A. & ACRIVOS, A. 1970 The constitutive equation for a dilute emulsion. *J. Fluid Mech.* **44**, 65–70.

[69] GAMAYUNOV, N. I., MANTROV, G. I. & MURTSOVKIN, V. A. 1992 Study of flows induced in the vicinity of conducting particles by an external electric field. *Colloid J. USSR* **54**, 20–23.

[70] GAMAYUNOV, N. I., MURTSOVKIN, V. A. & DUKHIN, A. S. 1986 Pair interaction of particles in electric field. 1. Features of hydrodynamic interaction of polarized particles. *Colloid J. USSR* **48**, 197–203.

[71] GLENDINNING, A. B. & RUSSEL, W. B. 1982 A pairwise additive description of sedimentation and diffusion in concentrated suspensions of hard spheres. *J. Colloid Interface Sci.* **89**, 124–143.

[72] GRASSIA, P. S., HINCH, E. J. & NITSCHE, L. C. 1995 Computer simulations of Brownian motion of complex systems. *J. Fluid Mech.* **282**, 373–403.

[73] GREENGARD, L. & ROKHLIN, V. 1987 A fast algorithm for particle simulations. *J. Comp. Phys.* **73**, 325–348.

[74] GUAZZELLI, É. 2001 Evolution of particle-velocity correlations in sedimentation. *Phys. Fluids* **13**, 1537–1540.

[75] GUCKEL, G. K. 1999 *Large-Scale Simulations of Particulate Systems Using the PME Method*, Ph.D. Thesis, University of Illinois at Urbana-Champaign.

[76] HABER, S. & HETSRONI, G. 1971 The dynamics of a deformable drop suspended in an unbounded Stokes flow. *J. Fluid Mech.* **49**, 257–277.

[77] HAM, J. M. & HOMSY, G. M. 1988 Hindered settling and hydrodynamic dispersion in quiescent sedimenting suspensions. *Int. J. Multiphase Flow* **14**, 533–546.

[78] HAN, S. P. & YANG, S.-M. 1996 Orientation distribution and electrophoretic motions of rod-like particles in a capillary. *J. Colloid Interface Sci.* **177**, 132–142.

[79] HAPPEL, J. & BRENNER, H. 1965 *Low Reynolds Number Hydrodynamics,* Prentice Hall.

[80] HARLEN, O. G., SUNDARARAJAKUMAR R. R. & KOCH, D. L. 1999 Numerical simulations of a sphere settling through a suspension of neutrally buoyant fibres. *J. Fluid Mech.* **388**, 355–388.

[81] HASIMOTO, H. 1959 On the periodic fundamental solutions of the Stokes equations and their application to viscous flow past a cubic array of spheres. *J. Fluid Mech.* **5**, 317–328.

[82] HENRY, D. C. 1931 The cataphoresis of suspended particles. I. The equation of cataphoresis. *Proc. Roy. Soc. Lond.* A **133**, 106–129.

[83] HERZHAFT, B., GUAZZELLI, É., MACKAPLOW M. B. & SHAQFEH, E. S. G. 1996 Experimental investigation of the sedimentation of a dilute fiber suspension. *Phys. Rev. Lett.* **77**, 290–293.

[84] HERZHAFT, B. & GUAZZELLI, É. 1999 Experimental study of the sedimentation of dilute and semi-dilute suspensions of fibres. *J. Fluid Mech.* **384**, 133–158.

[85] HIEMENZ, P. C. & RAJAGOPALAN, R. 1997 *Principles of Colloid and Surface Chemistry*, Marcel Dekker.

[86] HINCH, E. J. 1977 An averaged-equation approach to particle interactions in a fluid suspension. *J. Fluid Mech.* **83**, 695–720.

[87] HINCH, E. J. 1987 Sedimentation of small particles. In *Disorder and Mixing* (ed. E. Guyon, J.-P. Nadal & Y. Pomeau), chap. IX, pp. 153–161. Kluwer.

[88] HOCKNEY, R. W. & EASTWOOD, J. W. 1981 *Computer Simulation Using Particles,* McGraw-Hill.

[89] HÖFLER, K. & SCHWARZER, S. 2000 Navier-Stokes simulation with constraint forces: Finite-difference method for particle-laden flows and complex geometries. *Phys. Rev.* E **61**, 7146–7160.

[90] HOOGERBRUGGE, P. J. & KOELMAN, J. M. V. A. 1992 Simulating microscopic hydrodynamic phenomena with dissipative particle dynamics. *Europhys. Lett.* **19**, 155–160.

[91] HUNTER, R. J. 2001 *Foundations of Colloid Science*, Oxford University Press.

[92] ICHIKI, K. 2002 Improvement of the Stokesian Dynamics method for systems with a finite number of particles. *J. Fluid Mech.* **452**, 231–262.

[93] JEFFERY, G. B. 1922 The motion of ellipsoidal particles immersed in a viscous fluid. *Proc. R. Soc. Lond.* A **102**, 161–179.

[94] JENDREJACK, R. M., GRAHAM, M. D. & DE PABLO, J. J. 2000 Hydrodynamic interactions in long chain polymers: Application of the Chebyshev polynomial approximation in stochastic simulations. *J. Chem. Phys.* **113**, 2894–2900.

[95] JENDREJACK, R. M., DIMALANTA, E. T., SCHWARTZ, D. C., GRAHAM, M. D. & DE PABLO, J. J. 2003 DNA dynamics in a microchannel. *Phys. Rev. Lett.* **91**, 038102.

[96] JENDREJACK, R. M., SCHWARTZ, D. C., GRAHAM, M. D. & DE PABLO, J. J. 2003 Effect of confinement on DNA dynamics in microfluidic devices. *J. Chem. Phys.* **119**, 1165–1173.

[97] JENDREJACK, R. M., SCHWARTZ, D. C., DE PABLO, J. J. & GRAHAM, M. D. 2004 Shear-induced migration in flowing polymer solutions: Simulation of long-chain DNA in microchannels. *J. Chem. Phys.* **120**, 2513–2529.

[98] JONES, T. B. & WASHIZU, M. 1996 Multipolar dielectrophoretic and electrorotation theory. *J. Electrostat.* **37**, 121–134.

[99] JONES, R. B. 2004 Spherical particle in Poiseuille flow between planar walls. *J. Chem. Phys.* **121**, 483–500.

[100] JOHNSON, R. E. 1980 An improved slender-body theory for Stokes flow. *J. Fluid Mech.* **99**, 411–431.

[101] KIM, S. & KARRILA, S. P. 1991 *Microhydrodynamics: Principles and Selected Applications,* Butterworth-Heinemann.

[102] KOCH, D. L. & SHAQFEH, E. S. G. 1989 The instability of a dispersion of sedimenting spheroids. *J. Fluid Mech.* **209**, 521–542.

[103] KOCH, D. L. & SHAQFEH, E. S. G. 1991 Screening in sedimenting suspensions. *J. Fluid Mech.* **224**, 275–303.

[104] KOCH, D. L. 1994 Hydrodynamic diffusion in a suspension of sedimenting point particles with periodic boundary conditions. *Phys. Fluids* **6**, 2894–2900.

[105] KELLER, J. B. & RUBINOW, S. I. 1976 Slender-body theory for slow viscous flow. *J. Fluid Mech.* **75**, 705–714.

[106] KUMAR, P. & RAMARAO, B. V. 1991 Enhancement of the sedimentation rates of fibrous suspensions. *Chem. Eng. Comm.* **108**, 381–401.

[107] KUUSELA, E., HÖFLER, K. & SCHWARZER, S. 2001 Computation of particle settling speed and orientation distribution in suspensions of prolate spheroids. *J. Eng. Math.* **41**, 221–235.

[108] KUUSELA, E., LAHTINEN, J. M. & ALA-NISSILA, T. 2003 Collective effects in settling of spheroids under steady-state sedimentation. *Phys. Rev. Lett.* **90**, 094502.

[109] LADD, A. J. C. 1992 Dynamical simulations of sedimenting spheres. *Phys. Fluids A* **5**, 299–310.

[110] LADD, A. J. C. 1994 Numerical simulations of particulate suspensions via a discretized Boltzmann equation. Part 1. Theoretical foundation. *J. Fluid Mech.* **271**, 285–309.

[111] LADD, A. J. C. 1996 Hydrodynamic screening in sedimenting suspensions of non-Brownian spheres. *Phys. Rev. Lett.* **76**, 1392–1395.

[112] LADD, A. J. C. 2002 Effects of container walls on the velocity fluctuations of sedimenting spheres. *Phys. Rev. Lett.* **88**, 048301.

[113] LARSON, R. G. 1999 *The Structure and Rheology of Complex Fluids*, Oxford University Press.

[114] LEI, X., ACKERSON, B. L. & TONG, P. 2001 Settling statistics of hard sphere particles. *Phys. Rev. Lett.* **86**, 3300–3303.

[115] LEIGHTON, D. & ACRIVOS, A. 1987 Shear-induced migration of particles in concentrated suspensions. *J. Fluid Mech.* **181**, 415–439.

[116] LEVITAN, J. A., DEVASENATHIPATHY, S., STUDER, V., BEN, Y., THORSEN, T., SQUIRES, T. M. & BAZANT, M. Z. 2005 Experimental observation of induced-charge electro-osmosis around a metal wire in a microchannel. *Colloids Surfaces* A **267**, 122–132.

[117] LIRON, N. & MOCHON, S. 1976 Stokes flow for a Stokeslet between two parallel flat plates. *J. Eng. Math.* **10**, 287–303.

[118] LIRON, N. & SHAHAR, R. 1978 Stokes flow due to a Stokeslet in a pipe. *J. Fluid Mech.* **86**, 727–744.

[119] LOMHOLT, S. & MAXEY, M. R. 2003 Force-coupling method for particulate two-phase flow: Stokes flow. *J. Comp. Phys.* **184**, 381–405.

[120] LUKE, J. H. C. 2000 Decay of velocity fluctuations in a stably stratified suspension. *Phys. Fluids* **12**, 1619–1621.

[121] MA, H. & GRAHAM, M. D. 2005 Theory of shear-induced migration in dilute polymer solutions near solid boundaries. *Phys. Fluids* **17**, 083103.

[122] MACKAPLOW, M. B. & SHAQFEH, E. S. G. 1998 A numerical study of the sedimentation of fibre suspensions. *J. Fluid Mech.* **376**, 149–182.

[123] MANGA, M. & STONE, H. A. 1993 Buoyancy-driven interactions between two deformable viscous drops. *J. Fluid Mech.* **256**, 647–683.

[124] MANGA, M. & STONE, H. A. 1995 Collective hydrodynamics of deformable drops and bubbles in dilute low Reynolds number suspensions. *J. Fluid Mech.* **300**, 231–263.

[125] MAXEY, M. R. & PATEL, B. K. 2001 Localized force representations for particles sedimenting in Stokes flow. *Int. J. Multiphase Flow* **27**, 1603–1626.

[126] METZGER, B., GUAZZELLI, É. & BUTLER, J. E. 2005 Large-scale streamers in the sedimentation of a dilute fiber suspension. *Phys. Rev. Lett.* **95**, 164506.

[127] Metzger, B., Butler, J. E. & Guazzelli, É. 2006 Experimental investigation of the instability of a sedimenting suspension of fibres. *J. Fluid Mech.* (submitted).

[128] Mittal, R. & Iaccarino, G. 2003 Immersed boundary methods. *Ann. Rev. Fluid Mech.* **37**, 239–261.

[129] Mor, R., Gottlieb, M., Mondy, L. A. & Graham, A. L. 2003 Effect of surfaces on the static distribution of orientations in suspensions of rod-like particles. *J. Rheol.* **47**, 19–36.

[130] Morrison, F. A. 1970 Electrophoresis of a particle of arbitrary shape. *J. Colloid Interface Sci.* **34**, 210–214.

[131] Mucha, P. J. & Brenner M. P. 2003 Diffusivities and front propagation in sedimentation. *Phys. Fluids* **15**, 1305–1313.

[132] Mucha, P. J., Tee, S.-Y., Weitz, D. A., Shraiman, B. I. & Brenner M. P. 2004 A model for velocity fluctuations in sedimentation. *J. Fluid Mech.* **501**, 71–104.

[133] Murtsovkin, V. A. 1996 Nonlinear flows near polarized disperse particles. *Colloid J. USSR* **58**, 341–349.

[134] Nguyen, N.-Q. & Ladd, A. J. C. 2004 Microstructure in a settling suspension of hard spheres. *Phys. Rev. E* **69**, 050401.

[135] Nguyen, N.-Q. & Ladd, A. J. C. 2005 Sedimentation of hard-sphere suspensions at low Reynolds number. *J. Fluid Mech.* **525**, 73–104.

[136] Nicewarner-Peña, S. R., Freeman, R. G., Reiss, B. D., He, L., Peña, D. J., Walton, I. D., Cromer, R., Keating, C. D. & Natan, M. J. 2001 Submicrometer metallic barcodes. *Science* **294**, 137–141.

[137] Nicolai, H. & Guazzelli, É. 1995 Effect of the vessel size on the hydrodynamic diffusion of sedimenting spheres. *Phys. Fluids* **7**, 3–5.

[138] NICOLAI, H., HERZHAFT, B., HINCH, E. J., OGER L. & GUAZZELLI, É. 1995 Particle velocity fluctuations and hydrodynamic self-diffusion of sedimenting non-Brownian spheres. *Phys. Fluids* **7**, 12–23.

[139] NITSCHE, L. C. & HINCH, E. J. 1997 Shear-induced lateral migration of Brownian rigid rods in parabolic channel flow. *J. Fluid Mech.* **332**, 1–21.

[140] NOTT, P. R. & BRADY, J. F. 1994 Pressure-driven flow of suspensions: simulation and theory. *J. Fluid Mech.* **275**, 157–199.

[141] NYLAND, G. H., SKJETNE, P., MIKKELSEN, A. & ELGSAETER, A. 1996 Brownian dynamics simulation of needle chains. *J. Chem. Phys.* **105**, 1198–1207.

[142] O'BRIEN, R. W. 1983 The solution of the electrokinetic equations for colloidal particles with thin double layers. *J. Colloid Interface Sci.* **92**, 204–216.

[143] O'BRIEN, R. W. & WARD, D. N. 1988 The electrophoresis of a spheroid with a thin double layer. *J. Colloid Interface Sci.* **121**, 402–413.

[144] ONSAGER, L. 1949 The effects of shape on the interaction of colloidal particles. *Ann. (N.Y.) Acad. Sci.* **51**, 627–659.

[145] PESKIN, C. 2002 The immersed boundary method. *Acta Numerica* **11**, 479–517.

[146] PHUNG, T. N., BRADY, J. F. & BOSSIS, G. 1996 Stokesian dynamics simulation of Brownian suspensions. *J. Fluid Mech.* **313**, 180–207.

[147] POZRIKIDIS, C. 1992 *Boundary Integral and Singularity Methods for Linearized Viscous Flow,* Cambridge University Press.

[148] POZRIKIDIS, C. 1996 Computation of periodic Green's functions of Stokes flow. *J. Eng. Maths* **30**, 79–96.

[149] RAHNAMA, M., KOCH, D. L. & SHAQFEH, E. S. G. 1994 The effect of hydrodynamic interactions on the orientation distribution in a fiber suspension subject to simple shear flow. *Phys. Fluids* **7**, 487–506.

[150] RAMASWAMY S. 2001 Issues in the statistical mechanics of steady sedimentation. *Adv. Phys.* **50**, 297–341.

[151] REINHART, W. H., SINGH, A. & WERNER, S. 1989 Red blood cell aggregation and sedimentation: the role of cell shape. *Brit. J. Hematol.* **73**, 551–556.

[152] ROSE, K. A., MEIER, J. A., DOUGHERTY, G. M. & SANTIAGO, J. G. 2006 Rotational electrophoresis of striped metallic microrods. *Phys. Rev.* E (in press).

[153] RUSSEL, W. B., SAVILLE, D. A. & SCHOWALTER, W. R. 1989 *Colloidal Dispersions*, Cambridge University Press.

[154] SAAD, Y. & SCHULTZ, M. H. 1986 A generalized minimum residual algorithm for solving nonsymmetric linear systems. *SIAM J. Sci. Stat. Comput.* **7**, 856–869.

[155] SAAD, Y. 1996 *Iterative Methods for Sparse Linear Systems,* PWS Publishing Company.

[156] SAFFMAN, P. G. 1973 On the settling speed of free and fixed suspensions. *Stud. Appl. Math.* **52**, 115–127.

[157] SAINTILLAN, D., DARVE, E. & SHAQFEH, E. S. G. 2005 A smooth particle-mesh Ewald algorithm for Stokes suspension simulations: The sedimentation of fibers. *Phys. Fluids* **17**, 033301.

[158] SAINTILLAN, D., SHAQFEH, E. S. G. & DARVE, E. 2006 The growth of concentration fluctuations in dilute dispersions of orientable and deformable particles under sedimentation. *J. Fluid Mech* **553**, 347–388.

[159] SAINTILLAN, D., SHAQFEH, E. S. G. & DARVE, E. 2006 Effect of flexibility on the shear-induced migration of short-chain polymers in parabolic channel flow. *J. Fluid Mech* **557**, 207–306.

[160] SAINTILLAN, D., DARVE, E. & SHAQFEH, E. S. G. 2006 Hydrodynamic interactions in the induced-charge electrophoresis of colloidal rod dispersions. *J. Fluid Mech* **563**, 223–259.

[161] SAINTILLAN, D., SHAQFEH, E. S. G. & DARVE, E. 2006 The effect of stratification on the wavenumber selection in the instability of sedimenting spheroids. *Phys. Fluids* (accepted).

[162] SANGANI, A. S. & MO, G. 1996 An $O(N)$ algorithm for Stokes and Laplace interactions of particles. *Phys. Fluids* **8**, 1990–2010.

[163] SAVILLE, D. A. 1977 Electrokinetic effects with small particles. *Ann. Rev. Fluid Mech.* **9**, 321–337.

[164] SCHIEK, R. L. & SHAQFEH, E. S. G. 1997 Cross-streamline migration of slender Brownian fibres in plane Poiseuille flow. *J. Fluid Mech.* **332**, 23–39.

[165] SCHOENBERG, I. L. 1973 *Cardinal Spline Interpolation*, SIAM.

[166] SCHROEDER, C. M., BABCOCK, H. P., SHAQFEH, E. S. G. & CHU, S. 1997 Observation of polymer conformation hysteresis in extensional flow. *Science* **301**, 1515–1519.

[167] SEGRÈ, P. N., HERBOLZHEIMER, E. & CHAIKIN, P. M. 1997 Long-range correlations in sedimentation. *Phys. Rev. Lett.* **79**, 2574–2577.

[168] SELLIER, A. 2000 Electrophoretic motion of a slender particle embedded in an axisymmetric electric field. *C. R. Acad. Sci. Paris* **328**, 41–46.

[169] SHERWOOD, J. D. & STONE, H. A. 1995 Electrophoresis of a thin charged disk. *Phys. Fluids* **7**, 697–705.

[170] SIEROU, A. & BRADY, J. F. 2001 Accelerated Stokesian Dynamics simulations. *J. Fluid Mech.* **448**, 115–146.

[171] SIEROU, A. & BRADY, J. F. 2002 Rheology and microstructure in concentrated noncolloidal suspensions. *J. Rheol.* **46**, 1031–1056.

[172] SIEROU, A. & BRADY, J. F. 2004 Shear-induced self-diffusion in non-colloidal suspensions. *J. Fluid Mech.* **506**, 285–314.

[173] SMART, J. R. & LEIGHTON, D. T. 1991 Measurement of the drift of a droplet due to the presence of a plane. *Phys. Fluids* A **3**, 21–28.

[174] SMOLUCHOWSKI, M. 1903 Contribution à la théorie de l'endosmose électrique et de quelques phenomènes corrélatifs. *Bull. Int. Acad. Sci. Cracovie* **8**, 182–200.

[175] SOLOMENTSEV, Y. & ANDERSON, J. L. 1994 Electrophoresis of slender particles. *J. Fluid Mech.* **279**, 197–215.

[176] SOLOMENTSEV, Y. & ANDERSON, J. L. 1995 Electrophoretic transport of spheroidal colloids in nonhomogeneous electric fields. *Ind. Eng. Chem. Res.* **34**, 3231–3238.

[177] SOLOMENTSEV, Y., PAWAR, Y. & ANDERSON, J. L. 1993 Electrophoretic mobility of nonuniformly charged spherical particles with polarization of the double layer. *J. Colloid Interface Sci.* **158**, 1–9.

[178] SQUIRES, T. M. & BAZANT, M. Z. 2004 Induced-charge electro-osmosis. *J. Fluid Mech.* **509**, 217–252.

[179] SQUIRES, T. M. & BAZANT, M. Z. 2006 Breaking symmetries in induced-charge electro-osmosis. *J. Fluid Mech.* **560**, 61–101.

[180] STABEN, M. E., ZINCHENKO, A. Z. & DAVIS, R. H. 2003 Motion of a particle between two parallel plane walls in low-Reynolds-number Poiseuille flow. *Phys. Fluids* **15**, 1711–1733.

[181] STICKEL, J. J. & POWELL, R. L. 2005 Fluid mechanics and rheology of dense suspensions. *Ann. Rev. Fluid Mech.* **37**, 129–149.

[182] STOVER, C. A., KOCH, D. L. & COHEN, C. 1992 Observations of fibre orientation in simple shear flow of semi-dilute suspensions. *J. Fluid Mech.* **238**, 277–296.

[183] STRATTON, J. A. 1941 *Electromagnetic Theory*, McGraw-Hill.

[184] TAYLOR, G. I. 1932 The viscosity of a fluid containing small drops of another fluid. *Proc. R. Soc. Lond.* A **138**, 41–48.

[185] TAYLOR, G. I. 1934 The deformation of emulsions in definable fields of flow. *Proc. R. Soc. Lond.* A **146**, 501–523.

[186] TEE, S.-Y., MUCHA, P. J., CIPELLETTI, L., MANLEY, S., BRENNER, M. P., SEGRÈ, P. N. & WEITZ, D. A. 2002 Long-range correlations in sedimentation. *Phys. Rev. Lett.* **89**, 054501.

[187] TORNBERG, A.-K. & GUSTAVSSON, K. 2006 A numerical method for simulations of rigid fiber suspensions. *J. Comp. Phys.* **215**, 172–196.

[188] TURNEY, M. A., CHEUNG, M. K., POWELL R. L. & MCCARTHY, M. J. 1995 Hindered settling of rod-like particles measured with magnetic resonance imaging. *AIChE J.* **41**, 251–257.

[189] USTA, O. B., LADD, A. J. C. & BUTLER, J. E. 2005 Lattice-Boltzmann simulations of the dynamics of polymer solutions in periodic and confined geometries. *J. Chem. Phys.* **122**, 094902.

[190] USTA, O. B., BUTLER, J. E. & LADD, A. J. C. 2006 Flow-induced migration of polymers in dilute solution. *Phys. Fluids* **18**, 031704.

[191] VAN DER ZANDE, B. M. I., KOPER, G. J. M. & LEKKERKERKER, H. N. W. 1999 Alignment of rod-shaped gold particles by electric fields. *J. Phys. Chem.* B **103**, 5754–5760.

[192] WALTON, I. D., NORTON, S. M., BALASINGHAM, A., HE, L., OVISO, D. F., GUPTA, D., RAJU, P. A., NATAN, M. J. & FREEMAN, R. G. 2002 Particles

for multiplexed analysis in solution: Detection and identification of striped metallic particles using optical microscopy. *Anal. Chem.* **74**, 2240–2247.

[193] WANG, H. & DAVIS R. H. 1995 Simultaneous sedimentation and coalescence of a dilute dispersion of small drops. *J. Fluid Mech.* **295**, 247–261.

[194] WOO, N. J., SHAQFEH, E. S. G. & KHOMAMI, B. 2004 Effect of confinement on dynamics and rheology of dilute DNA solutions. I. Entropic spring force under confinement and a numerical algorithm. *J. Rheol.* **48**, 281–298.

[195] WOO, N. J., SHAQFEH, E. S. G. & KHOMAMI, B. 2004 Effect of confinement on dynamics and rheology of dilute DNA solutions. II. Effective rheology and single chain dynamics. *J. Rheol.* **48**, 299–318.

[196] YAMANE, Y., KANEDA, Y. & DIO, M. 1994 Numerical simulation of semi-dilute suspensions of rodlike particle in shear flow. *J. Non-Newtonian Fluid Mech.* **54**, 405–421.

[197] YARIV, E. 2005 Induced-charge electrophoresis of nonspherical particles. *Phys. Fluids* **17**, 051702.

[198] YOUNGREN, G. K. & ACRIVOS, A. 1975 Stokes flow past a particle of arbitrary shape: a numerical method of solution. *J. Fluid Mech.* **69**, 377–403.

[199] ZINCHENKO, A. Z. & DAVIS, R. H. 2000 An efficient algorithm for hydrodynamical interaction of many deformable drops. *J. Comp. Phys.* **157**, 539–586.

[200] ZINCHENKO, A. Z. & DAVIS R. H. 2003 Large-scale simulations of concentrated emulsion flows. *Phil. Trans. R. Soc. Lond.* A **361**, 813–845.